Low Energy Neutron-Proton Interactions

by

Brian Daub

B. A. in Physics Carleton College, June 2006

Submitted to the Department of Physics
in partial fulfillment of the requirements for the degree of

Doctor of Philosophy

at the

MASSACHUSETTS INSTITUTE OF TECHNOLOGY

June 2012

Author .....
Department of Physics
April 17, 2012

Certified by .....
June L. Matthews
Professor of Physics
Thesis Supervisor

Accepted by .....
Krishna Rajagopal
Associate Department Head for Education

Low Energy Neutron-Proton Interactions

by
Brian Daub

Submitted to the Department of Physics
on April 17, 2012, in partial fulfillment of the
requirements for the degree of
Doctor of Philosophy

Abstract

There have been few measurements of cross sections for neutron-proton scattering and radiative capture below 1 MeV. Those measurements which do exist are at a small number of energies and are often inconsistent with theoretical models and with each other. We have conducted several experiments with the goal of obtaining improved data on these cross sections at the University of Kentucky (UKY) and the Los Alamos Neutron Science Center (LANSCE). Feasibility studies for measuring the low energy cross section for np radiative capture have been conducted at both UKY and LANSCE, culminating in a measurement of the cross section at 0.5, 0.9, 1.5, 2.0, and 2.5 MeV at UKY, using a plastic scintillator to detect recoiling deuterons and two BGO scintillators to detect the γ-ray yields at 64.6° and 106.6°. We also performed measurements of the response of BC418 plastic scintillator to low energy protons during these studies, and conducted several additional measurements of the scintillator response at LANSCE and UKY, yielding very precise results from 100 keV to 3.6 MeV. The total cross section for np scattering was measured at UKY from 150 to 800 keV by neutron transmission, measuring the neutron yields in a liquid scintillator with various targets in the beam. The cross section was determined by taking ratios of neutron yields with and without the target, giving cross sections which are independent of detector efficiency and dead time. These results fill a significant gap in the available data below 500 keV.

Thesis Supervisor: June L. Matthews
Title: Professor of Physics

Acknowledgments

To thank everyone who helped make this possible would end up being longer than the thesis itself, and I would like to thank everyone who has ever encouraged me in science, ever. These people in particular, though, I would like to expressly thank.

My advisor, June Matthews, has always provided me with the guidance and motivation to continue looking for deuterons, even when it seemed they would never appear. She was always there to puzzle over results that made no sense or to celebrate when my patient fitting of slices finally paid off. I would especially like to thank her for giving me the opportunity to work on all aspects of such a variety of experiments.

Michael Kovash, my "other" advisor, taught me so much about designing and building experiments, and the importance of finishing the analysis of the old data even when someone is building a table in the other room. He also pushed me to be more confident in what I know, telling me that I designed this experiment, so I should know what to do next, and, as it turned out, I usually did.

There are also countless other people from MIT, LANSCE, and UKY that I need to thank. Vlad Henzl: for his extensive work on the LANSCE hardware, and for teaching me about analysis and Czech rock music. Mark Yuly: for shocking me into the transition from student to colleague. Steve Wender and the LANSCE-NS group: for their support and encouragement and for telling me that negative deuterons was a result I should publish. Joanne Gregory: for getting me where I needed to go and finding me when I didn't check my email. Katrina Koehler, Jen French, Zach Miller, and Hongwei Yang: for their work and support on the hardware and waking me up at 4 AM so I could "fix" the acquisition.

Finally, I would like to thank my parents, for their support and encouragement through all my education, and my fiancee, soon to be wife, Ginger, for providing emotional support for all these years, and putting up with my long trips and late shifts. Without her, I don't think I could have ever completed this work.

Contents

List of Figures

List of Tables

Chapter 1

Introduction

There have been very few measurements of cross sections for neutron-proton interactions below 500 keV. Measurements of these quantities are important for understanding the nuclear force and elucidating the potential models for nucleon interactions and applications of these models to other experimental and theoretical work.

Big Bang Nucleosynthesis, the process by which light elements are formed immediately following the Big Bang, requires accurate nuclear data inputs in order to predict the primordial baryon mass density. This result is most sensitive to the np radiative capture cross section, which is not well measured in the relevant energy range.

Additionally, more low energy total np scattering cross section measurements are required in order to test predictions from different nucleon-nucleon potential models. Fitting the existing measurements with effective range theory yields parameters which show the errors in the data rather than the differences in potential models.

We conducted a series of experiments aimed at measuring low energy cross sections for np radiative capture and the total np scattering cross section. In the course of these experiments, we discovered that the response of plastic scintillators to heavy charged particles is not well known at these low energies. Since understanding this response was important to reducing the backgrounds for the radiative capture experiment, we were prompted to perform systematic measurements of the response of plastic scintillators to protons using the np elastic scattering process to provide protons of variable, known energies.

1.1 Neutron-Proton Radiative Capture

The process called np radiative capture is the formation of a deuteron from a neutron and proton:

$$n + p \rightarrow d + \gamma. \tag{1.1}$$

Kinematically, in the rest frame of the proton, the deuteron receives approximately half of the neutron kinetic energy, and the γ-ray receives approximately the other half of the kinetic energy, plus the deuteron binding energy of 2.235 MeV.

1.1.1 Big Bang Nucleosynthesis

The primary motivation for measuring the $p(n,\gamma)d$ cross section below 500 keV is to improve the nuclear data set used in the models of Big Bang Nucleosynthesis. Production of light elements depends on the early conditions of the universe, in particular the baryon density. During the first second following the Big Bang, the temperature was high enough such that the weak nuclear interactions

$$\begin{aligned} n + \nu_e &\leftrightharpoons p + e^- \\ n + e^+ &\leftrightharpoons p + \bar{\nu}_e \end{aligned} \tag{1.2}$$

were in thermal equilibrium. In this case, the number density for a particle with statistical factor g and a mass m is given by

$$n_{eq} = g(\frac{mT}{2\pi\hbar^2})^{\frac{3}{2}} e^{-\frac{m}{T}} \tag{1.3}$$

Using this, the ratio of the neutron and proton number densities is $n_n/n_p = e^{-Q/T}$, where $Q = m_n - m_p = 1.293$ MeV and using the approximation that $m_n/m_p \approx 1$.

As the temperature dropped below 1 MeV, the Hubble expansion rate caused the number density to decrease such that the average time between collisions became larger than the age of the universe. This resulted in the reaction freezuing out, leaving a fixed ratio of protons to neutrons defined by $n_n/n_p = e^{-Q/T_{\text{Freeze}}}$, where $T_{\text{Freeze}} = 0.8$ MeV. This gives a neutron to proton ratio of 1:5 at freeze-out. This occured approximately 1 second after the Big Bang. Since the weak interactions are no longer in equilibrium, the free neutrons also began to β-decay.

At this point, nucleosynthesis began, with three possible interactions involving

protons and neutrons:

$$\begin{array}{rcl} p+p & \rightarrow & d+e^{+}+\nu_e \\ p+n & \leftrightharpoons & d+\gamma \\ n+n & \rightarrow & d+e^{-}+\nu_e \end{array} \tag{1.4}$$

The nn and pp capture reactions proceed via the weak nuclear force, and so the rate was negligible compared to the np capture reaction, which proceeds via the strong nuclear force. The reverse interaction, photodisintegration of deuterium, could occur until the universe cooled sufficiently such that there are no longer a significant number of 2.235 MeV γ-rays. Once the universe has cooled to this point, deuterium can accumulate. Using equation 1.3, the values for $g_d = 3$, $g_n = g_p = 2$, and the approximation that $m_n \approx m_p \approx m_d/2$, one obtains

$$\frac{n_d}{m_n m_p} = 6(\frac{m_n T}{\pi\hbar^2})^{-\frac{3}{2}} e^{\Delta_m/T} \tag{1.5}$$

where $\Delta_m = 2.235$ MeV is the deuteron binding energy. To define a "start" of Big Bang nucleosynthesis, we consider the point where an appreciable amount of deuterium has formed, such as when $n_p = n_d$. We recast this in terms of $\eta \equiv n_b/n_\gamma$, the ratio of baryons to γ-rays. Based on the freeze-out ratio, $n_p \approx \frac{5}{6} n_b = \frac{5}{6}\eta n_\gamma$, and for a blackbody at temperature T, $n_\gamma \approx 0.24(\frac{T}{\hbar c})^3$, the condition for the "start" of Big Bang nucleosynthesis is

$$1 \approx 6.5\eta(\frac{T}{m_n})^{\frac{3}{2}} e^{\Delta_m/T}. \tag{1.6}$$

This depends on η, so this start time is dependent on the baryon density of the universe. For a fiducial η of 5×10^{-10}, the start temperature is $T \approx 70$ keV, which occurs 200 seconds after the Big Bang.

Once there were an appreciable number of deuterons, production of higher mass number nucleons was possible through the reactions:

$$\begin{array}{rcl} d+n & \rightarrow & t+\gamma \\ d+p & \rightarrow & {}^3\mathrm{He}+\gamma \\ d+d & \rightarrow & t+p \\ d+d & \rightarrow & {}^3\mathrm{He}+n \\ d+d & \rightarrow & {}^4\mathrm{He}+\gamma \end{array} \tag{1.7}$$

Once these heavier isotopes were formed, they could also interact to produce more

^{4}He, which has the largest binding energy of the hydrogen and helium isotopes:

$$\begin{aligned} t + d &\rightarrow {}^4\mathrm{He} + n \\ t + p &\rightarrow {}^4\mathrm{He} + \gamma \\ t + t &\rightarrow {}^4\mathrm{He} + 2n \\ t + {}^3\mathrm{He} &\rightarrow {}^4\mathrm{He} + n + p \\ {}^3\mathrm{He} + n &\rightarrow {}^4\mathrm{He} + \gamma \\ {}^3\mathrm{He} + d &\rightarrow {}^4\mathrm{He} + p \\ {}^3\mathrm{He} + {}^3\mathrm{He} &\rightarrow {}^4\mathrm{He} + 2p \end{aligned} \tag{1.8}$$

A network of these interactions is shown in figure 1-1. To a lesser extent, the interactions that produce higher mass number interactions are also relevant:

$$\begin{aligned} {}^3\mathrm{He} + {}^4\mathrm{He} &\rightarrow {}^7\mathrm{Be} + \gamma \\ t + {}^4\mathrm{He} &\rightarrow {}^7\mathrm{Li} + \gamma \\ {}^7\mathrm{Li} + p &\rightarrow {}^4\mathrm{He} + {}^4\mathrm{He} \\ {}^7\mathrm{Be} + n &\rightarrow {}^4\mathrm{He} + {}^4\mathrm{He} \\ {}^8\mathrm{Be} + \gamma &\rightarrow {}^4\mathrm{He} + {}^4\mathrm{He} \end{aligned} \tag{1.9}$$

These reactions have high Coulomb barriers, so their rate was significantly lower than that for the production of hydrogen and helium isotopes. Additionally, there are no stable isotopes with mass number 8, so producing any elements beyond lithium was impossible before the era of stellar nucleosynthesis. [1]

In order to determine the final isotope abundances, the equations involving the reaction rates and number densities of all these reactions and isotopes must be solved simultaneously. The isotope abundances as a function of time are shown in figure 1-2. [1] The abundances become fixed at late times due to the freeze-out of the nuclear interactions. This happens at $T \approx 35$ keV, approximately 20 minutes after the Big Bang. This depends only on the cross sections for the nuclear interactions and the expansion of the universe, so is insensitive to η. The value of η determines the "start" time of Big Bang nucleosynthesis, and so determines the total duration of the process.

The abundances of the light elements as a function of the baryon mass density, which is directly related to η, are shown in figure 1-3. The bands show the 95% confidence level.[2] The slope of the deuterium curve is extremely steep, indicating that the abundance of ^{2}H has the most sensitive dependence on the baryon density. The higher the value of the baryon mass density, and thus the higher value of η, the earlier the start of nucleosynthesis, and the more time available for deuterons to be fused into ^{4}He. Deuterium has been referred to as the "baryometer of choice" for

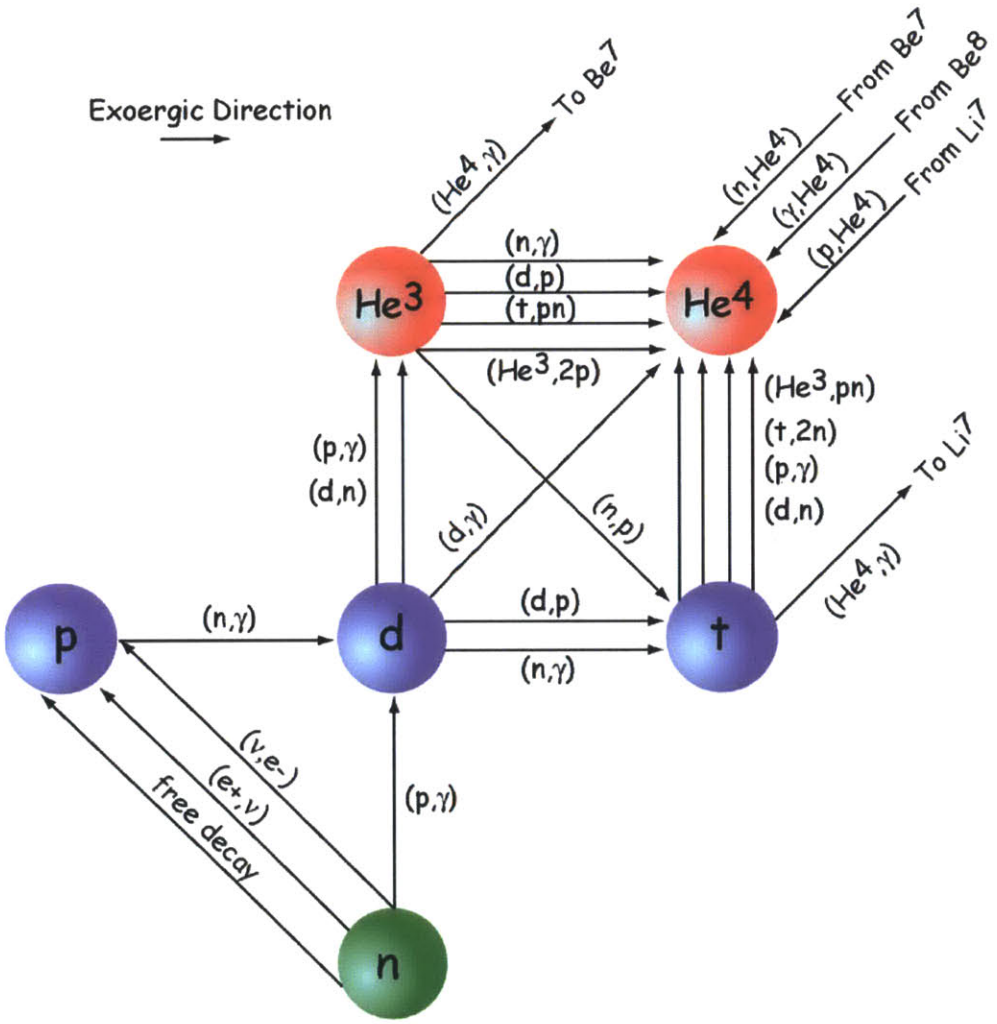

Figure 1-1: Network of interactions of hydrogen and helium isotopes for Big Bang nucleosynthesis models.

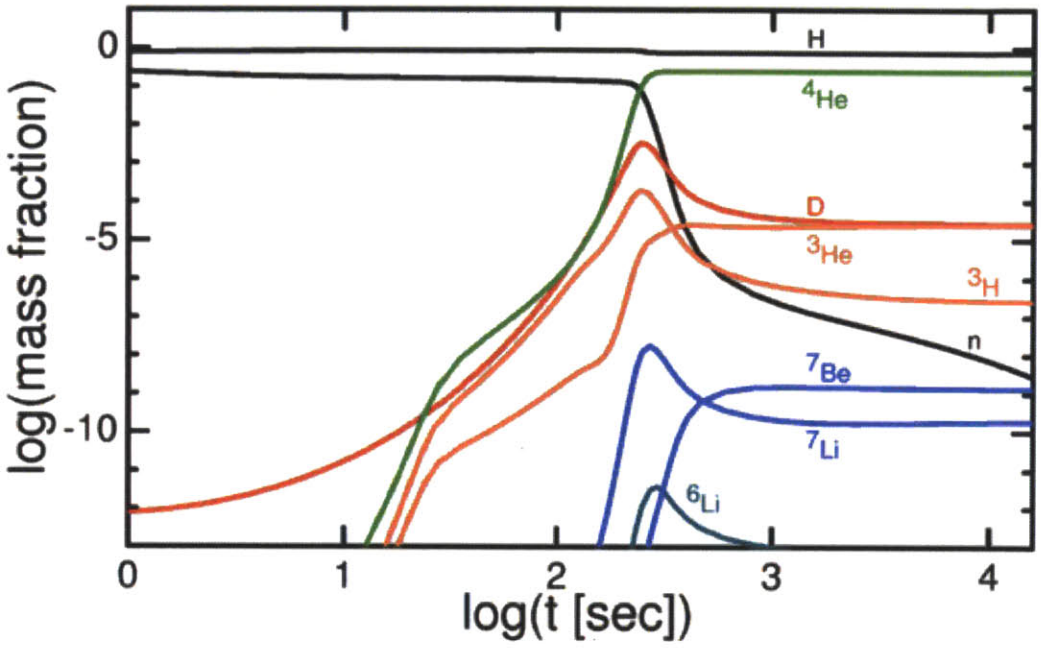

Figure 1-2: Isotope abundances as a function of time. [1]

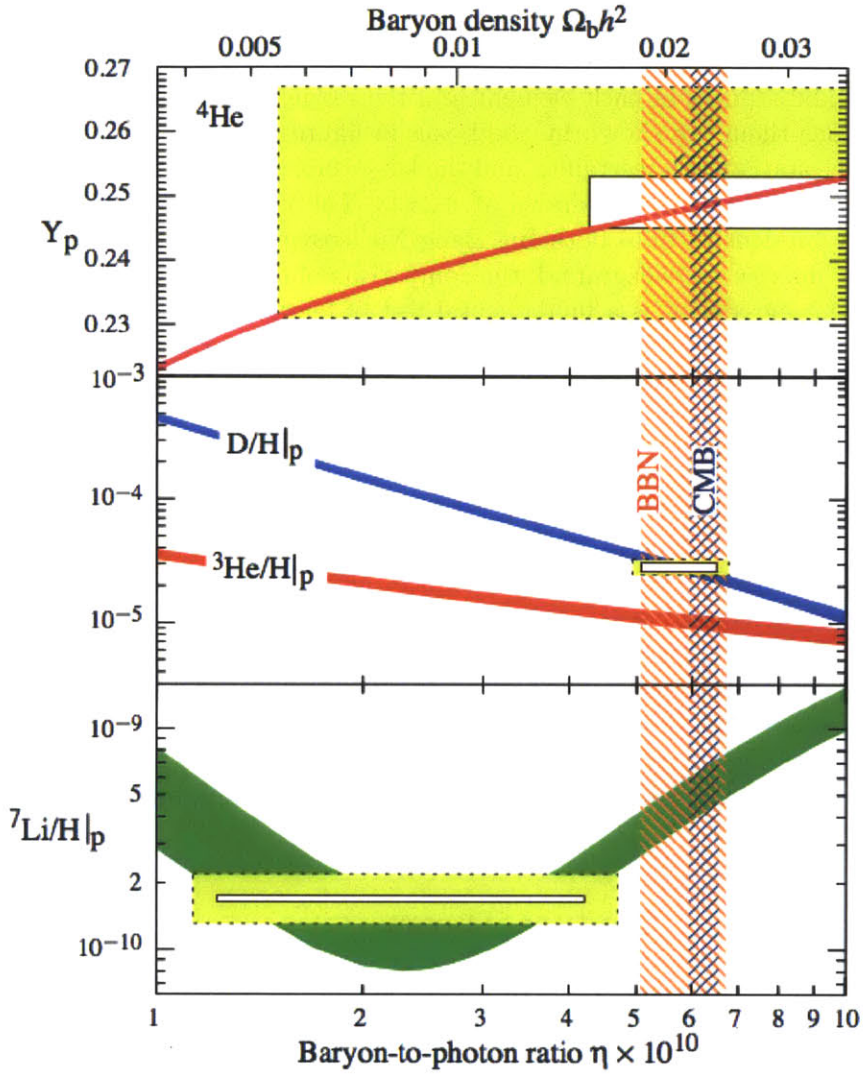

Figure 1-3: Predicted light element abundances from Big Bang Nucleosynthesis as a function of baryon mass density and the baryon-to-photon ratio bands show the 95% confidence level range.[2] The boxes indicate the observed light element abundances, with the smaller boxes indicating $\pm 2\sigma$ statistical errors, and the larger boxes indicating $\pm 2\sigma$ statistical and systematic errors. The narrow vertical band shows the value of the primordial baryon density as measured by the cosmic microwave background (CMB), with the wider band indicating the value predicted by Big Bang Nucleosynthesis, both at the 95% confidence level. [3]

the early universe.[37] Recent measurements of high-redshift hydrogen clouds have yielded deuterium abundances with approximately 10% uncertainty.[38, 39] The measured abundances of each element and the range of allowed baryon densities that produce them are shown by the boxes in figure 1-3, with the smaller boxes showing the statistical uncertainty, and the larger boxes showing the statistical and systematic uncertainty, both drawn at $\pm 2\sigma$.[3] The vertical bands show the predicted baryon density from both Big Bang Nucleosynthesis and measurements of the cosmic microwave background; the comparison of these two measurements and their current agreement is a fundamental test of big-bang cosmology. A detailed comparison with light element abundances predicted by Big Bang nucleosynethesis models allowed for a determination of the baryon density [40]

$$\rho_b = (3.6 \pm 0.4) \times 10^{-31} g/cm^3. \tag{1.10}$$

The uncertainty in the deuterium-inferred baryon density comes in approximately equal parts from the deuterium abundance measurement and from the theoretical error in predicting the deuterium abundance. Due to the lack of data at relevant energies for the $n + p \rightarrow d + \gamma$ reaction, this prediction uses the ENDF-B/VI evaluation [12], normalized to high-precision thermal neutron capture cross section measurements. The uncertainty of this evaluation is difficult to quantify, and there are known systematic problems with the input data. The authors of the ENDF-B/VI evaluation estimate a 1 σ uncertainty of 5% in the overall normalization, [12, 40] which was used in the determination of the baryon mass density.

1.1.2 Radiative Capture Theory

For thermal neutrons, the $p(n,\gamma)d$ reaction proceeds via the $M1$ transition between a $^1S_0$, isospin $T = 1$ scattering state and the deuteron ground state with $^3S_1$ and $^3D_1$ components of $T = 0$. The strength of the $M1$ transition decreases with energy, falling in proportion to $(E_n)^{-1/2}$. The $E1$ transition, connecting a $^3P_1$ $T = 1$ scattering state to the deuteron ground state, increases approximately in proportion to $(E_n)^{1/2}$. The $E1$ and $M1$ strengths are approximately equal at $T_n \approx 500$ keV, and $E1$ begins to dominate above 2 MeV. Figure 1-4 shows the theoretical curve separating the $M1$ and $E1$ transitions, compared to the capture cross section multiplied by the neutron velocity, versus the neutron energy, with some experimental measurements. [4]

The angular distribution of the differential cross section is described by a mul-

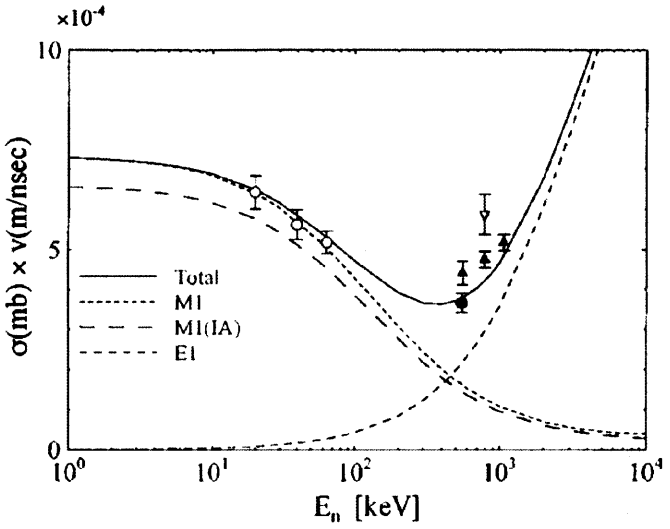

Figure 1-4: Theoretical curves showing the $M1$ and $E1$ strength for the cross section times velocity versus the neutron energy. Figure is taken from Nagai et. al. [4]

tipole expansion

$$\frac{d\sigma}{d\Omega} = a_0 + a_2 P_2(\cos\theta) \tag{1.11}$$

where $P_2(\cos\theta)$ is the second order Legendre polynomial. The $M1$ magnetic transition is isotropic, and so the coefficient a_0 is mostly determined by this transition strength, but may have some contribution from the tensor force in the electric dipole transition. The a_2 coefficient is determined primarily by the electric transition $E1$.[41] Since the Legendre polynomial is zero at an angle of 125.3°, measuring the cross section at this angle gives a measurement of the total cross section for the dipole transition. [4]

1.1.3 Existing Low Energy Capture Measurements

There have been several measurements of the $p(n,\gamma)d$ cross section in this energy range in recent years. [4, 5, 42] The measurements were performed as a single detector experiment, using a NaI γ-ray detector to detect capture events from neutrons on a solid polyethylene target. Neutrons were produced by a pulsed beam of protons on a thin Li target, and the capture cross section was normalized by making an identical measurement using gold, for which the capture cross section is well known. Results were obtained at energies between 100 and 350 keV, and at 550 keV.

There have been more experiments investigating the inverse reaction, $d(\gamma,n)p$, which is related to the capture cross section by detailed balance. Since the cross section is larger and γ sources are more readily available than neutron sources, the experiments are easier to conduct. The difficulty lies in reaching the correct energy above threshold relevant for Big Bang nucleosynthesis. The early measurements used high energy γ-ray sources [7, 11] and γ-rays produced by proton capture on nuclei [8] incident on a deuterium filled ionization chamber. The number of photo-protons identified in the ionization chamber was used to determine the rate of deuteron disintegration events. More recent experiments use neutron capture to produce γ-rays, determining the cross section by passing the photons through 2-m long H_2O and D_2O absorbers. [9] A wider range of γ-ray energies has become available recently; Laser-Compton scattering allowed measurement at multiple energies near threshold by detecting the neutrons produced when the photons were incident on heavy water. [10] Currently, precision measurements of the deuteron photodisintegration cross section close to threshold are ongoing at Forschungszentrum Dresden-Rossendorf, using the bremsstrahlung photons produced by electrons from the ELBE radiation source (Electron Linac for beams

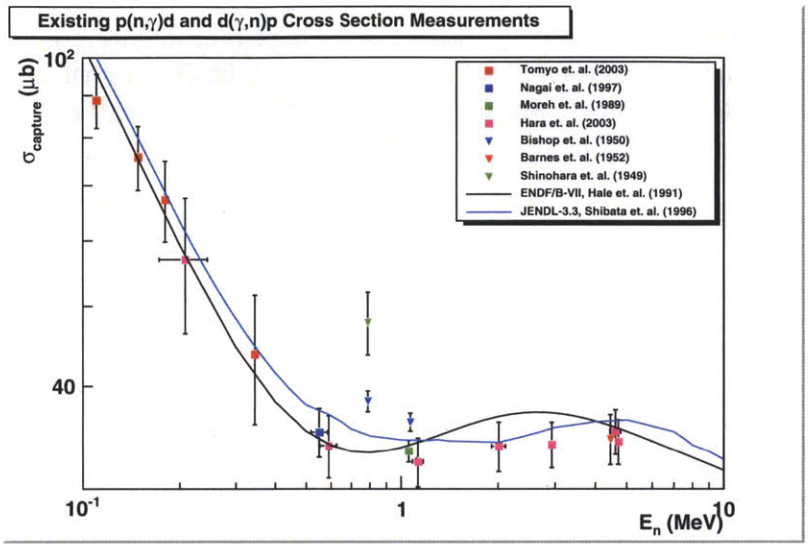

Figure 1-5: Existing $p(n,\gamma)d$ and $d(\gamma,n)p$ cross section measurements and theoretical curves. [4–13] Photodisintegration cross sections have been converted into capture cross sections by detailed balance. There is significant disagreement among the measurements and theories.

with high Brilliance and low Emittance). These photons are incident on a CD_2 target, and the neutrons freed by the photodissociation of the deuterium are detected using plastic scintillators. [43]

Other deuteron interactions also allow for investigation of the capture and photodisentegration cross sections. Measurements of the $d(e,e')np$ cross section close to the breakup threshold at $\theta_e = 180°$ at momentum transfer $q = 0.27$ fm^{-1} have been able to extrapolate the $M1$ transition close to the deuteron breakup threshold, which dominates at the lower range of the relevant Big Bang Nucleosynthesis energies.[44] These extrapolated measurements are in good agreement with the $M1$ transition cross sections calculated by pionless effective field theory. [45]

These results, along with theories, [12, 13] are shown in figure 1-5. The uncertainty in the very low energy points is quite large; the most precise measurement in the range relevant for Big Bang Nucleosynthesis is at 550 keV, with approximately 6.7% uncertainty. [4] Consistent data with less than 5% uncertainty in the 10-600 keV lab energy range are required to improve on the prediction of the primordial baryon density.

To improve on these measurements, we proposed to use a fast plastic scintillator

as an active target, serving as the target for the neutrons and as a detector for the deuterons formed by capture. If we could detect recoiling deuterons in coincidence with a prompt gamma ray, we could overdetermine the kinematics, using this to exclude events involving neutron capture on shielding or other materials near the target.

1.2 Neutron-Proton Total Scattering Cross Section

Nucleon-nucleon interactions and NN potential models are an important representation of the strong interaction. The NN potential models are often used in low-energy applications, including nuclear structure and binding energy;[46] neutrino-deuteron interactions, as used by SNO to detect neutrinos; [47] and proton-proton capture.[48] In order to provide accurate results for these low energy applications, NN potential models must incorporate accurate low-energy data.

1.2.1 Effective Range Theory

Following the treatment in Sachs [41], the exact neutron-proton s-wave elastic cross section is given by

$$\sigma = \frac{3}{4}\sigma_t + \frac{1}{4}\sigma_s, \tag{1.12}$$

where σ_t and σ_s are the cross sections in the triplet state and singlet state, respectively. To determine the cross section, we look at the asymptotic behavior of the wave function

$$\psi \to e^{\imath \mathbf{p}\cdot\mathbf{r}} - \frac{e^{\imath pr}}{r} f(\theta). \tag{1.13}$$

Then the differential cross section is given by the square of the function $f(\theta)$

$$\frac{d\sigma}{d\Omega} = |f(\theta)|^2. \tag{1.14}$$

$f(\theta)$ can be expressed in terms of the phase shifts δ_ℓ of the partial wave components with angular momentum ℓ by

$$f(\theta) = -\frac{1}{2\imath p}\sum_\ell (2\ell+1)(e^{2\imath\delta_\ell} - 1)P_\ell(\cos\theta), \tag{1.15}$$

where P_ℓ is the ℓth order Legendre polynomial. At very low energies, the angular momentum is small if the particle is within the range of the potential, so only the s-wave phase shift will contribute significantly. So as $p \to 0$ the cross section will be determined by $f_0(p)$

$$f(\theta) \approx f_0(p) = -\frac{1}{p} e^{\imath\delta_0} \sin\delta_0, \tag{1.16}$$

and thus

$$\sigma_0(\theta) = |f_0|^2 = \frac{1}{p^2} \sin^2\delta_0. \tag{1.17}$$

As this is an S-wave, the angular distribution is isotropic, and so the total cross section will simply be given by 4π times the differential cross section.

As the energy approaches zero, the cross section is determined by $f_0(0)$, which is defined as the scattering length, a. In the general case, the zero energy cross section is then

$$\sigma_0 = 4\pi a^2 \tag{1.18}$$

Considering both the singlet and triplet states, the zero energy np cross section is given by

$$\sigma_0 = \pi(3a_t^2 + a_s^2), \tag{1.19}$$

where a_t and a_s are the triplet and singlet scattering lengths. A geometric interpretation of a can be obtained by considering the asymptotic form of the wave function

$$u_0 \equiv r\psi = re^{\imath \mathbf{p}\cdot\mathbf{r}} - f_0 e^{\imath pr} \tag{1.20}$$

and substituting $a = f_0$ and taking $p \to 0$

$$u_0 = r - a, \tag{1.21}$$

giving a as the intercept for the asymptotic solution. [41]

Now we assume that the nuclear potential has some form W which is unknown, except that it has a finite range. Consider scattering at two energies E_1 and E_2. For S-waves, the radial equations are

$$u''_{1,2} + (p^2_{1,2} + W)u_{1,2} = 0. \tag{1.22}$$

We also introduce the auxiliary functions $v_{1,2}$ which satisfy the auxiliary equation

$$v''_{1,2} + p^2_{1,2} v_{1,2} = 0 \tag{1.23}$$

and have the same asymptotic form as $u_{1,2}$

$$\lim_{r\to\infty}(u_{1,2}(r) - v_{1,2}(r)) = 0. \tag{1.24}$$

If we multiply equation 1.22 by $u_{2,1}$, then subtract the two equations and integrate, we obtain

$$u_2u_1' - u_1u_2'\Big|_0^\infty = (p_2^2 - p_1^2)\int_0^\infty u_1u_2dr. \tag{1.25}$$

By a similar process, we obtain

$$v_2v_1' - v_1v_2'\Big|_0^\infty = (p_2^2 - p_1^2)\int_0^\infty v_1v_2dr \tag{1.26}$$

for $v_{1,2}$. Subtracting these equations gives

$$v_1(0)v_2'(0) - v_2(0)v_1'(0) = (p_2^2 - p_1^2)\frac{1}{2}\rho(E_1, E_2), \tag{1.27}$$

using equation 1.24, $u_{1,2}(0) = 0$, and defining the effective range as

$$\rho(E_1, E_2) \equiv 2\int_0^\infty (v_1v_2 - u_1u_2)dr. \tag{1.28}$$

If we use the normalization that $v_{1,2}(0) = 1$, then

$$v_2'(0) - v_1'(0) = (p_2^2 - p_1^2)\frac{1}{2}\rho(E_1, E_2). \tag{1.29}$$

Now take $E_1 = 0$ and $E_2 = T$, $p_1 = 0$ and $p_2 = p$ where T and p are the center of mass kinetic energy and momentum, which are related by relativistic kinematics,

$$E = m_n + m_p + T = \sqrt{p^2 + m_n^2} + \sqrt{p^2 + m_p^2}, \tag{1.30}$$

$$p^2 = \frac{1}{4}[E^2 - 2(m_n^2 + m_p^2) + (m_n^2 - m_p^2)^2/E^2]. \tag{1.31}$$

From equations 1.21, 1.24, and the normalization $v_{1,2}(0) = 1$, we can determine functional forms for $v_{1,2}$,

$$v_1 = 1 - \frac{r}{a} \tag{1.32}$$

and

$$v_2 = \frac{\sin(pr + \delta)}{\sin \delta}. \tag{1.33}$$

The derivatives then become

$$v_1'(0) = -\frac{1}{a} \tag{1.34}$$

and

$$v_2'(0) = p \cot \delta. \tag{1.35}$$

Substituting these and rearranging equation 1.29 gives

$$p \cot \delta = \frac{1}{2}\rho(0, T)p^2 - \frac{1}{a}, \tag{1.36}$$

which is substituted into equation 1.17 using the trigonometric identity $\csc^2 \theta = 1 - \cot^2 \theta$ to give the total S-wave scattering cross section for both the singlet and triplet states, [41]

$$\sigma_d = \frac{4\pi}{(a_d^{-1} - \frac{1}{2}\rho_d(0, T)p^2)^2 + p^2)}, \tag{1.37}$$

where the subscript d is t for the triplet and s for the singlet. The partial cross section has a pole at $p = \imath\gamma_d$, where γ_d is the scattering wave number, defined as $\gamma_d^2 = -p^2$ from equation 1.30 for $T = -\epsilon_d$, where ϵ_d is the binding energy.[36]

If p^{-1} is much larger than the well size, the shape of the nuclear potential W has a limited effect on the spectrum. Based on this, the shape independent approximation can be used to replace $\rho_d(0, T)$ with a constant r_d

$$\sigma_d \cong \frac{4\pi}{(a_d^{-1} - \frac{1}{2}r_d p^2)^2 + p^2}. \tag{1.38}$$

The triplet effective range is taken to be the "mixed effective range," which is given exactly as [49]

$$r_t = \rho_t(0, -\epsilon_t) = 2\gamma_t^{-1}\left(1 - \frac{1}{a_t\gamma_t}\right). \tag{1.39}$$

Measuring the elastic cross section σ_p at momentum p can then be used to determine r_s as r_{sp}, the apparent singlet effective range at p, and the parameters a_t, a_s, and r_t.

$$r_s = 2p^{-2}(a_s^{-1} + \sqrt{4\pi/\sigma_{sp} - p^2}) \tag{1.40}$$

where $\sigma_{sp} \equiv 4\sigma_p - 3\sigma_t(p)$ is the estimated singlet partial cross section and $\sigma_t(p)$ is the theoretical cross section determined by equation 1.38. The shape dependence at low energies is measured by a parameter Δr_d, defined such that $\rho_d(0,0) = \rho_d(0,-\epsilon_d) + \Delta r_d$. The condition that $\Delta r_d \neq 0$ is referred to as "zero-energy shape dependence."

Due to correlation of a_t and a_s, we require measurements and parameters which incorporate both and are independent of the correlation. For this, we consider neutron scattering from H_2 gas. We define an operator

$$a = \frac{a_s + 3a_t}{4} + \frac{a_t - a_s}{4}(\boldsymbol{\sigma}_n \cdot \boldsymbol{\sigma}_p) \tag{1.41}$$

where $\boldsymbol{\sigma}_n$ and $\boldsymbol{\sigma}_p$ are the neutron and proton spin operators. Since $(\boldsymbol{\sigma}_n \cdot \boldsymbol{\sigma}_p) = 1$ for the triplet state and $(\boldsymbol{\sigma}_n \cdot \boldsymbol{\sigma}_p) = -3$ for the singlet state, so a will give the correct scattering length for any spin state. The proton spins for H_2 can either form a triplet (orthohydrogen) or a singlet (parahydrogen). The total H_2 scattering length can then be written as

$$a = \frac{a_s + 3a_t}{2} + \frac{a_t - a_s}{2}(\boldsymbol{\sigma}_n \cdot \boldsymbol{S}) \tag{1.42}$$

where $(S) = \frac{1}{2}(\boldsymbol{\sigma}_{p1} + \boldsymbol{\sigma}_{p2})$ denotes the total spin of the H_2 molecule. The zero energy cross section for an unpolarized neutron beam is then

$$\sigma_0 = \pi[(a_s + 3a_t)^2 + (a_t - a_s)^2\overline{(\boldsymbol{\sigma}_n \cdot \boldsymbol{S})^2}], \tag{1.43}$$

since $\overline{(\boldsymbol{\sigma}_n \cdot \boldsymbol{S})} = 0$. Expanding $(\boldsymbol{\sigma}_n \cdot \boldsymbol{S})^2$ leads to the spin identity

$$(\boldsymbol{\sigma}_n \cdot \boldsymbol{S})^2 = \boldsymbol{S}^2 - (\boldsymbol{\sigma}_n \cdot \boldsymbol{S}) \tag{1.44}$$

and averaging over the spins yields

$$\overline{(\boldsymbol{\sigma}_n \cdot \boldsymbol{S})^2} = S(S+1). \tag{1.45}$$

For parahydrogen, $S = 0$, so

$$\sigma_{\text{para}} = \pi(a_s + 3a_t)^2, \tag{1.46}$$

and the parahydrogen scattering length is given by

$$a_c = \frac{3}{2}a_t + \frac{1}{2}a_s. \tag{1.47}$$

This scattering length can be measured from the neutron reflectivity of hydrogenous surfaces.[50]

To fit the parameters a_s, a_t, and r_{s0}, we use measurements of σ_0, the zero energy cross section given by equation 1.19; a_c, the parahydrogen scattering length given by equation 1.47; and σ_p, the total np cross section at center of mass momentum p. To remove the correlation between a_s and a_t, we use σ_0 and a_c as fit parameters instead, relating them to a_s and a_t by

$$s \equiv \sqrt{\frac{1}{12}(\sigma_0/\pi - a_c^2)}, \tag{1.48}$$

and

$$a_s = \tfrac{1}{2}a_c - 3s, \quad a_t = \tfrac{1}{2}a_c + s. \tag{1.49}$$

Extensive work on fitting these parameters to existing σ_0, a_c, and σ_p measurements has been done by Hackenburg, [36] yielding the parameters

$$\begin{aligned}
\sigma_0 &= 20.4278 \pm 0.0078 \text{ b}, && (1.50)\\
a_c &= -3.7406 \pm 0.0010 \text{ fm}, && (1.51)\\
r_{s0} &= 2.750 \pm 0.018_{\text{stat}} - 0.059_{\text{syst}} \text{ fm}, && (1.52)\\
a_t &= 5.4112 \pm 0.0015 \text{ fm}, && (1.53)\\
a_s &= -23.7148 \pm 0.0043 \text{ fm}, && (1.54)\\
\rho_t(0, -\epsilon_t) &= 1.7437 \pm 0.0019 \text{ fm}, && (1.55)\\
\epsilon_s &= 66.26 \pm 0.05_{\text{stat}} + 0.14_{\text{syst}} \text{ keV}. && (1.56)
\end{aligned}$$

Due to the correlation of r_t and r_s, errors for $\rho_t(0,0)$ and $\rho_s(0,0)$ are determined using a new fit parameter $\Delta\rho_t$, with

$$r_t = \rho_t(0,0) + \Delta\rho_t, \quad r_s = \rho_s(0,0) + \langle \partial r_s/\partial r_t \rangle \Delta\rho_t. \tag{1.57}$$

$\Delta\rho_t$ fits to zero, but the standard deviation is used for the fit error to determine

statistically meaningful errors. [36]

$$\rho_t(0,0) = 1.718 \pm 0.025 \text{ fm}, \quad (1.58)$$
$$\rho_s(0,0) = 2.696 \pm 0.059 \text{ fm}, \quad (1.59)$$
$$\Delta r_t = -0.025 \pm 0.025 \text{ fm}. \quad (1.60)$$

This correlation and these uncertainties result in a large shift in the calculated cross section below 1.5 MeV. The maximum deviation occurs at a lab energy of 130 keV, so a simultaneous determination of $\rho_t(0,0)$ and $\rho_s(0,0)$ is most sensitive to a measurement at this energy. A single cross section with a precision of 0.4 mb near 130 keV would reduce the errors on $\rho_t(0,0)$ and Δr_t to 0.001 fm. [36]

1.2.2 Existing *np* Total Scattering Cross Section

Figure 1-6 shows existing neutron-proton cross section data taken from the National Nuclear Data Center. [14–23] There are only eight data points between 100 and 500 keV, which disagree with each other and with the theoretical models. [13, 24] With current results, Δr_t is a measure of errors in the data rather than a measure of zero-energy shape dependence.

The motivation for the present experiment is to allow comparison to predictions from nuclear potential models, the uncertainty on$\rho_t(0,0)$ and Δr_t must be reduced. This is most sensitive at a neutron energy of 130 keV, with the sensitivity dropping to half of it's maximum value at 23 and 620 keV. We measured the total cross section in the energy range of 100 to 800 keV, focusing the majority of our data between 100 and 600 keV.

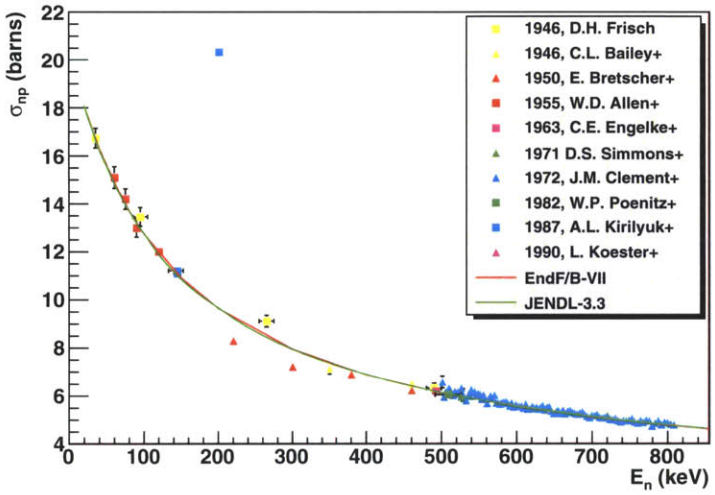

Figure 1-6: Existing *np* total scattering cross section data below 800 keV,[14–23] with theoretical curves.[13, 24] There is a lack of consistent data between 100 and 500 keV.

Chapter 2

Neutron Production Facilities

Our group had two facilities available for neutron production, the University of Kentucky and the Weapons Neutron Research Facility at the Los Alamos Neutron Science Center. Each facility offered different neutron energy ranges and fluxes.

2.1 University of Kentucky

The University of Kentucky houses a 7 MeV Van de Graaff accelerator which is used to accelerate charged particles, typically protons, deuterons, or ^{3}He ions. For our experiments, we used protons. Gaseous hydrogen is ionized by a radio-frequency electric field. A DC beam is produced by accelerating the positive plasma that leaks out of the ion source and then focusing the ions together into the beam.

To pulse the beam, a radio-frequency sweeping magnetic field is produced, which causes the focused beam to travel in an ellipse. This ellipse lands on the chopping apparatus, so that the beam only passes through the chopper once per rotation. Since the period of the sweep magnet is 1.875 MHz, the beam pulsing has this same period, which results in 533 ns between beam pulses. The pulsing is further refined by a bunching magnet, which squeezes the beam in time, so that all the protons arrive at the neutron production target within one nanosecond. The accelerator configuration is shown in figure 2-1.

Two types of neutron production targets were used, a solid lithium fluoride target and a tritium gas cell. These produced neutrons via the ^{7}Li(p,n)^{7}Be reaction and the ^{3}H(p,n)^{3}He reaction, which have Q values of -1.644 and -0.764 MeV, respectively.[51, 52] The tritium cell has a fixed length of 3 cm and a gas density of 0.24975 mg/cm^3, so that for a given proton energy, the flux and energy spectrum is fixed for the tritium cell. The LiF targets were produced by evaporating LiF onto

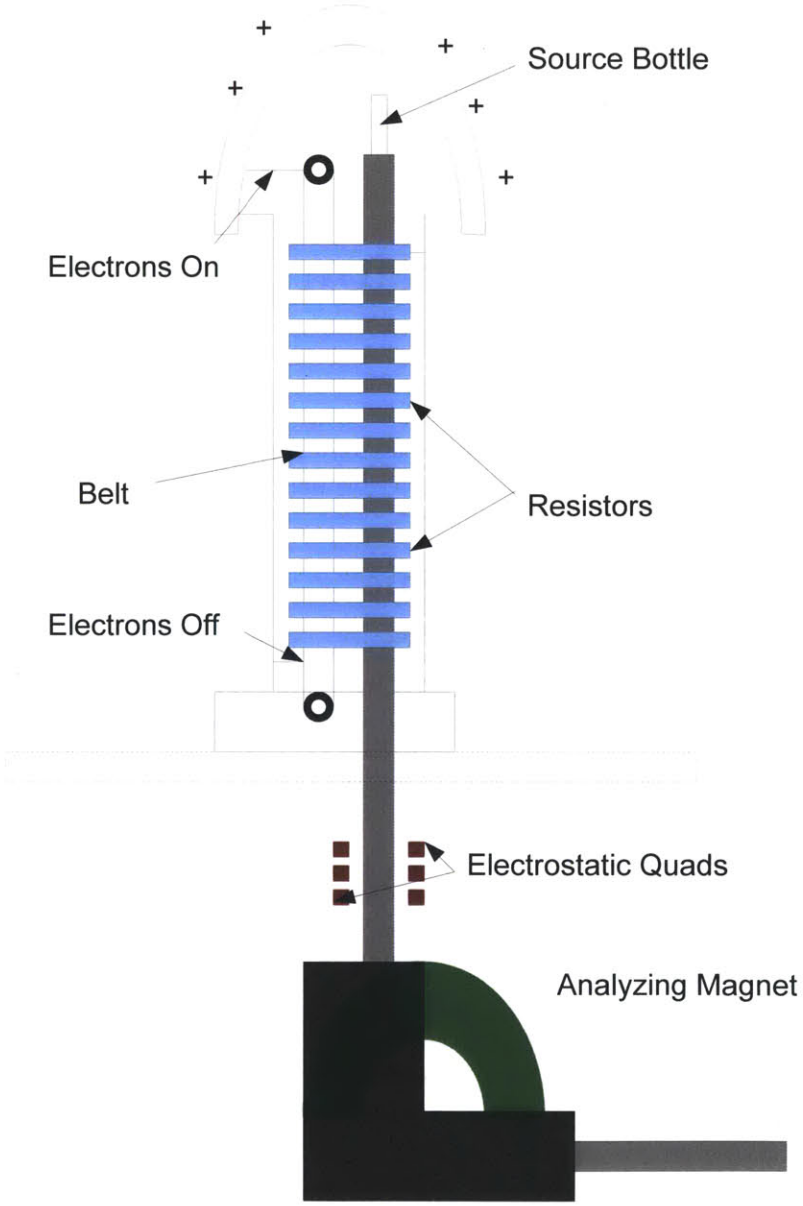

Figure 2-1: The ion source and accelerator at UKY.

a tantalum disc, allowing them to be made with varying thicknesses. So while the flux at a given neutron energy will be approximately fixed, the range of the energy spectrum will vary with the target thickness, allowing us to either produce a wide range of neutron energies with a thick target, or a very narrow energy range with a very thin target.

2.1.1 Neutron Yields

To determine the neutron energy spectrum and yield, we need to know the rate of energy loss in the production target. As protons pass through the target, they lose energy until they interact and produce a neutron or fall below the production threshold. So the energy spectrum and flux will depend on the thickness and density of the target and the rate of proton energy loss in the target medium. This energy loss is determined by the Bethe-Bloch formula,[53]

$$-\frac{dE}{dx} = 2\pi N_a r_e^2 m_e c^2 \rho \frac{Z}{A}\frac{z^2}{\beta^2}[ln(\frac{2m_e c^2\gamma^2\beta^2 W_{\max}}{I^2}) - 2\beta^2] \tag{2.1}$$

where N_a is Avogadro's number, r_e is the classical electron radius 2.817×10^{-13} cm, m_e is the electron mass, ρ is the density of the target material, Z is the atomic number of the absorbing material, A is the atomic weight of the absorbing material, z is the charge of the incident particle in units of e, $W_{\max}$ is the maximum energy transfer in a single collision, and I is the mean excitation potential. Based on kinematics,

$$W_{\max} = \frac{2m_e c^2\beta^2\gamma^2}{1 + 2\frac{m_e}{M}\sqrt{1+\beta^2\gamma^2} + \frac{m_e^2}{M^2}} \tag{2.2}$$

where M is the mass of the incident particle. For the mean excitation potential, we used the semi-empirical formulas [53]

$$\begin{aligned} \tfrac{I}{Z} &= 12 + \tfrac{7}{Z} \text{ eV} && Z < 13 \\ \tfrac{I}{Z} &= 9.76 + 58.8Z^{-1.19} \text{ eV} && Z \geq 13 \end{aligned} \tag{2.3}$$

Using equations 2.1, 2.2, and 2.3, we can determine how much material the protons will travel through for a given proton energy, and then use the cross sections for ^{3}H(p,n)^{3}He [52] and ^{7}Li(p,n)^{7}Be [51] to determine the neutron yield.

Using LiF target instead of metallic Li made the target easier to produce and handle, but it decreased the potential neutron flux. The addition of the fluorine

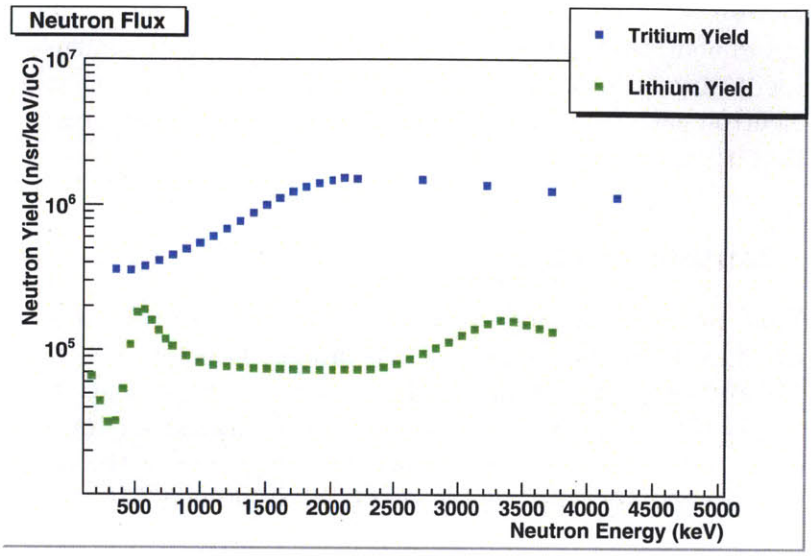

Figure 2-2: Calculated neutron yields for the LiF and Tritium targets. The thickness determined the range of neutron energies produced for a given proton energy.

atoms increased the rate of proton energy loss without providing additional targets for the ^{7}Li(p,n)^{7}Be reaction. A pure Li target would yield an increased flux at all neutron energies.

The neutron yields for the tritium and LiF targets are shown in figure 2-2. The target thickness determined the range of neutron energies produced by a given proton beam energy. This plot shows that the neutron yield for tritium is significantly higher than for LiF at all energies. However, this does not include the limitations of the accelerator. The maximum current for pulsed protons is 2.0 μA, but a lower current was required for use of the tritium cell to avoid rupturing of the cell, resulting in a tritium leak. Including this limitation gives the maximum neutron yield, which is shown in figure 2-3. The limit on the current causes the falloff in the tritium yield at lower energies, and the two become comparable below 1 MeV.

The radiative capture data were taken using both LiF and tritium. The scintillator response and total scattering cross section data were taken using only LiF, as the more precise control over the neutron energy spectrum was more useful than the increased flux.

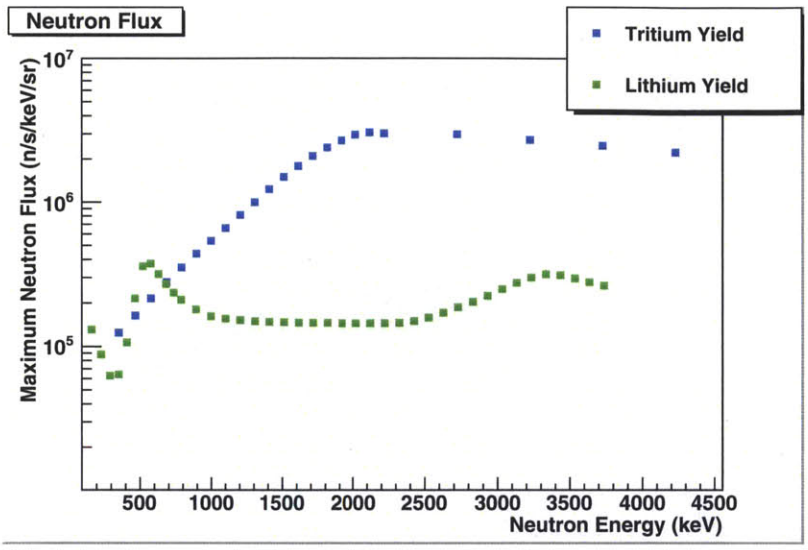

Figure 2-3: Calculated maximum neutron yields for the LiF and Tritium targets, incorporating the current limits for the facility.

2.1.2 Flight Path

The target room contained a large pit, designed to trap some of the neutrons which scatter downward out of the beam. This significantly reduced the room background caused by neutrons scattering on the collimation and shielding. Above this, a large, rotating arm allowed us to place collimation, targets, and detectors above the pit, either along the beam line for the radiative capture and total cross section measurements, or at an angle for the scintillator response measurements, as shown in figure 2-4.

2.2 Los Alamos Neutron Science Center

We also took data at the Weapons Neutron Research (WNR) Facility at the Los Alamos Neutron Science Center (LANSCE). LANSCE has an 800 MeV proton linear accelerator (linac) that generates the primary beam for the production of neutron beams.

The protons for the linac are initially produced in the injector system, where the ion source produces H^- ions inside high voltage domes. These ions are run

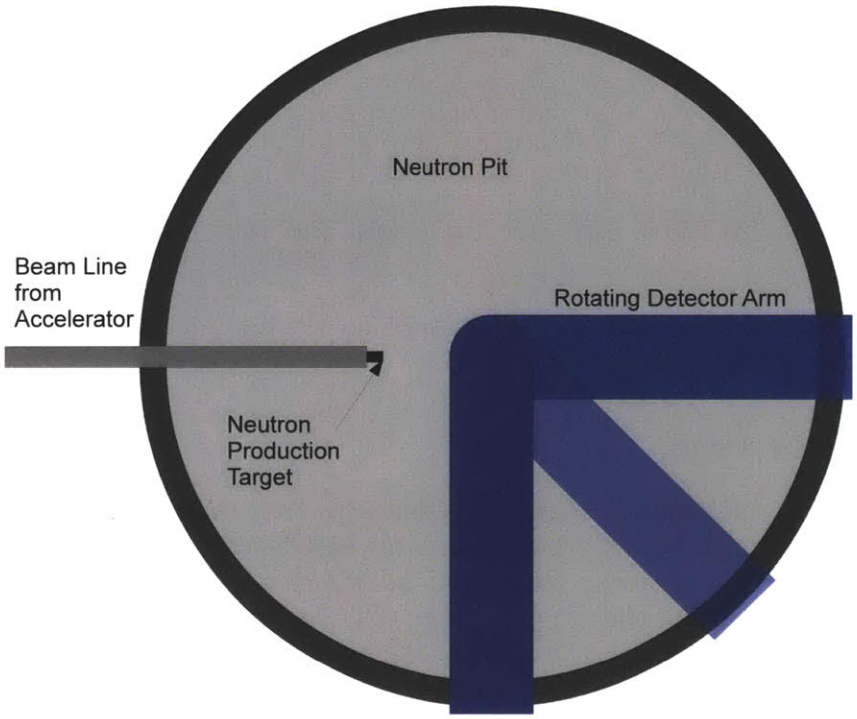

Figure 2-4: Top view of the flight path at UKY, showing the rotating detector arm and neutron pit beneath.

through a Cockroft-Walton generator, which accelerates the particles to 750 keV when they leave the injector. The beam is bunched and matched into a 201.25 MHz drift tube linac, where the protons are accelerated to 100 MeV. From here, the particles are directed into an 805 MHz side-coupled-cavity linac, which accelerates the particles up to 800 MeV.

Once this final energy has been reached, the proton beam can be directed into several experimental areas, including Area-B, the Lujan Neutron Scattering Center, and WNR. Beam is controlled independently in these areas, allowing most experiments to run simultaneously.

2.2.1 Beam Time Structure

The time structure of the beam was important for our measurements of time of flight. Proton beam macropulses were directed at the WNR spallation target at a rate of 40 Hz. Each macropulse is approximately 625 μs long, leaving approximately 24 ms of time with no beam between macropulses. During this time, electronics could be read out by the DAQ computer, minimizing the deadtime that occurs during beam.

Each macropulse is further divided into micropulses. The micropulses are very narrow, 0.2 ns in width, and are separated by either 1.8 or 3.6 μs. The beam with 3.6 μs spacing was specifically requested by our group in order to reach extremely low energies. For our 16 m flight path, neutrons below 500 keV have a time of flight greater than 1.8 μs, the standard micropulse spacing, so that these neutrons arrive at the same time as higher energy neutrons from the following micropulse. With neutrons produced within a 0.2 ns window and a full 3.6 μs window for time of flight, we were in principle able to reach neutron energies as low as 100 keV.

The neutron beam for this experiment was produced by directing the chopped proton beam onto an unmoderated tungsten spallation target (target 4). A sweep magnet removes charged particles from the beam, and the resulting neutrons have a continuous energy spectrum from approximately 0.1 MeV up to 800 MeV. The neutrons are scattered to all kinematically possible angles, but there are primary shutters which deliver the neutron beam at specific angles with respect to the proton beam. Our experiment was located at a 15° angle, at the flight path designated as 4FP15R, shown in figure 2-5, with our experimental shed approximately 16 m from the spallation target.

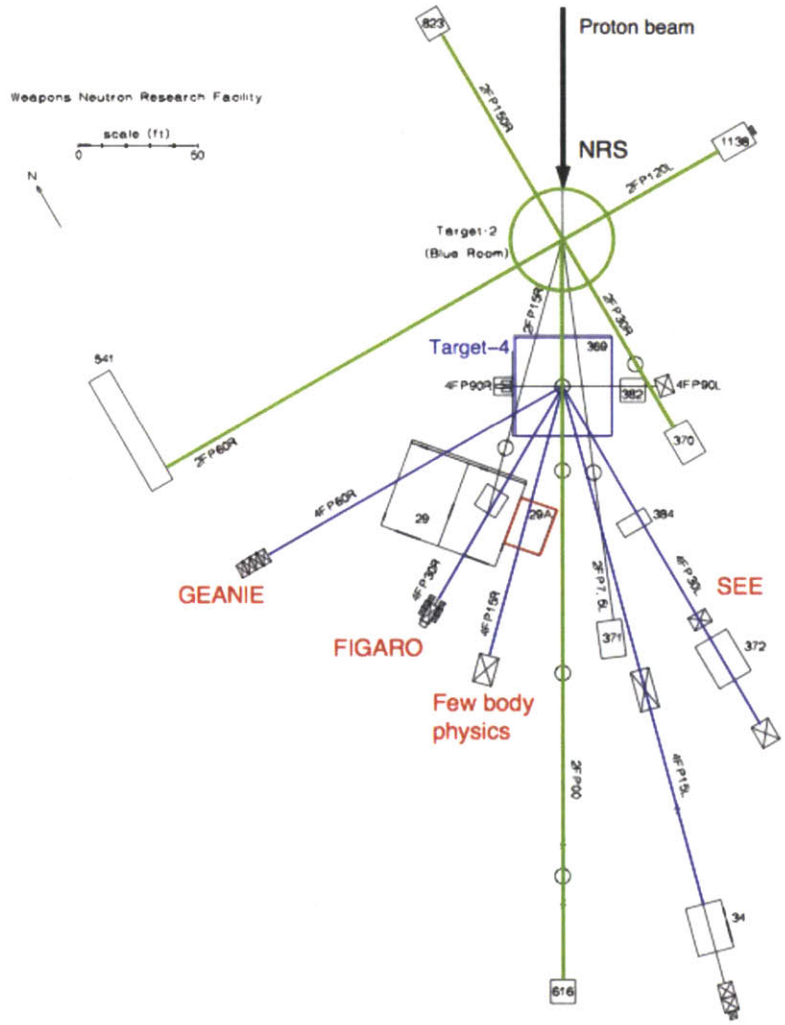

Figure 2-5: Flight paths at WNR as of 2010. Our experiment ran on 4FP15R, the flight path labeled Few Body Physics. Other experiments include the Germanium Array for Neutron Induced Excitations (GEANIE), a large scale, high precision γ-ray spectrometer; the Fast-neutton Induced Gamma Ray Observer (Figaro), an array of neutron detectors used to measure neutron emissions from neutron induced reactions; and Single Event Effect (SEE) testing, now renamed Irradiation of Chips and Electronics (ICE), which measures the effects of neutrons on computer and electronic components.

2.2.2 Neutron Flux

Since we are interested in neutron energies below 1 MeV, it may seem inefficient to use such a high energy neutron beam for this experiment. However, even with the maximum neutron energy of 800 MeV, the flux at low energies is much larger than the flux at high energies. The calculated neutron flux is shown in figure 2-6 for multiple angles with respect to the proton beam direction. With our flight path at 15°, the red curve shows the neutron flux, which is highest below 1 MeV. This angle is not optimal for experiments in the 1 MeV range, as the ratio of low to high energy neutrons decreases with decreasing angle. However, the our group's previous experiments, which used the 100 to 700 MeV range, were set up on this flight path, and no other flight path was available. The higher energy neutrons still constitute a significant background. Even using an electronic veto to prevent higher energy events from triggering the electronics, the high energy neutrons produce extremely large pulses in the active target which lasted for several microseconds. In order to prevent these large pulses from overwhelming the active target, we were forced to run with a very small shutter opening, significantly reducing the neutron flux.

2.2.3 Flight Path

The beam to the experimental shed was controlled by two copper shutters. The horizontal shutter was 18″ thick, and the vertical shutter was 14″ thick. Previous experiments on this flight path used a shutter opening of 1.5″ × 1.5″. This shutter opening allowed the beam to completely and uniformly illuminate the 3 m long, 1″ diameter iron collimator upstream of the experimental target, as shown in figure 2-7. In order to limit the neutron flux, which was necessary, due to backgrounds arising from much higher energy neutrons, we ran with a shutter opening of 1.0″ × 0.55″ .

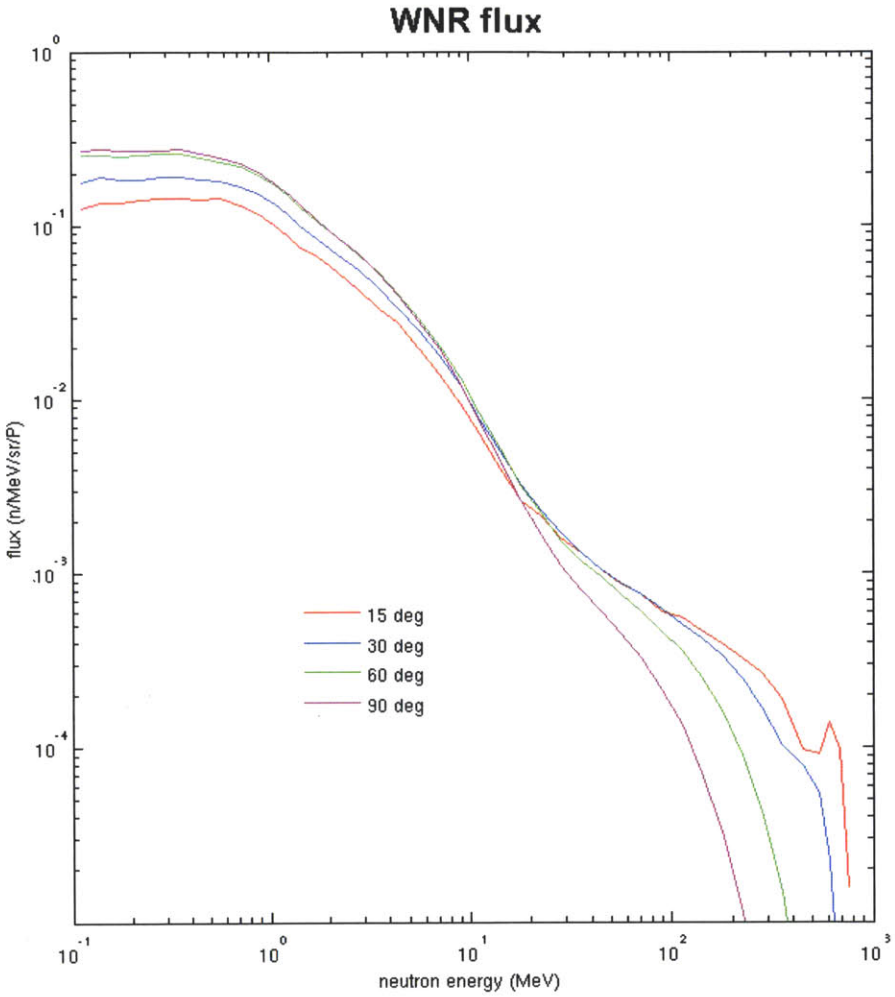

Figure 2-6: Calculated neutron spectrum from target 4 at LANSCE. Our flight path was at 15 degrees, giving us the flux shown in the red curve. While this angle is not optimal for the 1 MeV range, our group's previous experiments were set up on this flight path, and no other flight paths were available.

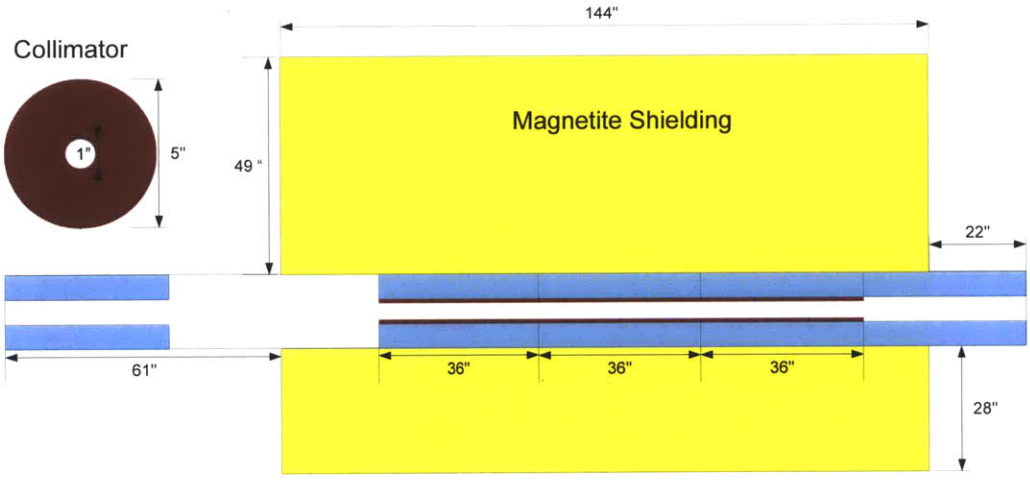

Figure 2-7: The collimation consisted of a beam pipe which ran through a magnetite shielding wall (yellow). Iron sleeves (blue) are fitted in the beam pipe, and the final collimation is provided by 18 iron rings (red) with 1″ diameter holes.

Chapter 3

Experimental Setup

While the configurations of the experiments conducted at LANSCE and UKY were significantly different, they shared a common overall plan as well as a common detector, the active target.

3.1 Active Target

Our measurement of the $p(n,\gamma)d$ cross section is distinguished from previous measurements by our use of an active target. The target was composed of a fast, plastic scintillator, viewed by two photomultiplier tubes operated in coincidence to minimize single-photoelectron noise. For the original feasibility tests at both the University of Kentucky and LANSCE, a $76 \times 76 \times 2$ mm plastic scintillator was used with two 1.9 cm phototubes which matched the cross sectional area of the scintillator. These 10-stage photomultiplier tubes proved to have much too small gain to allow us to see the low energy signals which interested us without a factor of 100 amplification.

Following these initial tests, a higher gain active target was designed, with a $50 \times 50 \times 2$ mm BC418 scintillator. This target was designed for use at LANSCE, where the collimation limited the beam to a 2.2 cm diameter spot. Additional surface area of the scintillator would not be illuminated by the beam and so would only serve to create additional noise from background radiation.

Cylindrical light guides were attached to the two 50 mm diameter, 14-stage photomultiplier tubes with a notch cut along the opposite side such that the scintillator fit into it. The photomultiplier tubes were chosen for their high gain, fast response, and relatively low noise.

The scintillator and phototubes were wrapped in several layers of teflon tape

to enhance reflection and reduce light loss along the length of the scintillator, and then wrapped in several layers of black electrical tape to prevent light leaks.

Two aluminum bars were used to provide rigid support to the active target. These were a source of background at the University of Kentucky, as they were illuminated by the uncollimated neutron beam. The phototube bases were housed in metal boxes which were also wrapped in black electrical tape in order to prevent light leaks. A schematic drawing of the active target is shown in figure 3-1.

3.2 Radiative Capture and Scintillator Response at LANSCE

The earliest feasibility studies for the radiative capture measurement were performed at the University of Kentucky using several low gain active targets and a high purity germanium detector to detect the γ-rays. However, the signal to background ratio from these tests proved to be 1:1000. After these studies, we performed a similar feasibility test at the Los Alamos Neutron Science Center.

3.2.1 Detectors

The active target was used as the proton target. A BrilLanCe^{TM} scintillator was used to detect the γ-rays produced by capture, and a liquid scintillator was used to monitor elastic neutron scattering from the active target. Total neutron flux was measured by a fission ionization chamber.

3.2.1.1 Detector Configuration

The fission chamber and active target were placed directly in the beam. The fission chamber was placed directly at the end of the collimation, 15.45 m from the spallation target. The active target was placed 1 m downstream of the fission chamber.

The BrilLanCe detector was placed 14 cm away from the active target at an angle of 125° from the beam. This angle was chosen such that the second order Legendre polynomial in equation 1.11 will be zero, and so the measurement of the cross section at this angle would yield the total cross section for the dipole transition.

The elastic monitor was placed at a forward angle of 15°, 27 cm from the active target. The liquid scintillator was later moved to 45° to allow access to a larger

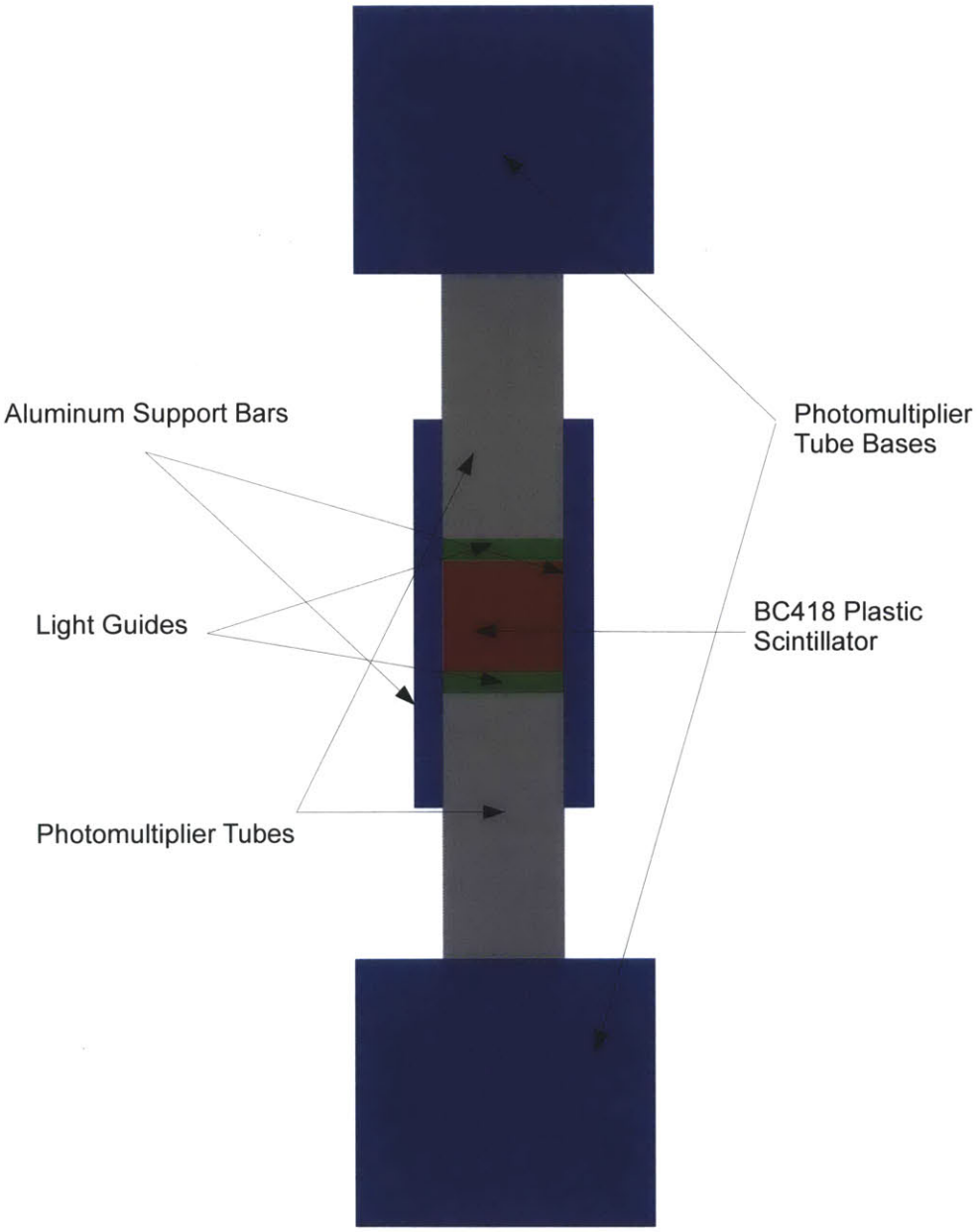

Figure 3-1: Schematic of the active target.

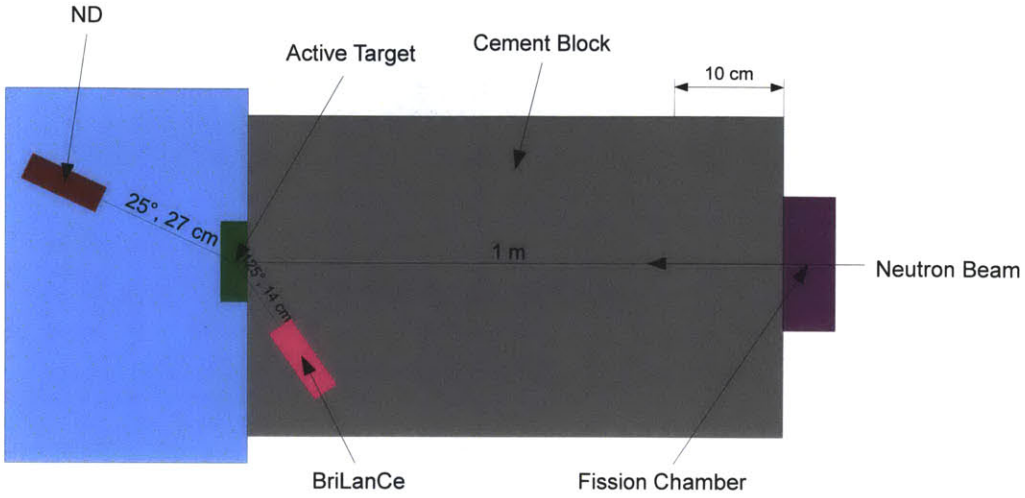

Figure 3-2: Detector configuration for the radiative capture and scintillator response measurements performed at LANSCE.

range of recoiling protons while measuring the scintillator response. The detector configuration is shown in figure 3-2.

3.2.1.2 BrilLanCe

To detect the γ-ray we used a 3″ by 3″ BrilLanCe 380 scintillator, composed of $LaBr_3$:Ce. These detectors have a much higher energy resolution and efficiency than NaI. The scintillation properties of BrilLanCe compared with several other scintillators is shown in table 3.1.[35]

With its high light output and fast decay time, the BrilLanCe detector gives very fast signals and clean timing. In this coincidence experiment, the relative timing of the active target and the BrilLanCe is crucial, making the BrilLanCe the best choice for γ-ray detector. The intense, fast output of light can cause nonlinear effects in the photomultiplier tube. This was seen in our calibrations of the BrilLanCe.

3.2.1.3 Fission Chamber

Beam flux was monitored by a fission ionization chamber. [54] Two foils, ^{235}U and ^{238}U, were placed inside an aluminum chamber. Thin (1/4 mm) stainless steel

Scintilator	Light Yield (photons /keV)	1/e decay time (ns)	F.O.M. $\sqrt{t/LY}$	Wavelength of Maximum Emission λ_m (nm)	Refractive Index at λ_m	Density (g/cm^3)	Thickness (cm) for 50% attenutation (662 keV)
NaI(TI)	38	250	2.6	415	1.85	3.67	2.5
BrilLanCe 350	29	28	0.8	350	~1.9	3.85	2.3
BrilLanCe 380	63	16	0.5	380	~1.9	5.08	1.8
BaF_2	1.8	0.7	0.6	~210	~1.54	4.88	1.9
PreLude 420	32	41	1.1	420	1.81	7.1	1.1
BGO	9	300	5.8	480	2.15	7.13	1.0

Table 3.1: Comparison of scintillation properties for BrilLanCe scintillators and several other γ-ray detectors, showing the improved light output and energy resolution.[35]

windows cover the chamber along the beam direction, and the internal chamber is filled with a mixture of 90% argon and 10% methane at 68 kPa gauge pressure. A schematic drawing of the fission chamber housing is shown in figure 3-3. Overall the entire chamber is thin enough to be placed directly in the beam with essentially no effect on the beam flux.

The electrical wiring inside the fission chamber is shown in figure 3-4. The first and last foils were used for grounding the circuit, while the other six foils were paired. On each pair, one has a deposit of fissionable material and the other is used to collect the signals generated by fission events. For our experiment, one deposit foil contained ^{235}U and one contained ^{238}U.

Beam flux is calculated by measuring the yield of neutron induced fission fragments from ^{235}U and ^{238}U. The ^{238}U fission is primarily used to determine the flux at higher energies, because its cross section below 1 MeV is extremely small. Below 1 MeV, fission of ^{235}U is used. Time of flight is used to determine the neutron energy, and the pulse height measured by the fission chamber is used to separate fission fragments from alpha particles. [54]

3.2.2 Electronics

The main components of the DAQ electronics were LeCroy's CAMAC Fast Encoding and Readout ADC (FERA) modules, along with their driver and memory modules. With the exception of the CAMAC linear gate modules, all other analog

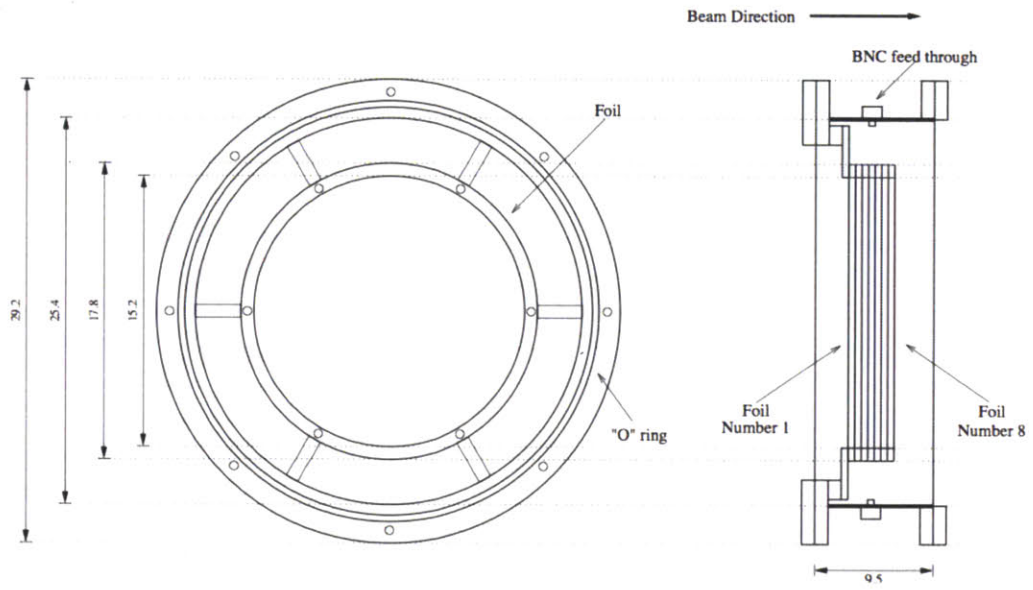

Figure 3-3: Schematic diagram of the fission chamber housing. Dimensions are in cm.

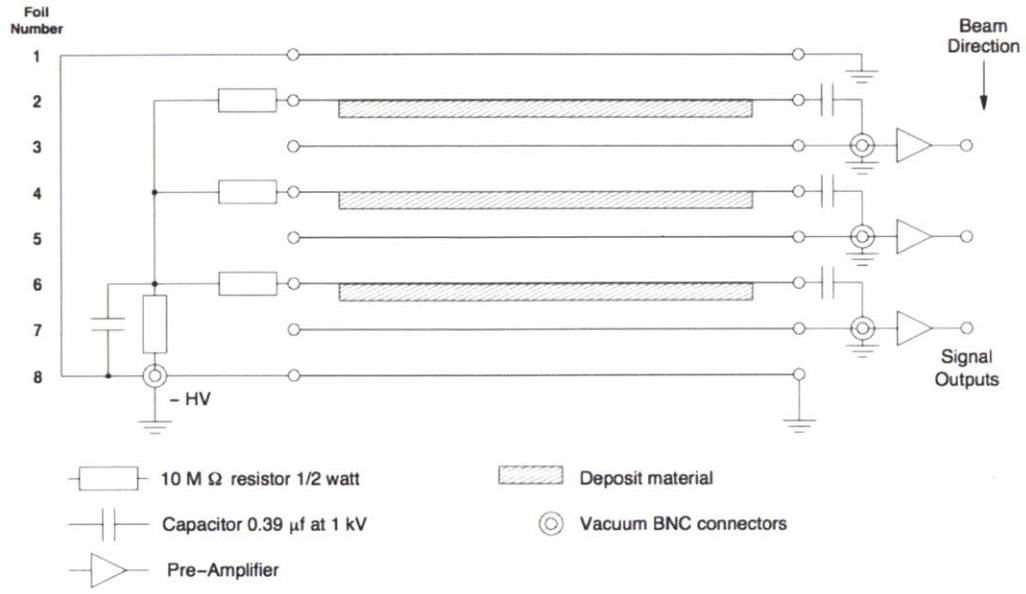

Figure 3-4: Electrical wiring diagram of the fission chamber.

and logic signals were handled by NIM electronics.

Three FERA modules were used, each with 16 channels, giving us up to 48 channels. The first FERA was used for the analog electronics readout. The second two were used for timing readouts using time to FERA converters (TFC). The first timing FERA read the timing signals from all detectors, while the second timing FERA read the timing signals from the beam.

The FERA modules were controlled by a FERA driver, which provides a common ADC conversion gate and clears the signals. The memory module was used to store the outputs of the FERAs so that the acquisition computer could wait until the time interval between macropulses to read out the FERA memory.

The different detectors had their own electronics arms which generate the analog and logic signals read in by the FERAs.

3.2.2.1 Active Target

The electronics diagram for the active target branch is shown in figure 3-5. The

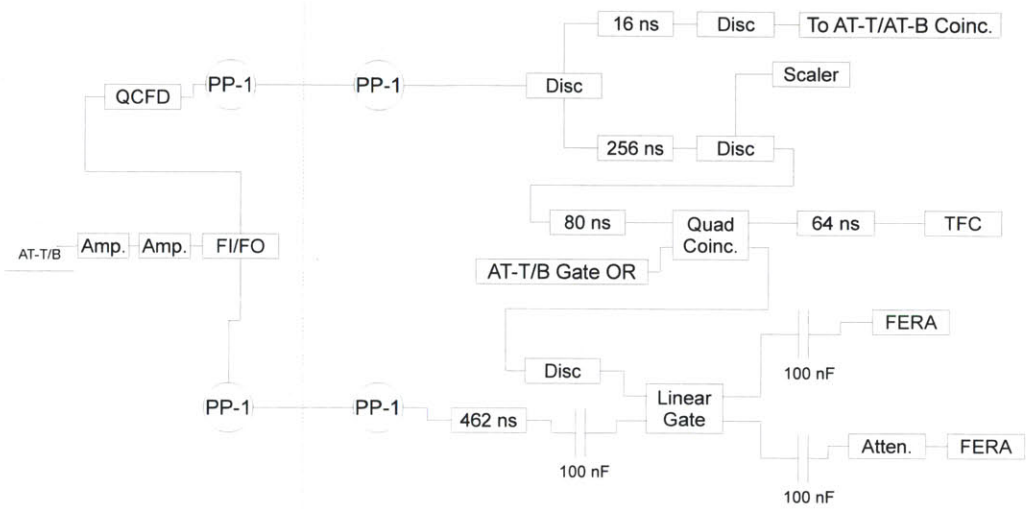

Figure 3-5: Active target electronics for the radiative capture measurement at LANSCE. The vertical dotted line separates electronics in the target room from electronics in the data room. The patch panels were connected by 100′ of RG48 cable.

two amplifiers shown were each set to unity.[1] The signals were then split into the analog branch and timing branch with a linear fan-in/fan-out. The timing branch signals were converted into a logic pulse using a constant fraction discriminator, and then the analog and timing branches were both patched into the control room by 100′ of RG48 cable.

In the control room, the timing branch went through a discriminator and split into another two branches. One branch was delayed and went to the AT-T (top) and AT-B (bottom) coincidence. The other branch was delayed and passed through another discriminator. These signals were counted and recorded by a scaler module and were delayed and put in coincidence with the AT-T/B Gate-OR so that the AT timing and analog signals were only recorded for AT triggers. This coincidence unit provided the stop signal for the TFC and the gate for the analog branch.

The analog branch signals were delayed and passed through 100 nF capacitors to remove baseline noise, and then went into the linear gate, with the gate generated from the timing branch. The gated signals were then split into the high gain

[1]The amplifiers were installed in the original tests with the low gain active target, which required x100 gain. They were left in place in the present setup to maintain the timing.

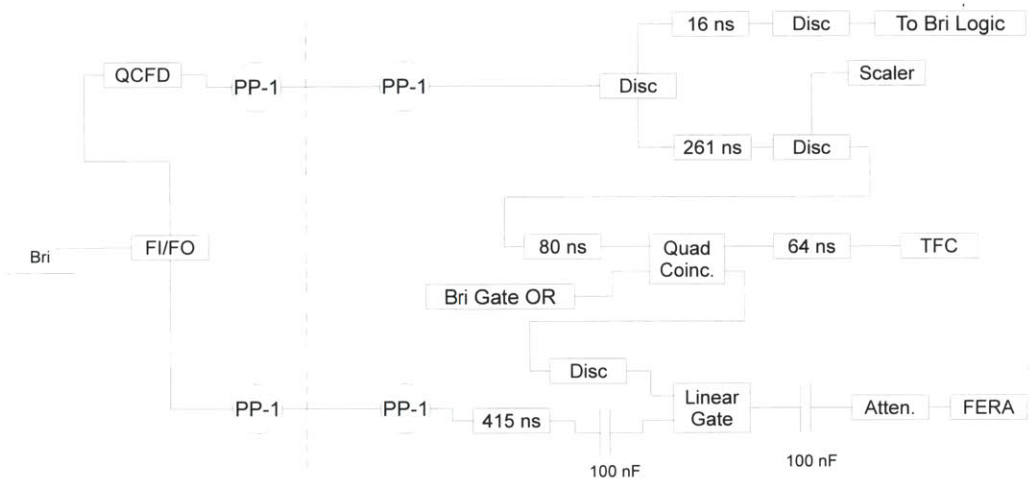

Figure 3-6: BrilLanCe electronics for the radiative capture measurement at LANSCE. The vertical dotted line separates electronics in the target room from electronics in the data room. The patch panels were connected by 100′ of RG48 cable.

and low gain analog branches and recorded by the FERA. The top and bottom active target photomultiplier tube electronics branches were identical.

3.2.2.2 BrilLanCe

The electronics diagram for the BrilLanCe branch is shown in figure 3-6. The BrilLance^{TM} signal was split into an analog branch and a timing branch with a linear fan-in/fan-out. The timing branch signal was converted into a logic pulse using a constant fraction discriminator, and then the analog and timing signals were both patched into the control room by 100′ of RG48 cable.

In the control room, the timing branch signal went through a discriminator and split into another two branches. One branch was delayed and went to the BrilLanCe logic. The other branch was delayed and passed through another discriminator. This signal was counted and recorded by a scaler module, and was delayed and put in coincidence with the Bri Gate-OR so that the timing and analog signals were only recorded for Bri triggers. This coincidence unit provided the stop signal for the TFC and the gate for the analog branch.

The analog branch signal was delayed and passed through a 100 nF capacitor to remove baseline noise, and then went into the linear gate, with the gate generated from the timing branch. The gated signal was attenuated and recorded by the

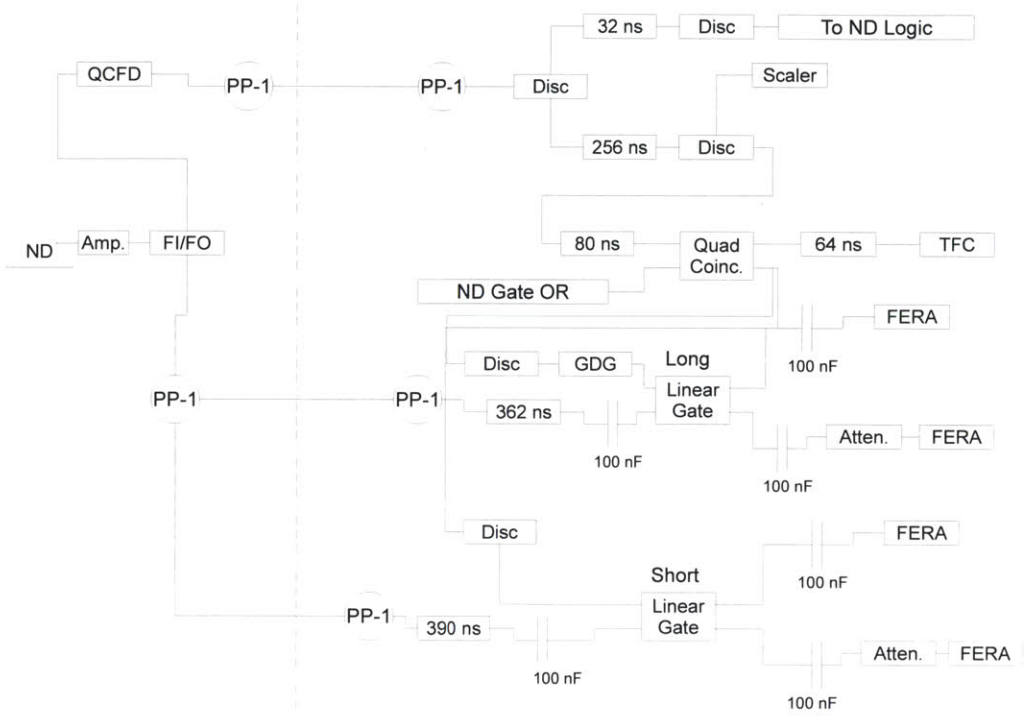

Figure 3-7: Neutron detector electronics for the radiative capture measurement at LANSCE. The vertical dotted line separates electronics in the target room from electronics in the data room. The patch panels were connected by 100′ of RG48 cable.

FERA.

3.2.2.3 Neutron Detector

The electronics diagram for the neutron detector branches is shown in figure 3-7. The neutron detector output was amplified in the detector shed, however, this amplification was often set at unity. The amplifier was retained to maintain the timing of the circuit and to allow us to adjust the gain if needed. The signals were then split into the analog branch and timing branch with a linear fan-in/fan-out. The timing branch signal was converted into a logic pulse using a constant fraction discriminator, and then the analog and timing branches were both patched into the control room by 100′ of RG48 cable.

In the control room, the timing branch signal went through another discriminator and was split into another two branches. One branch is delayed and went to the ND logic. The other branch was delayed and passed through another discriminator. This signal was counted by a scaler module, and was delayed and put in coincidence with the ND Gate-OR so that the ND timing and analog signals were only recorded for ND triggers. This coincidence unit provided the stop signal for the TFC and the generated the gates for the analog branches.

The analog branch signal was split into "long" and "short" branches so that pulse shape discrimination could be used for particle identification. Each was delayed and passed through a 100 nF capacitor to remove baseline noise, and then went into its respective linear gate, with the gates generated from the timing branch. Each of the long and short branches was then split into the high gain and low gain analog branches and recorded in the FERA.

3.2.2.4 Beam Timing Signals

Relative beam timing was measured by the T_0 pulse, which was generated by the proton beam each time it interacts with the spallation target. An inductive pickoff generates this signal, which was then delivered to each of the experimental areas at WNR. The T_0 signal performed three important functions: recording the relative timing of the event with respect to the beam, creating the T_0 vetos to prevent overflow of events due to fast neutrons, and generating the readout request for the FERA modules. Clock signals were also generated and recorded by scalers in order to measure the dead time and display the scalers as a function of time. The electronics for these scalers is shown in figure 3-8.

The output register generated a pulse at the start of each run, which triggered a series of gate and delay generators. Each of these generators was triggered by its own delay output so that it triggered repetitively at an adjustable rate. One was set such that it triggers at a rate of 1 Hz. Another was set to pulse at a rate of 1 MHz; this was vetoed by the T_0 veto, and then split into the 1 MHz Pulser scaler and Busy Pulser signal which was vetoed by the Busy Veto. A comparison of the two scalers allows determination of the live time. The others form an approximation of the beam timing structure, with macro and micropulses, to allow the electronics to function when there was no beam. This "Fake T_0" was connected to the T_0 input when the beam was off, and disconnected during data taking with the beam.

The T_0 input was split to perform its three functions, as shown in figure 3-9. A scaler recorded the number of T_0 pulses, and the signal was delayed and used

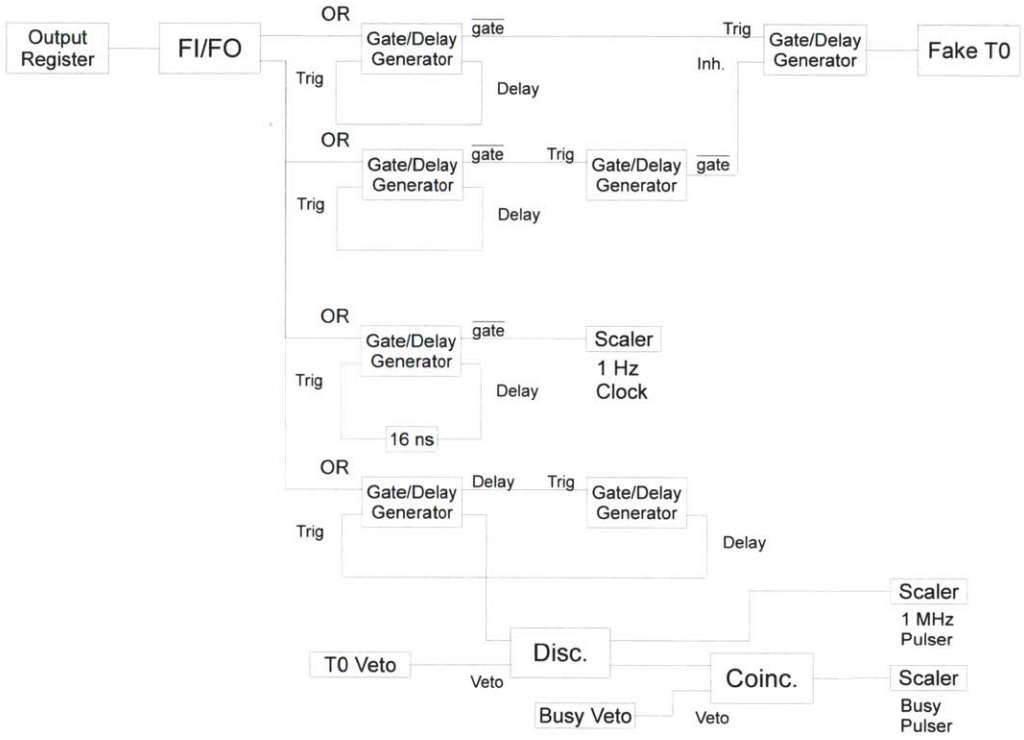

Figure 3-8: Electronics for the timing scalers.

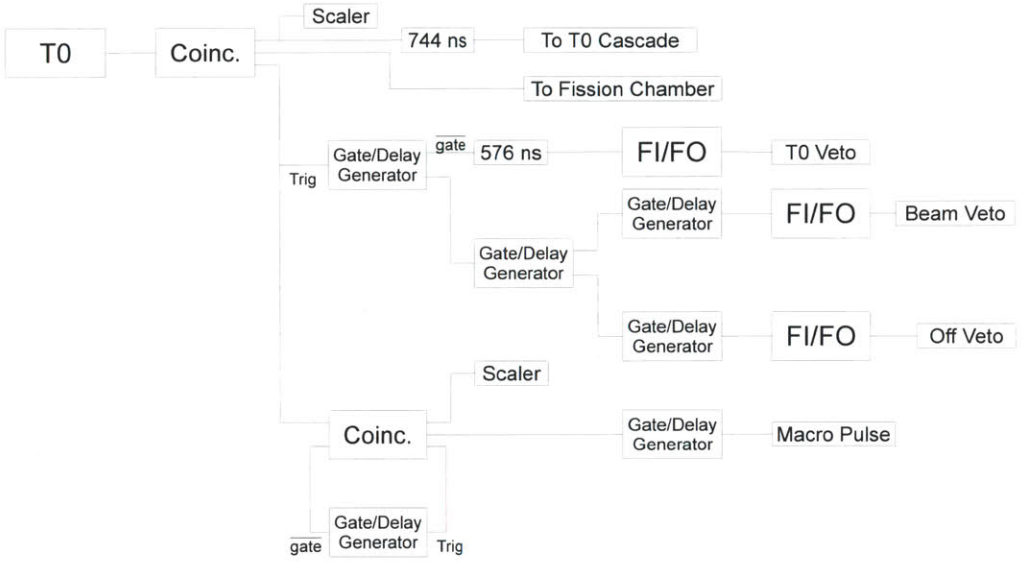

Figure 3-9: Electronics for the T_0 and associated vetoes.

to record the relative timing of the events versus the beam. The T_0 vetoes were generated with a gate and delay generator set to veto the first 300 ns after the T_0 pulse. The Beam and Off vetoes for the scalers were also generated for each T_0 pulse. For the readout electronics, the T_0 signal was vetoed by a 1.6 ms pulse generated by the T_0 pulse, so that only the first micropulse of each macropulse was allowed through the coincidence unit. This was counted by a scaler to give the number of macropulses, and then went to the readout electronics.

In order to measure precise neutron times of flight across the entire 1.8 or 3.6 μs range of the micropulse, we used a series of delayed T_0 signals such that each 200 ns range was covered by an individual time to FERA converter. This setup was designed by Vladimir Henzl, and was called the "T_0 Cascade." The electronics diagram for the T_0 cascade is shown in figure 3-10.

3.2.2.5 Fission Chamber

The electronics diagram for the fission chamber is shown in figure 3-11. The fission chamber signal was split using a dual PMT fan out into the logic side and the analog side. The analog side was amplified and then read into a CAMAC ADC. To maximize the live time for the fission chamber, the time to pulse height converter

Figure 3-10: Electronics for the T_0 cascade.

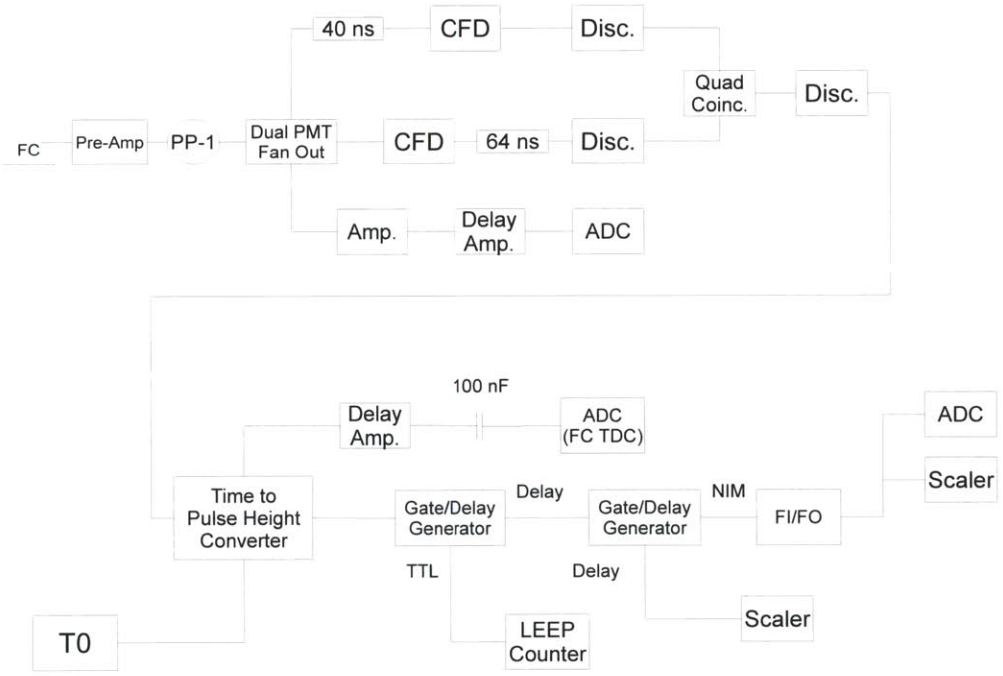

Figure 3-11: Fission chamber electronics for the radiative capture measurement at LANSCE.

was only started when there was a fission chamber event, and then stopped by the delayed T_0 signal, giving a reversed time spectrum. Additionally, the trigger electronics were set up such that the fission chamber trigger takes priority over the event triggers. The electronics setup for the ^{235}U and ^{238}U foils were identical.

3.2.2.6 Trigger Logic

There were seven different triggers. Each trigger had five monitoring scalers with different veto conditions. The "raw" scaler measured the total trigger rate for all times. The T_0 veto scaler measured the rate for the trigger during the time when events were recorded for the micropulses. The Beam veto scaler measured the trigger rate over the entire time when beam was present, including the high energy neutrons which were vetoed from the triggers by the T_0 veto. The Off scaler measured the trigger rate between macropulses. The Variable scaler had no specific veto, but could be set up to cover any specific time range that needed to be monitored.

Active Target Singles The electronics for the active target trigger are shown in figure 3-12. The logic signals from the AT-T and AT-B branches were put in coincidence, and the output of the coincidence unit was split to two discriminators. One of the discriminators was recorded by a scaler module as the raw AT scaler and went to the active target-neutron detector coincidence trigger. The other discriminator output went to the active target-BrilLanCe coincidence and to the four monitor scalers. Each monitor scaler was in coincidence with the corresponding veto.

The output of the coincidence unit for the T_0 Veto scaler went through a rate divider to form the prescaled active target singles trigger. This trigger went to the singles trigger OR, a scaler, and was delayed to create the AT FERA signals. It was split and put in coincidence with the FERA gate. The output of the coincidence was delayed and recorded in a TFC for the prescaled active target singles trigger bit, the AT-FERA scaler, and the AT-T and AT-B Gate OR signals which were used to create the digital and linear gates on the active target top and bottom branches.

Neutron Detector Singles The electronics for the neutron detector trigger are shown in figure 3-13. The logic signal went to the four monitor scalers. As with the other triggers, each monitor scaler was in coincidence with the corresponding veto.

Figure 3-12: Electronics for the AT trigger.

The output of the coincidence unit for the $T0$ Veto scaler went through a rate divider to form the prescaled neutron detecor singles trigger. This trigger went to the singles trigger OR, a scaler, and was delayed and put in coincidence with the FERA gate to create the ND FERA signals. The output of the coincidence was delayed and recorded in a TFC for the prescaled neutron detector singles trigger bit, the ND-FERA scaler, and the ND Gate OR signal which was used to create the digital and linear gates on the ND branch.

BrilLanCe Singles The electronics for the BrilLanCe trigger are shown in figure 3-14. The logic signal went to the four monitor scalers. As with the other triggers, each monitor scaler was in coincidence with the corresponding veto.

The output of the coincidence unit for the $T0$ Veto scaler went through a rate divider to form the prescaled neutron detector singles trigger. This trigger went to the singles trigger OR, a scaler, and was delayed and put in coincidence with the FERA gate to create the BrilLanCe FERA signals. The output of the coincidence was delayed and recorded in a TFC for the prescaled BrilLanCe detector singles trigger bit, the Bri-FERA scaler, and the Bri Gate OR signal which was used to

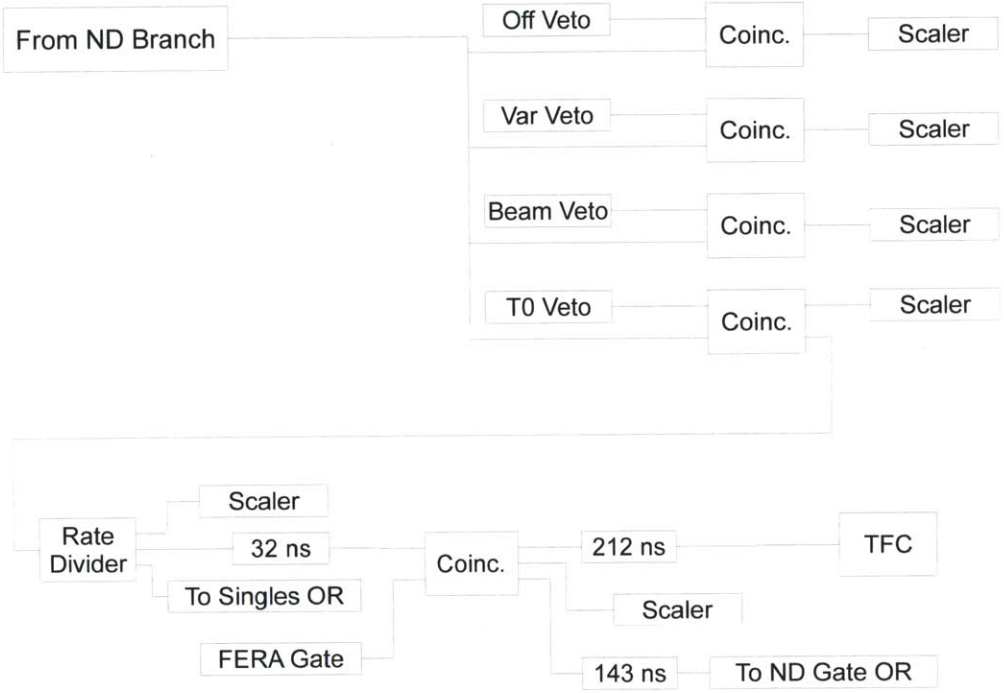

Figure 3-13: Electronics for the neutron detector singles trigger.

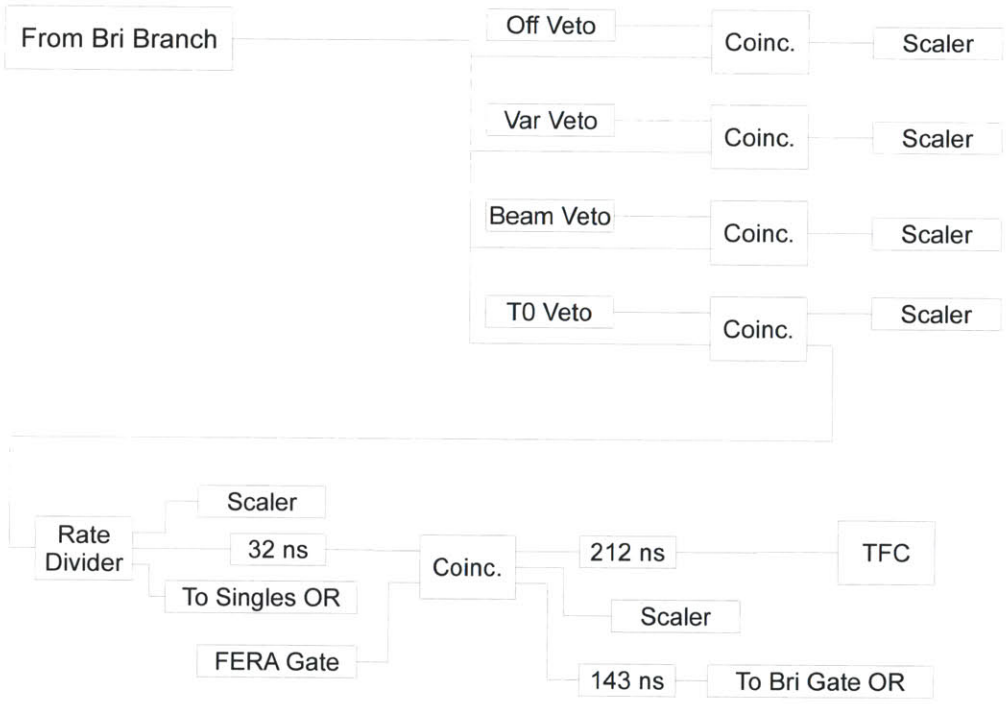

Figure 3-14: Electronics for the BrilLanCe singles trigger.

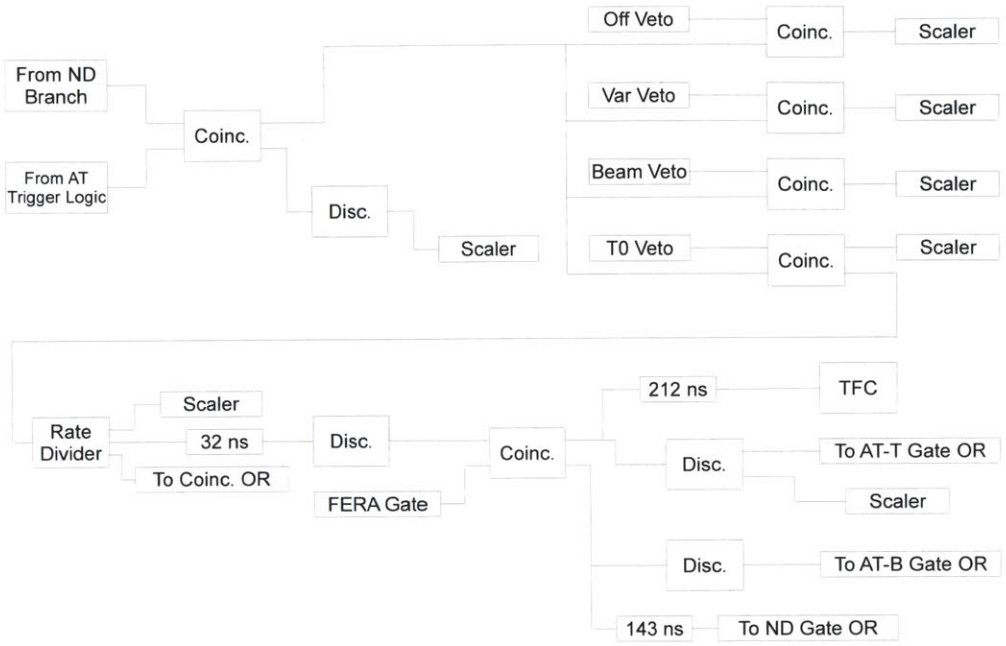

Figure 3-15: Electronics for the active target-neutron detector coincidence trigger.

create the digital and linear gates on the BrilLanCe branch.

Active Target-Neutron Detector Coincidence The electronics for the active target-neutron detector trigger are shown in figure 3-15. The signals from the active target trigger logic and the neutron detector branch were put in coincidence. This coincidence unit output went into the raw trigger scaler and the four monitor scalers. As with the other triggers, each monitor scaler was in coincidence with the corresponding veto.

The output of the coincidence unit for the T0 Veto scaler went through a rate divider to form the active target-neutron detector trigger. This trigger went to the coincidence trigger OR, a scaler, and was delayed and put in coincidence with the FERA gate to create the AT·ND FERA signals. The output of the coincidence was delayed and recorded in a TFC for the active target-neutron detector trigger bit, the AT·ND-FERA scaler, and went to both the AT-T, AT-B, and ND Gate OR signals which was used to create the digital and linear gates on the AT and ND branches.

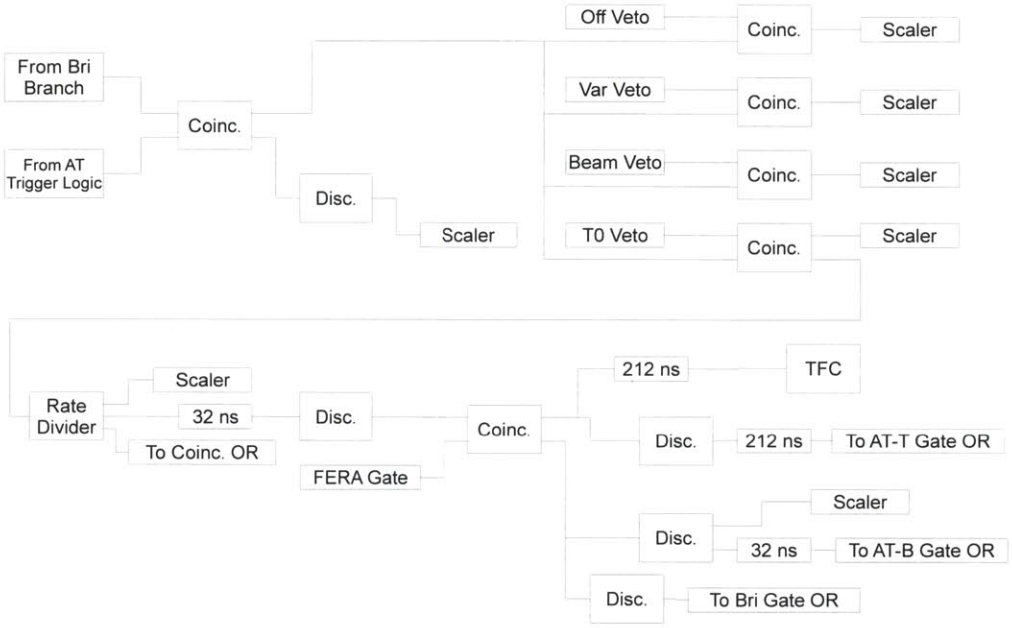

Figure 3-16: Electronics for the active target-BrilLanCe coincidence trigger.

Active Target-BrilLanCe Coincidence The electronics for the active target-BrilLanCe trigger is shown in figure 3-16. The signals from the active target trigger logic and the BrilLanCe branch were put in coincidence. This coincidence unit output went into the raw trigger scaler and the four monitor scalers. As with the other triggers, each monitor scaler was in coincidence with the corresponding veto.

The output of the coincidence unit for the $T0$ Veto scaler went through a rate divider to form the active target-neutron detector trigger. This trigger went to the coincidence trigger OR, a scaler, and was delayed and put in coincidence with the FERA gate to create the AT·Bri FERA signals. The output of the coincidence was delayed and recorded in a TFC for the active target-neutron detector trigger bit, the AT·Bri-FERA scaler, and went to both the AT-T, AT-B, and Bri Gate OR signals which was used to create the digital and linear gates on the AT and BrilLanCe branches.

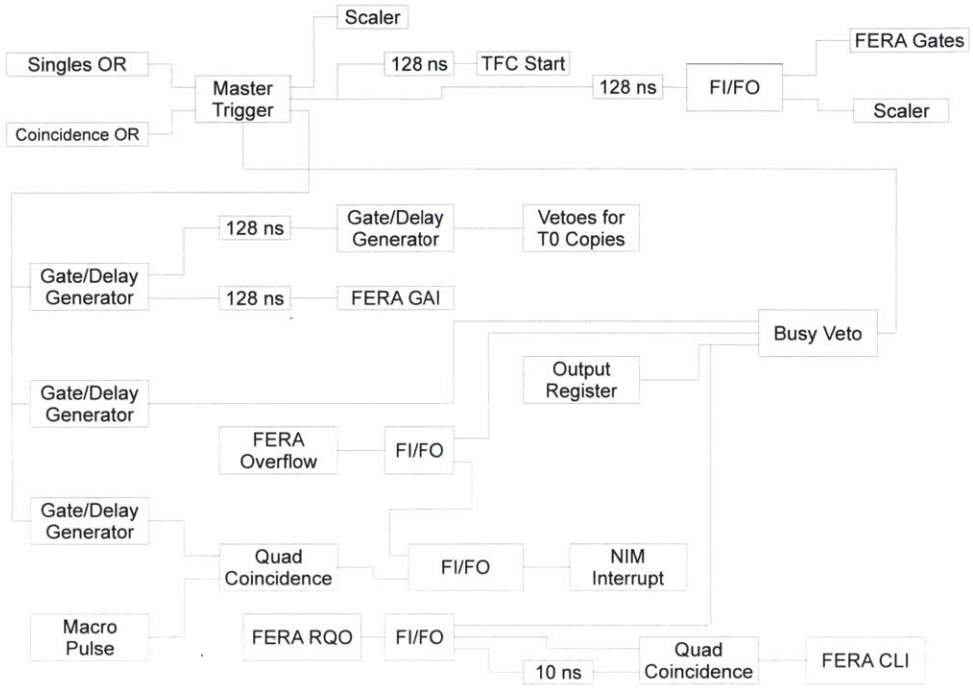

Figure 3-17: Readout electronics for the LANSCE configuration.

3.2.2.7 Readout Electronics

The singles and coincidence triggers were brought together to the master trigger, which starts the TFCs and provides the FERA gate signals for the triggers. The master trigger also provided the veto for the T_0 cascade (see figure 3-10, and was put in coincidence with the macro pulse to provide the signal which indicated to the acquisition that a macropulse has ended and that there have been triggers, so readout should begin. The busy veto was also generated while the acquisition computer reads out the FERA memory. The readout electronics diagram is shown in figure 3-17.

The data acquisition system was a linux computer which used the MIDAS package to record the data. [55] These data were automatically transferred to another computer at MIT and converted into text files. These files could then

easily be read into a simpler analysis script, since the full offline analyzer which had been previously written for this acquisition setup was unnecessary in the much simpler experimental setup constructed for by the radiative capture measurement. Analysis was performed using CERN's ROOT analysis package.

3.3 Radiative Capture and Scintillator Response at UKY

After the measurement at LANSCE, we returned to the University of Kentucky to attempt to improve our signal to background ratio using the new active target, additional shielding, and high efficiency γ-ray detectors. We also conducted several dedicated scintillator response measurements using a configuration designed for detecting elastic *np* scattering.

3.3.1 Detectors

The active target described in section 3.1 was used for both the radiative capture and scintillator response measurements. A liquid scintillator was used to detect elastically scattered neutrons, and two BGO scintillators were used to detect the γ-rays produced by capture.

3.3.1.1 Neutron Detector

Scattered neutrons were detected by a BC501 liquid scintillator.. The scintillator was 13.7 cm in diameter, with a fast, fourteen stage photomultiplier tube of the same diameter attached. Using a long and short ADC gate, we were able to use pulse shape discrimination to separate neutrons from γ-rays. For the radiative capture measurements, this detector served as a monitor, while the BGO events were of primary interest, but in the scintillator response measurements, the neutron detector allowed the determination of the recoiling proton energy.

3.3.1.2 BGO

Two bismuth germanate (BGO) scintillators were used. The scintillators were $3''$ thick and $7''$ in diameter. The BGO detectors have a very high efficiency for detecting γ-rays and a lower sensitivity to neutrons, making them ideal for reducing the backgrounds and increasing the signal. The tradeoff for this improved γ-ray

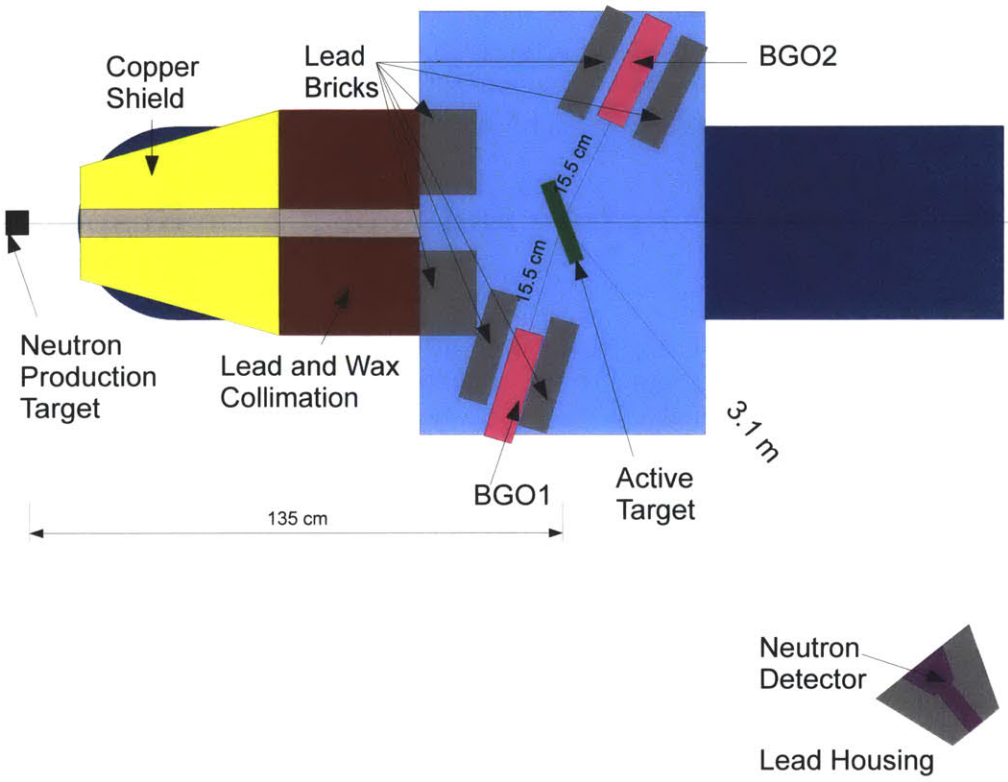

Figure 3-18: Top view of the experimental setup for the improved radiative capture experiment at the University of Kentucky.

detection efficiency is the lower energy resolution of the BGO detectors when compared to the BrilLanCe detectors used at LANSCE.

3.3.2 Configuration

Two different configurations were used, one for studying capture and one for studying scintillator response.

3.3.2.1 Radiative Capture

The experimental setup is shown in figure 3-18. The active target was placed in the beam, 135 cm from the neutron production target. It was placed at a slight

angle to keep the aluminum support bars from interfering with capture γ-rays. The neutrons were collimated with a large copper shield composed of a series of plates, increasing in size from 30.5 to 128.27 cm from the front of the shield to the back, with a total thickness of 50.8 cm. The aperture in the copper shield was 6.3 cm in diameter. Downstream of the copper shield was a 46.7 cm long wax shield with a 6.3 cm aperture which matched the aperture in the copper shield.

The BGOs were placed 15.5 cm from the active target, with BGO1 at 106.6° and BGO2 at 64.6° from the beamline. A small lead enclosure was built around each BGO, with additional lead shielding placed between the wax collimator and the lead housings of the BGOs.

The neutron detector was placed at an angle of 52°, 3.1 m from the active target. It was housed in a lead and wax shield with an outer diameter of 39.4 cm, and an inner diameter of 25.5 cm. The long flight path was required by the construction of the target room.[2]

3.3.2.2 Scintillator Response

The experimental setup for the dedicated light response measurement is shown in figure 3-19. This configuration was similar to that for the radiative capture measurement. The active target was placed ~30 cm downstream of the LiF target. By using an extremely thin LiF target, we were able to constrain the neutron beam energy without the need for a long flight path to determine time of flight.

The neutron detector was placed at a distance of approximately 1.5 m on a rotating arm that allowed measurement at multiple angles. Over the course of several runs we tried angles of 30°, 45°, and 60° and the data at 45° proved to be the cleanest. The same copper shield which was used to collimate the neutrons in the radiative capture measurement was placed at the front of the rotating arm. The neutron detector was housed in a large lead and wax shield, with a 4.4 cm lead lining in the internal aperture and a 7 cm wax lining around this lead. Ten wax cylinders, 15.24 cm in diameter, were placed around the internal aperture, 2.2 cm from the wax lining and 22 cm apart from each other.

[2]Since the neutron pit was covered with a relatively thin layer of metal which could not support the weight of the shield which was used to house the neutron detector, it was placed on the outer ring where the detector arm rotated.

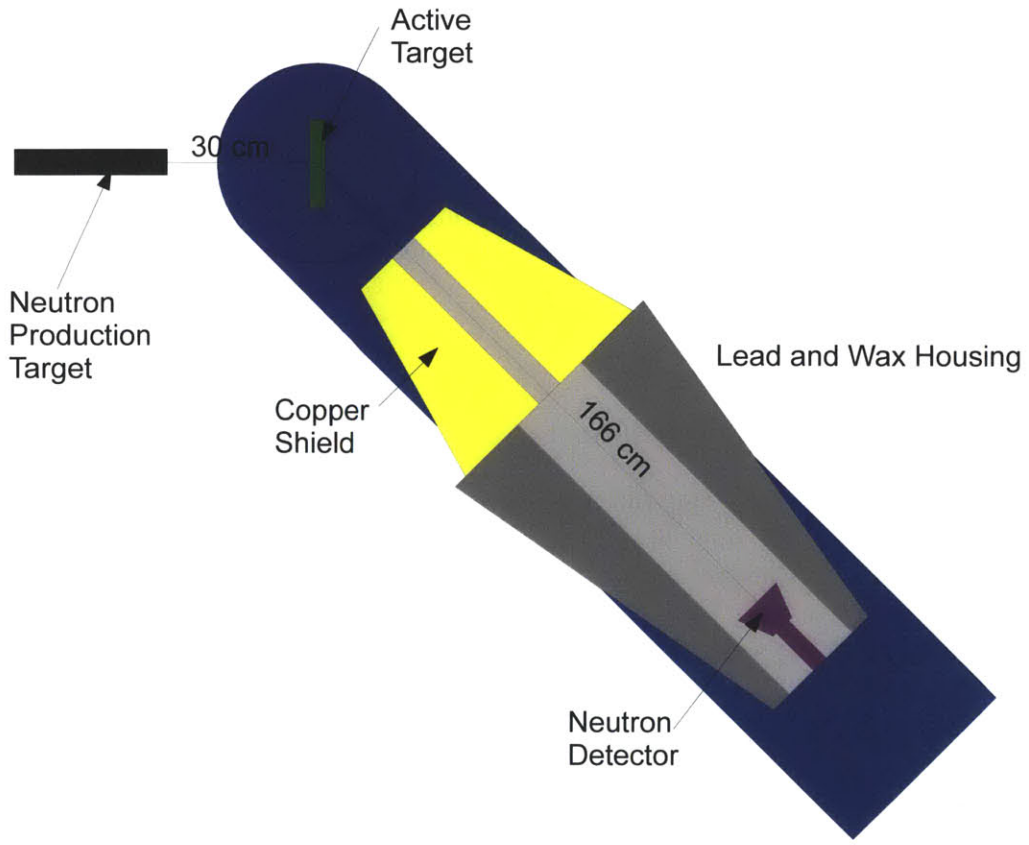

Figure 3-19: Top view of the detector setup for the dedicated scintillator response measurements.

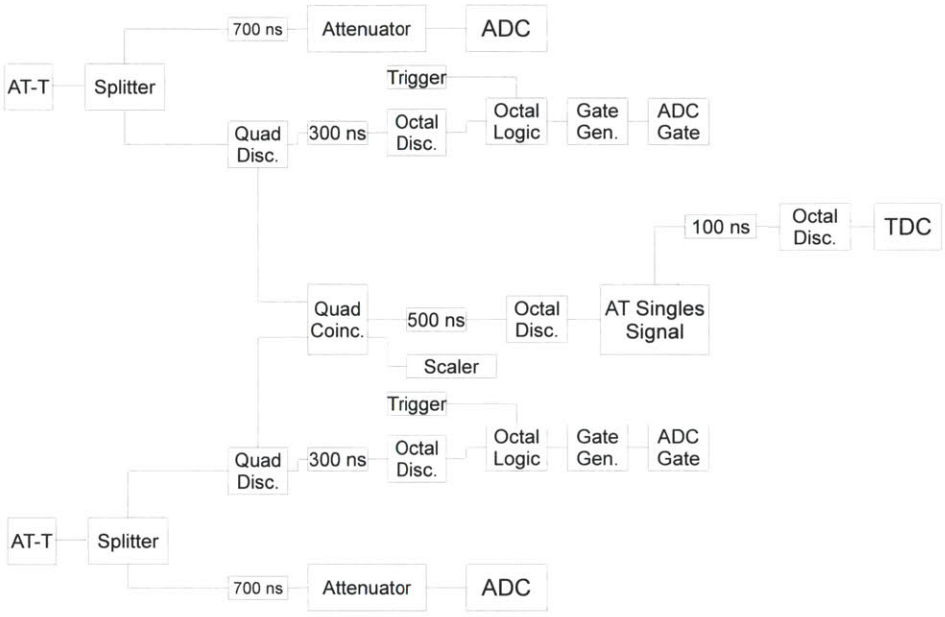

Figure 3-20: Active target electronics for the radiative capture and scintillator response measurements.

3.3.3 Electronics

The data were recorded with an XSYS program written by Tom Rinkel for the USB Crate Controller, which was used to interface the CAMAC crate and DAQ computer. [56]

3.3.3.1 Active Target

A diagram of the active target electronics is shown in figure 3-20. The signals from the top and bottom photomultiplier tubes were read out and transmitted from the target room into the control room. The signal was passed through a passive splitter, and divided into the analog branch and the timing and logic branch.

In the analog branch, the signal was delayed and then passed through a precision, variable attenuator before being read into the CAMAC ADC. During the dedicated scintillator response measurements, this signal was split a second time after being delayed, and each signal passed through a different channel of the at-

tenuator, so that a high gain signal and a low gain signal could be recorded for each event. This gave us the maximum dynamic range for the active target response.

In the logic branch, the signal passed into a discriminator with the threshold set at -30 mV. One output was delayed and used in coincidence with the master trigger to generate the ADC gate for the corresponding analog signal. This guarantees that the relative timing of the ADC and its gate was always consistent regardless of which trigger generated the master trigger.

The logic pulses from the top and bottom active target photomultiplier tubes were put in coincidence to generate the active target singles signal. This signal was delayed and used to stop the active target TDC and counted by a CAMAC scaler module.

3.3.3.2 BGO

A diagram of the BGO electronics is shown in figure 3-21. Before the BGO signals were transmitted into the control room, they were split using a three-way BNC connector, and one of the outputs was terminated. While this reduced the signal by half, it eliminated reflections which were causing significant electronic noise. After they were transmitted into the control room, they were passed through a capacitor in order to eliminate a shifting baseline, and then split into the analog branch and the logic branch using a passive splitter.

For each detector, the analog branch signal was delayed and passed through the precision, variable attenuator before being read into the CAMAC ADC.

The logic signal was generated using a constant fraction discriminator with a 10 ns delay. Each logic signal was used for the scalers, TDC stops, and to generate the ADC gates for the respective analog signals in the same manner as for the active target. The signals were combined in a logic fan-in/fan-out and delayed to generate the BGO singles signal.

3.3.3.3 Neutron Detector

A diagram of the ND electronics is shown in figure 3-22. As with the active target and BGO electronics, the neutron detector signals were split into the analog and logic branches with a passive splitter. The analog branch signal was delayed and passed through the precision, variable attenuator. This signal was then split using a linear fan-in/fan-out and read into two different CAMAC ADCs, one with a 190 ns gate and one with a 90 ns gate, in order to provide pulse shape discrimination.

The logic branch signal became the ND singles signal, which was used for the neutron detector scaler, the neutron detector TDC stop, and was delayed and

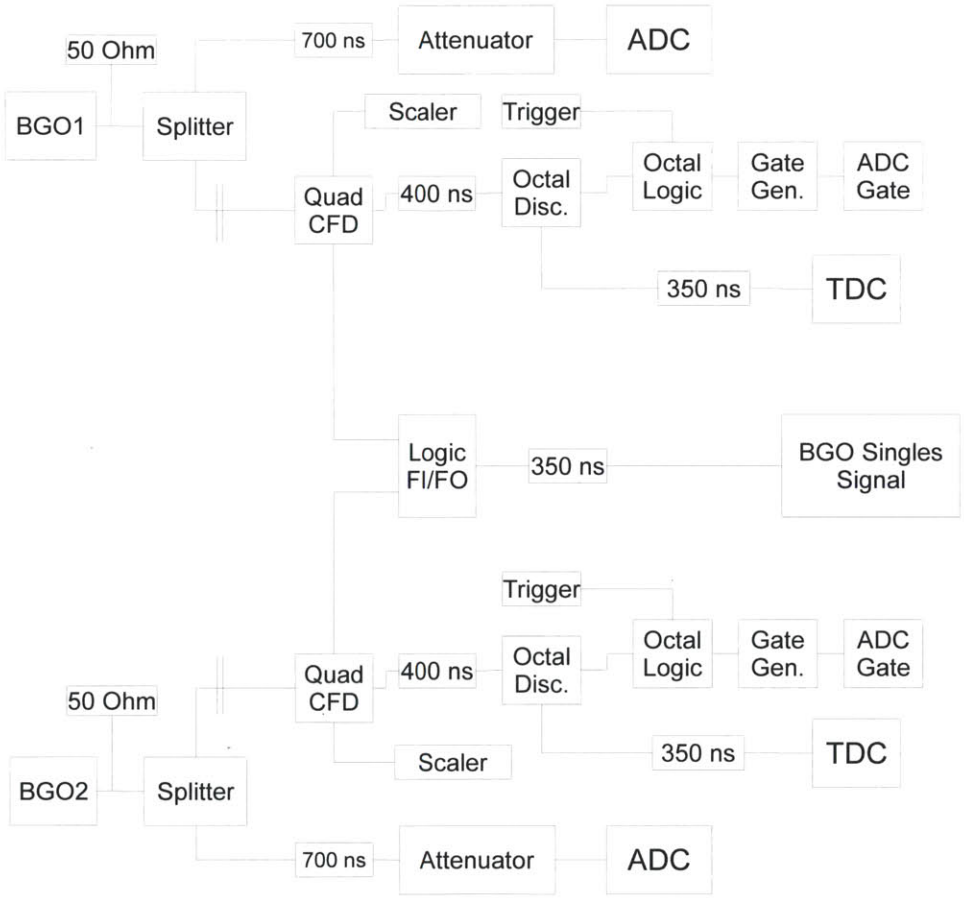

Figure 3-21: BGO electronics for the radiative capture measurement.

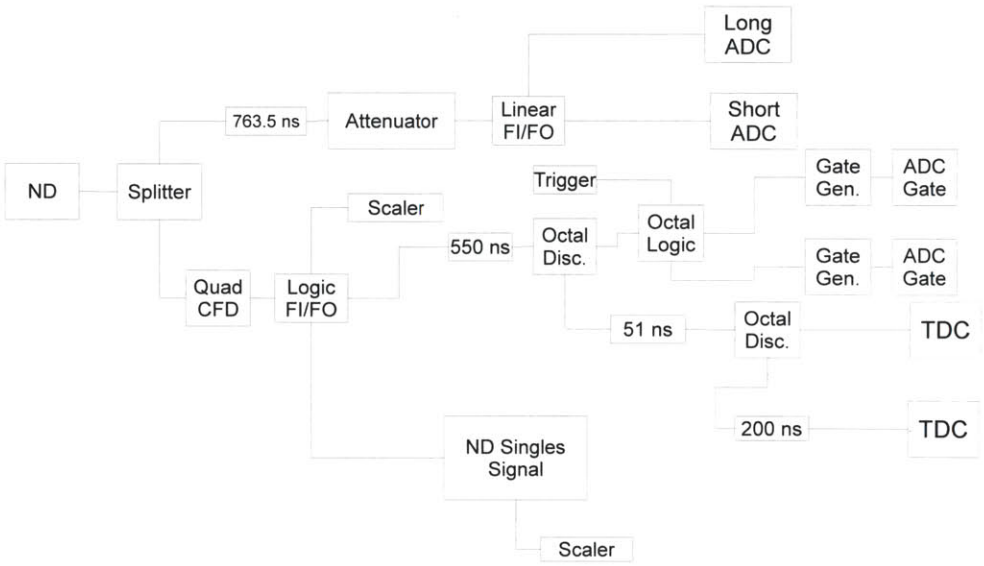

Figure 3-22: Neutron detector electronics for the radiative capture and scintillator response measurements.

put in coincidence with the trigger to generate the long and short ADC gates. A second neutron detector TDC with the stop delayed by 200 ns was used to ensure that the entire time of flight range was covered.

3.3.3.4 Proton Beam

A timing signal and a current integrator were used to measure the neutron time of flight and the total proton current.

The timing signal was generated by a beam pick-off just upstream of the neutron production target. When the protons passed, this signal produced a logic pulse which was delayed and used to stop the beam TDC. This TDC allowed us to determine the time of flight from the neutron production target to the detector which generated the master trigger. As the TDC was stopped by the beam pick-off, shorter flight times fall at higher TDC channels than longer flight times. Using the γ-rays produced by the protons on the neutron production target, we were able to calibrate the time of flight scale and calculate beam neutron energies.

The total proton current was recorded by a current integrator and converted into logic pulses such that the number of pulses was proportional to the total current. The current integrator was recorded by two scalers, one recording the total beam current, and one which was inhibited by the dead time. Using the live time scaler, and knowing the conversion factor for the current integrator, we were able to determine the neutron flux.

3.3.3.5 Triggers

The radiative capture measurements used five triggers, and the dedicated scintillator response measurements used three triggers. The three common triggers were the prescaled active target, the prescaled neutron detector, and the active target neutron coincidence.

Prescaled Active Target (pAT) The AT singles signal was run through a rate divider set to allow 1 in 500 events to trigger. Since the active target often triggered at a rate of 100 kHz, this rate divider was necessary to minimize the dead time generated by this trigger while allowing enough events to provide useful information.

Prescaled Neutron Detector (pND) As with the pAT trigger, the ND singles signal was run through a rate divider set to allow 1 in 500 events to trigger.

Active Target Neutron Detector Coincidence (ATcND) The ND singles signal was used to generate a 500 ns gate. This gate was placed in coincidence with the AT singles signal to generate the ATcND trigger. The delay on the AT singles signal was set such that a simultaneous triggering of the active target and neutron detector would result in the AT singles signal falling at the end of the coincidence gate generated by the ND singles signal. This ensured that any γ-ray events would fall into the coincidence gate, allowing us to calibrate the scattered neutron time of flight.

Two additional triggers were used in the radiative capture measurement, the prescaled BGO singles and the active target BGO coincidence.

Prescaled BGO (pBGO) As with the pAT and pND triggers, the BGO singles signal was run through a rate divider set to allow 1 in 200 events to trigger.

Active Target BGO Coincidence (ATcBGO) The BGO singles signal was used to generate a 250 ns gate, which was placed in coincidence with the AT singles signal to generate the ATcBGO trigger. In this case, the delay of the BGO singles signal was set such that simultaneous triggering of either BGO and the active target would result in the AT singles signal falling in the center of the gate.

The electronics diagram for the trigger logic is shown in figure 3-23.

The CAMAC crate was controlled by a CCUSB crate controller which connected to a Linux computer through a USB connection. The data acquisition and online histogram display was accomplished through the XSYS and PAW software. Scalers were read out every two seconds. The data were written to text files by an XSYS-based analyzer, and then read into a ROOT based analysis script.

3.4 Total Scattering Cross Section

We measured the total cross section using the method of neutron transmission. Neutrons produced by a pulsed proton beam on a LiF target, as discussed in section 2.1.1, were collimated by a copper shield, the same shield used to collimate the neutrons for the radiative capture measurement, with a 6.35 cm opening and 50.8 cm thickness. This led into a wax and lead shield, containing wax collimation which began with an opening matched to that of the copper shield and tapered down to a 2.2 cm opening. The sample was placed in the beam line past this collimation. The neutron detector was the same BC501 liquid scintillator as used in the scintillator response measurements, and was housed in the same lead and

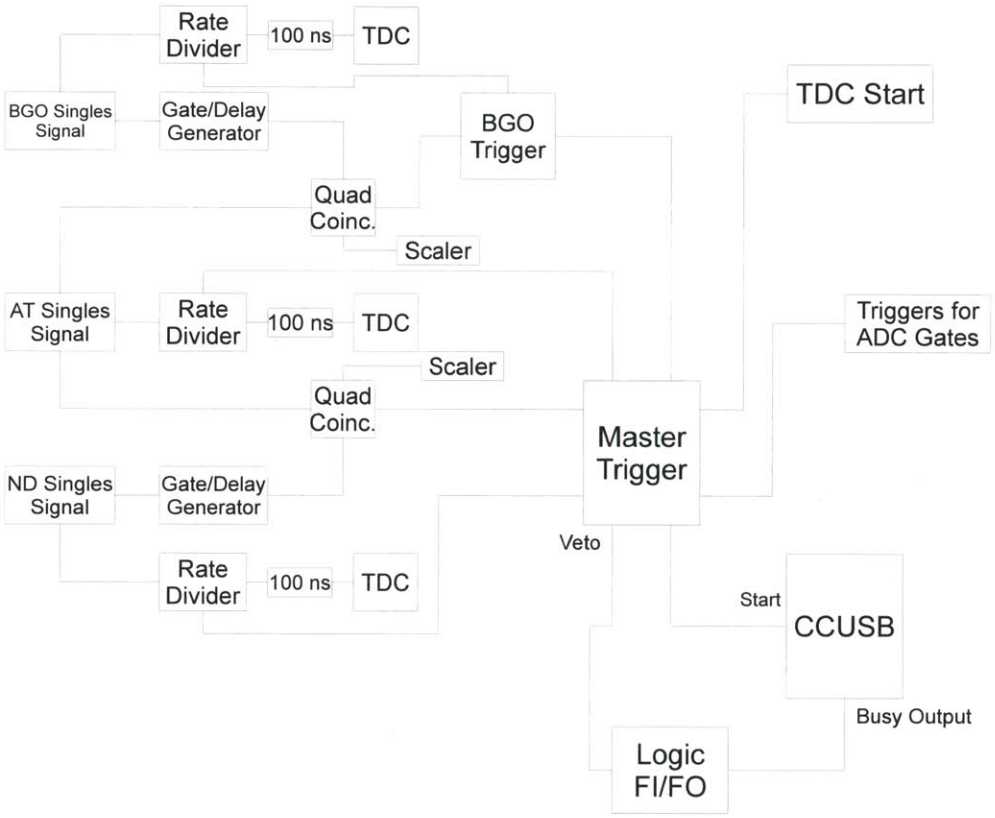

Figure 3-23: Trigger logic for the radiative capture and scintillator response measurements.

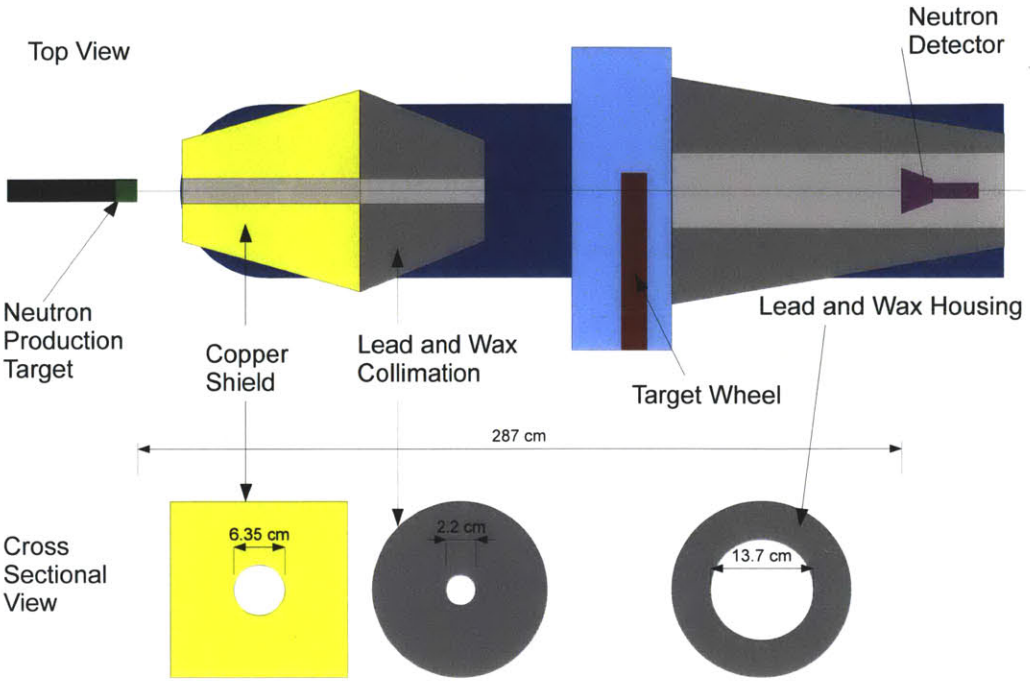

Figure 3-24: Top view of the detector setup for the transmission configuration.

wax shield as previously described in section 3.3.2. The experimental setup is shown in figure 3-24.

3.4.1 Targets

Data were taken with eight different targets, in addition to the "blank" target used to form the ratio of the yield with no target to yields with the targets in the beam. Four CH_2 targets were used for the *np* total scattering cross section, and three carbon targets were used to measure the *n*C total scattering cross section, in order to subtract it from the CH_2 results. Additionally, a sulfur target was used to calibrate the neutron energy using the well-known sulfur resonances. A target wheel was designed and built by Michael Kovash and Zachary Miller from the University of Kentucky. This wheel held up to twelve targets, as shown in figure 3-25, automatically moving them into and out of the beam. The targets were rotated while in the beam to average over any variations in thickness. The target thicknesses and dwell times are shown in table 3.2. The dwell times on each

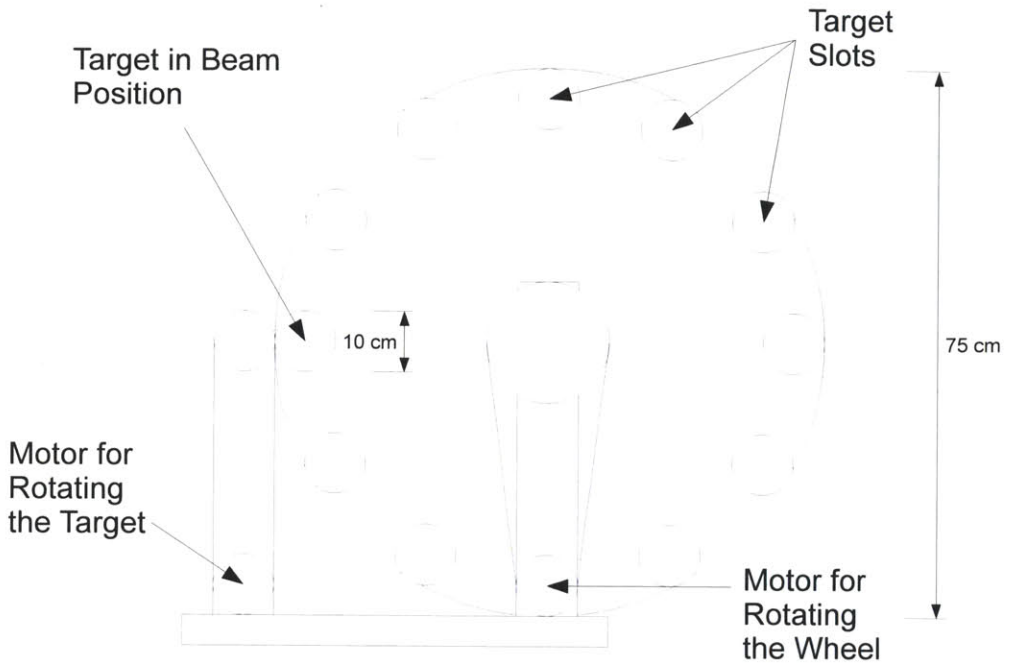

Figure 3-25: Schematic drawing of the target wheel.

Target	Material	Thickness (g/cm^2)	Dwell Time (s)
0	CH_2	0.452 ± 0.0049	101
1	CH_2	0.948 ± 0.0060	133
2	CH_2	1.806 ± 0.0086	232
3	CH_2	2.71 ± 0.012	420
4	C	5.17 ± 0.024	143
5	Blank	-	77
6	C	9.92 ± 0.045	284
7	S	-	126
8	-	-	-
9	C	7.48 ± 0.034	206
10	-	-	-
11	-	-	-

Table 3.2: Target configuration for the total cross section measurement. The sulfur target was used to calibrate the neutron time of flight. Dwell times were calculated to minimize statistical error within each illumination.

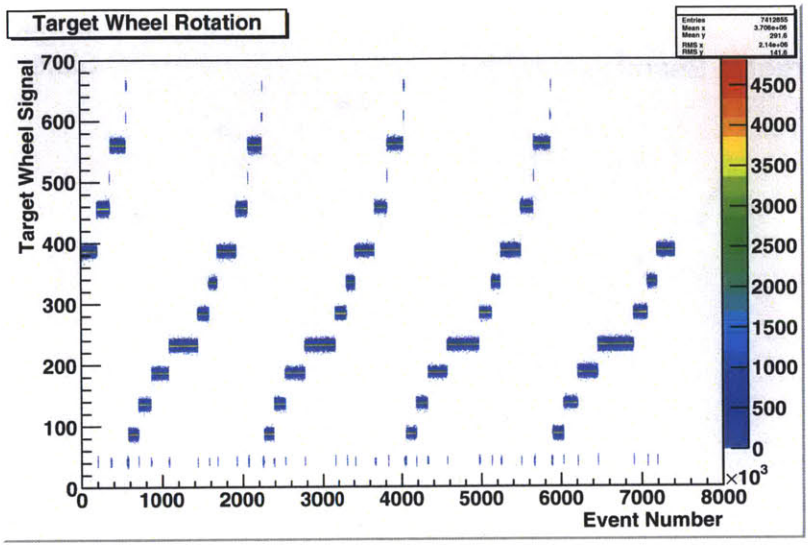

Figure 3-26: Target wheel signal versus event number, showing the target changes, and how each target illumination may be normalized to its corresponding integrated beam current. The horizontal bands show the events for which each target was in the beam.

target were chosen to minimize the statistical uncertainty in each illumination of the target.

The target wheel produces a varying DC output dependent on which target was currently in place and rotating. By plotting this signal for each event, we can see when the targets were switched and were able to normalize the yield from each illumination of the target to the corresponding integrated current. This is shown in figure 3-26. Each horizontal band corresponds to a different target, showing which events were taken with that target in the beam.

3.4.2 Electronics

The neutron detector electronics were the same as those described for the radiative capture measurement. Because this experiment used only a single detector, the only trigger was the neutron detector singles trigger, which was generated from the ND singles signal.

Determining which target was in place was done by using the outputs from the target wheel. The wheel provided two outputs, both as DC levels. One signal

Figure 3-27: Electronics diagram for reading the DC wheel signals into the CAMAC ADC.

indicated whether the wheel was moving between targets or a target was in the beam and rotating, and the other signal had twelve DC levels corresponding to each of the targets.

In order to translate these positive DC signals into pulses which can be measured by the CAMAC ADCs, we used linear gates. This electronics diagram is shown in figure 3-27. The positive DC signals were inverted using linear fan-in/fan-outs. The trigger signal was delayed by 100 ns and then inverted using a logic fan-in/fan-out. This inverted pulse was used as a linear gate for both the valid data signal and the wheel position signal, generating a negative pulse which was proportional to the magnitude of the original, positive DC output. These signals were then run through the precision attenuator in order to keep them on scale for the CAMAC ADCs.

The acquisition and analysis system was the same as for the radiative capture and scintillator response measurements performed at UKY.

Chapter 4

Calibrations

Accurate pulse height to energy calibrations of the detectors, especially the active target and the γ-ray detectors, were extremely important for these experiments. Due to the low rate of capture events, the "peak" of recoiling deuterons will not stand out above the background of *np* elastic events. Having an absolute measurement of the γ-ray energy is vital for identifying capture events.

Calibration of the active target was needed in order to compare our scintillator response results to existing measurements, and also to use these results for the capture measurements. Consistency of the calibrations across these different measurements was important so that we could use the proton response to predict the deuteron response and then use this to identify the capture events.

4.1 Active Target

With the active target, we were able to detect very small pulse heights, even measuring 30 keV X-rays and the 11.2 keV Compton edge from ^{241}Am.

4.1.1 Calibration at LANSCE

The active target was calibrated using ^{241}Am and ^{133}Ba sources.

The response of the top and bottom phototubes to the 59.5 keV γ-ray from ^{241}Am is shown in figures 4-1a and b, respectively. There is some structure at lower pulse height and some sort of shoulder at higher pulse heights.

When we plot the top and bottom photomultiplier tube responses, we see a strong correlation between them, shown in figure 4-2. The "shoulder" regions from the top and bottom form a broad two dimensional peak, marked as region II in

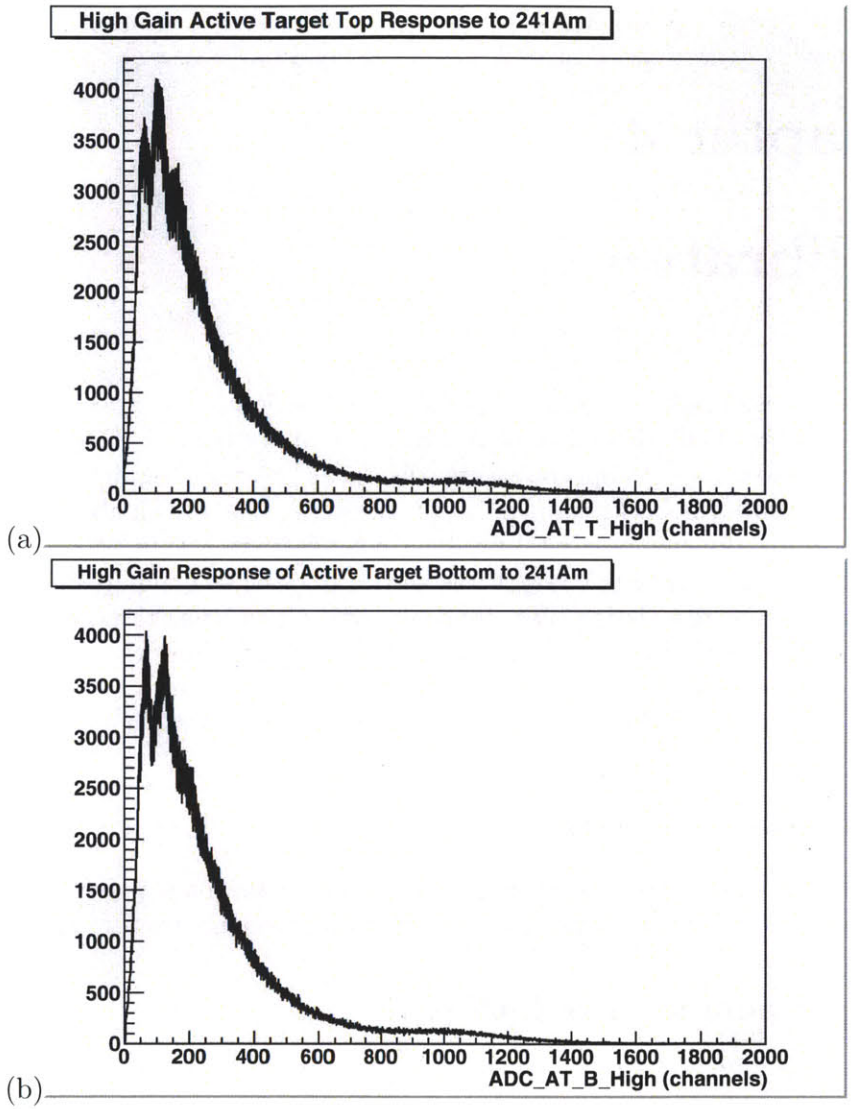

Figure 4-1: Active target (a) top and (b) bottom phototube response to ^{241}Am. The spectra are nearly identical, but do not show a strong photopeak due to the low Z of the plastic scintillator.

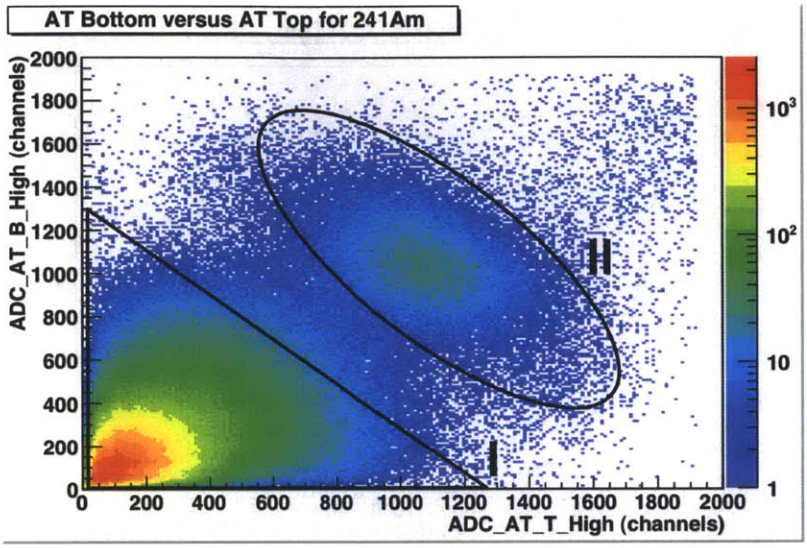

Figure 4-2: Active target bottom phototube response versus active target top phototube response for ^{241}Am. Region I shows the Compton events from ^{241}Am, and region II is the photopeak from ^{241}Am.

the figure, and the structure at lower pulse heights in the triangular region I are correlated, indicating this is the Compton edge for the 59.5 keV γ-ray.

While the total energy deposited in the scintillator for a photoelectric event is fixed, it will not be distributed evenly; the amount of light collected by the top and bottom phototubes will will depend on where the γ-ray interacts in the scintillator. Consider a γ-ray which strikes the active target at a position x and ejects an electron which produces L_0 light going toward each photomultiplier tube. The light collected in the top and bottom phototubes will fall off exponentially with the distance from the phototube

$$L_T(x) = L_0 e^{-\frac{x}{\tau}}, \tag{4.1}$$

$$L_B(x) = L_0 e^{-\frac{X-x}{\tau}}. \tag{4.2}$$

where X is the length of the scintillator and τ is the attenuation length of the scintillator. If we take the product of these,

$$L_T \times L_B = L_0 e^{-\frac{X-x}{\tau}} \times L_0 e^{-\frac{x}{\tau}} = L_0^2 e^{-\frac{X}{\tau}}, \tag{4.3}$$

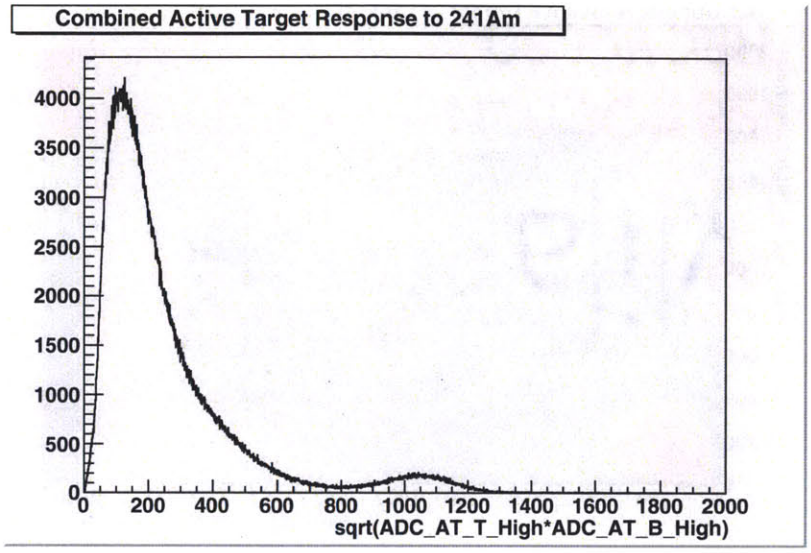

Figure 4-3: Combined top and bottom response to the 59.5 keV γ-ray from ^{241}Am, showing the photopeak at channel 1042 and the Compton edge at channel 255.

then the result is proportional to L_0^2 and independent of x. If we take the square root, then this is directly proportional to the amount of light generated. This geometric mean is used to combine the top and bottom responses into a single active target response.

The spectra from figures 4-1a and b are combined using the geometric mean to give the spectrum shown in figure 4-3. We can then fit to the photopeak at channel 1042, and the Compton edge at channel 255.

The response to the 30 keV X-ray from ^{133}Ba of the top and bottom phototube is shown in figures 4-4a and b. There is again some low energy structure, and then a shoulder which extends across the entire range of the spectrum.

Figure 4-5 shows the bottom phototube response versus the top phototube response. The low energy Compton events are in region I, but the Compton edge cannot be resolved. The outer edges of the photopeak are visible in region II, but it is largely obscured by the Compton events from the high energy γ-rays of ^{133}Ba, seen in region III. The level diagram for ^{133}Ba is shown in figure 4-6. [25]

As with ^{241}Am, the spectra from figures 4-4a and b are combined using the geometric mean to give the spectrum shown in figure 4-7. With the geometric mean, we can resolve the 30 keV X-ray at channel 620. While there are low pulse

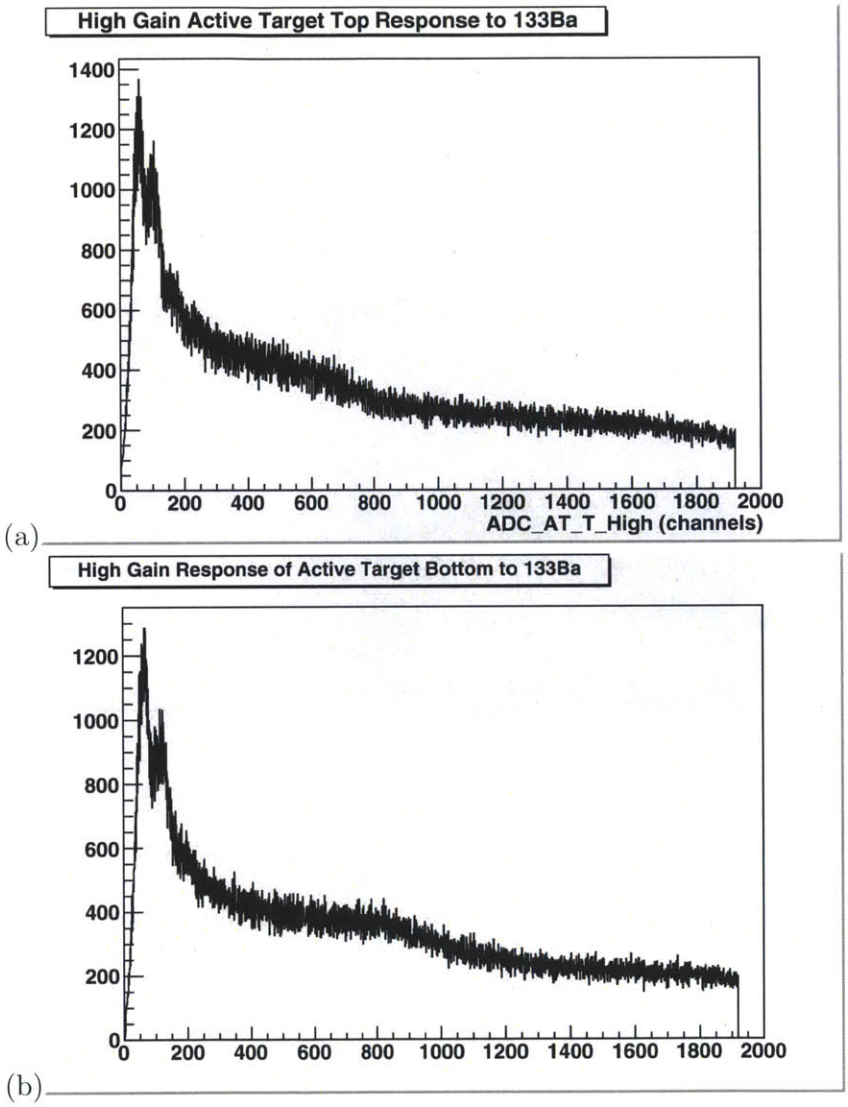

Figure 4-4: Active target (a) top and (b) bottom phototube response to ^{133}Ba.

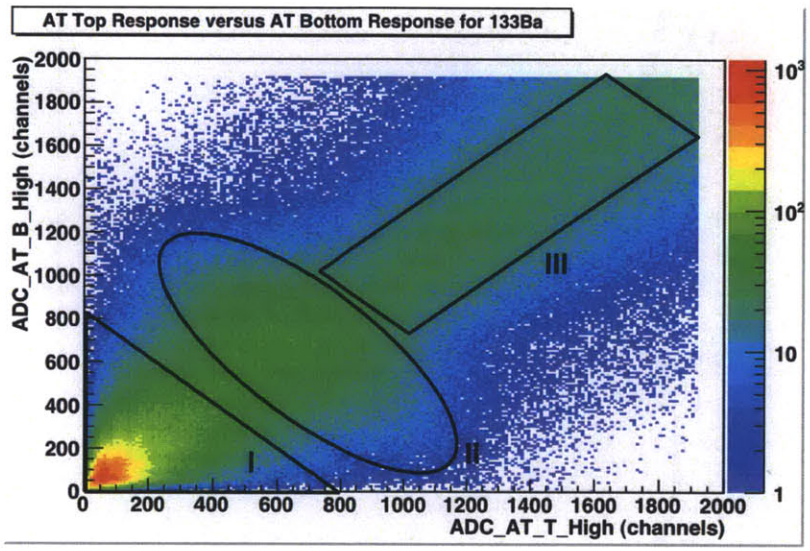

Figure 4-5: Active target bottom phototube response versus active target top phototube response for ^{133}Ba. Region I shows the low energy Compton edge from the 30 keV X-ray; however, it cannot be resolved. Region II is the photopeak, but it is obscured by the Compton events caused by ^{133}Ba's higher energy γ-rays, seen in region III.

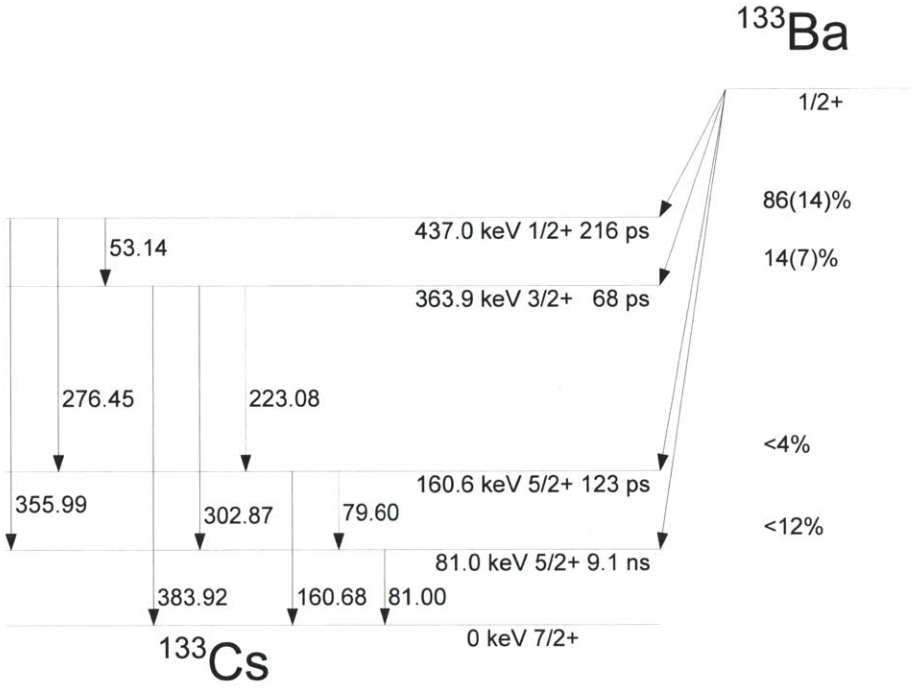

Figure 4-6: Level diagram for the higher energy γ-rays produced by the decay of ^{133}Ba into ^{133}Cs. [25]

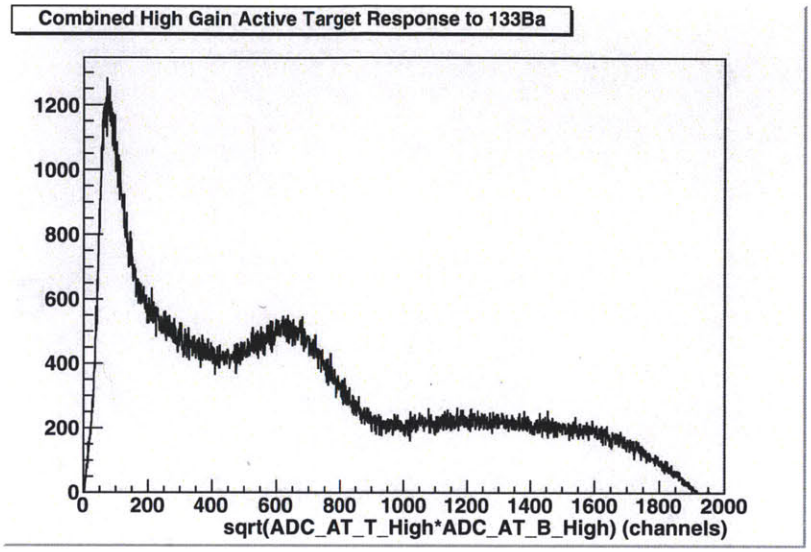

Figure 4-7: Combined top and bottom response to ^{133}Ba showing the 30 keV X-ray peak at channel 650, with the upper end of the Compton edge visible below channel 100.

height events, the Compton edge of the 30 keV X-ray is at 3 keV, below the threshold of the active target.

With these three low energy points, we are able to calibrate the active target response at low energies. The linear fit to these three points is shown in figure 4-8. The resulting calibration gives the response in keV electron equivalent

$$\begin{aligned} \text{AT Response (keVee)} &= P_1 \times \text{AT Response (channels)} + P_0 && (4.4)\\ \text{with } P_1 &= 0.062 \pm 0.0049, && (4.5)\\ P_0 &= -5.7 \pm 3.5. && (4.6) \end{aligned}$$

4.1.2 Calibration at UKY

The target was calibrated using ^{241}Am and ^{137}Cs sources. The ^{241}Am spectrum is shown in figure 4-9. The 59.5 keV γ-ray is visible near channel 130. The Compton edge for this γ-ray is also visible, 11.2 keV, falling at approximately channel 35. For both points, the channel numbers are approximately twice the energy with a 10 channel offset.

The ^{137}Cs spectrum is shown in figure 4-10. ^{137}Cs has a low energy x-ray at 30

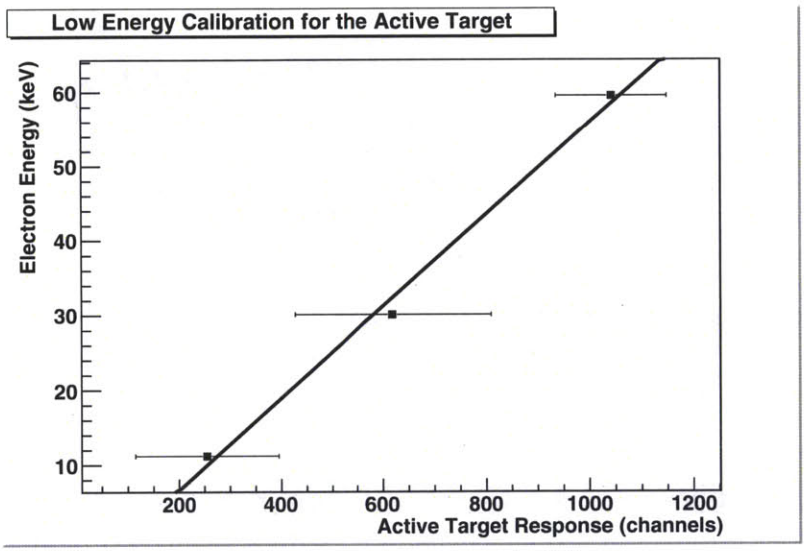

Figure 4-8: Low energy calibration of the active target at LANSCE. For the photopeaks at 30 and 59.5 keV, the error bars are determined by gaussian fits to the photopeaks. For the Compton edge at 11.2 keV, the full error bar is the full width of the edge.

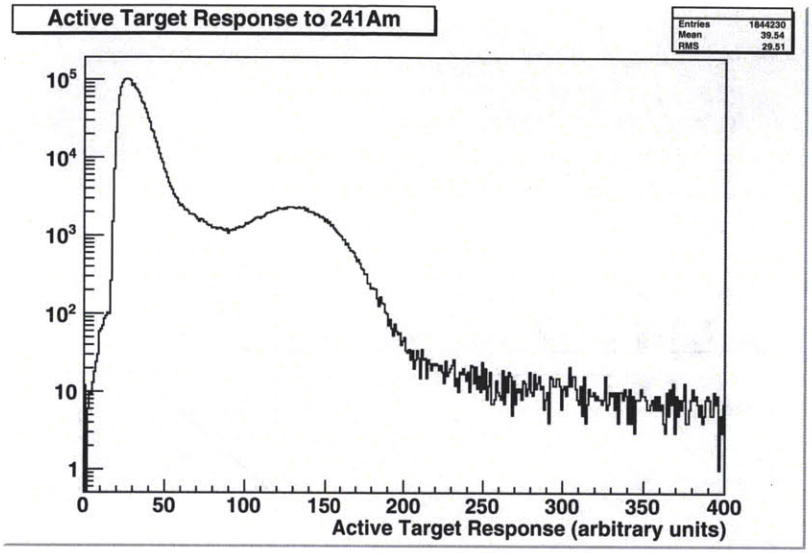

Figure 4-9: Active target response to ^{241}Am. The 59.5 keV γ-ray is visible near channel 130, and the 11.2 keV Compton edge is visible at low energies.

keV, which is visible in the wide peak near channel 75. This is again consistent with our previous estimate of 2 channels per keV, with a 10 channel offset. However, the Compton edge for ^{137}Cs's 667 keV γ-ray should fall at 478 keV. This indicates that the response of the photomultiplier tubes is not directly proportional to the electron energy across the full range, most likely due to saturation.

Using the low energy calibration points, we can find a linear calibration of the active target response. The resulting calibration is

$$\text{AT Response (keVee)} = (0.521 \pm 0.0066) \times \text{(channel)} - (7.8 \pm 0.58). \quad (4.7)$$

If we include the ^{137}Cs point, we can produce a quadratic calibration, shown in figure 4-12. As we will see in section 5.3, this nonlinearity may be due to saturation in the phototube. We will use the lower energy linear calibration to obtain the actual light response, and extrapolate to higher energies with the linear fit to compare the light response for protons of different energies.

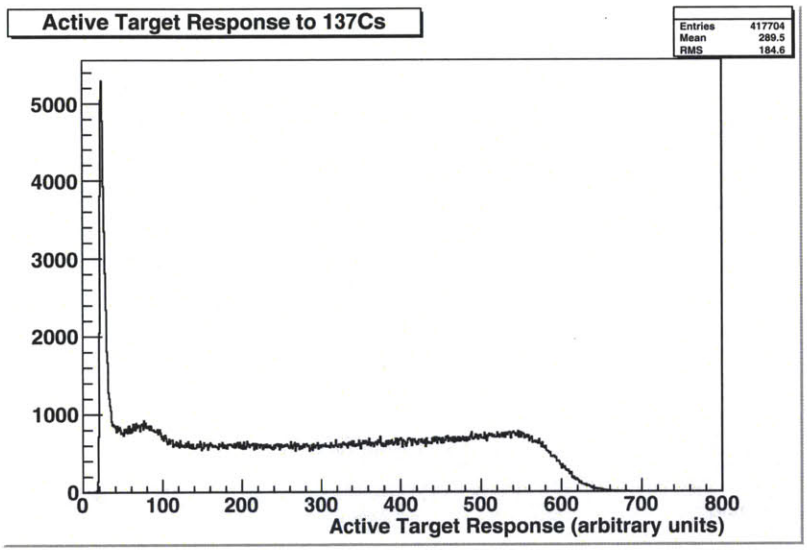

Figure 4-10: Active target spectrum with a ^{137}Cs source. The 30 keV x-ray is visible near channel 75, but the edge at approximately channel 600 is inconsistent with the 478 keV Compton edge we expect from the 667 keV γ-ray from ^{137}Cs, based on the other calibration points. We suspect this is due to non-linearity over this large a range in the pulse height spectrum.

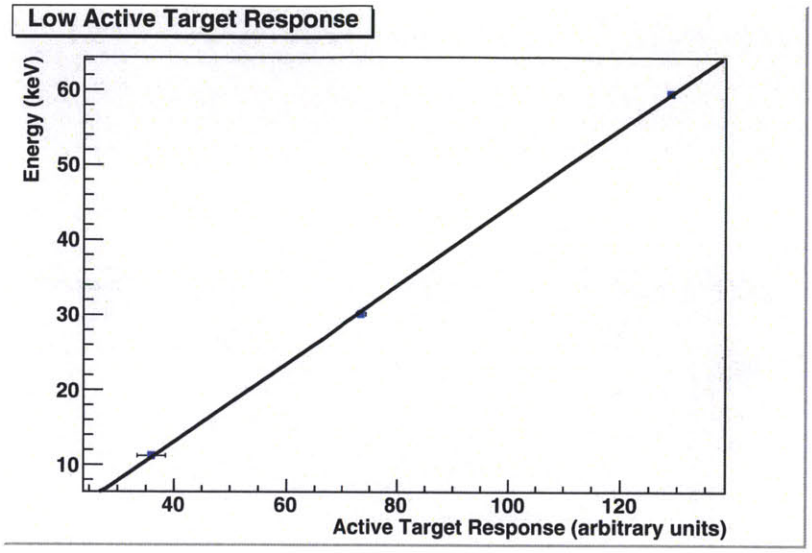

Figure 4-11: Linear calibration of the low energy active target.

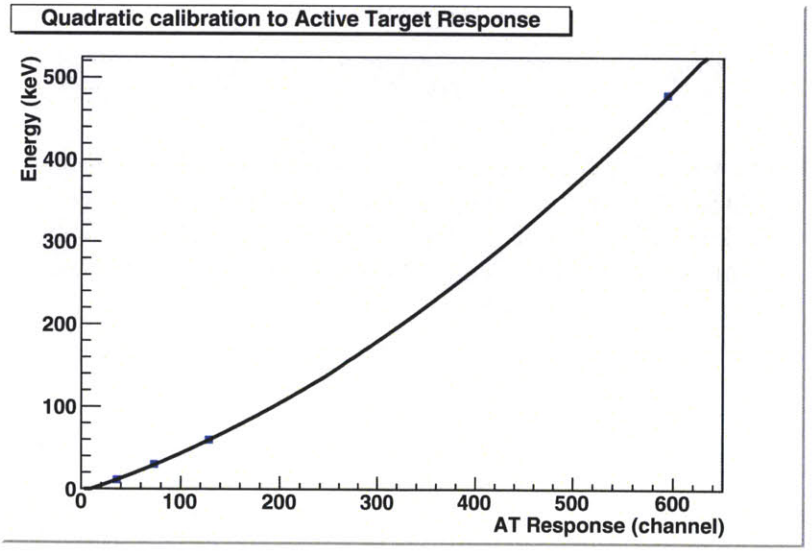

Figure 4-12: Quadratic calibration of the active target.

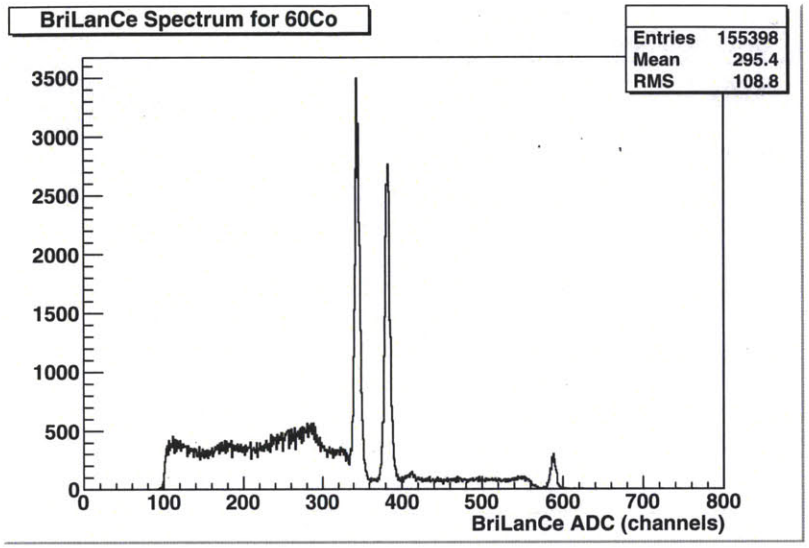

Figure 4-13: γ-ray spectrum for ^{60}Co with the BrilLanCe detector, with very sharp 1173 and 1332 keV peaks, and the 2505 keV sum peak is also visible.

4.2 BrilLanCe

BrilLanCe scintillators provide very precise γ-ray spectra; figures 4-13 and 4-14 show the γ-ray spectra for ^{60}Co and ^{137}Cs. For both sources, the γ-ray peaks are very sharp and distinct, and the sum peak for ^{60}Co is visible as well. Using these points and the 4.44 MeV γ ray produced by inelastic C(n,n')C* scattering, with the decay C* $\rightarrow$ C + 4.44 MeV γ (see section 6.1.1) we are able to calibrate the γ-ray energy across the entire region of interest for capture events. The resulting γ-ray energy calibration is shown in figure 4-15. The fit was not linear as a result of the extremely fast signals, as discussed in section 3.2.1.2. [35] We were able to fit the data with a quadratic calibration

$$E_\gamma \text{ (keV)} = 200 \pm 11.1 + (1.25 \pm 0.059) \times ch + ((4.55 \pm 0.072) \times 10^{-3}) \times ch^2. \quad (4.8)$$

4.3 BGO

The BGOs were calibrated using ^{60}Co and ^{228}Th sources. The low resolution of the BGOs made calibration with the ^{60}Co source difficult, as the two lower energy

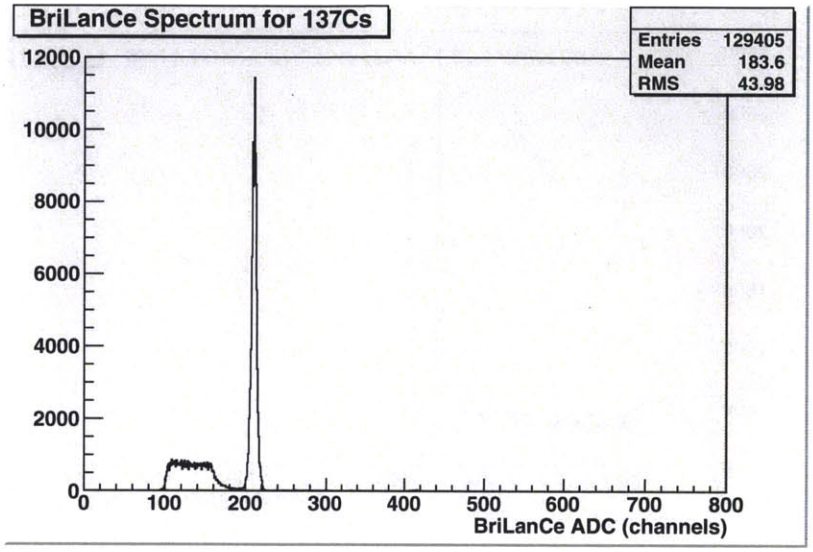

Figure 4-14: γ-ray spectrum for ^{137}Cs with the BrilLanCe detector, with the very sharp 667 keV peak.

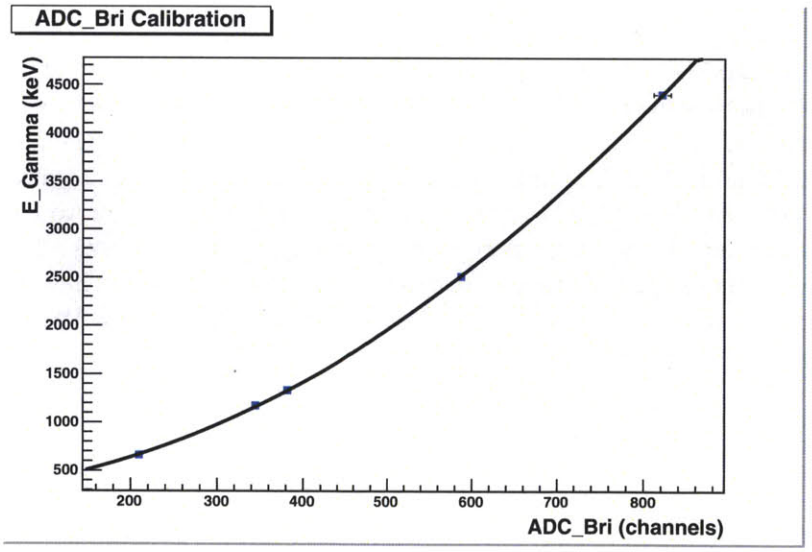

Figure 4-15: γ-ray energy calibration for the BrilLanCe detector. The calibration was not linear, but was well described by a quadratic form.

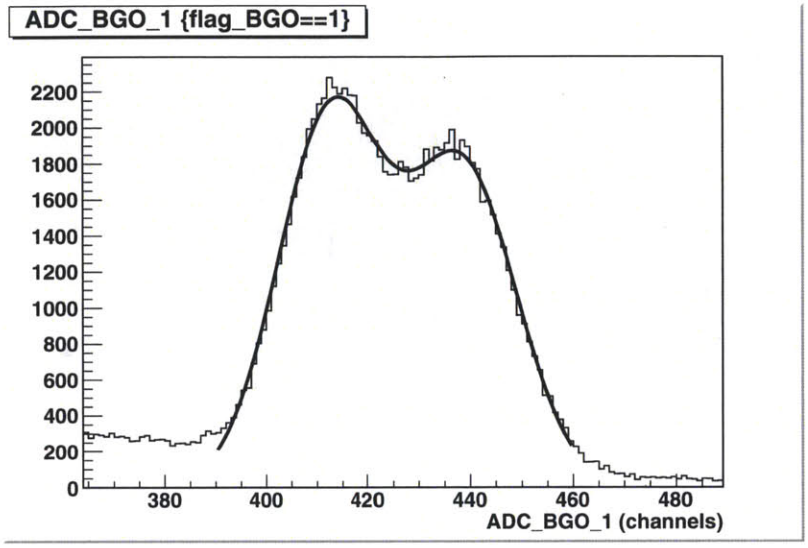

Figure 4-16: Calibration spectrum for BGO1 for ^{60}Co, fitted with two summed gaussian plots. The peaks from each γ-ray are overlapping.

γ-rays overlapped. This is shown for each BGO in figures 4-16 and 4-17. The overlapping peaks could be fitted with two gaussian functions added together. When compared to the spectrum from the BrilLanCe detector previously shown in figure 4-13 we can see the inferior energy resolution of the BGO detectors. These points, along with the sum peak from ^{60}Co and the 2.614 MeV γ-ray from ^{228}Th, were used to calibrate the γ-ray energy in the BGOs.

$$E_{\gamma,\,\mathrm{BGO1}}\ (\mathrm{keV}) = 9.828 \pm 0.0052 \times ch - 2256 \pm 2.1 \tag{4.9}$$

$$E_{\gamma,\,\mathrm{BGO2}}\ (\mathrm{keV}) = 10.953 \pm 0.0069 \times ch - 3078 \pm 3.0 \tag{4.10}$$

4.4 Time of Flight

Neutron energies were determined by time of flight. γ-rays produced in the neutron production target were used to calibrate the absolute time of flight.

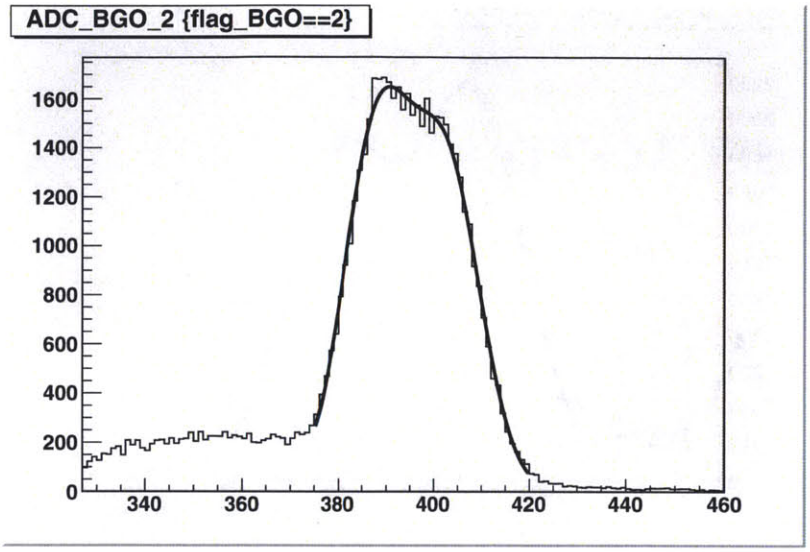

Figure 4-17: Calibration spectrum for BGO2 for ^{60}Co, fitted with two summed gaussian plots. The peaks from the γ-rays are nearly merged in this result.

4.4.1 UKY

Time of flight was calibrated using the γ-rays produced by the $^{7}\mathrm{Li}(p,\gamma)^{8}\mathrm{Be}$ reaction for the LiF target, and by the $^{3}\mathrm{H}(p,\gamma)^{4}\mathrm{He}$ reaction. The CAMAC TDC modules had an intrinsic channel width of 0.25 ns, so a single absolute time of flight measurement was all that was necessary to calibrate the time of flight.

Figure 4-18 shows the beam TDC stop for the LiF target at $T_p = 1.615$ MeV. This signal is started by the event trigger and stopped by a delayed pick-off signal generated when the proton burst reaches the neutron production target, measuring of the time between neutron production and event trigger. For the LiF target, the γ-ray is clearly visible on the right side of the figure. We can use this to calibrate the time of flight of the neutrons, which fall in the center of this figure.

The cross section for the $^{3}\mathrm{H}(p,\gamma)^{4}\mathrm{He}$ reaction is much smaller, so the position of the γ-flash for the tritium data is much more uncertain. Figure 4-19 shows the beam TDC stop for the tritium cell at $T_p = 1.615$ MeV. The neutrons are clearly visible in approximately the same position as in figure 4-18 for the LiF target. However, the gamma flash is not clearly visible at this scale. If we focus on the region where we expect the γ-flash, we can see a small peak that corresponds to the γ-flash. This is shown in figure 4-20.

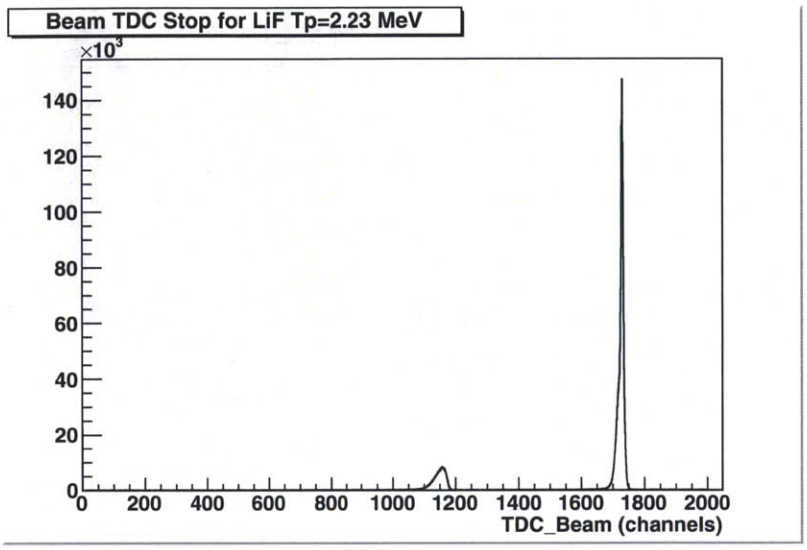

Figure 4-18: Beam TDC stop for the LiF target at $T_p = 2.23$ MeV. The γ-flash is clearly visible on the right side of the figure, with neutrons in the smaller peak near the center.

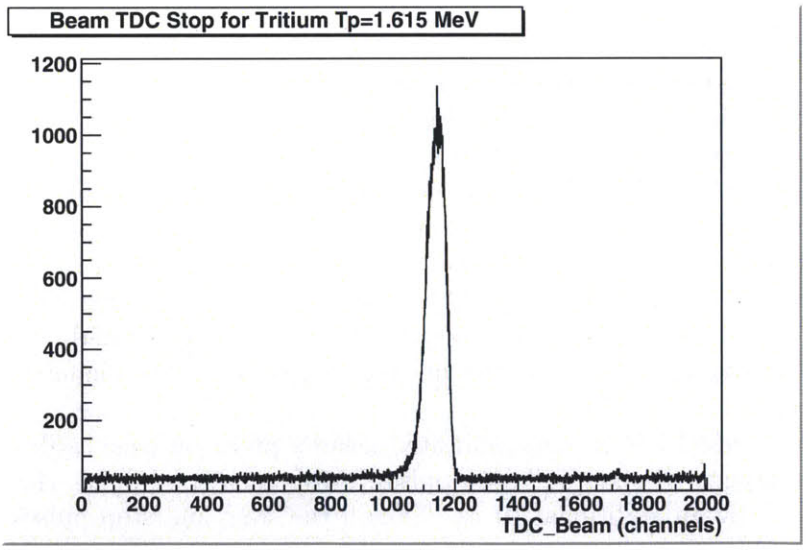

Figure 4-19: Beam TDC stop for the tritium cell at $T_p = 1.615$ MeV. The large peak is the neutrons, the gamma flash cannot be clearly seen at this scale.

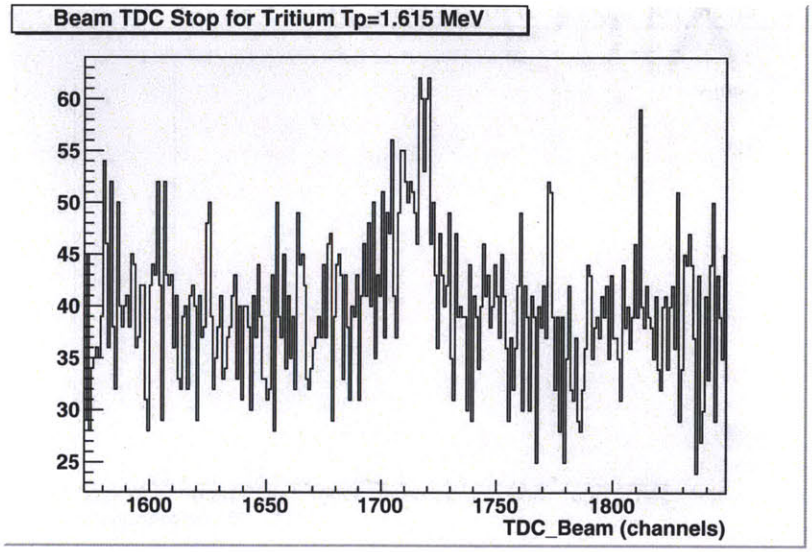

Figure 4-20: Beam TDC stop for the tritium cell at $T_p = 1.615$ MeV focused on the region with the γ-flash.

4.4.2 LANSCE

Neutron beam time of flight was measured using the T_0 cascade described in section 3.2.2.4. For 1.8 μs beam micropulse spacing, eight time to FERA converters covered the possible time of flight ranges. These eight raw spectra are shown in figure 4-21. The structure seen in the first and last T_0 spectrum are the γ-ray flashes produced by the spallation target. There are multiple peaks because of slight differences in the timing of the triggers; the neutron beam time of flight for each trigger is determined separately using that trigger's γ-flash. The structure appears in both the first and last spectra because of "wrap-around:" the T_0 signal from a following beam pulse arrives in time to generate a stop signal in the eighth spectrum.

The individual TFCs were calibrated using a precision time calibrator, which generated staggered start and stop pulses. After each start pulse, the stop pulse was delayed by an additional 10 ns. Thus if the start and stop pulses were used to start and stop the TFC, a series of peaks separated by 10 ns would appear in the TDC. Figure 4-22 shows an example of this for TDC_T0_1. With these peaks, we can fit the TFC response to determine the calibration. This was done for each TFC, with the result 0.15-0.2 ns per channel.

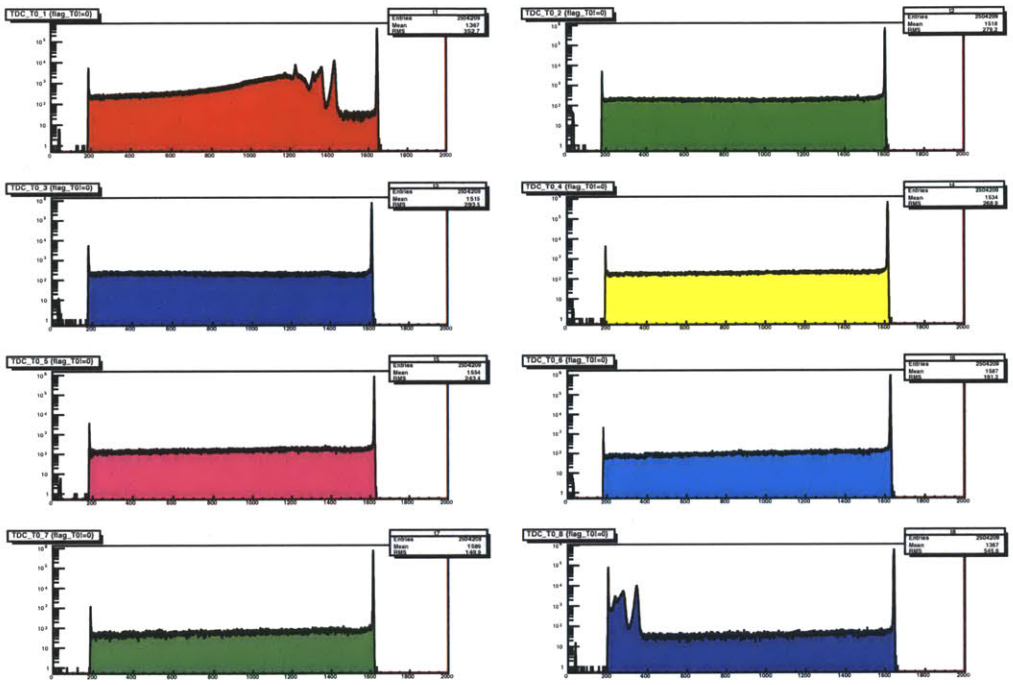

Figure 4-21: The eight TDC_T0 spectra used to calculate time of flight for the neutron beam with 1.8 s spacing. For 3.6 s beam spacing, eight more were used to cover the entire range. The colors correspond to the regions covered in figure 4-25.

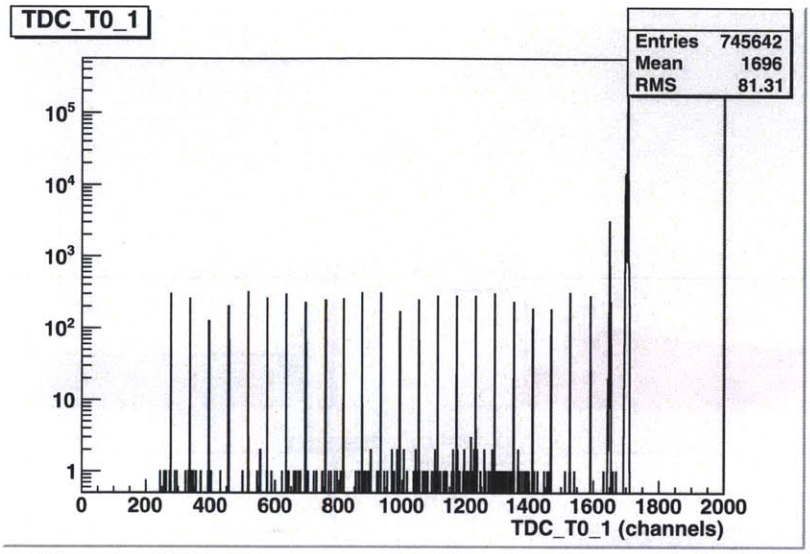

Figure 4-22: Calibration of TDC_T0_1 with a calibrating pulser set to 10 ns intervals.

To determine the total time of flight for an event, the offsets between the different T_0 spectra must be determined. Finding these offsets and determining the total time of flight spectrum was referred to as "gluing" the T_0 spectra together. To determine these offsets, a two dimensional plot of each T_0 versus the preceding T_0 was made, and the overlapping regions could be seen. This plot is shown for T0_3 and T0_4 in figure 4-23. The offset of the time scales on the axes is arbitrary. The vertical band is composed of events that are covered by T0_4, and have an underflow value in T0_3. The horizontal band is composed of events that are covered by T0_3, and so have an underflow value in T0_4. At the upper end of the horizontal band is the overlapping region, where the events form a band with slope $\sim$ unity, ending in a vertical band composed of T0_4 events with an overflow signal in T0_3. A magnified version of this overlapping region is shown in figure 4-24.

To determine the offset between T0_3 and T0_4, a linear function is fitted to this region. The intercept of the fit gives the time offset between them, and allows us to glue all the T_0 signals together. The glued together T_0 spectra, called T0_Time, is shown in figure 4-25. This time is then used with the individual trigger time of flight calibrations to determine the time of flight and neutron energy.

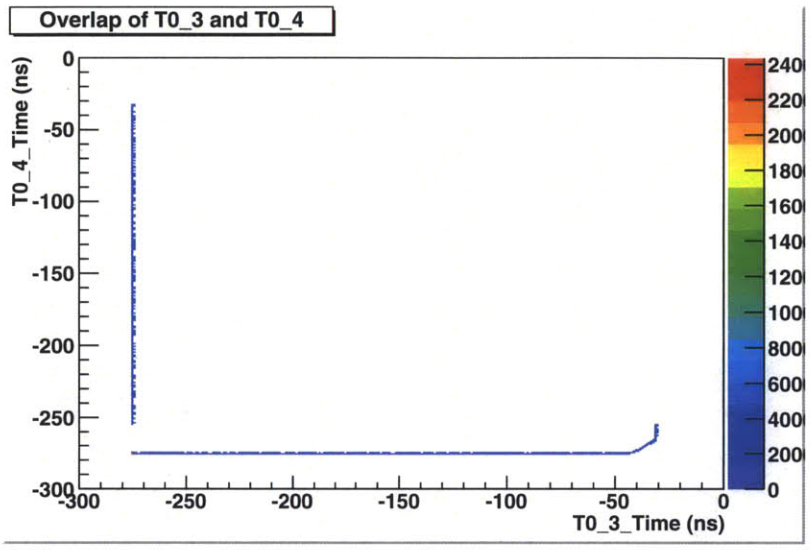

Figure 4-23: Overlap of T0_3 and T0_4. The offset of the times in the axes are arbitrary. Fitting to the sloping region can determine the offset between T0_3 and T0_4.

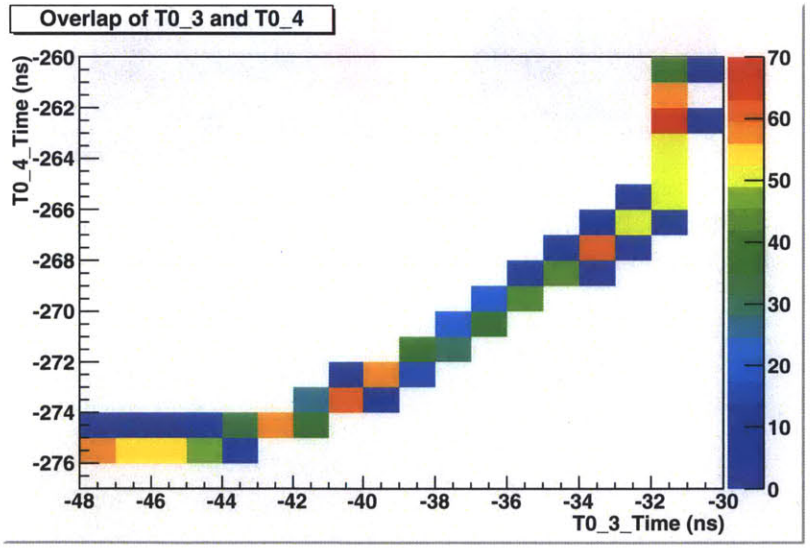

Figure 4-24: The overlapping region of T0_3 and T0_4 magnified.

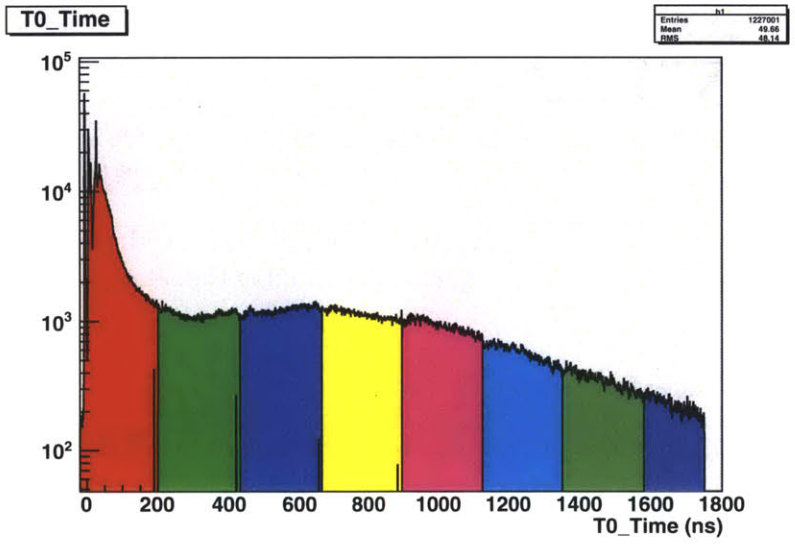

Figure 4-25: Plot of T0_Time, which is used to calculate neutron time of flight. The color of each region indicates the TDC_T0 in figure 4-21 that covers the region.

Chapter 5

Characterization of the Active Target

Understanding the response of our scintillator, BC418, to heavy charged particles such as protons and deuterons was important in order to identify capture events and reduce backgrounds. The recoiling deuteron in a capture event below 600 keV has approximately half the energy of the incident neutron in the lab frame, but there have not been many measurements of plastic scintillator response to heavy particles below 300 keV, and none specifically with BC418.

In order to characterize our active target, we measured the response to recoiling protons produced by *np* elastic scattering both during the radiative capture measurement and in dedicated light response measurements, and determined the scintillator response to protons from 100 keV to 3.6 MeV.

5.1 Scintillator Response Measurement at LANSCE

The liquid scintillator used to detect scattered neutrons was initially placed at 25° with respect to the beam, so that 90% of the kinetic energy of the incident neutron went to the scattered neutron, and 10% went to the recoil proton. In order to measure the response at higher proton energies, the liquid scintillator was moved to 45° so that half of the incident neutron kinetic energy was imparted to the recoiling proton.

Scattered neutrons were identified via three conditions: pulse shape discrimination, dynamical biasing, and time of flight correlations. For pulse shape dis-

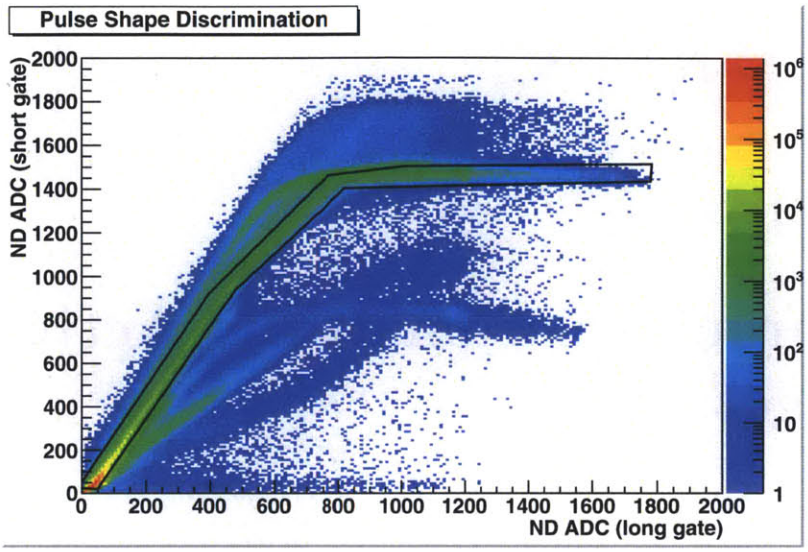

Figure 5-1: Short gate ND ADC versus the long gate ND ADC. The neutron band is indicated by the black outlined region. The γ-ray band lies just above this band.

crimination, two different ADC signals were recorded from the neutron detector, one with a short linear gate and one with a longer linear gate. Neutrons and γ-rays produce light pulses with different shapes in time; the pulses produced by neutrons will have a much longer tail than the pulses produced by γ-rays, so that particles can be identified by plotting the pulse height spectrum from the short gate versus that from the long gate ADC. This pulse shape discrimination for the lower gain ADC for the neutron detector is shown in figure 5-1. This plot shows some very unusual features, with up to five different bands. The neutron band is the most prominent central band which extends up from the origin and becomes flat near channel 1500 of the short gate ADC. The band of γ-rays extends above the neutron band. This flattening is caused by saturation in the electronics; while the pulse continues to increase in length, it's maximum voltage output is fixed by the electronics. The short gate cuts off the increased length, resulting in a flat short gate ADC while the long gate ADC continues to increase. The lower bands are recoiling carbons in the liquid scintillator. Cutting on these bands yields the neutron energy spectrum shown in figure 5-2. These peaks in the neutron energy correspond to resonances in the nC cross section, indicating that the bands are due to recoiling carbons in the liquid scintillator.

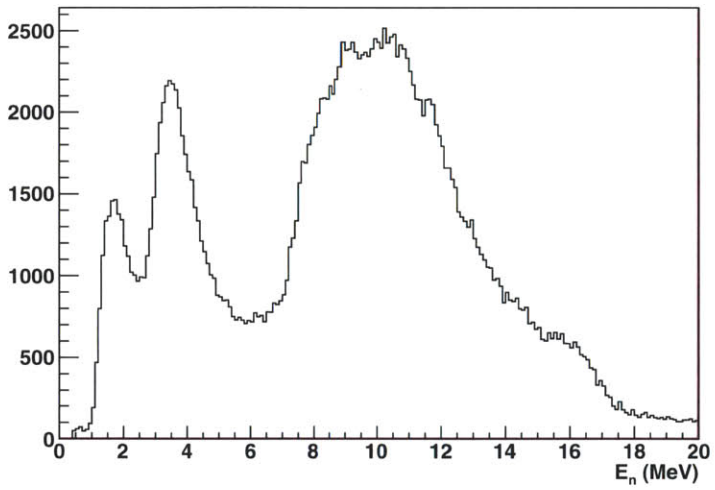

Figure 5-2: Neutron energy spectrum for the extra bands from figure 5-1. The peaks correspond to resonances in the nC cross section.

Backgrounds are further reduced by applying a dynamical biasing condition. For this condition, we plot the ND ADC response versus the scattered neutron time of flight, as shown in figure 5-3. When a neutron enters the detector, the recoil protons from elastic scattering cause scintillation. The light produced will be proportional to the proton energy, not the neutron energy, so a range of pulse heights will be produced due to the range in proton recoil angles up to a maximum pulse height corresponding to $E_p = E_n$ (recoil angle 0°). The outlined region indicates the region where real neutrons fall.

For the timing conditions, we plot the time of flight from the active target to the neutron detector versus the time of flight from the spallation target to the active target. In this plot with the PSD and dynamical biasing cuts, we can see the elastic band as shown in figure 5-4. The black outlined region shows the cut applied to the elastic band. The red outlined region is an identical cut which has been shifted away from the elastic band to determine the background.

5.1.1 Active Target Response

With the black outlined cut on the elastic band in figure 5-4, the active target response versus recoiling proton energy is shown in figure 5-5. The recoil proton

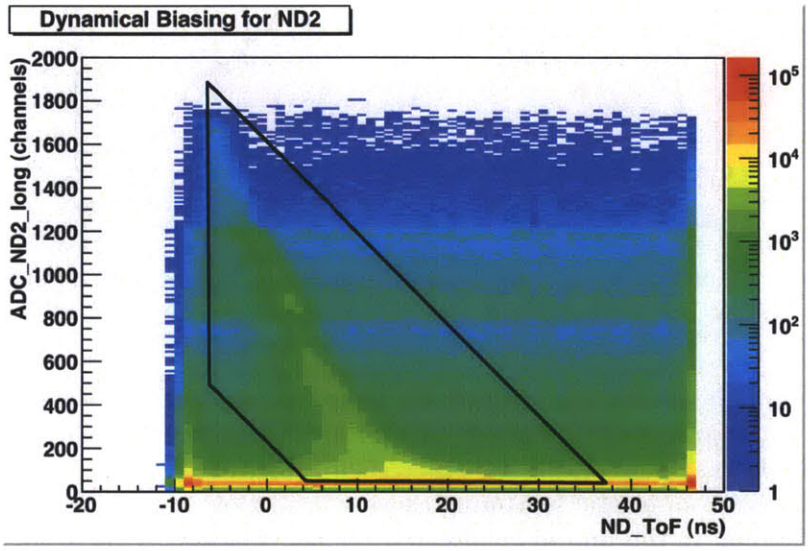

Figure 5-3: Dynamical biasing for ND2. Faster (higher energy) neutrons can deposit more energy, resulting in higher pulse heights, allowing us to exclude backgrounds by cutting on the outlined region. The scattered neutron time of flight is not absolutely calibrated, due to the short flight path and low incidence of γ-rays, but the relative time of flight is accurate.

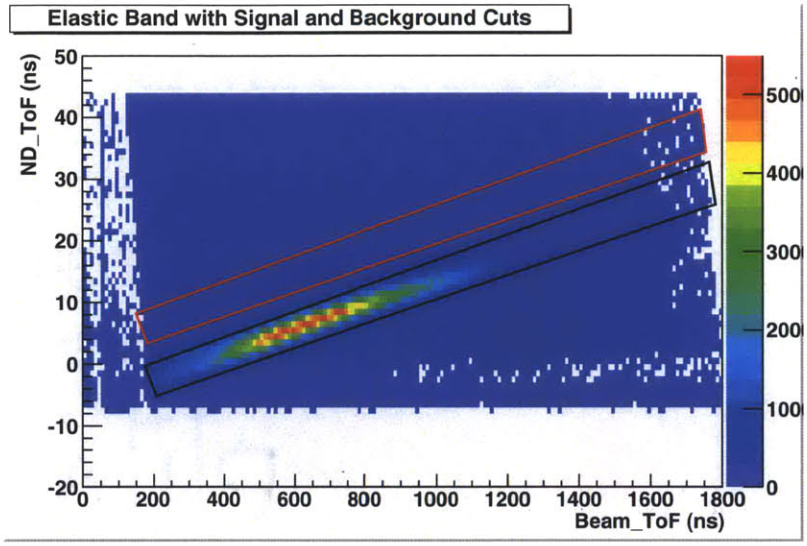

Figure 5-4: Elastic band for ND2. The black outlined region is the elastic band cut, and the red outlined region is an identical cut which has been shifted away from the elastic band to determine the background.

energy is calculated from the kinematics, taking either 10% or 50% of the beam energy depending on the neutron detector angle.[1] A broad, correlated region is visible in this plot, but a significant number of accidental coincidences make resolving the extent of the band difficult. A background timing cut was created by shifting the black outlined region of figure 5-4 off of the elastic band, becoming the red outlined region shown there. This background in the active target response is shown in figure 5-6. Low energy noise is present across all beam energies. The "recoil energy" plotted in this figure is the recoil energy which an elastically scattered proton would have at the corresponding beam energy.

Subtracting this background gives the active target response shown in figure 5-7. While the very low pulse height backgrounds are not completely eliminated, the backgrounds at higher pulse heights are almost entirely eliminated, allowing us to resolve the upper edge of the recoil band.

Seven different active target high voltage settings were used to cover a wide

[1]The uncertainty in the scattered neutron energy is too large to determine the recoil energy by taking the difference between the beam neutron energy and scattered neutron energy calculated by time of flight.

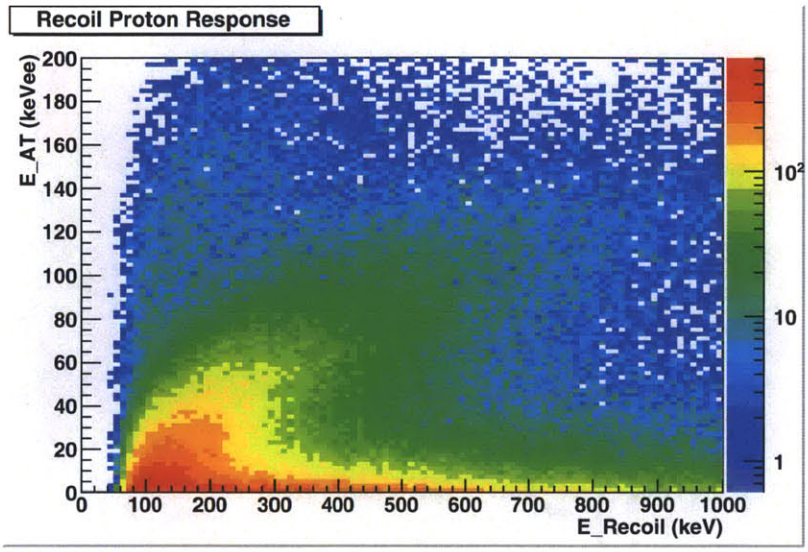

Figure 5-5: Active target response for recoiling protons in *np* elastic scattering. While a broad, correlated region is visible, a significant number of accidental counts makes determining the location of this band difficult.

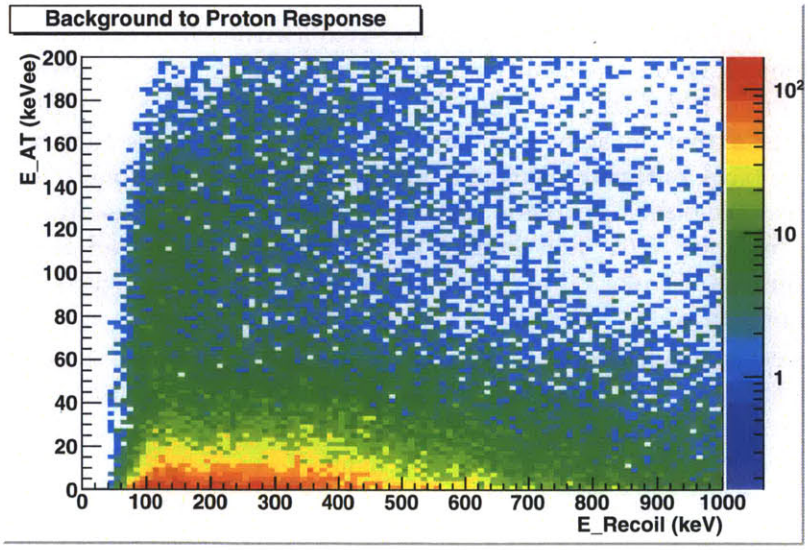

Figure 5-6: Background in the active target response, created by cutting on the red outlined region in figure 5-4.

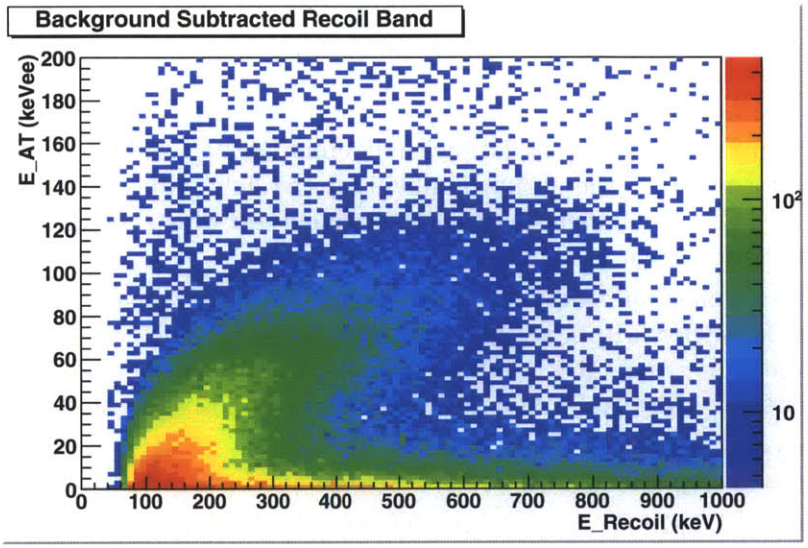

Figure 5-7: Active target response for recoiling protons with the background from figure 5-6 subtracted. The very low pulse height noise is still present, but the backgrounds at higher pulse heights is eliminated almost entirely, allowing us to resolve the upper edge of the recoil band.

Group	Top Phototube Voltage (V)	Bottom Phototube Voltage (V)	Gain Sequence (low to high)
24	-2300	-2325	7
26	-1750	-1750	2
28	-1800	-1900	3
29	-1580	-1650	1
30	-2150	-2300	6
31	-1975	-2100	4
32	-2065	-2200	5

Table 5.1: High voltage settings for the different light response data groups.

dynamic range. Each group of data with different timing and high voltage settings is assigned a number; the group numbers for the light response data are shown in table 5.1. Group numbers indicate the sequence in which the data were taken. The recoil band shown in figure 5-7 is from group 24.

The background subtraction was performed for all the groups. The recoil band for group 26 is shown in figure 5-8. For this group, the noise at low pulse height that was seen in group 24 is no longer visible, but the upper edge of the band is not as distinct. Above approximately 3 MeV, the band begins to flatten.

The recoil band for group 28 is shown in figure 5-9. Flattening similar to that in group 26 is seen above 3 MeV.

The recoil band for group 29, the lowest gain group, is shown in figure 5-10. In this case, however, there is no flattening above 3 MeV. The range of $\sim$ 3.6 MeV protons in the active target is 0.2 mm, 10% of the target thickness, and so significant proton escaping may begin in this region. Since there is no flattening until much higher energies for group 29, we believe that the flattening is likely due to electronic saturation and not to protons escaping the target.

The recoil band for group 30 is shown in figure 5-11. This group has much higher gain than groups 26-29, and so the recoil band only extends up to approximately 3 MeV. There is significant noise at low pulse heights, as was seen in group 24, but here it is distinct from the recoil band, allowing much easier fitting.

The recoil band for group 31 is shown in figure 5-12. This group again has much higher gain than groups 26-29, and shows a similar low pulse height distribution.

The recoil band for group 32 is shown in figure 5-13. This group shows characteristics similar to those of group 31, with a similar low pulse height noise distribution and asymmetry in the recoil band.

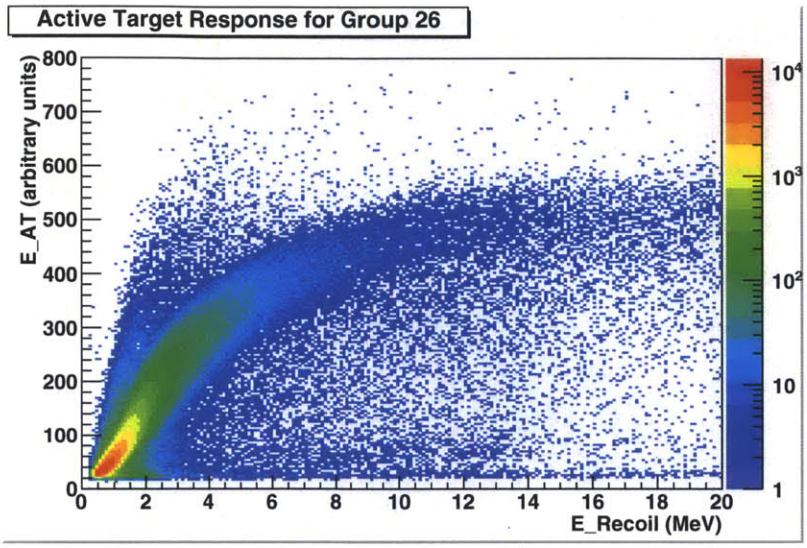

Figure 5-8: Active target response for recoiling protons from group 26. The band begins to flatten above 3 MeV.

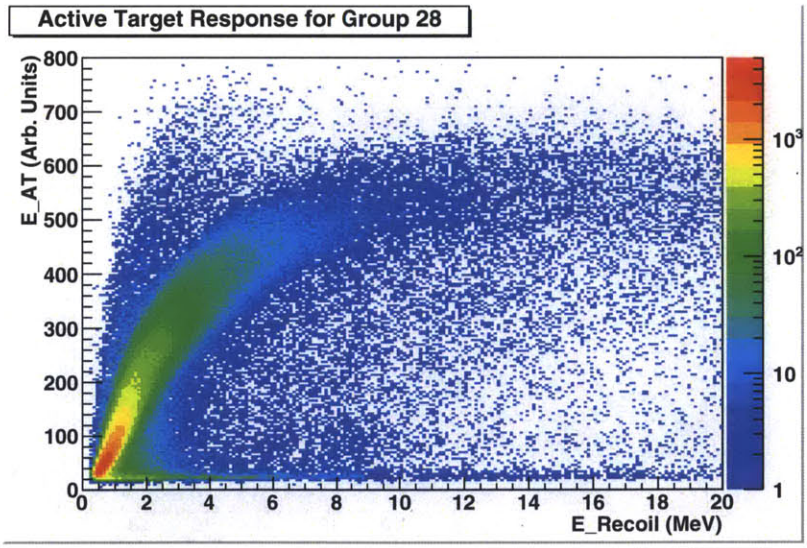

Figure 5-9: Active target response for recoiling protons from group 28. As with group 26, the band begins to flatten above 3 MeV.

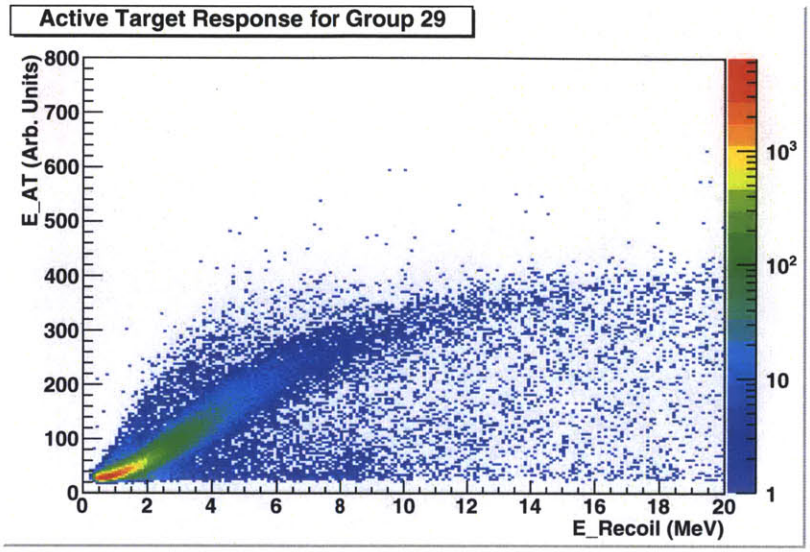

Figure 5-10: Active target response for recoiling protons from group 29. There is no flattening seen above 3 MeV as with groups 26 and 28, indicating that this may be due to electronic saturation and not protons escaping the active target.

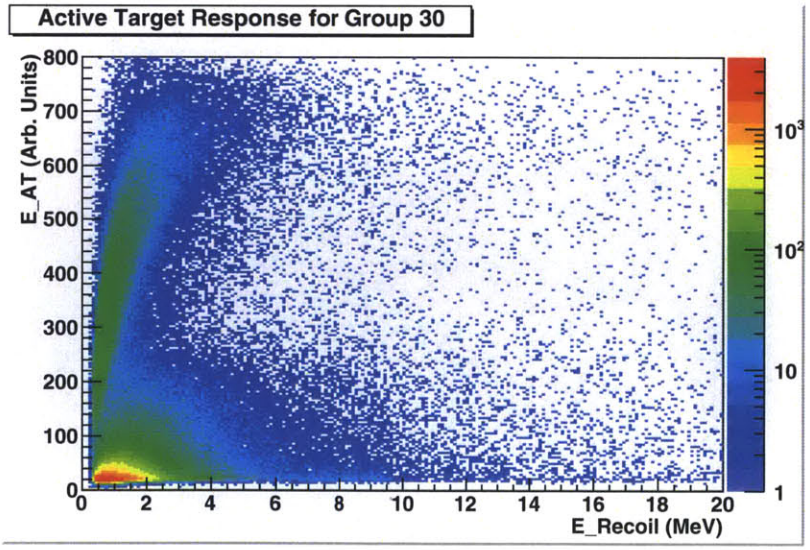

Figure 5-11: Active target response for recoiling protons from group 30. The recoil band only extends as high as ~3 MeV due to the higher gain of this data.

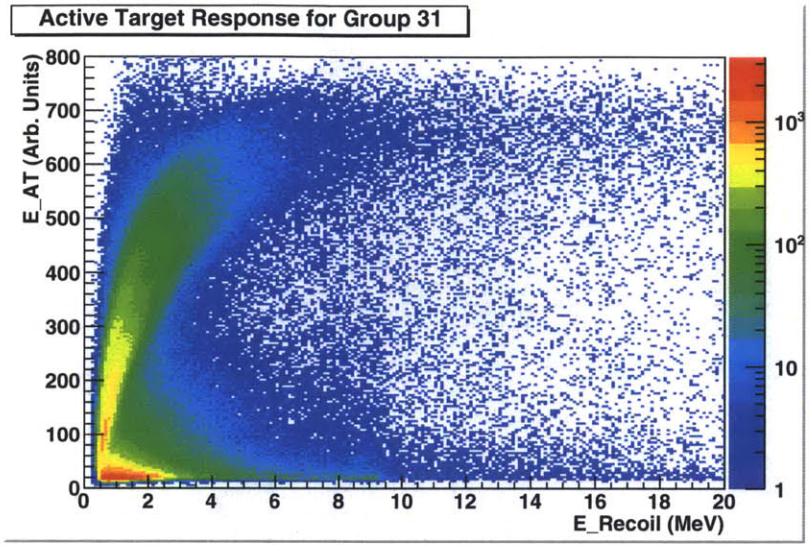

Figure 5-12: Active target response for recoiling protons from group 31. This recoil band shows significant asymmetry.

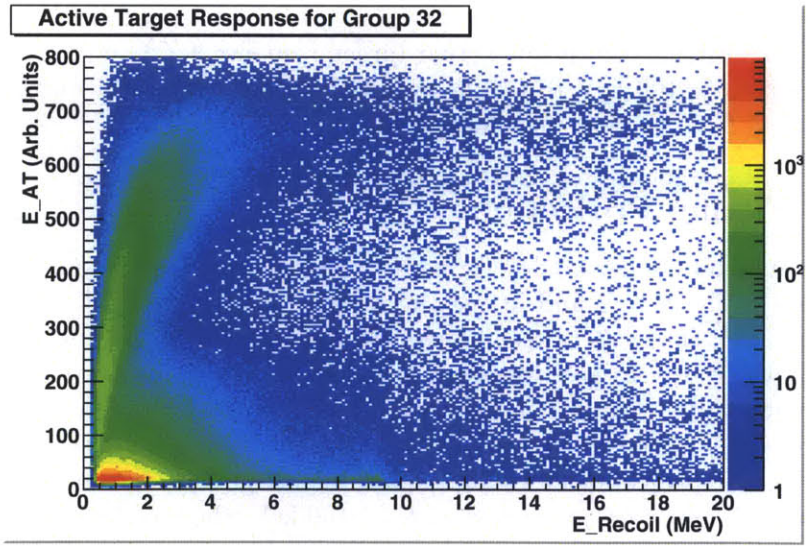

Figure 5-13: Active target response for recoiling protons from group 32. As with group 31, this recoil band shows significant asymmetry.

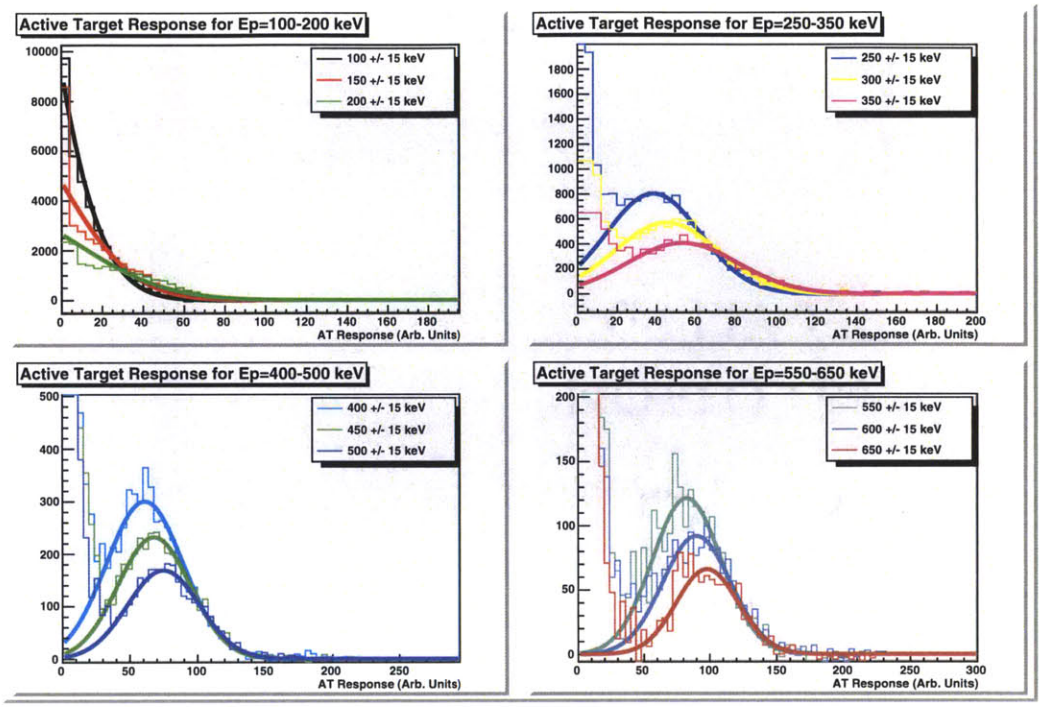

Figure 5-14: Fitting the mean active target response for Group 24 for proton energies for E_p = 100 keV to 650 keV. Below 250 keV the recoil peak cannot be distinguished from the low pulse height noise.

5.1.2 Fitting Projections

From these recoil bands, we determine the mean active target response by taking projections of the Y-axis and fitting the resulting distribution. These slices were taken at 50 keV intervals in recoil energy, ranging from 100 keV up to 7 MeV. A minimum width of $\pm$15 keV was used for all slices to provide adequate statistics, and this range was increased as the uncertainty in beam energy increased. Fits to these projections of the recoil band for Group 24 are shown in figure 5-14 for 100 to 650 keV. Fits to projections for all groups at all energies are shown in appendix A.

While we hoped to reach as low as E_p = 100 keV, the recoil band for group 24 becomes indistinguishable from the low pulse height noise below 250 keV. Above 250 keV, we are able to distinguish the peak from the low pulse height noise and can fit gaussian distributions to these recoil peaks up to E_p = 650 keV. The mean values of these fits are plotted versus proton energy in figure 5-15. The relationship

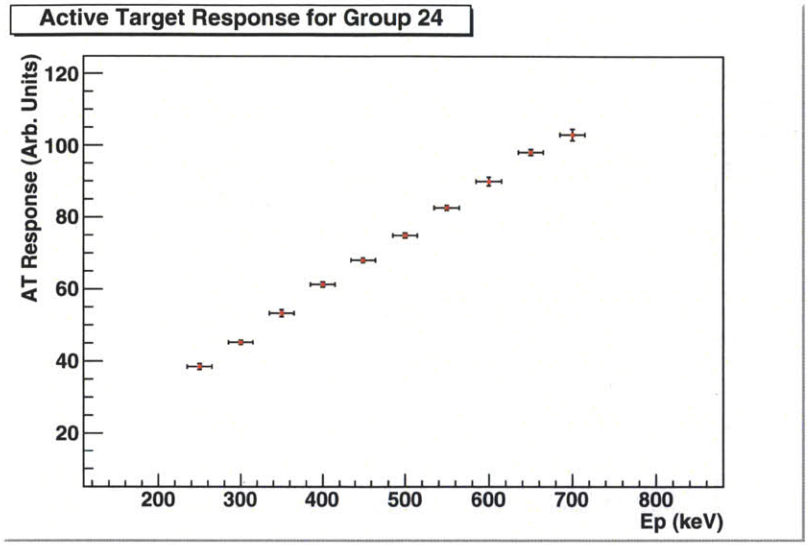

Figure 5-15: Mean active target response versus proton energy for Group 24. The relationship between proton energy and active target response is approximately linear.

between the proton energy and the active target response is approximately linear in this range.

Below approximately 1900 keV, group 26 shows significant asymmetry in the distributions. The leading edge and peak are well described by a gaussian fit, but the trailing edge falls off much more slowly. As the proton energy increases, the peaks become more symmetric. At 1900 keV the trailing edge matches the gaussian and the mean value shifts forward, creating a discontinuity in the mean response. This can be seen in figure 5-16, which shows the mean active target response versus proton energy. At the discontinuity, there is a shift in the slope of the active target response. Below the discontinuity, the trend is concave up, and then above it is concave down, showing significant flattening in this region.

Group 28 shows a similar asymmetry to that in group 26 at low energies. In this case, the asymmetry does not end until $E_p = 1750$ keV, again with an associated discontinuity. The mean values of these fits are plotted versus proton energy in figure 5-17. As with group 26, the mean response is concave up below the discontinuity and concave down above it.

There is no asymmetry in group 29; the recoil peaks are well described by gaussian fits down to 450 keV. Above approximately 5 MeV the number of counts

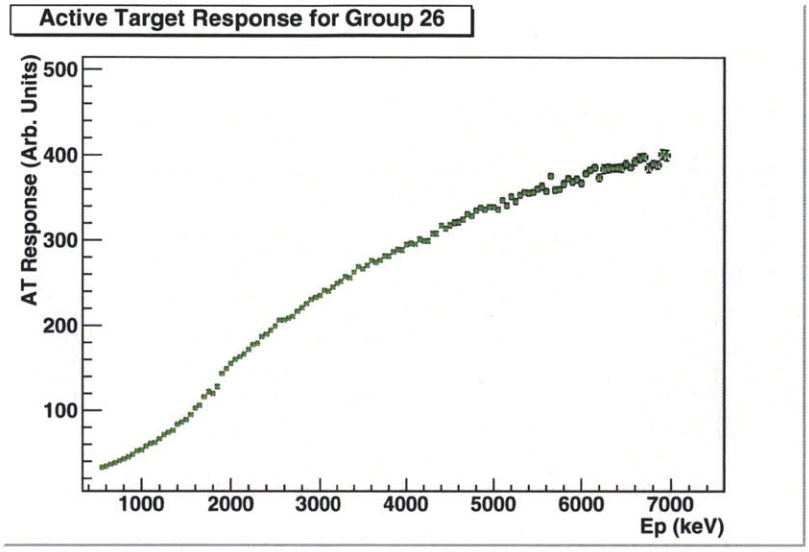

Figure 5-16: Mean active target response versus proton energy for Group 26. The discontinuity created by the shift from the asymmetric peaks to the symmetric peaks is visible at 1900 keV.

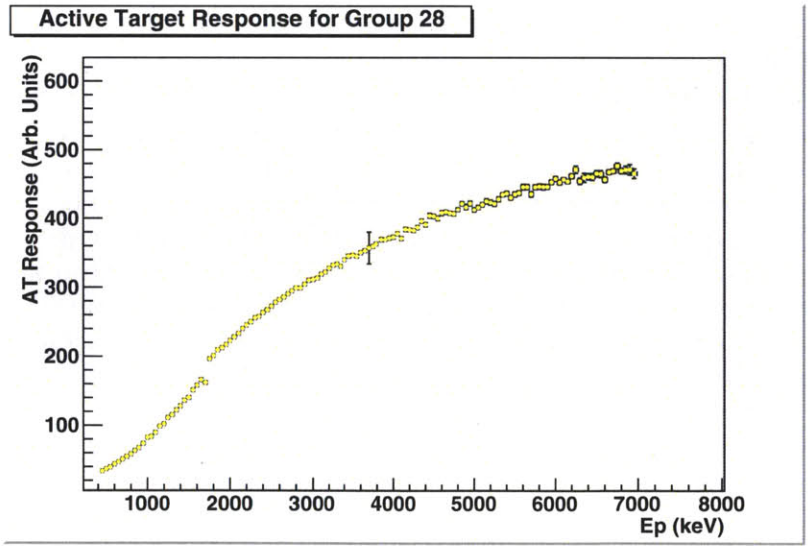

Figure 5-17: Mean active target response versus proton energy for Group 28. The discontinuity is visible at 1800 keV.

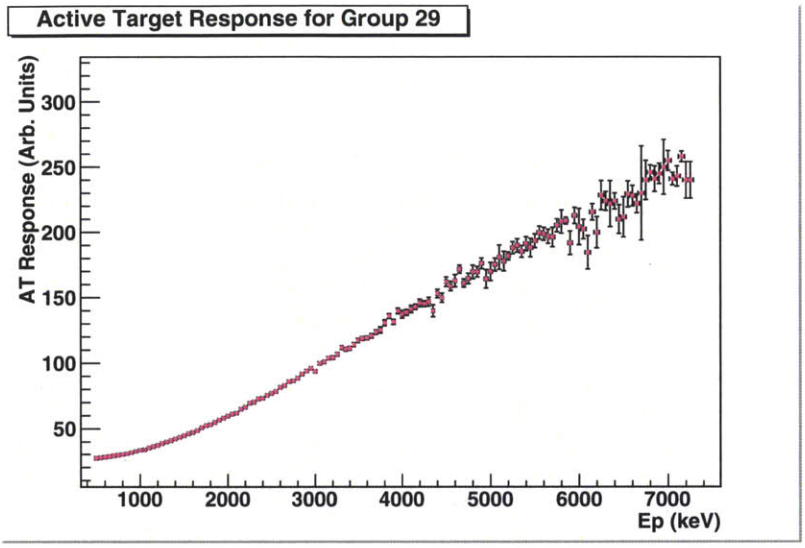

Figure 5-18: Mean active target response versus proton energy for Group 29. There is no discontinuity, the trend of the response is concave up across the entire range.

begins to decline, and it becomes more difficult to fit. Above 6 MeV the scatter in the means begins to increase, as seen in figure 5-18, showing the mean active target response versus proton energy. The trend of the response is concave up across its entire range. This contrasts with the higher gain runs, which are concave down above 2 MeV. There is a slight shift in the second derivative near 3.6 MeV, showing a flattening of the response above this. This is probably caused by the protons beginning to escape the active target; the range of a 3.6 MeV proton in the active target is approximately 10% of the total width, and so the response will begin to broaden downward and flatten compared to the response without escaping protons.

Group 30 is a higher gain group, and so we are able to clearly see much lower recoil energies. There are no asymmetries in this group. The mean values of these fits are plotted versus proton energy in figure 5-19. The response is approximately linear at very low energies, with a declining slope beginning in the 700 keV range. There is no sharp discontinuity in this group.

Group 31 shows significant asymmetry, to the point where there are almost two distinct peaks. This asymmetry continues for the entire range. At some points, the asymmetries become approximately equal and can be fitted with a gaussian, but for the most part the peaks would be best fitted separately. The mean values

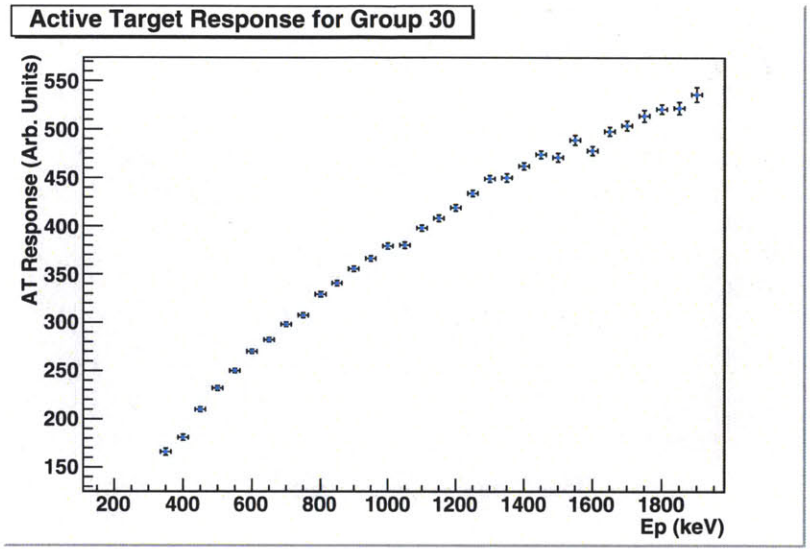

Figure 5-19: Mean active target response versus proton energy for Group 30. There is no discontinuity visible, but the slope begins to decline above 700 keV.

of these fits are plotted versus proton energy in figure 5-20. This figure shows repeated discontinuities due to fitting to the two peaks. There is a sharp change in the slope at approximately 1 MeV, though the concavity is unclear on either side of this change.

As with group 31, group 32 shows significant asymmetry at low energies. At 1350 keV the asymmetry ends and the peaks can be fitted with a single gaussian. The mean values of these fits are plotted versus proton energy in figure 5-21. The transition to symmetric peaks again shows a discontinuity, and the trend is significantly flatter above the discontinuity.

5.1.3 Gain Matching

The proton responses at each gain were matched to each other using linear transformations in order to convert the arbitrary units into the electron equivalent responses measured in section 4.1.1. The electron responses were measured at the highest gain, group 24 (average voltage = -2312 V), and so in order to fit the responses we compare this run to each of the lower gain runs in order of decreasing gain. With the different gains and the changing concavity, the range across which we use each gain setting and how we match the gains is important.

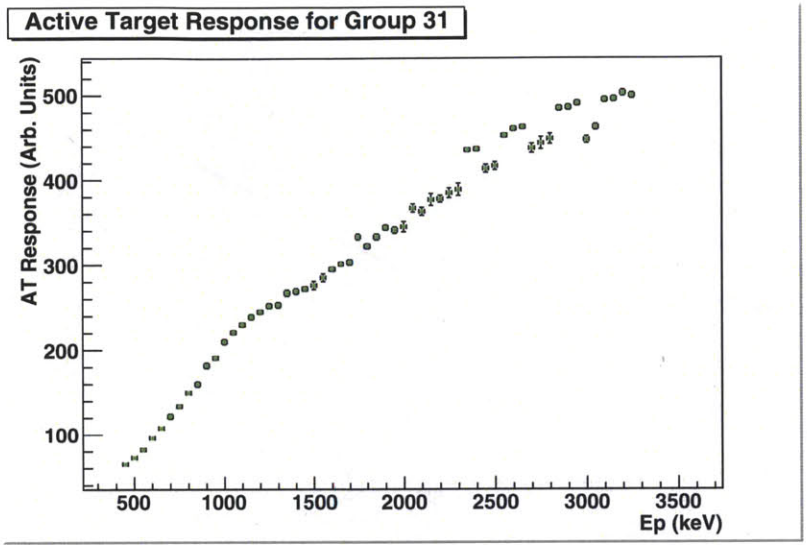

Figure 5-20: Mean active target response versus proton energy for Group 31. There is a sharp change in the slope at approximately 1200 keV.

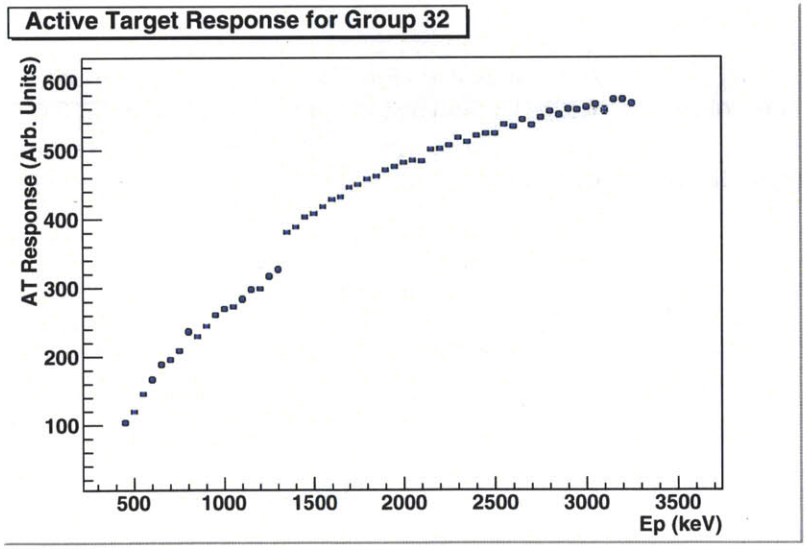

Figure 5-21: Mean active target response versus proton energy for Group 32. There is a sharp discontinuity at 1400 keV.

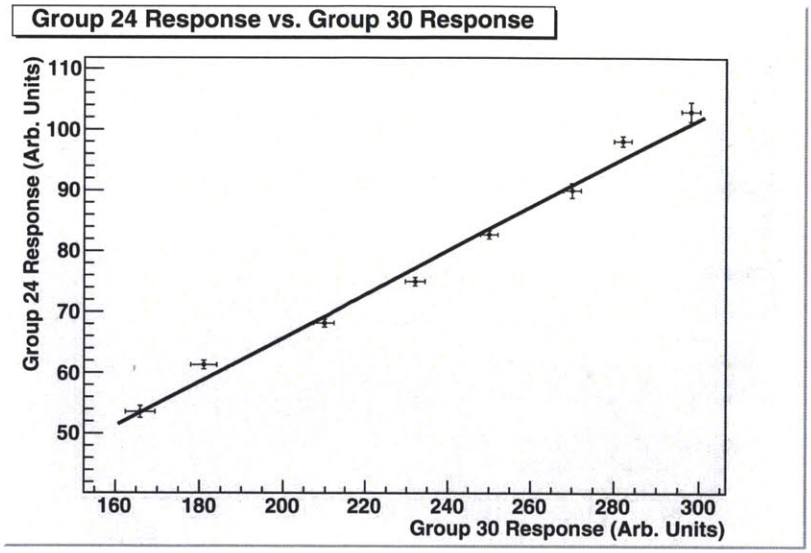

Figure 5-22: Mean active target responses for group 24 (average voltage = -2312 V) versus group 30 (average voltage = -2225 V), the two highest gain runs. A linear fit to match the gains is shown.

Figure 5-22 shows the mean active target responses for group 24 versus group 30 (average voltage = -2225 V) at each energy. There is a linear relationship between them, allowing us to make a linear fit to convert between the two gains. The resulting linear transformation is

$$Y_{24} = (0.359 \pm 0.0075) \times Y_{30} + (-6 \pm 1.7) \tag{5.1}$$

Plotting the gain matched results for groups 24 and 30 is shown in figure 5-23. In the range where both groups have responses, there is no significant difference between the two.

The next highest gain group is group 32 (average voltage = -2128 V). The response of this group is plotted against group 24 (average voltage = -2312 V) for each energy in figure 5-24. We can again fit the relationship between them linearly, resulting in

$$Y_{24} = (0.35 \pm 0.010) \times Y_{32} + (32 \pm 1.5) \tag{5.2}$$

Plotting the gain matched results for groups 24 (average voltage = -2312 V), 30 (average voltage = -2225 V), and 32 (dark blue points, average voltage = -

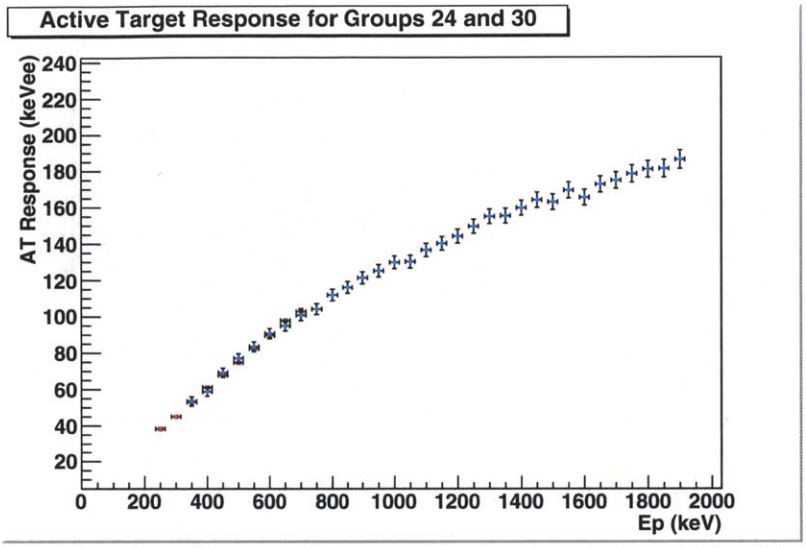

Figure 5-23: Gain matched responses for groups 24 (red points, average Voltage = -2312 V) and 30 (light blue points, average Voltage = -2225 V).

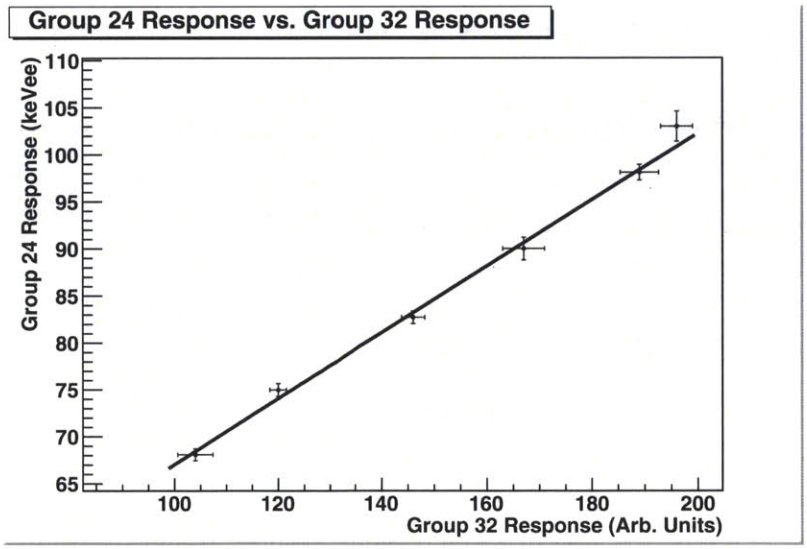

Figure 5-24: Mean active target responses for group 24 (average voltage = -2312 V) versus group 32 (average voltage = -2128 V). A linear fit to match the gains is shown.

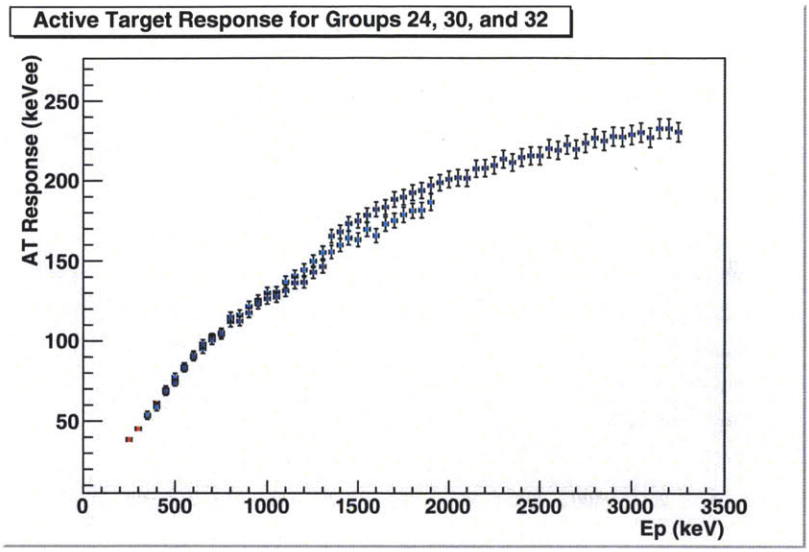

Figure 5-25: Gain matched responses for groups 24 (red points, average voltage = -2312 V), 30 (light blue points, average voltage = -2225 V), and 32 (dark blue points, average voltage = -2128 V). We begin to see the shift between the groups at higher energies, with group 32 lying consistently above group 30.

2128 V) is shown in figure 5-25. Below approximately 1 MeV, the three groups agree, but above 1 MeV groups 30 and 32 deviate from each other as they flatten. The discontinuity shifts the response of group 32 from below to above group 30. Ultimately the flat region for group 32 lies consistently above group 30.

Continuing to move towards lower gain runs, the response of group 31(average voltage = -2038 V) is plotted against group 24 (average voltage = -2312 V) in figure 5-26. The linear transformation between the two is

$$Y_{24} = (0.65 \pm 0.019) \times Y_{31} + (27 \pm 1.6) \tag{5.3}$$

Plotting the gain matched results for groups 24 and 30-32 shows an interesting result, as seen in figure 5-27. Below 750 keV, all the groups agree, but group 31 continues to follow the upwards trend while groups 30 and 32 begin to flatten. Group 31 then begins to flatten at 1 MeV, remaining consistently above groups 30 and 32.

The highest gain of the set of lower gain runs is group 28 (average voltage = -1850 V). It is plotted against group 24 (average voltage = -2312 V) in figure 5-28.

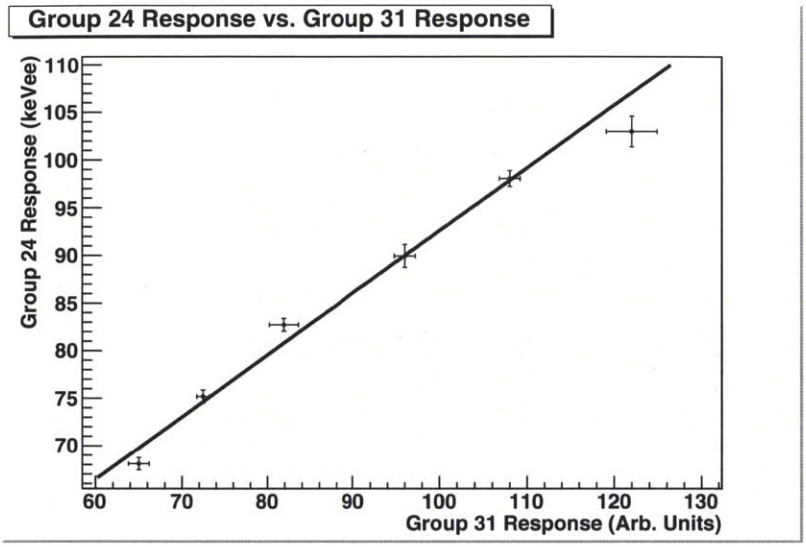

Figure 5-26: Mean active target responses for group 24 (average voltage = -2312 V) versus group 31 (average voltage = -2038 V). A linear fit to match the gains is shown.

The linear transformation between the two is

$$Y_{24} = (2.18 \pm 0.064) \times Y_{28} + (-4 \pm 2.5) \tag{5.4}$$

Plotting the gain matched results for groups 24, 28, and 30-32 is shown in figure 5-29. Group 28 continues the trend of continuing to rise past the flattening of the previous group, before the discontinuity and flattening of the response spectrum, in this case reaching 1700 keV before the discontinuity and the change in the second derivative.

Continuing down in gain, group 26 (average voltage = -1750 V) is plotted against group 31(average voltage = -2128 V) in figure 5-30. To increase the accuracy of the fit we moved to a group with additional points before the flattening. The shift in the slope of group 31 can be quite clearly seen here, and the data are fitted at the lower energies before this shift happens. The linear transformation is

$$Y_{31} = (4.0 \pm 0.24) \times Y_{26} + (-48 \pm 8.3) \tag{5.5}$$

Plotting the gain matched results for groups 24, 26, 28, and 30-32 is shown in

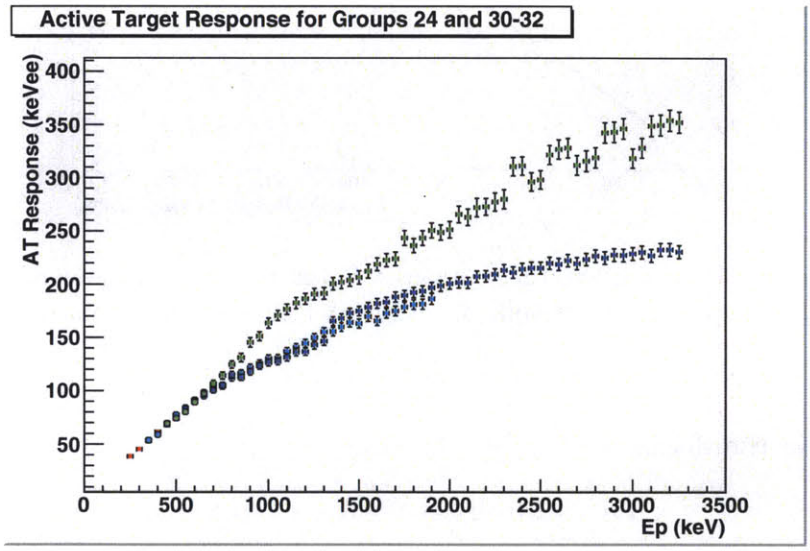

Figure 5-27: Gain matched responses for groups 24 (red points, average voltage = -2312 V), 30 (light blue points, average voltage = -2225 V), 31 (dark green points, average voltage = -2038 V), and 32 (dark blue points, average voltage = -2128 V). Group 31 continues to rise above groups 30 and 32, until group 31 also flattens at 1 MeV.

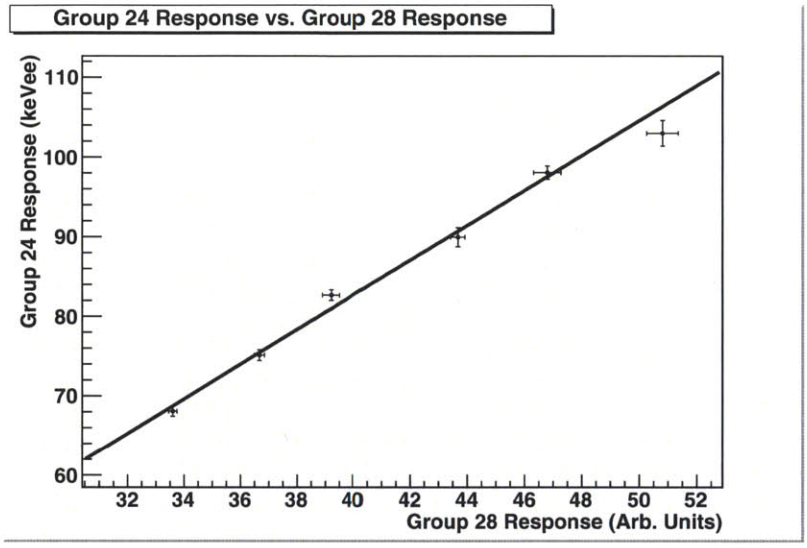

Figure 5-28: Mean active target responses for group 24 (average voltage = -2312 V) versus group 28 (average voltage = -1850 V). A linear fit to match the gains is shown.

figure 5-31. The flattening of group 26 occurs at approximately the same energy as group 28. However, the flattening jumps up to a much higher pulse height while still flattening.

The lowest gain run is group 29 (average voltage = -1615 V), and it is plotted against group 28 (average voltage = -1850 V) in figure 5-32. Again, we used a lower gain group for the fitting to increase the range where we can fit. The discontinuity and the flattening of group 28 can be seen quite clearly, and the fit is applied to the lower energy region before this discontinuity. The linear fit is

$$Y_{28} = (13.1 \pm 0.22) \times Y_{29} + (-273 \pm 7.1) \tag{5.6}$$

Plotting the gain matched results for groups 24, 26, and 28-32 is shown in figure 5-33. Group 29, being significantly lower gain than any of the others, shows no discontinuity or flattening until it approaches 3.6 MeV, where escaping protons will begin to broaden and flatten the distribution.

This flattening, which corresponds with the increasing gain, is most likely due to saturation in the electronics or in the photomultiplier tube. As the amount of light produced increases, the output of the phototube increases, but eventually it

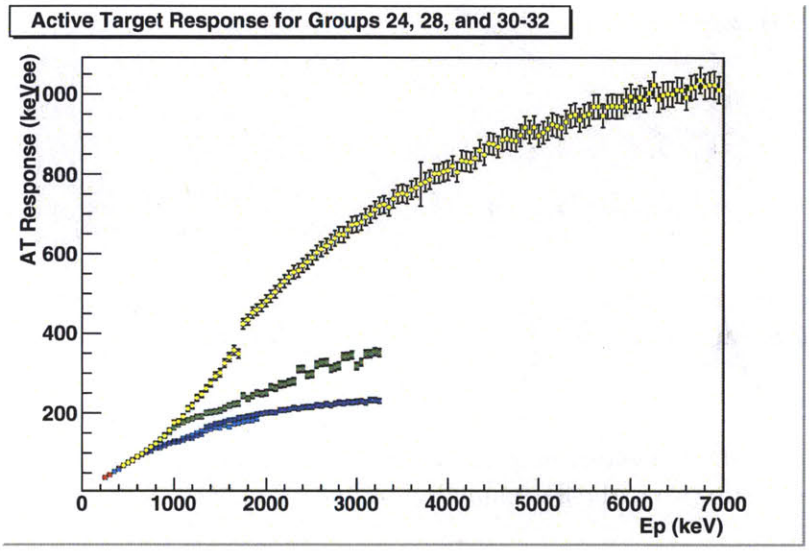

Figure 5-29: Gain matched responses for groups 24 (red points, average voltage = -2312 V), 28 (yellow points, average voltage = -1850 V), 30 (light blue points, average voltage = -2225 V), 31 (dark green points, average voltage = -2038 V), and 32 (dark blue points, average voltage = -2128 V). The pattern continues, with the lower gain group 28 rising above groups 30-32 until reaching its discontinuity point at 1700 keV.

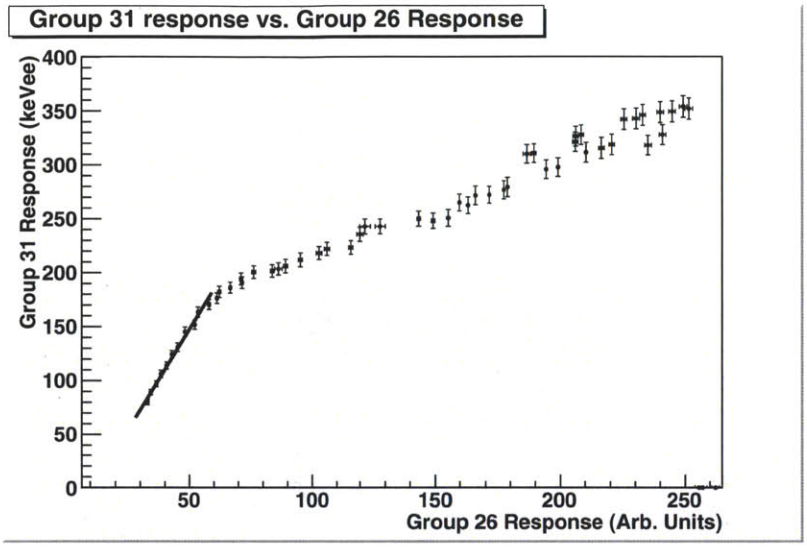

Figure 5-30: Mean active target responses for group 31(average voltage = -2128 V) versus group 26 (average voltage = -1750 V). A linear fit to match the gains is shown.

begins to saturate in the electronics. The output pulse is greater in magnitude than the maximum that the electronics which process the signal can accept, or even of the output signal the phototube is capable of producing. In this case, the increasing magnitude of the phototube output would result in a broader electronics output pulse, but without a greater magnitude, which would result in an increasing response in the electronics, but not as large as it should be for the amount of scintillation light generated in the active target.

The response normalized to the proton energy for each group is shown in figure 5-34. Once each group reaches its saturation point, the normalized response begins to slope downward. However, group 24 is already sloping downwards in its range, indicating that this run may already be in the saturation region. If this is the case, then the calibration of these data is invalid.

5.2 Scintillator Response Measurement at UKY

In the dedicated light response configuration, we measured *np* elastic scattering from the active target, using a very thin LiF target to produce a nearly monochro-

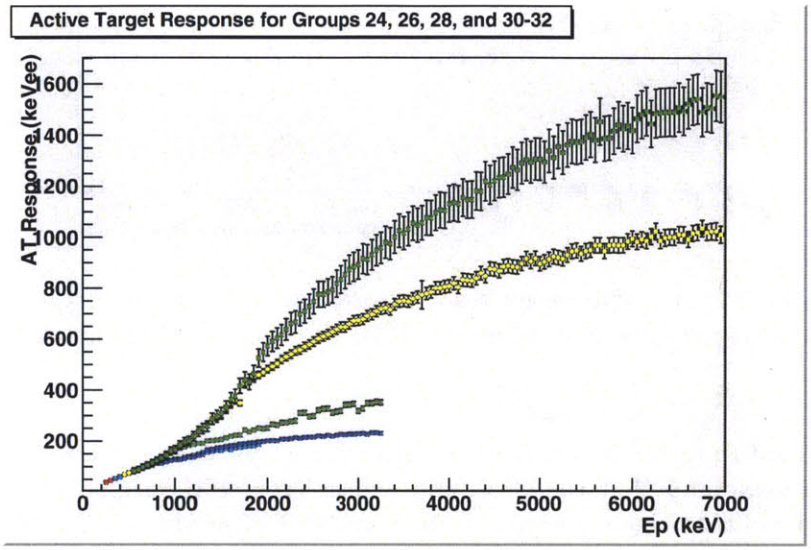

Figure 5-31: Gain matched responses for groups 24 (red points, average voltage = -2312 V), group 26 (light green points, average voltage = -1750 V), 28 (yellow points, average voltage = -1850 V), 30 (light blue points, average voltage = -2225 V), 31 (dark green points, average voltage = -2038 V), and 32 (dark blue points, average voltage = -2128 V). Group 26 falls above all the flattened regions of the higher gain groups.

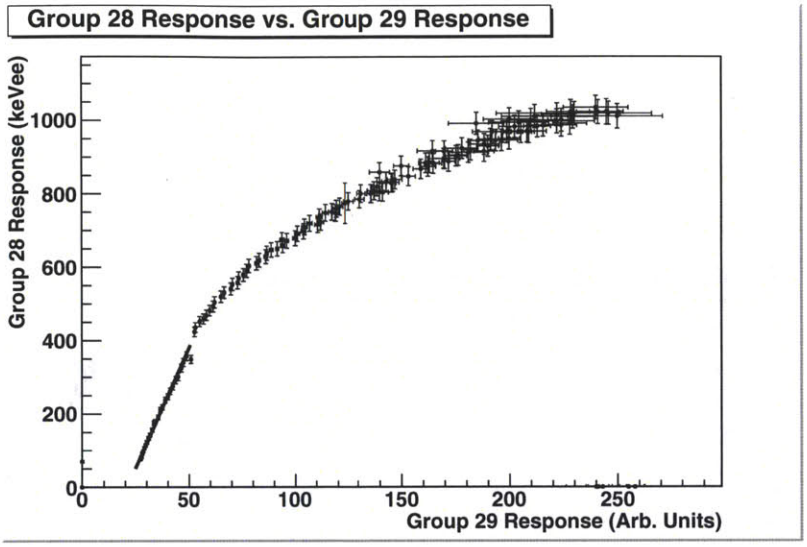

Figure 5-32: Mean active target responses for group 28 (average voltage = -1850 V) versus group 29 (average voltage = -1615 V). A linear fit to match the gains is shown.

matic neutron beam. Using this, and the spread of scattered energies which were accepted by our neutron detector, we were able to cover recoil energies from 1 MeV down to 100 keV.

5.2.1 Neutron Energies

With the γ-flash from protons incident on the LiF target, we were able to calibrate the neutron time of flight from the LiF target to the active target, and from the active target to the neutron detector. These plots are shown in figures 5-35a and 5-35b. With the 30 cm flight path from the LiF target to the active target, a 2.5 ns uncertainty in the time of flight becomes an uncertainty in beam energy of ± 90 keV for a 500 keV neutron, and we are unable to see any correlation between the active target time of flight and the neutron detector time of flight. However, we can cut on the time of flight peaks in both to exclude events which are not initiated by neutrons in both the active target and neutron detector.

With at least a 20% uncertainty in neutron energy from time of flight, it was more useful and accurate to determine the neutron energy based on the proton beam energy. The LiF target used was extremely thin, such that 2.25 MeV protons

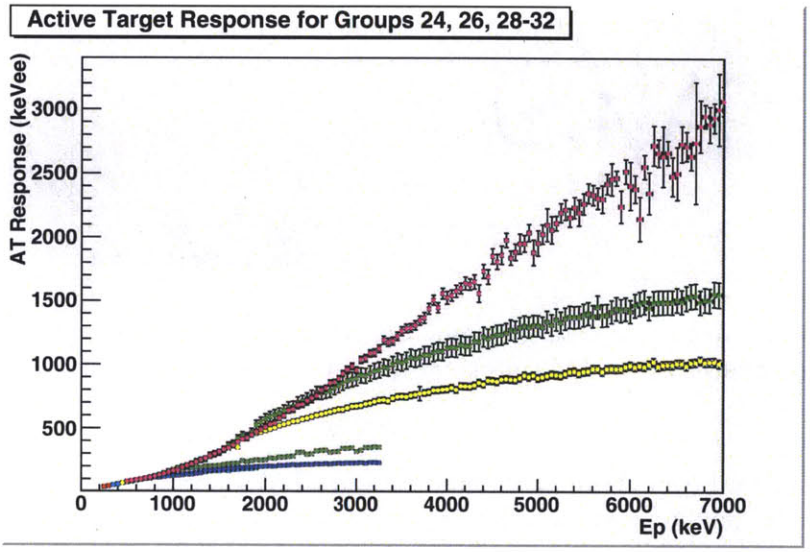

Figure 5-33: Gain matched responses for groups 24 (red points, average voltage = -2312 V), group 26 (light green points, average voltage = -1750 V), 28 (yellow points, average voltage = -1850 V), 29 (purple points, average voltage = -1615 V), 30 (light blue points, average voltage = -2225 V), 31 (dark green points, average voltage = -2038 V), and 32 (dark blue points, average voltage = -2128 V). The energy at which the discontinuity and flattening begin is correlated with the gains of the different groups, indicating that this shift in the behavior of the mean light response is presumably due to electronic saturation.

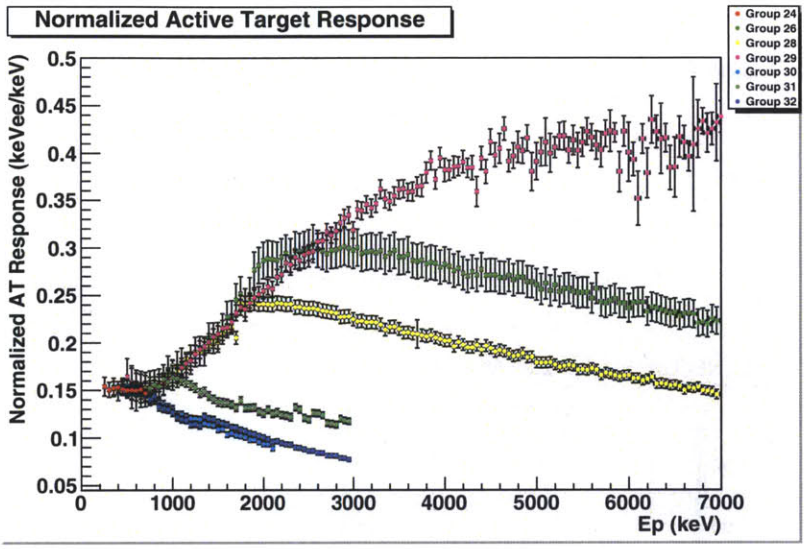

Figure 5-34: Gain matched responses normalized to proton energy for groups 24 (red points, average voltage = -2312 V), group 26 (light green points, average voltage = -1750 V), 28 (yellow points, average voltage = -1850 V), 29 (purple points, average voltage = -1615 V), 30 (light blue points, average voltage = -2225 V), 31 (dark green points, average voltage = -2038 V), and 32 (dark blue points, average voltage = -2128 V).

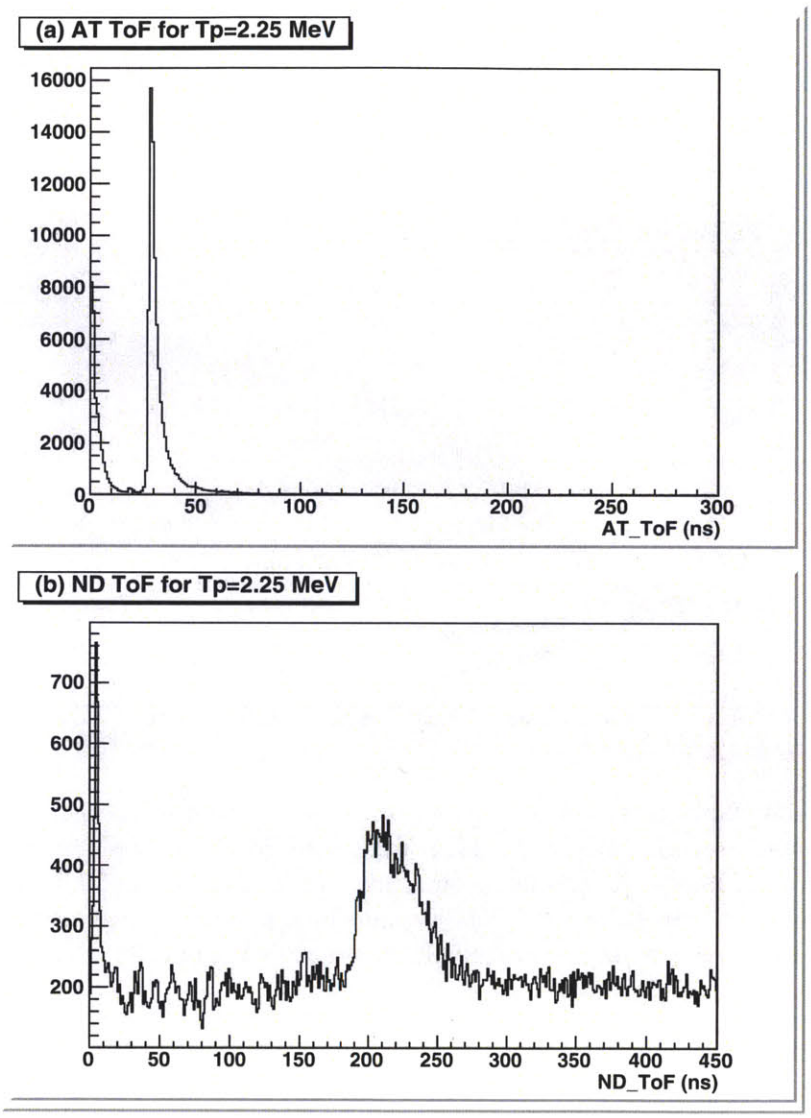

Figure 5-35: (a) Time of flight from the LiF target to the active target at $T_p = 2.25$ MeV. (b) Time of flight from the active target to the neutron detector at $T_p = 2.25$ MeV.

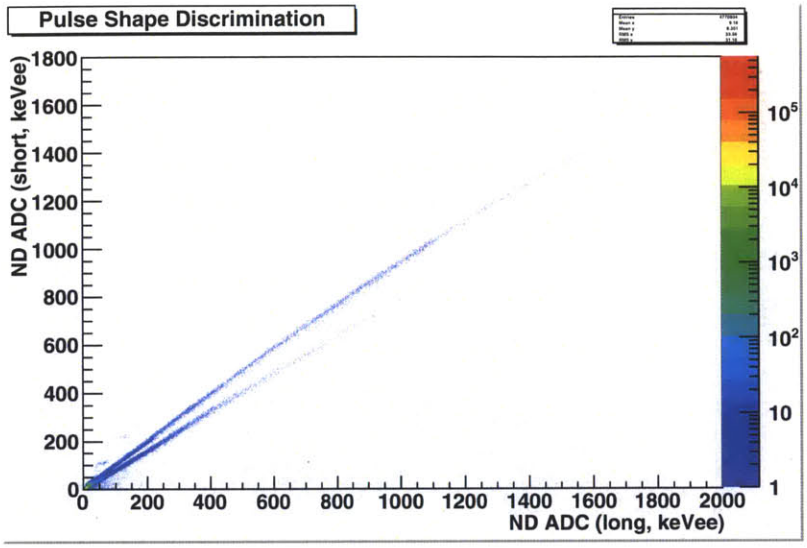

Figure 5-36: Pulse shape discrimination plot for the liquid scintillator, showing the ND ADC with a short gate versus the ND ADC with a long gate. The upper band consists of γ-rays, and the lower band is neutrons.

should only lose approximately 5 keV in passing through the target and therefore have a 5 keV spread for 500 keV neutrons.

5.2.2 Identifying Scattered Neutrons

With the limited information from the active target time of flight, the bulk of the analysis was aimed at identifying scattered neutrons. In addition to restricting possible scattered time of flights, we can use long and short ADC gates to identify neutrons by pulse shape discrimination as discussed previously. Figure 5-36 shows the short gate ADC plotted against the long gate ADC; the upper band is gamma rays, the lower band is neutrons. By cutting on this neutron band, we can significantly reduce the background.

Additionally, we can use a dynamical biasing cut to eliminate noise. For this experiment, the dynamical biasing focused on eliminating low pulse height noise instead of the larger pulse height noise seen at LANSCE. The plot of neutron detector response versus scattered neutron energy is shown in figure 5-37. By cutting on this region, we exclude low energy noise.

The time of flight from the LiF target to the active target and from the active

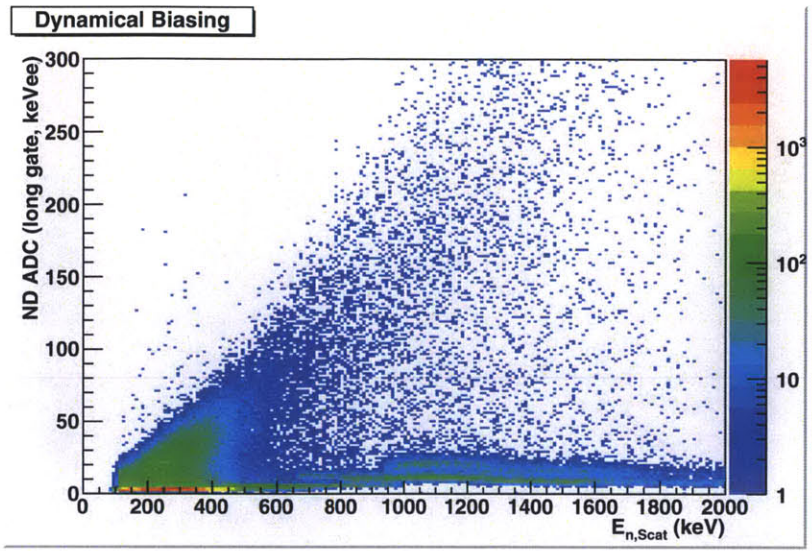

Figure 5-37: Neutron Detector ADC versus scattered neutron energy, with pulse shape discrimination and time of flight cuts. By cutting on the correlated band, we can exclude the low energy noise.

target to the neutron detector with the pulse shape discrimination and dynamical biasing cuts is shown in figures 5-38a and 5-38b, respectively. While the shape of the active target time of flight spectrum is mostly unchanged when compared to figure 5-35a, the neutron detector time of flight spectrum is significantly altered compared to figure 5-35b, with the noise effectively eliminated outside the time of flight peak, with almost no loss to the signal. The smaller peak at 150 ns corresponds to a neutron energy of 450 to 500 keV and is due to nC elastic scattering. The peaks in the 250-325 ns range correspond to neutron energies of 110 and 150 keV; the source of these peaks is currently unknown. In summary, using the pulse shape discrimination, the dynamical biasing, and the timing cuts, we are able to isolate the scattered neutrons and eliminate almost all of the background.

5.2.3 Recoil Proton Pulse Heights

With the scattered neutron identified and the beam neutron energy constrained by the proton beam energy and LiF target thickness, we can determine the recoil proton energy by subtracting the calculated scattered neutron energy from the average beam energy. The active target response is measured in keVee as cali-

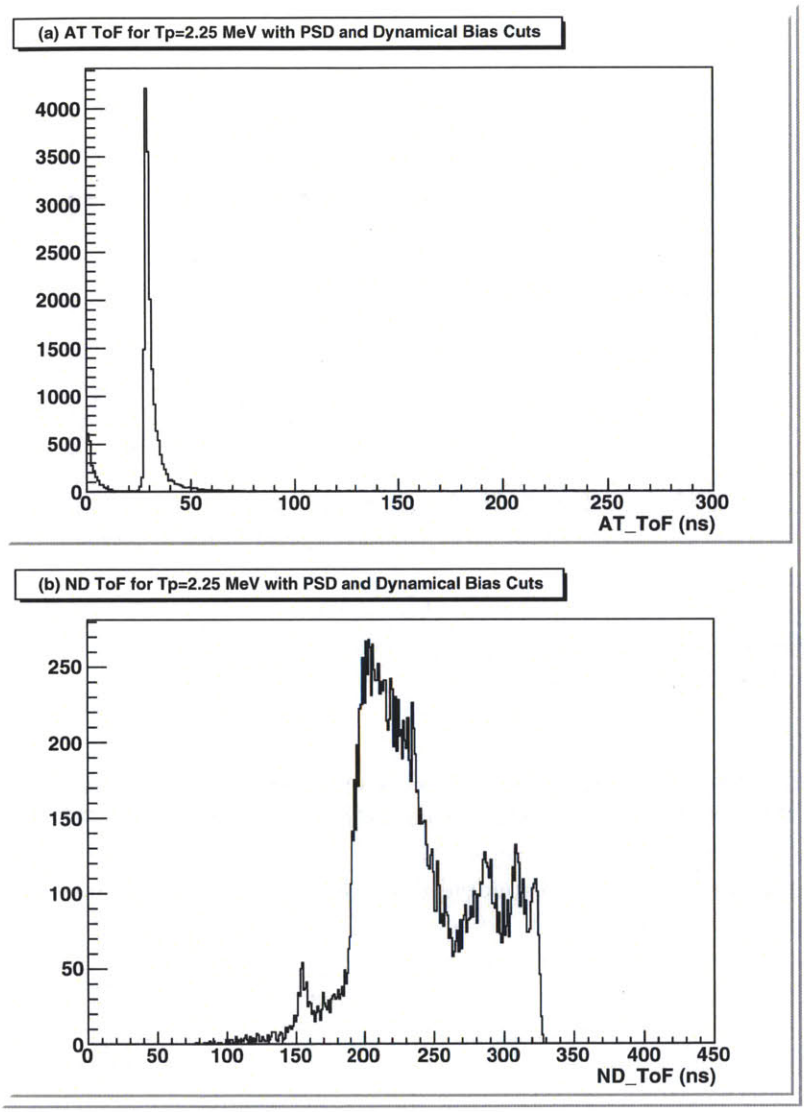

Figure 5-38: (a) Time of flight from the LiF target to the active target at $T_p = 2.25$ MeV with PSD and dynamical biasing cuts. (b) Time of flight from the active target to the neutron detector at $T_p = 2.25$ MeV. The neutron peak is visible from 200 to 250 ns; these times correspond to 200 to 300 keV, consistent with elastic scattering at a 45° angle. There is a nearly complete elimination of backgrounds outside of the 150 to 325 ns range. The peak near 150 ns corresponds to a neutron energy of approximately 450 to 500 keV and is due to nC elastic scattering. The peaks in the 250-325 ns range correspond to neutron energies of 110 and 150 keV; the source of these peaks is currently unknown.

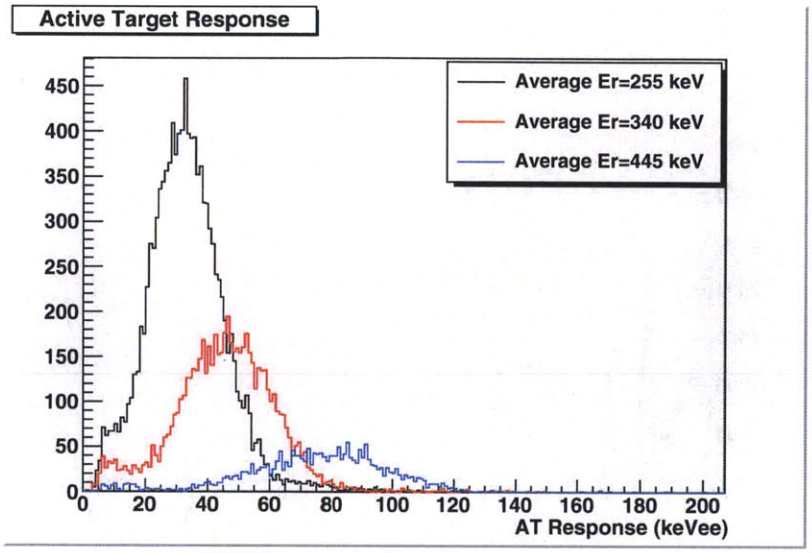

Figure 5-39: Light response in active target for $T_p = 2.25$, 2.4, and 2.6 MeV, with the average proton recoil energy given in the legend. The means of the distributions shift upwards with energy, as expected.

brated in section 3.1. Figure 5-39 shows the active target response for $T_p = 2.25$, 2.4, and 2.6 MeV, which gives an average recoil proton energy of 255, 340, and 445 keV, respectively. As expected, the active target response increases with increasing recoil energy. The broadening of the peaks at higher energies is due to the acceptance of the neutron detector; at 45°, the neutron detector acceptance allowed scattered neutrons from 42° to 47°, which gives recoil energies from 45% to 55% of the neutron beam energy. So as the energy increases, the spread of recoil energies increases. By subtracting the scattered neutron energy from the beam neutron energy determined by the proton energy, we can account for this spread and cover the recoil energies between the average points.

With this we can plot the active target response in keVee versus recoil proton energy, shown in figure 5-40. This figure shows that with pulse shape discrimination, and the precise neutron beam energy determination from the thin LiF target, we obtain a very narrow band of proton light response, and we will be able to use this to determine the average light response at proton energies as low as 100 keV.

As with the data from LANSCE, to determine the average light response, we take projections of figure 5-40 and fit each slice with a gaussian distribution. Plots

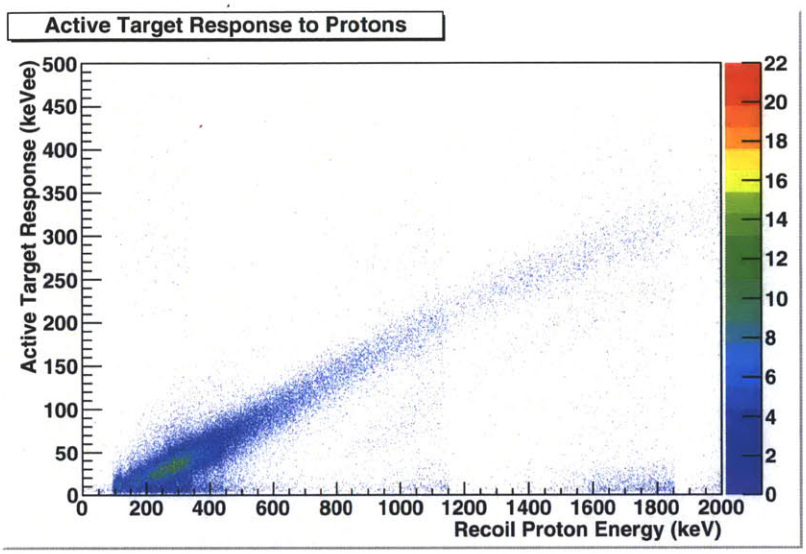

Figure 5-40: Light response in active target versus recoil proton energy, calculated by subtracting the scattered neutron energy from the average neutron beam energy.

of all the fits to slices are shown in appendix A. The spacing between the slice energies is determined by the maximum uncertainty in recoil energy. The slices are well fitted by the gaussian distributions below 1 MeV. Above this, the number of events begins to decline and fitting becomes much more difficult. The mean response is plotted against the proton energy in figure 5-41. At approximately 1.2 MeV, there appears to be a discontinuity in the second derivative, and slope shifts downward as it did previously in the LANSCE results. The electronics of the UKY setup were specifically designed to prevent any saturation in the electronics, so this is most likely due to saturation in the phototube or to the declining statistics above 1 MeV. Repeating the measurement with lower gain would confirm this hypothesis.

5.3 Results

The average light responses are shown in figure 5-42. The numerical results from each experiment appear to be approximately consistent with each other in the ranges where they overlap.

However, if we normalize this response to the proton energy, shown in figure 5-43, we see that the two experiments show very different results in the regions

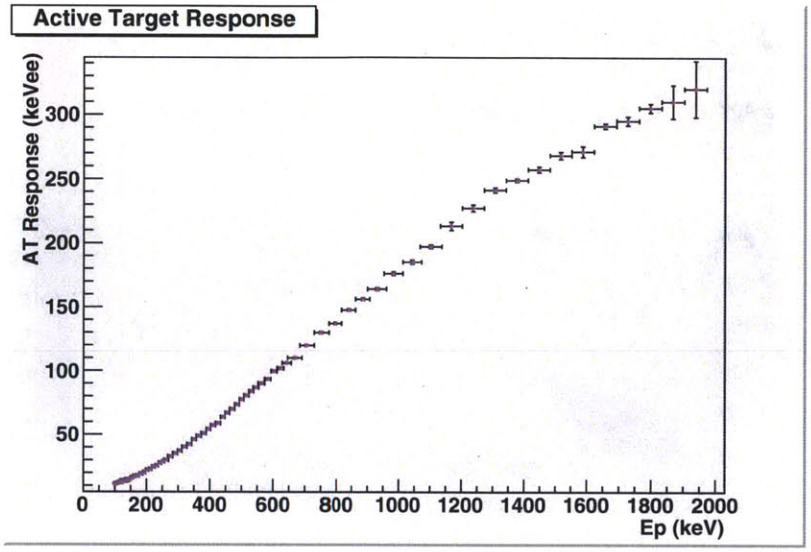

Figure 5-41: The mean active target response for each proton energy.

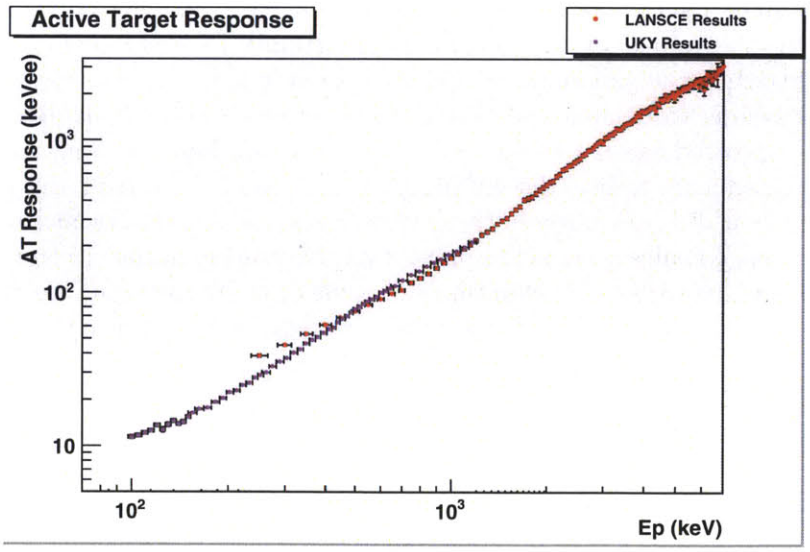

Figure 5-42: Average light response to protons of BC418 plastic scintillator from both the LANSCE and UKY experiments.

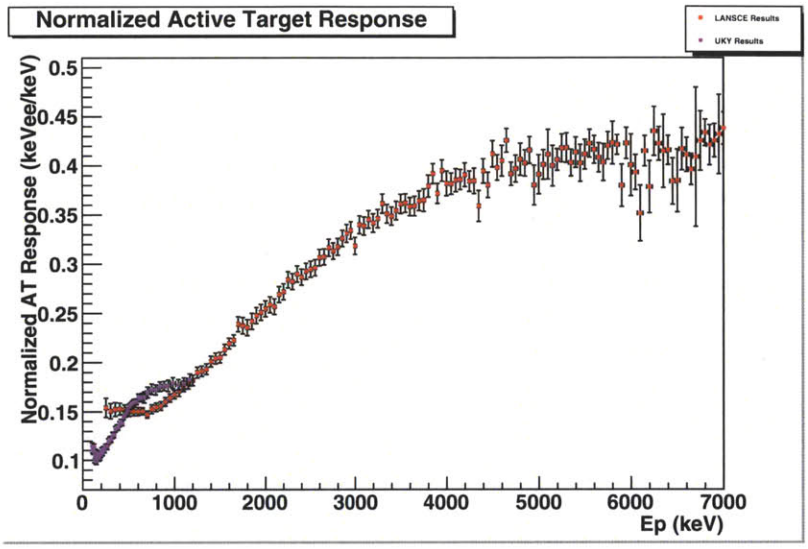

Figure 5-43: BC418 response to protons, normalized by proton energy. The red points show the data from LANSCE, the magenta points show the data from UKY.

where they overlap. For the UKY results, the response per keV is approximately constant above 800 keV, and begins falling off below. It is approximately linear below 600 keV until it reaches 200 keV, where the response begins to increase. For the LANSCE results, the normalized response at very low energies is constant at approximately 15% of the electron energy, and then rises above 1 MeV. It begins to flatten as it approaches 3 MeV, and then continues to flatten as protons begin to escape from the active target above 3.6 MeV. This plot may no longer be showing us anything interesting, or may indicate that saturation is occurring much earlier than expected in the UKY results, as low as 800 keV, and that there may be saturation in group 24 (Average Voltage = -2312 V), causing a downward shift in the entire response of the LANSCE results above 700 keV. However, if this is the case, then saturation is occurring at an extremely small pulse height, below channel 230 in the low gain ADC. There is no consistent channel level where the saturation begins, so it is possible that it reached this low. With these two issues corrected the rising portions of each curve could match to each other. With the demolition of the flight path at WNR, obtaining additional calibration data at LANSCE is impossible for the foreseeable future. Studies of the photomultiplier at UKY have indicated that saturation begins below 200 keVee at the voltage

settings used for this experiments, consistent with our proton results.

Birks [57] developed a formula which has been very successful in explaining the features of the response of organic scintillators. [53] The high ionization density along the particle track results in a quenching effect for protons and other heavily ionizing particles. This yields the formula

$$\frac{dL}{dx} = \frac{S\frac{dE}{dx}}{1 + kB\frac{dE}{dx}}, \tag{5.7}$$

where $\frac{dL}{dx}$ is the fluorescence light energy emitted per unit length, $\frac{dE}{dx}$ is the specific energy loss for the charged particle, S is the scintillation efficiency, and kB parameterizes the nonradiatively dissipated energy. [28] A semi-empirical extension of this formula includes a term which is second order in $\frac{dE}{dx}$ [58]

$$\frac{dL}{dx} = \frac{S\frac{dE}{dx}}{1 + kB\frac{dE}{dx} + c(\frac{dE}{dx})^2}. \tag{5.8}$$

For electrons, the small $\frac{dE}{dx}$ values cause this formula to reduce to the linear expression $L_e(E) = SE + L_0$; by calibrating the response in keVee we set $L_0 = 0$ and expect $S = 1 \pm 0.04$, including the uncertainty in the keVee calibration. This empirical equation was used by Craun [28] to fit to the data taken by Smith et al. [26] We used it to fit to our data from both UKY and LANSCE. The $\frac{dE}{dx}$ values were taken from Craun's values for NE-102, which is nearly identical in carbon and hydrogen composition to BC418. [59, 60] The parameters resulting from our fit were

$$S = 1.05 \pm 0.02 \text{ keVee}, \tag{5.9}$$
$$kB = (1.26 \pm 0.03) \times 10^{-2} \text{ g/cm}^2/\text{MeV}, \tag{5.10}$$
$$c = -(3.4 \pm 0.2) \times 10^{-6} \text{ g}^2/\text{cm}^4/\text{MeV}^2. \tag{5.11}$$

As predicted, our fit yields $S = 1$ within the combined error of the fit and the calibration. For comparison, the kB and c parameters obtained by Craun for NE-102 are [28]

$$kB = 1.29 \times 10^{-2} \text{ g/cm}^2/\text{MeV}, \tag{5.12}$$
$$c = 9.59 \times 10^{-6} \text{ g}^2/\text{cm}^4/\text{MeV}^2. \tag{5.13}$$

The kB parameters are consistent, indicating that BC418 and NE-102 show similar

quenching characteristics. This is expected, due to their nearly identical composition. The negative c parameter from our fit results from the increased response at low energies, seen when we compare our fit and data to the fits and data from Craun and Smith in figure 5-44. The responses have been normalized such that the response to electrons is the same across the different detector materials. The response of the fast plastic materials, BC418 and Pilot B, to protons are consistent with each other above 1 MeV, but the BC418 relative response increases compared to the PilotB and NE102 data below 1 MeV. This results in the negative c parameter for the fit to the BC418 data; since $\frac{dE}{dx}$ increases with decreasing energy for protons, a negative c parameter will increase the fitted response at low energies.

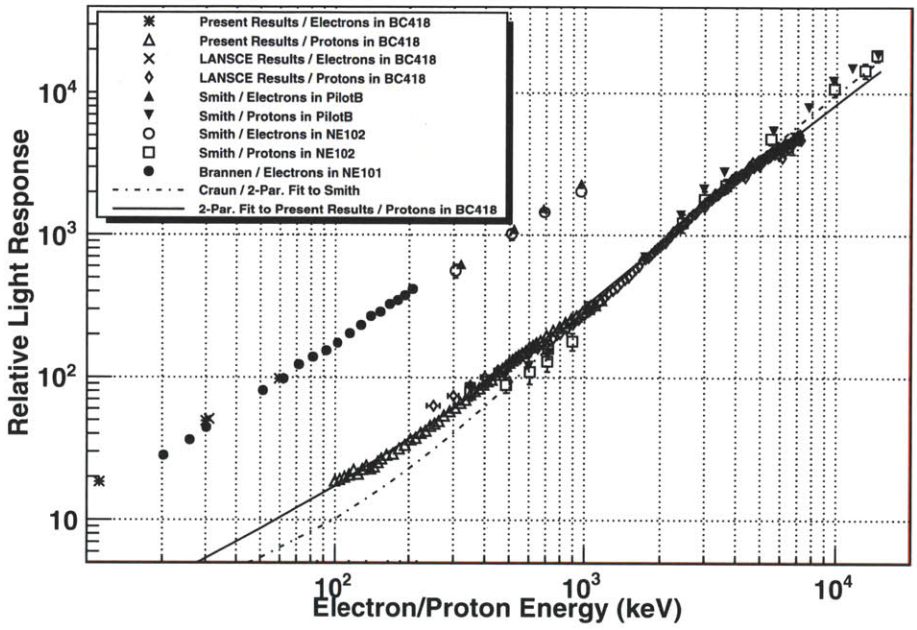

Figure 5-44: Response of protons and electrons in various scintillation materials as measured by our group, Smith et al. [26], and Brannnen et. al. [27] The responses have been normalized to each other such that the response to electrons is the same across the different materials. The two parameter fits to the LANSCE and UKY data and to the NE102 data [28] are also shown. Above 1 MeV, the results from LANSCE and the fit to our present results match the response of protons in PilotB and NE102 and the second order Birks' equation fit. Below 1 MeV, the relative response of BC418 increases compared to the responses of PilotB and NE102 and the fit.

Chapter 6

Analysis of Radiative Capture Data

With the limited data taken for the radiative capture measurement, our focus was on identifying capture events to prove the feasibility of the active target for detecting deuterons and to determine how much data taking time would be necessary to achieve the desired statistical uncertainty.

6.1 Measurements at LANSCE

6.1.1 BrilLanCe Timing Cuts

With the very fast timing signals of both the active target and the BrilLanCe detector, one of our best methods for identifying capture events is the time of flight between the active target and the BrilLanCe. The fixed time of flight for γ-rays allows us to put a very narrow constraint on this time of flight. However, finding the prompt γ-ray peak among the very large background peaks was difficult. The time of flight from the active target to the BrilLanCe detector is shown in figure 6-1 for the coincidence trigger. There is no sharp prompt peak visible.[1]

There was an additional process which allows us to identify the prompt peak. Figure 6-2 shows the γ-ray energy in the BrilLanCe detector versus the neutron beam energy measured by time of flight. There are three distinct bands at fixed γ-ray energy, centered on $E_\gamma \sim 4100$ keV, which begin at neutron energy of approximately 5 MeV. These bands are evidence of inelastic scattering from carbon-12,

[1] The sharp peak at 25 ns is due to the self-timing peak generated at the edge of the coincidence gate.

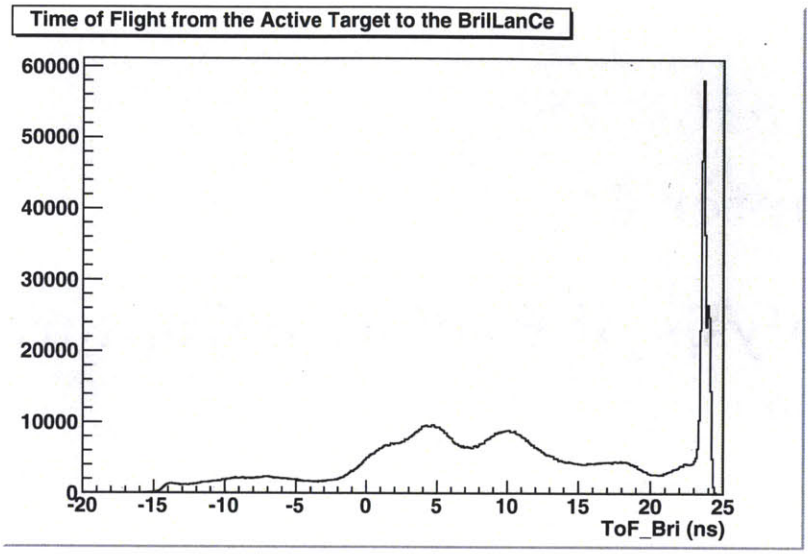

Figure 6-1: Time of flight from the active target to the BrilLanCe detector for the AT·Bri coincidence trigger. The location of the prompt peak is unclear. (The peak at 23-24 nanoseconds is due to self timing.

$^{12}C(n,n')^{12}C^*$. The first excited state of carbon-12 is 4.44 MeV above the ground state, so including the threshold of the active target, we would expect to begin seeing these events at $E_n \sim 5$ MeV. What is detected is the decay of this excited carbon nucleus; the 4.44 MeV γ-ray is detected by the BrilLanCe detector, while the recoiling carbon nucleus is detected by the active target. Three distinct bands are visible because of the high resolution of the BrilLanCe detector. The bands are a result of these 4.44 MeV γ-rays producing e^+e^- pairs and one or both of the 511 keV γ-rays produced by the positron's annihilation escaping from the BrilLanCe. This is evidenced by the 500 keV spacing of the bands.

Since these events are caused by a γ-ray travelling between the active target and the BrilLanCe, we can use these events to find the prompt γ-ray peak. A cut on the three bands is applied to figure 6-1, and the resulting time of flight spectrum is shown in figure 6-3 This produces a clear prompt γ-ray peak, and allows us to constrain the time of flight of γ-rays within 2.5 ns. Additionally, we were able to use the 4.44 MeV γ-ray in the calibration of the BrilLanCe detector (see section 4.2).

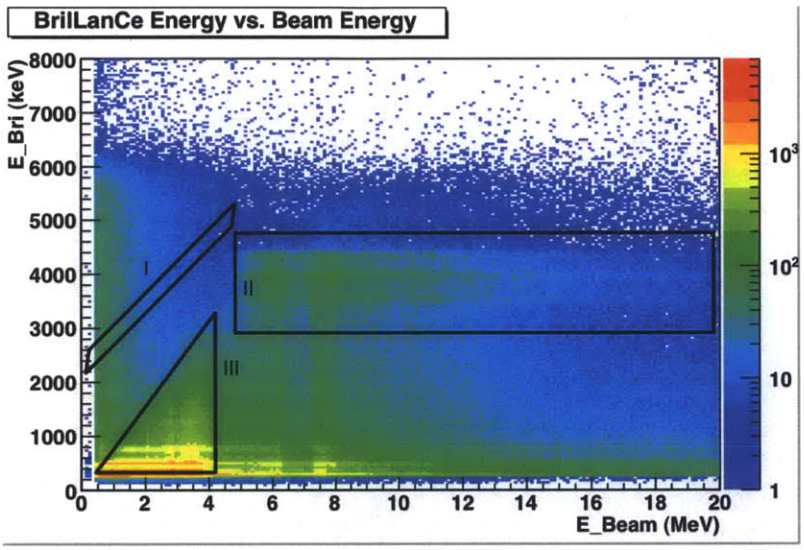

Figure 6-2: γ-ray energy as measured by the BrilLanCe versus the neutron beam energy measured by time of flight for the AT·Bri coincidence trigger. Region I shows the kinematic region where capture events would fall, there is no obvious excess. Region II shows three bands at fixed energy, centered on approximately 4000 keV γ-ray energy and beginning at $\sim$ 5 MeV neutron energy indicate that we are detecting inelastic scattering from carbon. Region III is consistent with elastic scattering from the active target; this region corresponds to the peak at 5 ns in figure 6-1.

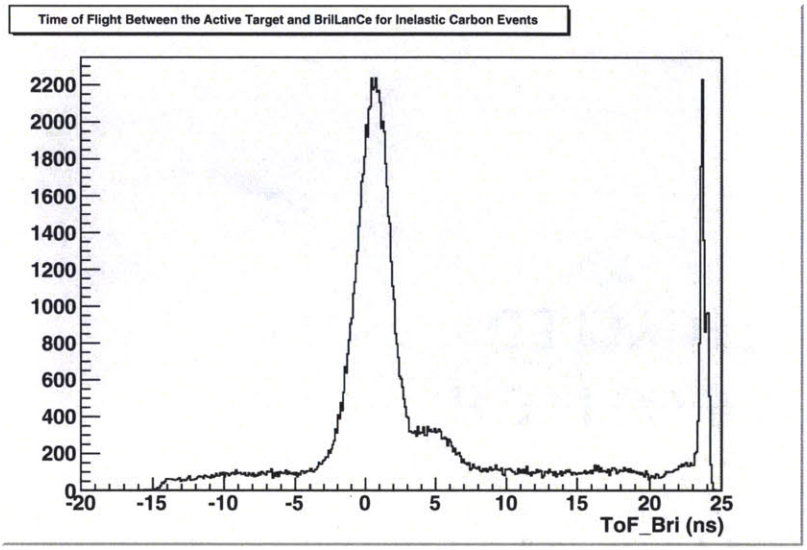

Figure 6-3: Time of flight from the active target to the BrilLanCe detector for the AT·Bri coincidence trigger with the cut on inelastic scattering from carbon. We can now see the prompt peak and use it to identify γ-ray events in the BrilLanCe detector.

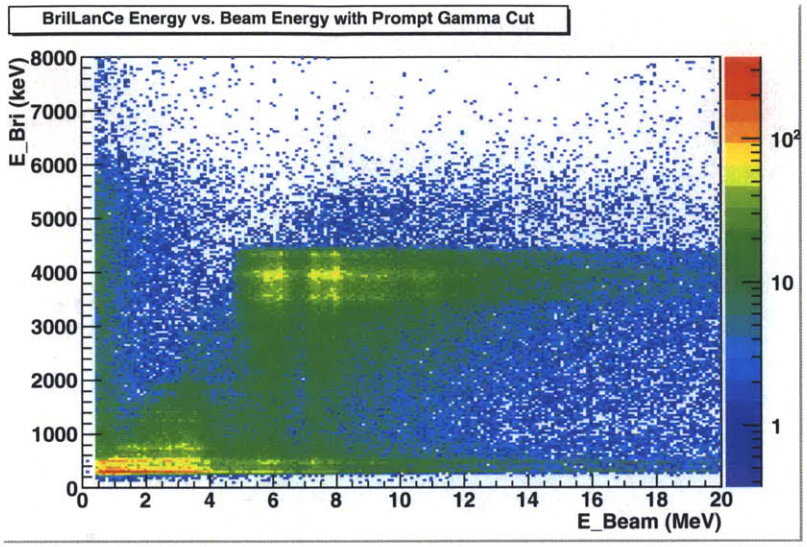

Figure 6-4: γ-ray energy measured by the BrilLanCe versus beam energy for the AT·Bri coincidence trigger, with the prompt γ condition.

6.1.2 BrilLanCe Energy versus Neutron Energy

Figure 6-4 shows the γ-ray energy plotted against the beam energy for the prompt γ peak. Even with this prompt γ condition, the most prominent features are the bands from inelastic scattering off of carbon and a triangular region at lower energies. We expect the capture events to fall into a band that begins at a γ energy of 2.2 MeV for a neutron at rest and rises with neutron energy, with approximately half of the neutron kinetic energy being added to the γ-ray energy. We see no obvious excess in this region, but seeing a radiative capture band in a run of the length that produced the data in the figure is extremely unlikely given the small cross section and thus the very low event rate.

We focus on the incident neutron energy range of 1 to 5 MeV, where we have the best neutron flux normalization. Based on kinematics, the signal (black) and background (red) cuts for this region are shown in figure 6-5. With these conditions, there are 678 events in the foreground cut and 577 events in the background cut. To reduce these backgrounds, we examine the active target response versus neutron energy.

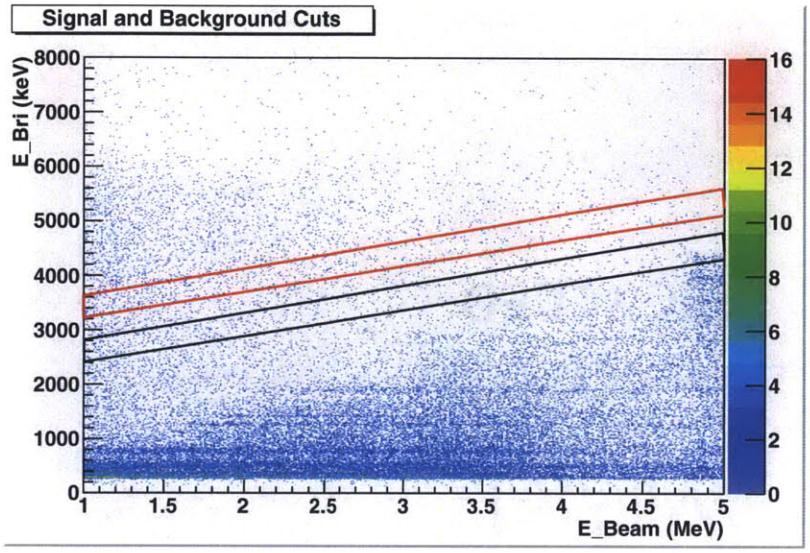

Figure 6-5: γ-ray energy versus neutron beam energy for the AT·Bri coincidence trigger, with the prompt γ condition. Signal (black) and background (red) cuts based on kinematics for capture at incident neutron energies from 1 to 5 MeV.

6.1.3 Active Target Energy Cuts

Existing measurements of plastic scintillator response to protons and deuterons have found a ratio of 0.75 between deuteron response and proton response at the same kinetic energy.[29, 30] Using this empirical relationship, we can convert the proton light response measured in figure 5-42 to deuteron responses, and plot the deuteron light response, shown in figure 6-6 For our range of 1 to 5 MeV, the recoiling deuterons will have energies ranging from 0.5 to 2.6 MeV, which fall in the range of 60 to 600 keVee. With the extremely limited statistics and low resolution of the active target, the best we could do was eliminate the very low pulse height events which were most likely caused by noise or by recoiling carbon nuclei. This condition is shown in figure 6-7. With this condition, we had 60 counts in the deuteron cut and and 36 counts in the background cut, giving 24 ± 10 total capture events in the incident neutron energy range from 1 to 5 MeV.

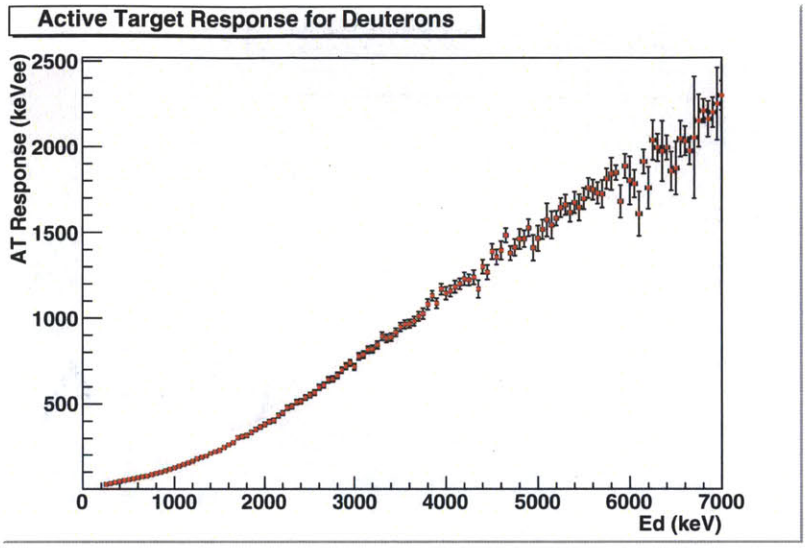

Figure 6-6: Estimated active target response to deuterons based on the proton light responses seen in figure 5-42 and the previously measured empirical relationship between proton response and deuteron response.[29, 30]

6.1.4 Neutron Flux

To convert this yield to a cross section, we need to determine the total neutron flux. As discussed in section 3.2.1.3, the neutron flux was measured by the fission chamber.

The fission chamber produced an analog signal and a logic timing signal, which we could use to determine if an event was a real fission event. Figure 6-8 shows the fission chamber ADC for the ^{238}U foil. This spectrum has two prominent features. The broad peak centered near channel 600 corresponds to the fission fragments produced from a uranium nucleus which has been struck by a neutron. The lower energy distribution results from α particles. The goal is to separate the fission products from the background so that the total neutron flux can be determined.

To determine the neutron energy, we look at figure 6-9, showing the fission chamber TDC for the ^{238}U foil. We can use this to determine the time of flight and thus the energy of the neutron.

In order to effect the cleanest separation of the fission fragments from the α particles, we plot the ADC signal versus the TDC signal, shown in figure 6-10. For the slowest neutrons, this is done with a simple condition requiring that the ADC

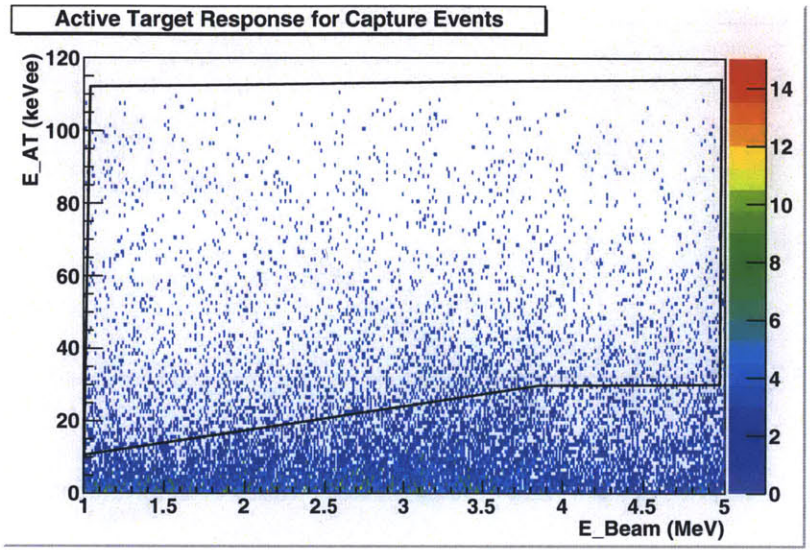

Figure 6-7: Active target response versus neutron beam energy showing the condition which excludes the very low energy pulses which are caused by recoiling carbon nuclei.

be greater than channel 372. For the faster neutrons, a curve was fitted along the edge of this distribution and then used to exclude the α particles. The raw fission fragment counts are shown in figure 6-11

To turn these raw counts into an integrated beam flux, we must use the ^{238}U fission cross section. To relate the number of fission counts $N_f(E)$ to the incident neutron flux N_iE, we use the equation

$$N_f(E) = N_i(E) \times \rho_f \times \epsilon_f \times \sigma(E), \tag{6.1}$$

where ρ_f is the areal density of the ^{238}U, ϵ_f is the efficiency of detecting fission fragments, and $\sigma(E)$ is the fission cross section at neutron energy E. The areal density is determined directly by measuring the yield of the α particle decays and comparing this to the known rate of ^{238}U decays. This yielded a value for the areal denstiy of $\rho_f = 0.9080 \times 10^{-6}$ atoms/barn.[54]

The efficiency for detecting fission fragments is very high. The fragments are not detected only in cases where the fission fragments are emitted almost parallel to the foil surface, such that they do not reach the next foil. In this case, the fragment would strike the wall of the fission chamber and never produce an event. Based

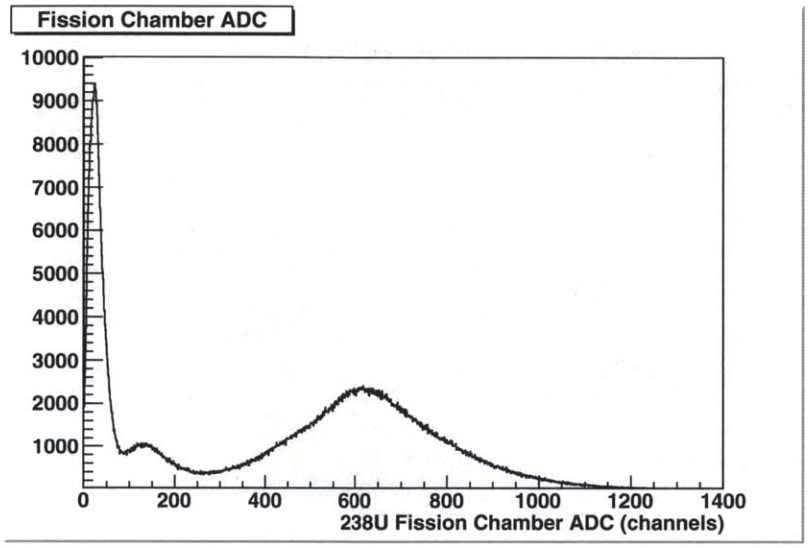

Figure 6-8: Analog signal from the fission chamber. The large peak centered near channel 600 is the fission fragments, and the lower pulse height distribution is the α particles produced by ^{238}U α decay.

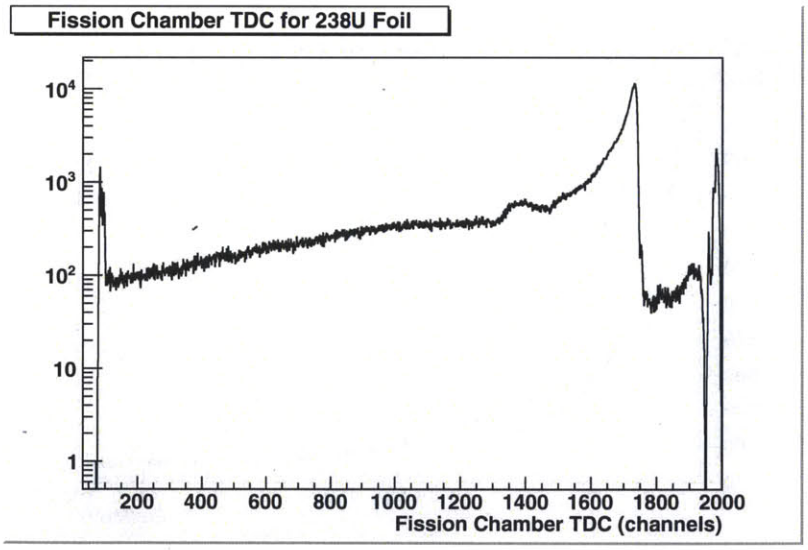

Figure 6-9: Timing signal from the fission chamber.

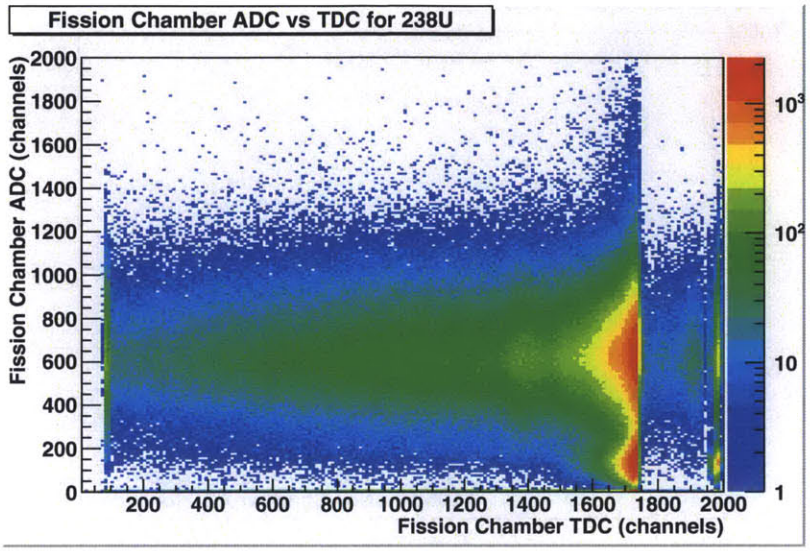

Figure 6-10: ADC vs. TDC for the ^{238}U foil in the fission chamber.

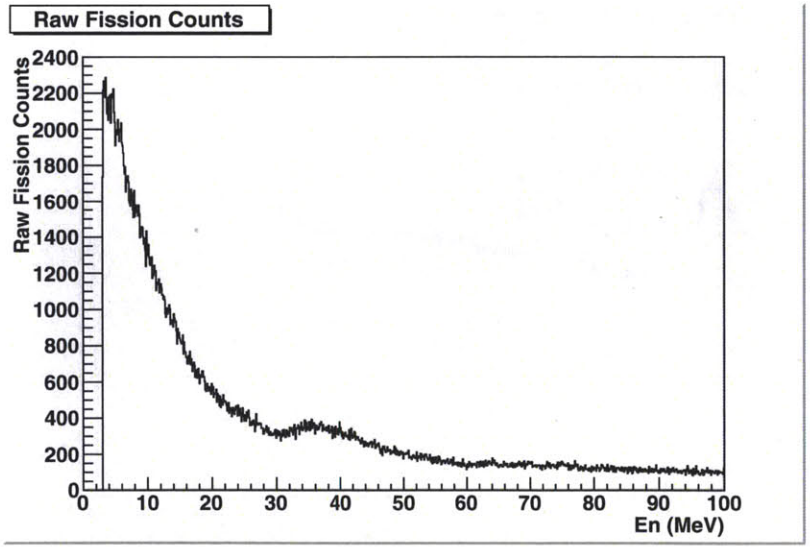

Figure 6-11: Raw fission counts for the ^{238}U foil.

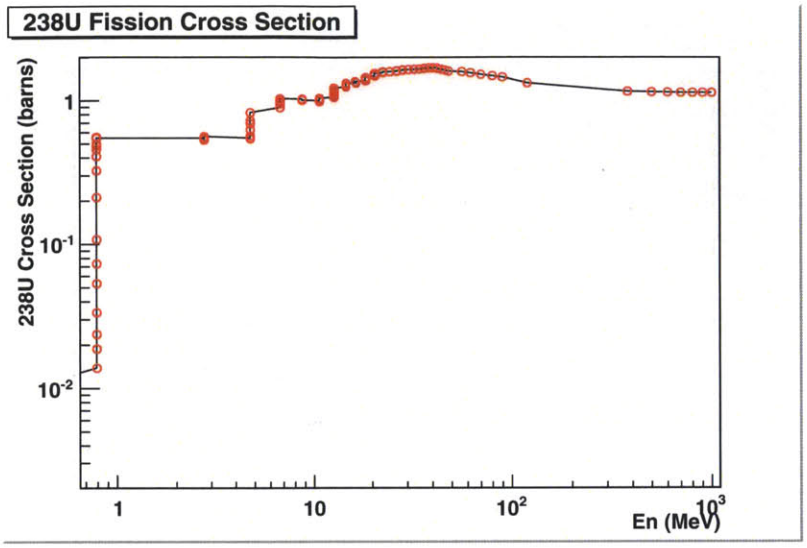

Figure 6-12: ^{238}U fission cross section.

on the geometry of the chamber design, the efficiency for detection is estimated to be $\epsilon_f = 0.98$. [54]

The fission cross section for ^{238}U is shown in figure 6-12. The red circles indicate data points, with an interpolation between them. Our region of interest is at the very low end, where the cross section is falling very rapidly. We had intended to use a ^{235}U foil to reach these low energies, since it has a much higher cross section below 1 MeV, but difficulties in the electronics prevented us from accurately measuring the flux, and thus led to the restriction to the range 1 to 5 MeV. The total neutron flux above 1 MeV is shown in figure 6-13 for the runs in group 24.

To determine the expected number of capture events, we use the equation

$$N_d = N_n \times \sigma_{capture} \times \frac{\Omega_{Bri}}{4\pi} \times \epsilon_{Bri} \times \rho_{AT} \tag{6.2}$$

where N_d is the estimated deuteron rate, N_n is the total neutron flux, $\sigma_{capture}$ is the capture cross section, Ω_{Bri} and ϵ_{Bri} are the solid angle and efficiency of the BrilLanCe detector, and ρ_{AT} is the AT thickness. The active target was designed to cover the entire beam spot allowed into the target room, and so its solid angle is already included in the total neutron flux measured by the fission chamber. Based on measurements and estimates, $\sigma_{capture} = 35.2 \pm 2.4$ μb,[4] $\Omega_{Bri} = 0.1$

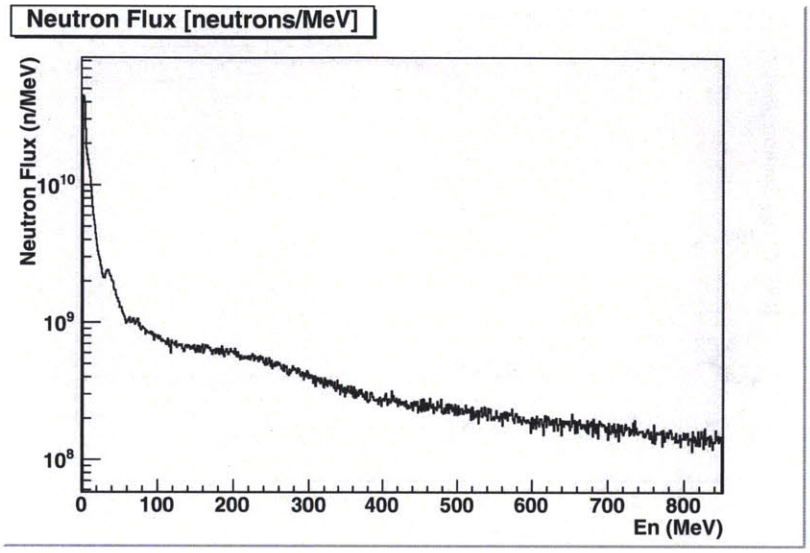

Figure 6-13: Total neutron flux received during group 24.

sr, $\epsilon_{Bri} = 0.1$, and $\rho_{AT} = 7.8 \times 10^{21}$ p/cm^2. Using these numbers and the total integrated beam flux from 1 to 5 MeV, we predict 30 ± 3 deuteron events, which is consistent with our measured rate of 24 ± 10.

6.1.5 Signal to Background Ratio

While there are too few events to calculate meaningful cross sections, we can use these results to determine the signal to background ratio, which we can compare with the signal to background ratio at the University of Kentucky experiment in order to determine which facility is better suited for the continuation of the experiment. The signal to background ratio for this set of data is approximately 0.66:1.

6.2 Measurements at UKY

Neutrons were produced using both a LiF target and a tritium cell, using the ^{7}Li(p,n)^{7}Be and ^{3}H(p,n)^{3}He reactions to generate neutrons. Tritium was used at proton beam energies of 1.615, 2.0, 2.5, 3.0, and 3.5 MeV, yielding maximum neutron energies of 0.5, 0.9, 1.5, 2.0, and 2.5 MeV. The LiF target was 21 kÅthick,

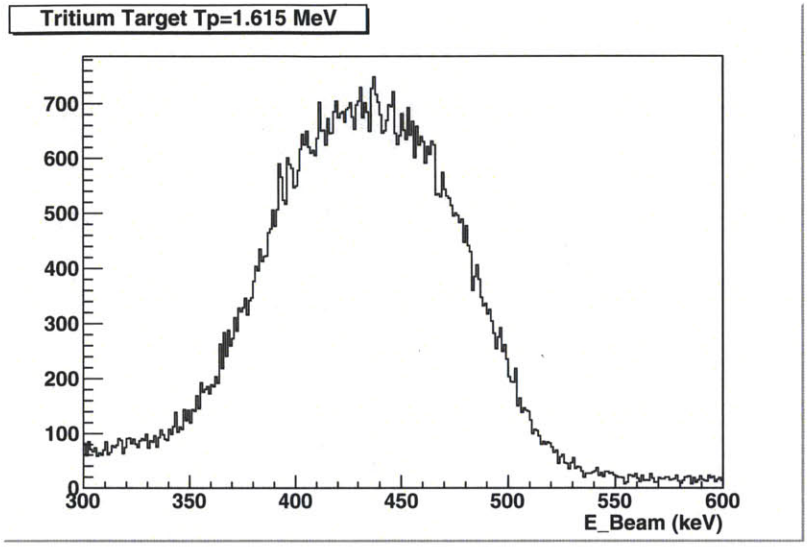

Figure 6-14: Neutron energy spectrum for the tritium target for T_p=1.615 MeV.

and was used at 2.23 MeV proton beam energy, yielding a maximum neutron energy of 0.5 MeV.

Due to the small cross section for the capture reaction, we applied numerous cuts to the timing and energy measurements for each detector in order to isolate the capture events.

6.2.1 Neutron Energy

With the active target in the beam, we are able to determine the time of flight of the beam neutrons, and use this to calculate the neutron energy. The uncertainty in time of flight for the active target is ± 1 ns, determined from the width of the γ-ray time of flight peak in the LiF data. Additionally, for the data taken with the tritium cell, there is an additional one sided uncertainty of -5 ns due to the uncertainty in position of the γ-ray flash in the tritium data. This uncertainty is not present in the LiF data due to the much higher rate of γ-ray production from the ^{7}Li(p,γ)^{8}Be reaction.

With 1.615 MeV protons incident on the tritium cell, the maximum neutron energy is 500 keV, and the neutron energy at the midpoint of the cell is 420 keV, which is consistent with the spectrum in figure 6-14. For these data, an energy cut of 350 to 500 keV was used to exclude background events which were not

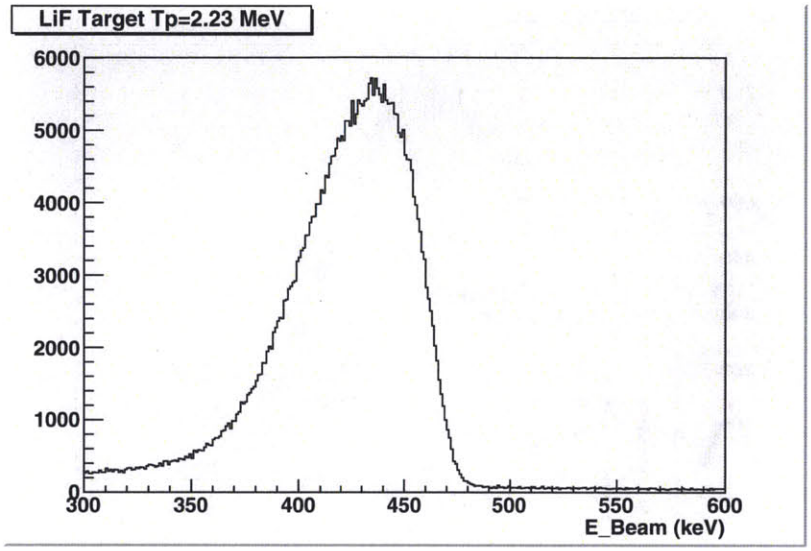

Figure 6-15: Neutron energy spectrum for the lithium fluoride target for T_p=2.23 MeV.

initiated by a neutron in the active target. The uncertainty in energy for these data from the active target time resolution and the uncertainty in the γ-ray flash is $\pm$8 keV+34 keV.

The LiF target was manufactured such that 2.225 MeV protons would lose 50 keV on average in passing through it. This resulted in a thickness of 21 kÅ. Thus, with 2.23 MeV protons, we expect neutron energies ranging from approximately 400 to 450 keV, as seen in the spectrum in figure 6-15. For these data, that energy cut was used to exclude background events which were not initiated by a neutron in the active target. Even though the total neutron production rate is approximately the same for both sets of data, the number of counts in this figure is much higher than in figure 6-14 due to the increased rate of accidental coincidences in the LiF data (see figures 6-24, 6-25, 6-25, and 6-26 below). Based on the time of flight resolution of the active target, the uncertainty in energy for a 500 keV neutron is $\pm$8 keV.

The neutron energy spectrum for 2.0 MeV protons incident on the tritium target is shown in figure 6-16. Based on the energy loss in the tritium cell, these protons should produce neutrons in the 800 to 950 keV range. The high end of the energy spectrum begins at 950 keV, as expected, and extends down to 750 keV. The uncertainty in the energy due to the time of flight resolution of the active

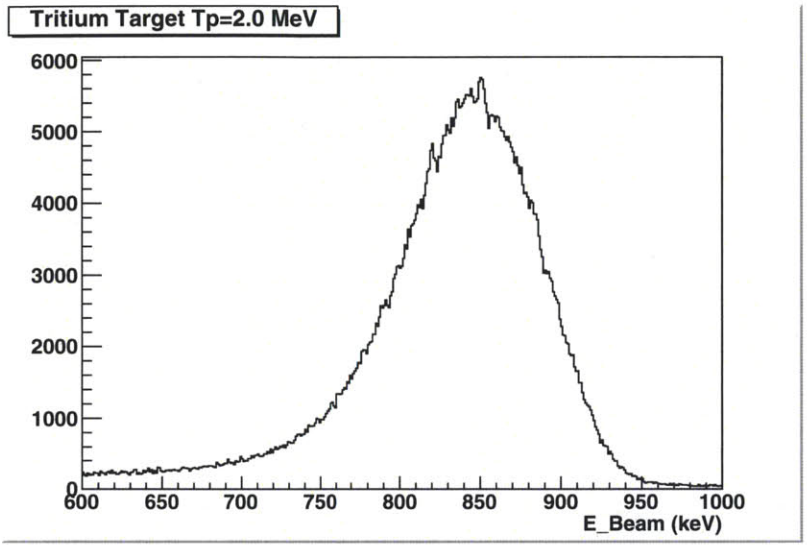

Figure 6-16: Neutron energy spectrum for the tritium target for T_p=2.0 MeV.

target and the uncertainty in position of the γ-flash is $\pm$22 keV +93.2 keV.

At $T_p = 2.5$ MeV, the neutron energy spectrum for tritium is shown in figure 6-17. Based on the thickness of the tritium cell, the neutron energy spectrum should extend from 1.4 to 1.5 MeV, but it extends down to 1.2 MeV in the real spectrum. The uncertainty in neutron energy based on the uncertainty in time of flight is $\sim$ 45 keV for 1.5 MeV neutrons, but the uncertainty in the position of the γ-flash contributes an additional one sided uncertainty of $\sim$ +180 keV at this energy range. A cut on the energy range of 1200 to 1500 keV was used to exclude background events which are inconsistent with neutrons in the active target.

The neutron energy spectrum for 3.0 MeV protons on the tritium target is shown in figure 6-18. At this energy, energy loss in the tritium cell predicts neutrons from 1.95 to 2.0 MeV. Uncertainty in energy due to the time resolution and the uncertainty in the position of the γ-flash is $\sim \pm$66 keV+280 keV. With this uncertainty, the spectrum shown from 1.6 to 2.1 MeV is consistent with the predicted spectrum, and this range is used to exclude background events not produced by neutrons in the active target.

At the highest proton energy, $T_p = 3.5$ MeV, the neutron energy spectrum is shown in figure 6-19. The spectrum extends from approximately 2 to 2.6 MeV. Based on energy loss in the tritium cell, we predict neutrons in the 2.51 to 2.54

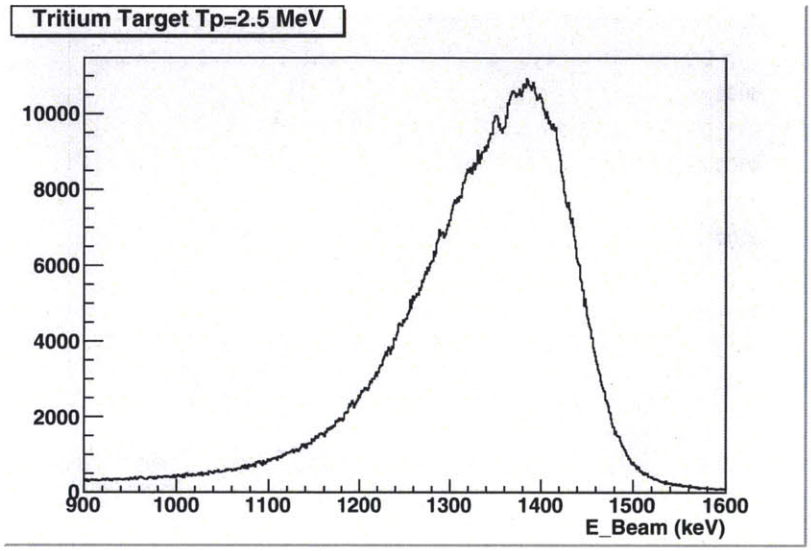

Figure 6-17: Neutron energy spectrum for the tritium target for T_p=2.5 MeV.

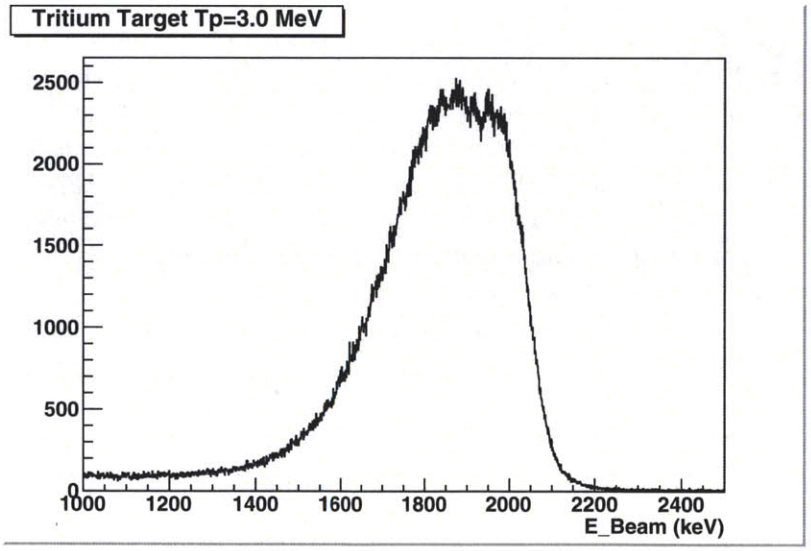

Figure 6-18: Neutron energy spectrum for the tritium target for T_p=3.0 MeV.

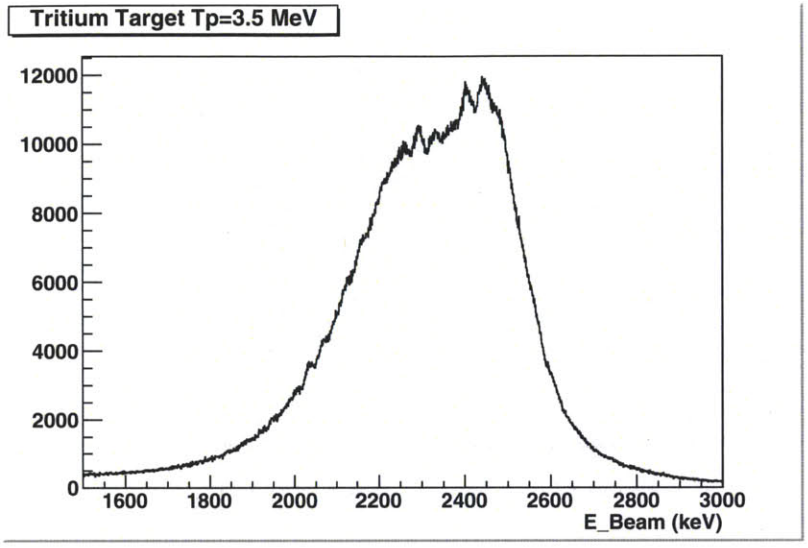

Figure 6-19: Neutron energy spectrum for the tritium target for T_p=3.5 MeV.

MeV range. The uncertainty in neutron energy due to the time resolution and the uncertainty in the position of the γ-flash is $\sim \pm 95$ keV+400 keV, accounting for the extended spectrum seen in the figure. A cut of 2.0 to 2.6 MeV was placed on the neutron energy to exclude background events without neutrons in the active target.

6.2.2 Elastic Monitor at UKY

A liquid scintillator was used to monitor elastic scattering to verify the active target calibrations and as a potential monitor of the neutron flux. Unfortunately, an error in the electronics cut off most of the relevant active target-neutron detector coincidence data. Figure 6-20 shows the neutron detector TDC in the upper figure, and the neutron detector TDC versus the neutron detector ADC in the lower figure, both at $T_n = 2.0$ MeV maximum beam energy. In the upper figure, the spectrum extends across the entire range of channels. However, in the lower spectrum, no events above channel 1300 in the TDC have any non-zero ADC information. A timing mismatch in the electronics resulted in the ADC gate being generated for these faster events only. This cutoff remains consistent across all beam energies. Unfortunately, for all but $T_n = 2.5$ MeV maximum beam energy, elastic events fall into the region with no ADC information, limiting the usefulness of the elastic

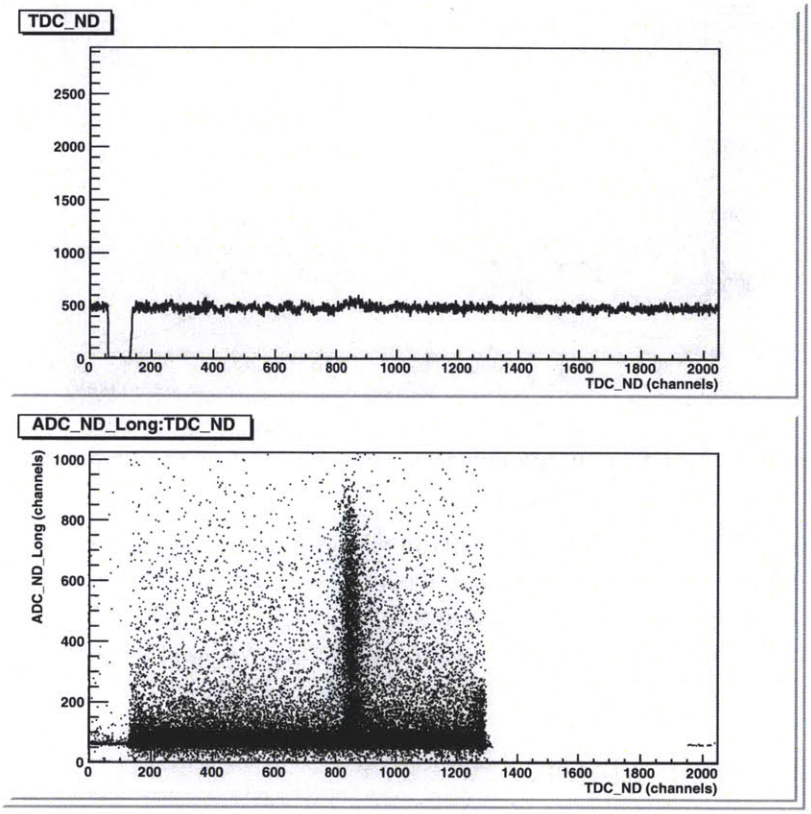

Figure 6-20: (Upper) The neutron detector TDC for the active target-neutron detector coincidence trigger at $T_n = 2.0$ MeV maximum beam energy. The spectrum extends across the entire range of channels. (Lower) Neutron detector ADC versus neutron detector TDC for the coincidence trigger at $T_n = 2.0$ MeV maximum beam energy. No events above channel 1300 in the TDC has an ADC value above zero. This is consistent across all neutron energies, the electronics were cutting off the ADC gates, preventing us from receiving ADC information for these slower events.

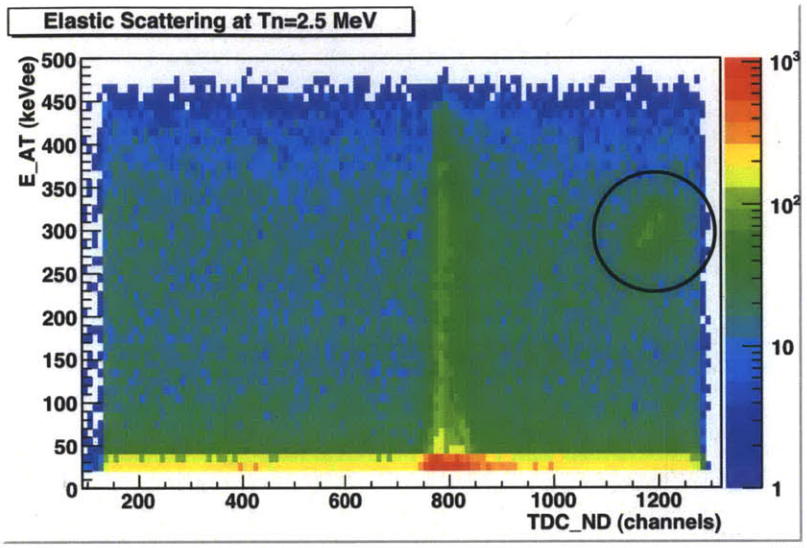

Figure 6-21: Active Target response versus neutron detector TDC for $T_n = 2.5$ MeV maximum beam energy. The vertical band is consistent with the AT singles spectrum, indicating that it is composed of the accidental coincidences between neutrons traveling directly from the tritium cell to the neutron detector and with neutrons in the active target. The circled region shows real elastic scattering events

monitor.

At the highest beam energy, $T_n = 2.5$ MeV, the scattered neutrons are fast enough to fall within the range of the TDC with non-zero ADC information. Applying neutron time of flight and pulse shape discrimination cuts to this data yields figure 6-21, showing the active target response versus the neutron detector TDC. The vertical band at channel 800 is consistent with the active target singles spectrum and appears at all energies, indicating that this is the result of accidental coincidences between neutrons in the active target and neutrons traveling directly from the tritium target to the neutron detector. The circled peak at TDC channel 1200 contains the real elastic scattering events.

Cutting on the neutron detector TDC for this region gives the active target pulse height spectrum shown in figure 6-22. The elastic peak is visible at 300 keVee. The neutron detector was at 52°; for 2.5 MeV neutrons this yields a recoil proton energy of 1.6 MeV. This is consistent with the results of the light response measurement, as shown in figure 5-40. This demonstrates the consistency of the light response results and supports our use of the same calibration for both this

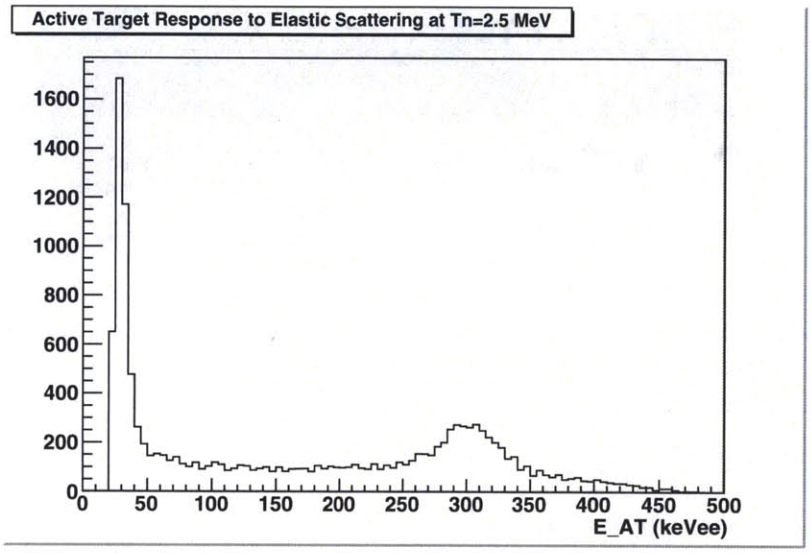

Figure 6-22: Active target response to elastic scattering for $T_n = 2.5$ MeV beam energy. The scattering angle is 52°, giving a proton recoil energy of 1.6 MeV. This peak at 300 keVee matches the results from the light response measurement shown in figure 5-40.

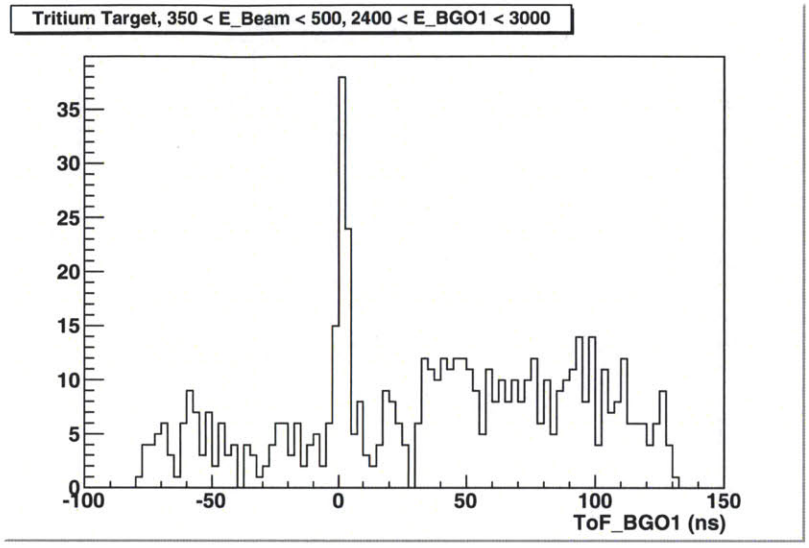

Figure 6-23: Time of flight between the active target and BGO1 for the tritium target at T_p=1.615 MeV.

measurement and the light response measurement.

6.2.3 BGO Timing Cuts

In addition to the time of flight between the neutron production target and the active target, we are able to use the BGO time signal to cut on the time of flight between the active target and the BGO detectors. The BGO detectors were placed 15.5 cm away from the active target, and thus γ-rays will take approximately one-half nanosecond to travel from the active target to the BGO detectors.

The time of flight from the active target to BGO1 is shown in figure 6-23 for the tritium target at T_p=1.615 MeV and in figure 6-24 for the LiF target at T_p=2.23 MeV. The figures are cut on the events which are initiated by neutrons in the active target, with a restriction on the γ-ray energy to be between 2400 and 3000 keV. This eliminates a significant number of the events where a neutron is detected in the BGO. In both figures, the prompt peak is visible at 0.5 ns time of flight. The accidental coincidence rate for the LiF data is a factor of two higher than the Tritium data, even though the total neutron production for each set of data is approximately equal. This is most likely due to the much higher cross section for producing γ-rays from protons incident on lithium than for protons incident

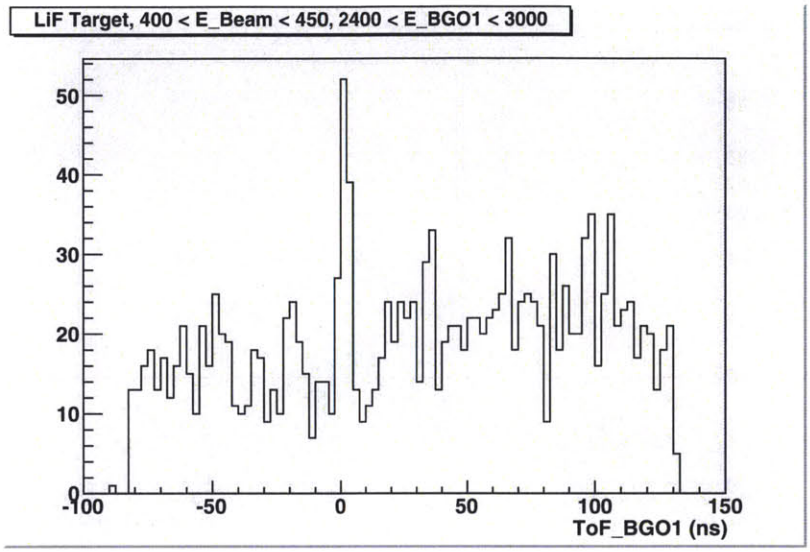

Figure 6-24: Time of flight between the active target and BGO1 for the LiF target at T_p=2.23 MeV.

on tritium.

The time of flight from the active target to BGO2 is shown in figure 6-25 for the tritium target at T_p=1.615 MeV and in figure 6-26 for the LiF target at T_p=2.23 MeV. These figures have the same cuts on neutron energy and γ-ray energy as figures 6-23 and 6-24. In addition to the increased accidental coincidence rate for LiF as observed in BGO1, BGO2 shows a very large, broad peak in the 20 to 60 ns range. BGO2 was placed at a forward angle, which may have resulted in more neutrons scattering into BGO2, or neutrons were capturing on some piece of shielding near BGO2 that was not near BGO1.

Figure 6-27 shows the time of flight from the active target to BGO1 for 2.0 MeV protons incident on the tritium target. The data in this figure are cut on the events which are initiated by neutrons in the active target, and restricted to γ-ray energies from 2400 to 3000 keV, again to eliminate the events produced by neutrons in the BGO. The prompt peak is visible above the accidental coincidence backgrounds at 0.5 ns.

The time of flight spectrum for BGO2 with 2.0 MeV protons incident on the tritium target is shown in figure 6-28. Again the data in this figure are cut on neutron initiated events and γ-ray energies from 2400 to 3000 keV. As with the

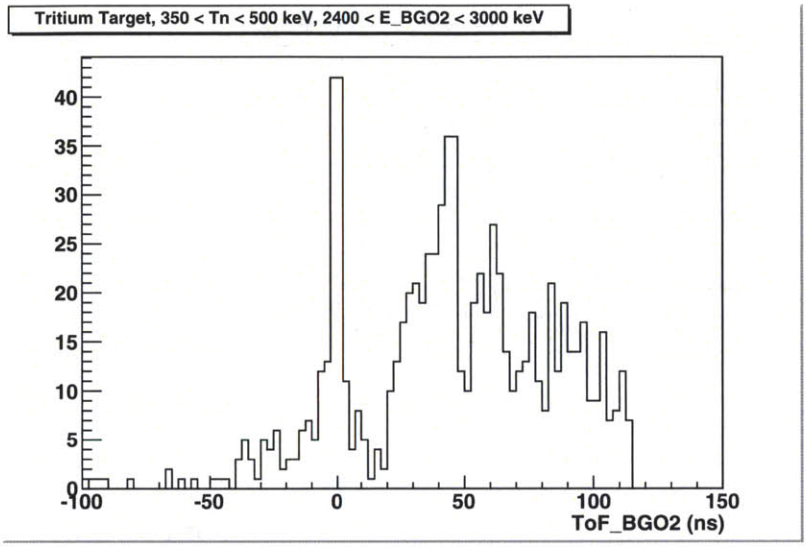

Figure 6-25: Time of flight between the active target and BGO2 for the tritium target at T_p=1.615 MeV.

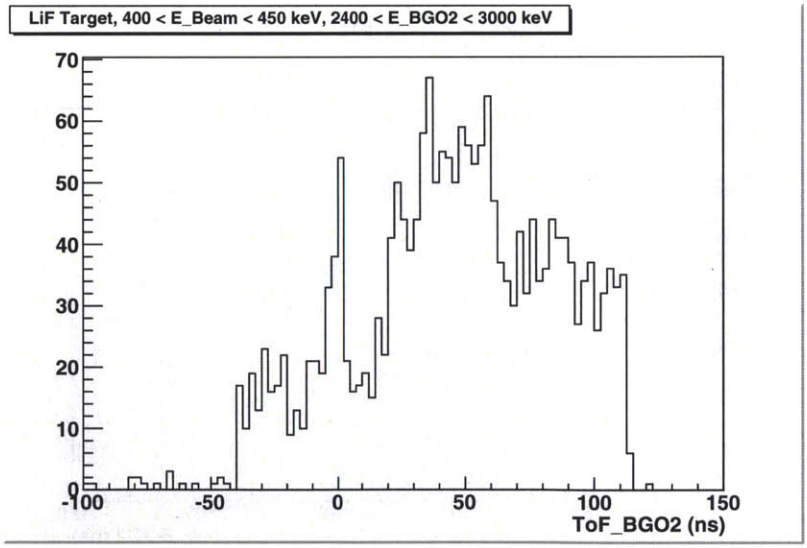

Figure 6-26: Time of flight between the active target and BGO2 for the LiF target at T_p=2.23 MeV.

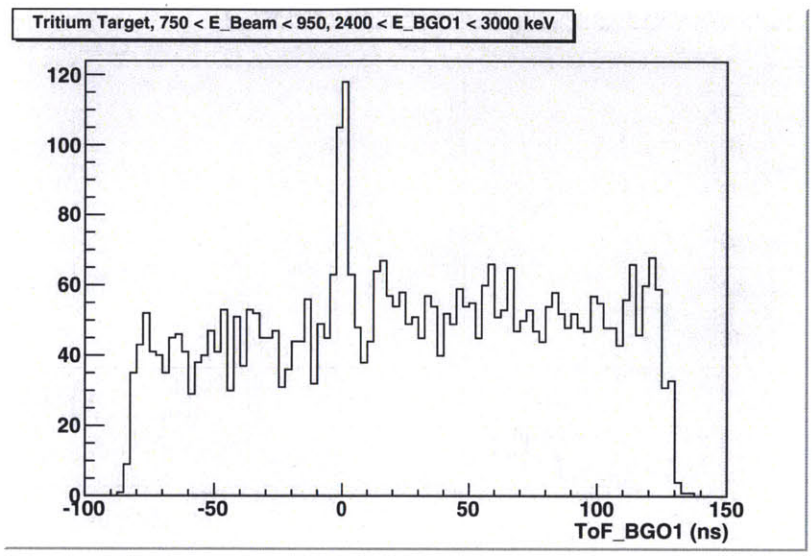

Figure 6-27: Time of flight between the active target and BGO1 for the tritium target at T_p=2.0 MeV.

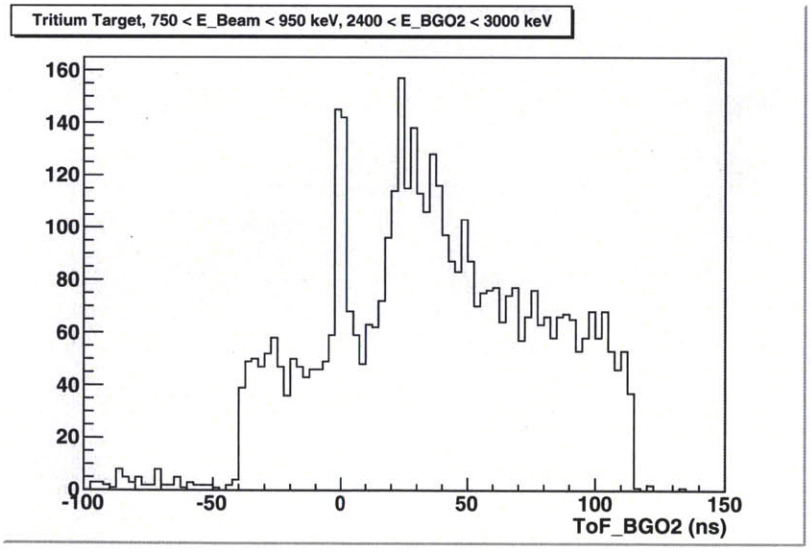

Figure 6-28: Time of flight between the active target and BGO2 for the tritium target at T_p=2.0 MeV.

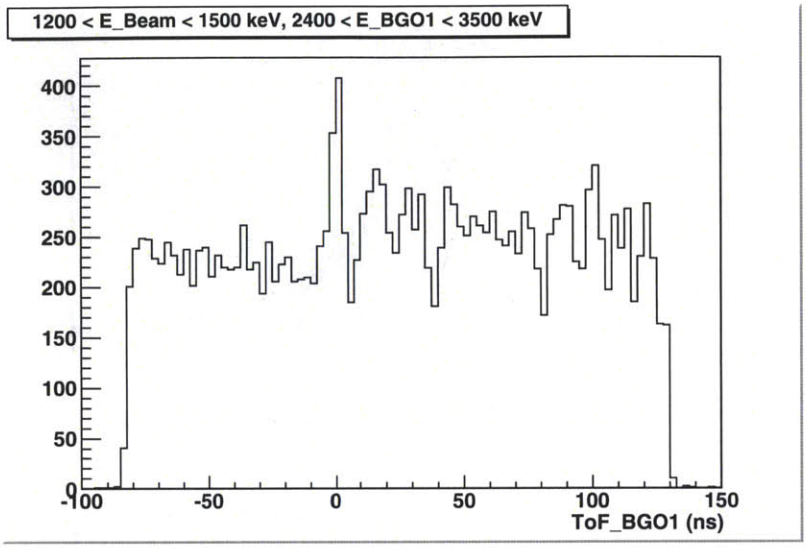

Figure 6-29: Time of flight between the active target and BGO1 for the tritium target at T_p=2.5 MeV.

BGO2 spectra at other energies, there is a large, broad peak at slower flight times than the prompt peak, shifting to higher times of flight as the neutron energy increases.

For 2.5 MeV protons, figures 6-29 and 6-30 show the time of flight spectra from the active target to BGO1 and BGO2. Both spectra are cut on neutron energies from 1200 to 1500 keV, and are cut on γ-ray energies between 2400 and 3500 keV. As with the previous energies, a prompt peak is visible above the background at 0.5 ns. BGO2 shows the large peak above background in the 15 to 40 ns region, similar to the results at lower energies.

Figures 6-31 and 6-32 show the active target to BGO1 and BGO2 time of flight spectra for T_p=3.0 MeV. As with the spectra at lower energies, these are cut on neutron energies from 1600 to 2100 keV, and restricted to γ-ray energies from 2400 to 4000 keV. Prompt peaks are visible at 0.5 ns for both BGO1 and BGO2. BGO2 again shows the large peak above background at slower times of flight, in the 10 to 30 ns region at this energy. This peak may arise from neutrons capturing on shielding near BGO2.

The time of flight spectra from the active target to BGO1 and BGO2 are shown in figures 6-33 and 6-34 for 3.5 MeV protons on the tritium target. These spectra

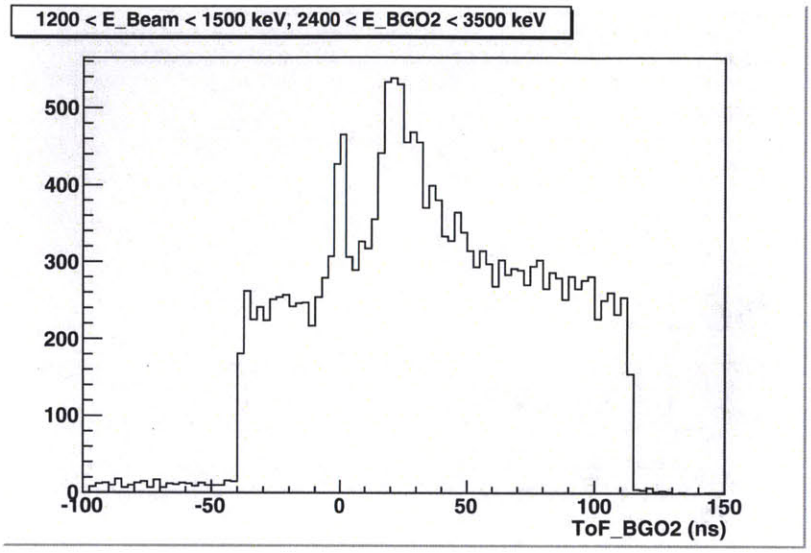

Figure 6-30: Time of flight between the active target and BGO2 for the tritium target at T_p=2.5 MeV.

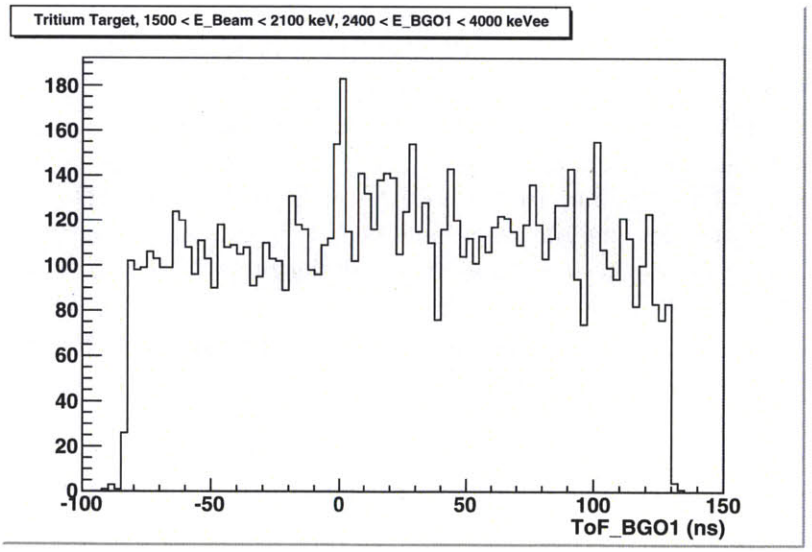

Figure 6-31: Time of flight between the active target and BGO1 for the tritium target at T_p=3.0 MeV.

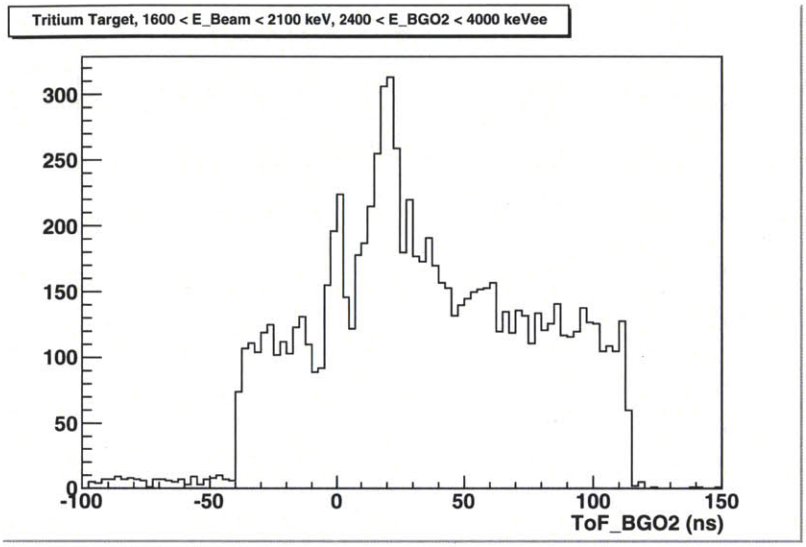

Figure 6-32: Time of flight between the active target and BGO2 for the tritium target at T_p=3.0 MeV.

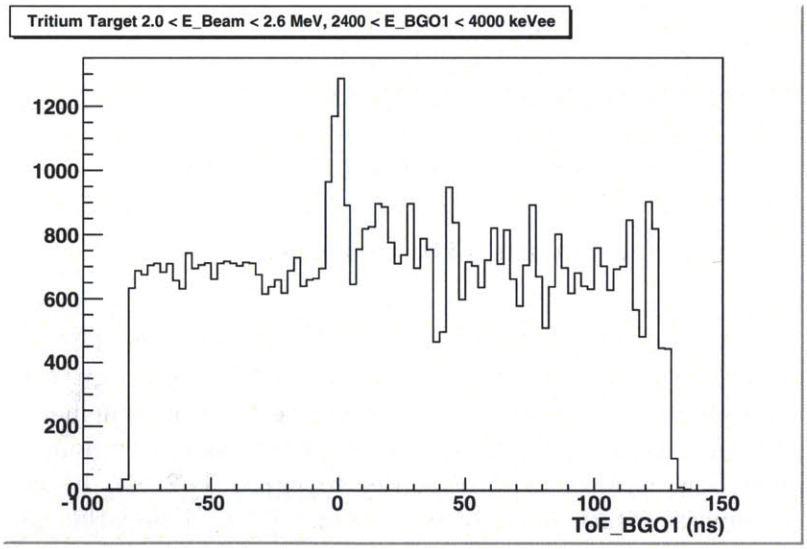

Figure 6-33: Time of flight between the active target and BGO1 for the tritium target at T_p=3.5 MeV.

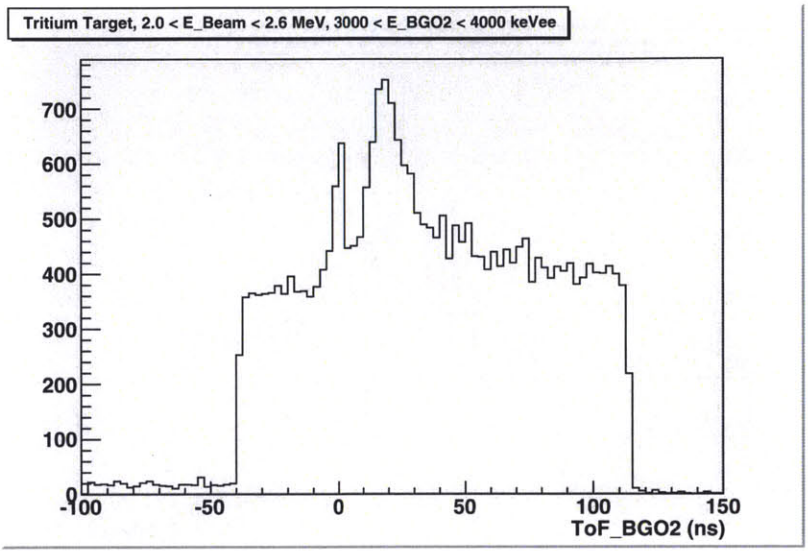

Figure 6-34: Time of flight between the active target and BGO2 for the tritium target at T_p=3.5 MeV.

are cut on neutron energies from 2.0 to 2.6 MeV, and γ-ray energies from 2.4 to 4.0 MeV for BGO1, and 3.0 to 4.0 MeV for BGO2. For BGO1, the prompt peak is visible above the background as with previous energies. For BGO2, the lower cut on the BGO response was moved up to 3.0 MeV because the prompt peak was not visible above background when extended down to 2.4 MeV.

6.2.4 Active Target and BGO Energies

Using the cuts on the neutron beam energy and the prompt peak in the active target to BGO time of flight, we can examine the active target response versus the BGO response to try to identify capture events by examining the pulse height regions corresponding to the particle energies expected from kinematics.

Using the same empirical relationship between proton light response and deuteron light response, the proton light responses in figure 5-42 can be converted to deuteron responses, which are plotted in figure 6-35. Using this plot, we can estimate the response we expect for deuterons in capture events.

Figures 6-36 and 6-37 show this plot for the combined tritium and LiF data at $T_n \sim 500$ keV. For BGO1, there is an enhancement in active target response in the 35-45 keVee range, which is consistent with the response we expect for 260 keV

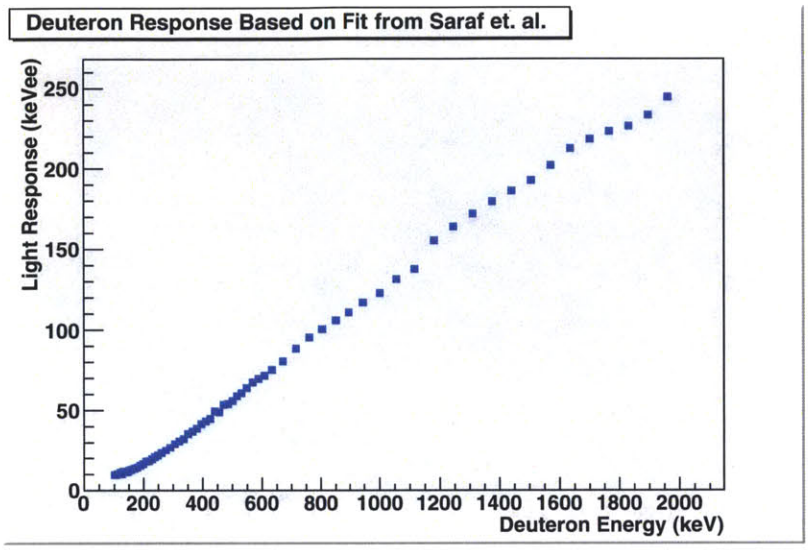

Figure 6-35: Light response data from figure 5-42 converted to deuteron response from the fits done by Saraf et. al.[29, 30].

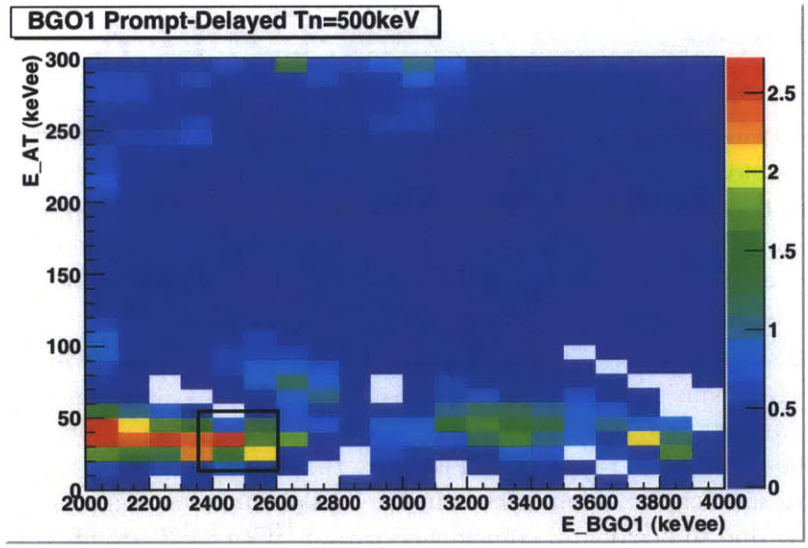

Figure 6-36: Background subtracted spectra for the active target response versus the BGO1 response for the $T_n \sim 500$ keV data. The region where we expect capture events based on kinematics is indicated by the black box.

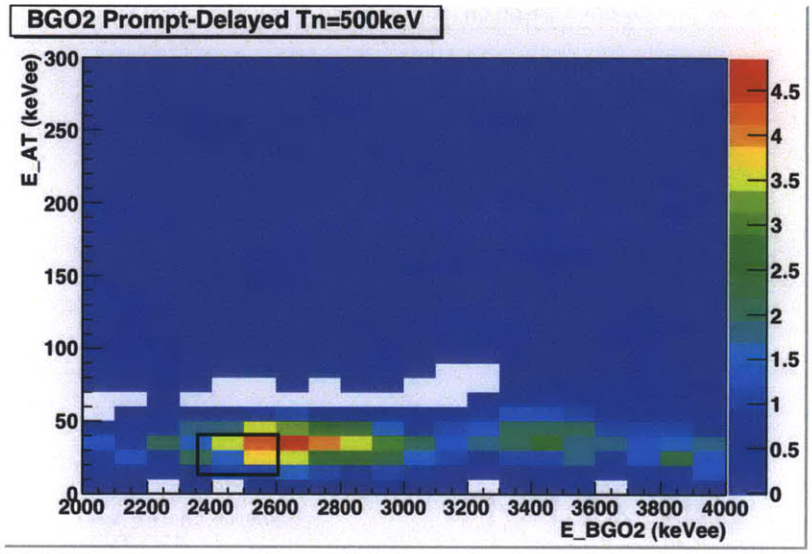

Figure 6-37: Background subtracted spectra for the active target response versus the BGO2 response for the $T_n \sim 500$ keV data. The kinematic region for capture events is indicated by the black box, and it does not correspond with the peak in the BGO response.

deuterons, the approximate recoil energy for a γ-ray angle of 106.6°. The BGO response is more spread out, however, due to the low resolution of the BGOs, but does seem to be enhanced in the 2400-2600 keVee range, as we expect based on kinematics. The additional enhancment in the 3200-3400 keVee range is most likely caused by neutron capture on carbon in coincidence with an elastically scattered neutron; ^{12}C has thermal capture lines at 3 MeV and 3.6 MeV.

BGO2 shows a similar peak in active target response in the 30-40 keVee range, which is again consistent with the response for the 230 keV deuterons produced for the γ-ray angle of 64.6°. The enhancement in BGO response is somewhat higher, in the 2500-2700 keVee range, which is above the expected kinematic result of 2500 keVee. We still see the enhancement in the 3200-3400 keVee range, which is again most likely due to accidental coincidence with a ^{12}C(n,γ)^{13}C event.

For the $T_n \sim 900$ keV data, the active target versus BGO1 and BGO2 plots are shown in figures 6-38 and 6-39. For BGO1, there is no enhancement in the active target response above BGO1 response of 2500 keVee. There is a small excess in the BGO1 range of 2800-3000 keVee, in the 40-50 keVee active target response range.

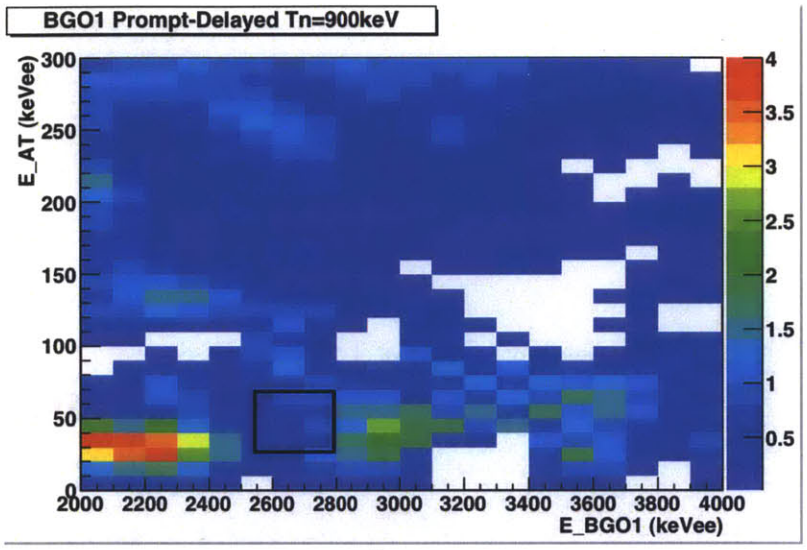

Figure 6-38: Background subtracted spectra for the active target response versus the BGO1 response for the $T_n \sim 900$ keV data. The kinematic region for capture events is indicated by the black box.

This range is consistent with recoil deuterons in the $\sim$ 450 keV range, which we expect from kinematics. However, we expect the γ-ray energy to be $\sim$ 2700 keV, somewhat below the excess we see in the 2800 to 3000 keVee range for the BGO1 response. The resolution of the BGO detectors is unable to distinguish between two peaks which are 200 keV apart in energy, so this region may in fact represent the capture events.

The active target response for BGO2 (figure 6-39) is much clearer, again in the 30-50 keVee range, but with a very broad distribution in BGO2 response. It is centered in the region we expect based on kinematics, in the 2700 keV γ-ray energy range.

The background subtracted response plots for $T_n \sim 1.5$ MeV are shown in figures 6-40 and 6-41 for BGO1 and BGO2. Based on kinematics, the active target response should fall at $\sim$ 100 keVee for 750 keV deuterons, and the γ-ray energy should be 3000 keV. For BGO1, there is a small enhancement to the kinematically correct range, at BGO1 response of 2900 to 3100 keVee, as expected, but with a slightly higher active target response than predicted, centered on approximately 125 keVee. This is the only elevated region near the expected kinematically correct

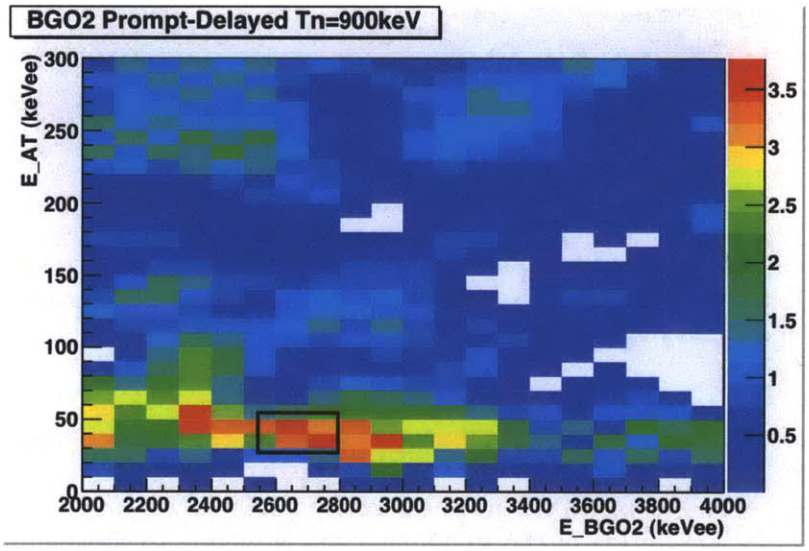

Figure 6-39: Background subtracted spectra for the active target response versus the BGO2 response for the $T_n \sim 900$ keV data. The kinematic region for capture events is indicated by the black box, and it does correspond to a peak in the spectrum.

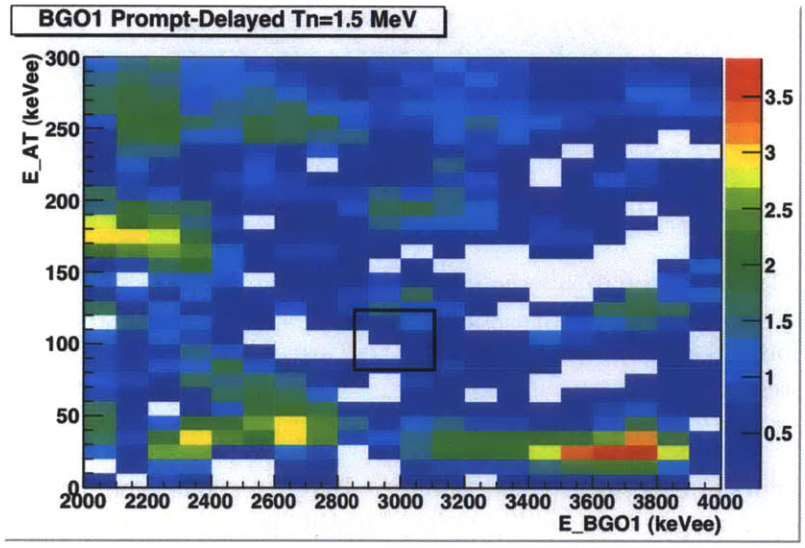

Figure 6-40: Background subtracted spectra for the active target response versus the BGO1 response for the $T_n \sim 1500$ keV data. The kinematic region for capture events is indicated by the black box, and there is a small excess of events at slightly higher AT response, along the upper edge of the box.

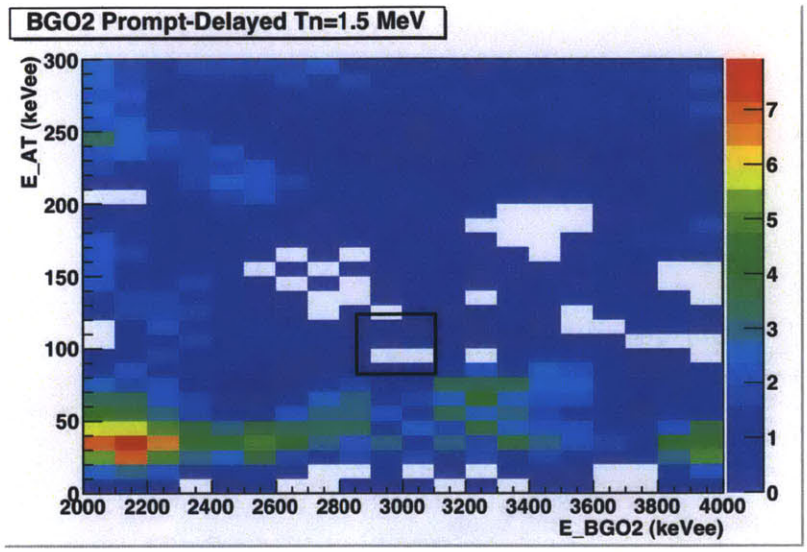

Figure 6-41: Background subtracted spectra for the active target response versus the BGO2 response for the $T_n \sim 1500$ keV data. The kinematic region for capture events is indicated by the black box, but there are no enhancement in the spectrum near this region.

region, so cuts of 2900 to 3100 keVee on the BGO1 response and 100 to 150 keVee on the active target were used. Other identifiable features seem to fall in the thermal capture region near 2.2 MeV, and the 3200-3800 keVee region for BGO1 which could again be from capture on carbon.

BGO2 is less clear, with no peaks of any sort near the kinematically correct region. At slightly higher BGO2 response, in the 3100 to 3300 keVee region, there is an excess for the active target response from 50 to 75 keVee, which is slightly lower than expected from kinematics. There is also a band at lower BGO2 response, extending down from 2900 keVee to the thermal capture peak at 2200 keVee. The region from 50 to 100 keVee in the active target response and 3100 to 3300 keVee in the BGO2 response was used for capture events.

For $T_n \sim 2.0$ MeV, the background subtracted response plots are shown in figures 6-42 and 6-43. Neither of these plots show a significant peak over background. The capture cuts will have to be based on kinematics; for these neutron energies we expect deuteron recoil energies in the 1 MeV range, which will give an active target response in the 50 to 150 keVee range, and we expect γ-ray energies

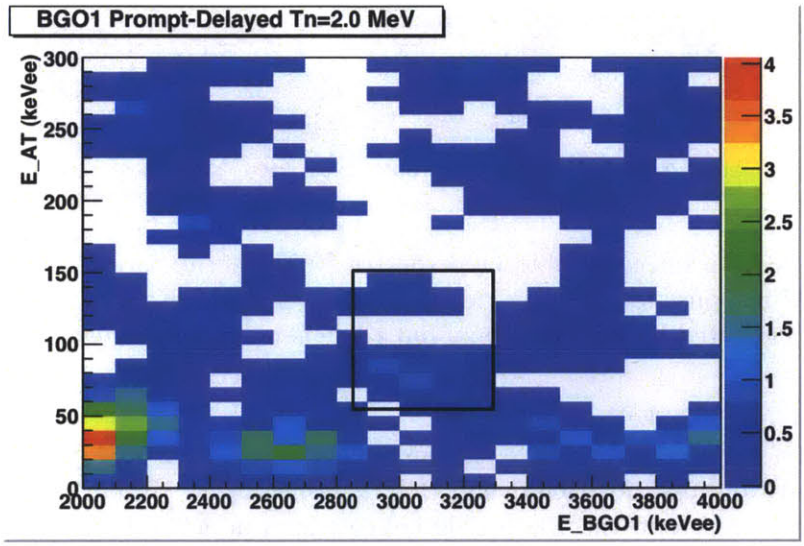

Figure 6-42: Background subtracted spectra for the active target response versus the BGO1 response for the $T_n \sim 2.0$ MeV data. The kinematic region for capture events is indicated by the black box, but there is no excess of events near it.

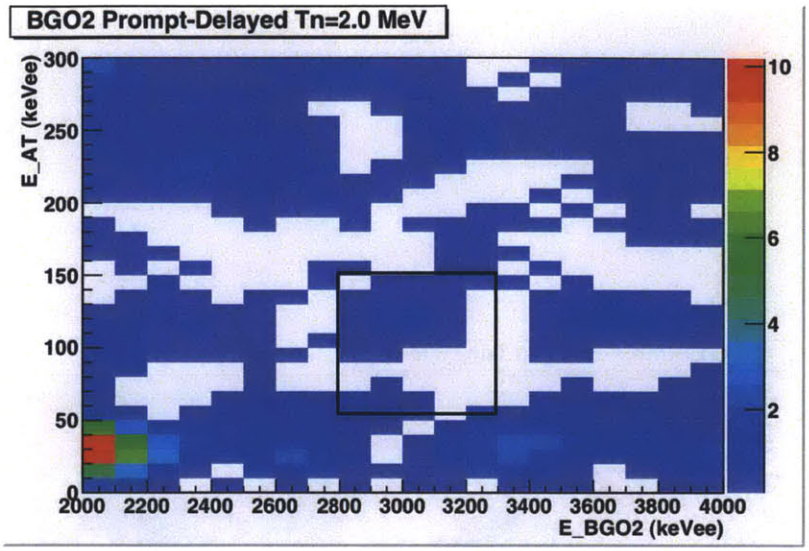

Figure 6-43: Background subtracted spectra for the active target response versus the BGO2 response for the $T_n \sim 2.0$ MeV data. The kinematic region for capture events is indicated by the black box, but there is no excess of events near it.

in the 2800 to 3300 keV range.

The background subtracted response plots for $T_n \sim 2.5$ MeV are shown in figures 6-44 and 6-45 for BGO1 and BGO2, respectively. In both plots, there is an excess of events in the 150 to 200 keVee region in active target response and 3400 to 3800 keVee in BGO response. These are consistent with the expected kinematics of radiative capture at this energy; 1.2 MeV recoiling deuterons and 3.6 MeV γ-rays. The active target region was extended to 120 to 220 keVee based on these kinematics and the active target resolution.

6.2.5 Backgrounds

Since the peaks are not clear in the background subtracted prompt plots, due to the low rate, we characterize the background by shifting the energy cuts. To ensure the same accidental coincidence rate, the background cuts are chosen such that the singles triggers have the same rate in the shifted cuts as in the original capture cuts. The background is then determined by averaging the number of counts in the prompt region for the shifted cuts.

The background time of flight spectra for BGO1 for the combined tritium and

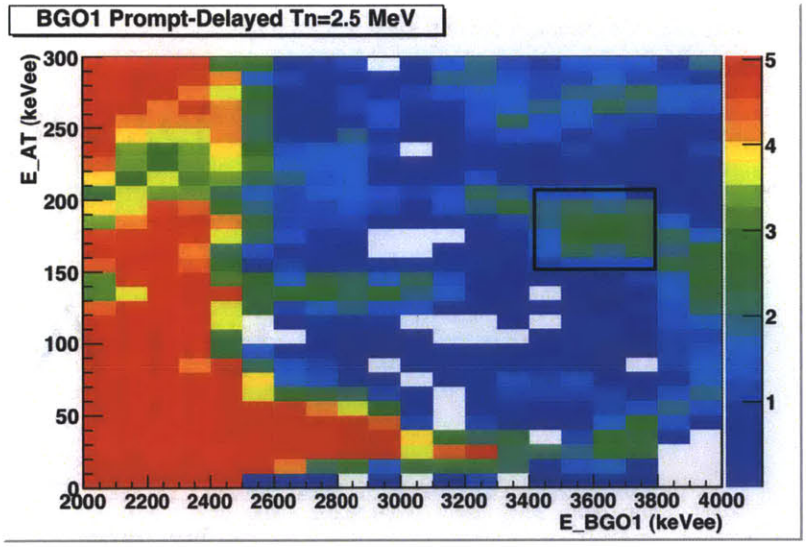

Figure 6-44: Background subtracted spectra for the active target response versus the BGO1 response for the $T_n \sim 2.5$ MeV data. The kinematic region for capture events is indicated by the black box, and there is a small excess of events within it.

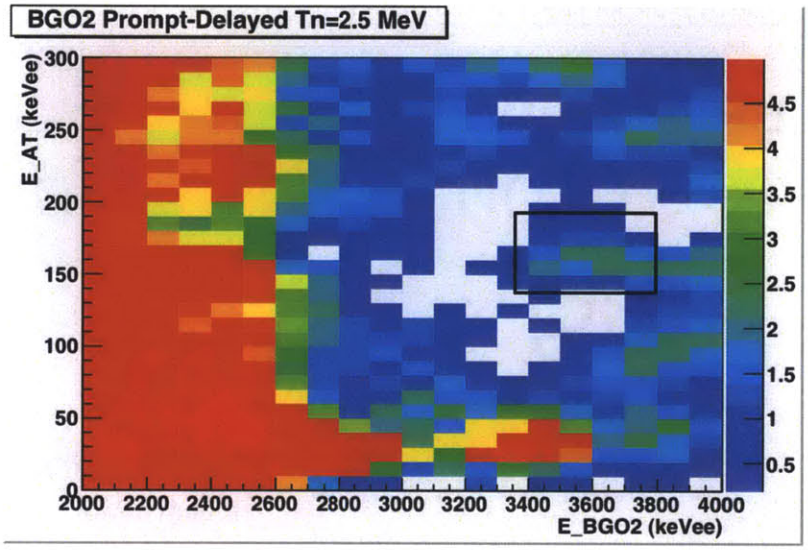

Figure 6-45: Background subtracted spectra for the active target response versus the BGO2 response for the $T_n \sim 2.5$ MeV data. The kinematic region for capture events is indicated by the black box, and there is a small excess of events within it.

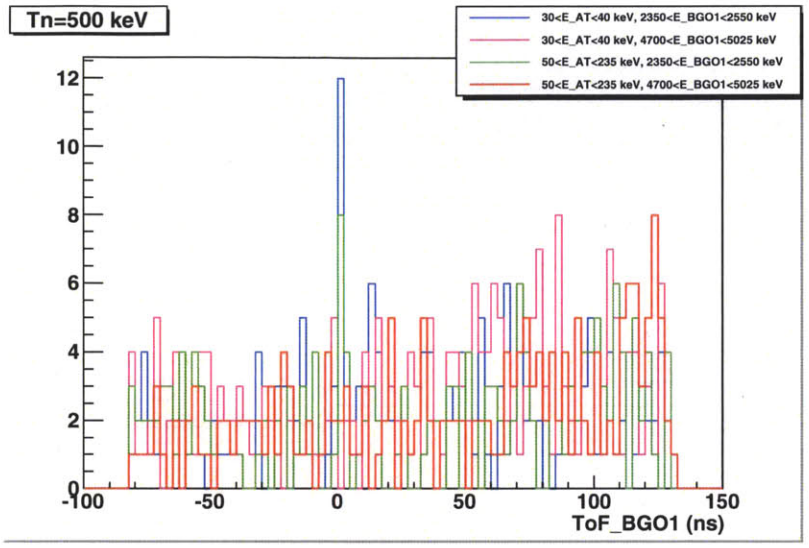

Figure 6-46: Comparison of BGO1 ToF spectra for the capture kinematics (blue) and the background kinematics (red, green, magenta) for $T_n \sim 500$ keV. There is an excess of events for the capture kinematics

LiF data at $Tn \sim 500$ keV are shown in figure 6-46. In this case, we see a slight excess of prompt events with the conditions which correspond to radiative capture events. The resulting signal over background is 8 ± 4.5 capture events.

The background time of flight spectra for BGO2 for the combined tritium and LiF data at $Tn \sim 500$ keV are shown in figure 6-47. In this case, there is no clear excess of prompt events for the radiative capture events. The resulting signal over background in this case is 5.7 ± 4.8.

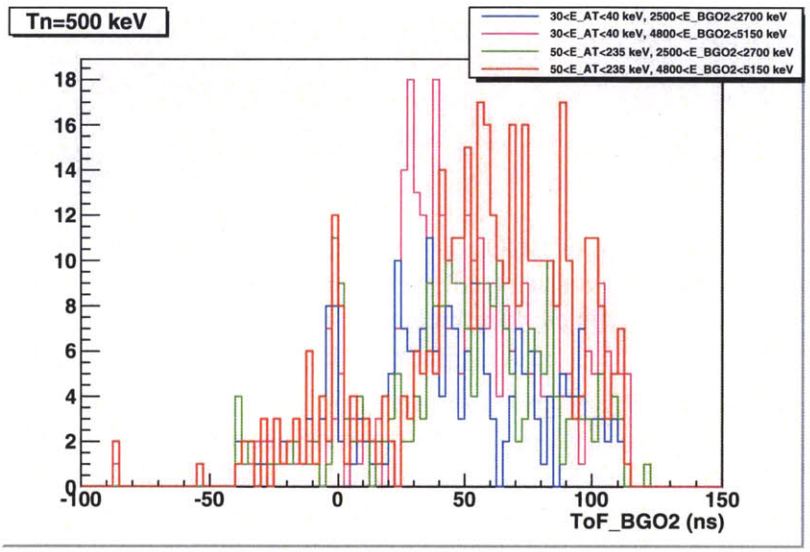

Figure 6-47: Comparison of BGO2 ToF spectra for the capture kinematics (blue) and the background kinematics (red, green, magenta) for $T_n \sim 500$ keV. There is no clear excess for capture kinematics.

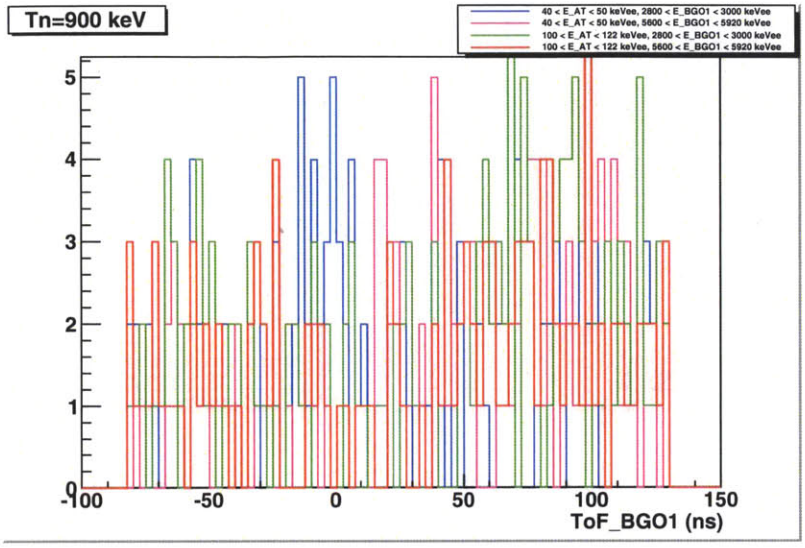

Figure 6-48: Comparison of BGO1 ToF spectra for the capture kinematics (blue) and the background kinematics (red, green, magenta) for $T_n \sim 900$ keV. There are very few statistics, but there is a small excess in the prompt region for capture kinematics.

The background time of flight spectra for the $T_n \sim 900$ keV data for BGO1 and BGO2 are shown in figures 6-48 and 6-49. BGO1 shows a slight excess of events in the prompt region, though the backgrounds at longer time of flights fluctuate just as highly as this peak. The resulting counts over background is 9.7±3.4. In BGO2, it is again much less clear whether there is a significant excess of events in the prompt peak. Additionally, there is still the large peak at greater times of flight. The prompt region does not show a statistically significant signal over background, 3±3.7 counts.

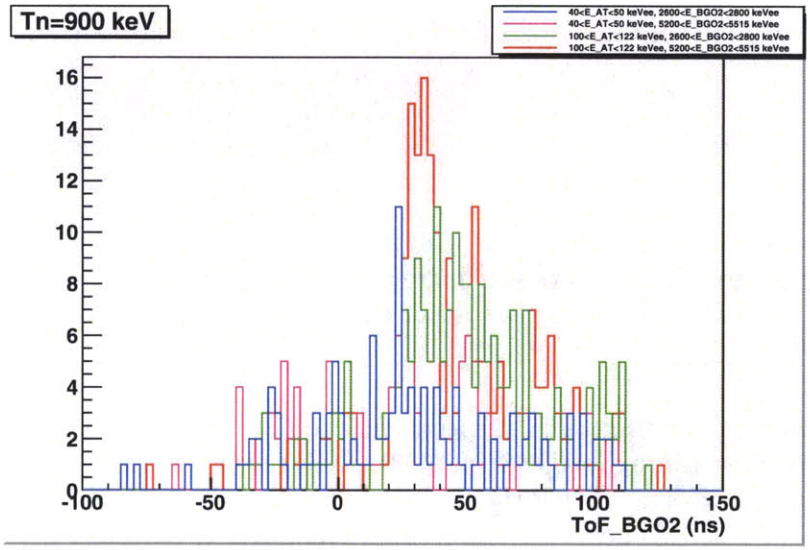

Figure 6-49: Comparison of BGO2 ToF spectra for the capture kinematics (blue) and the background kinematics (red, green, magenta) for $T_n \sim 900$ keV. There is no clear excess of events in the prompt region for any kinematic region.

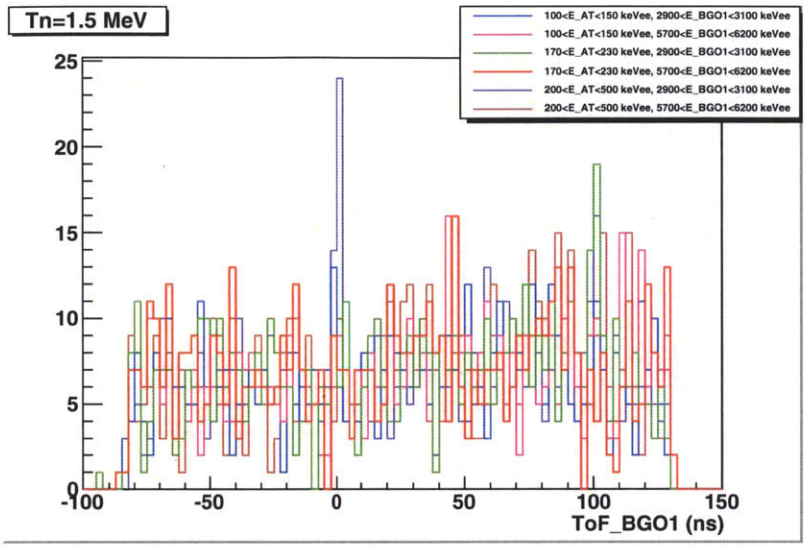

Figure 6-50: Comparison of BGO1 ToF spectra for the capture kinematics (blue) and the background kinematics (red, green, magenta, orange, purple) for $T_n \sim 1.5$ MeV. There is no excess of events for capture kinematics, the peak in the prompt region is from active target responses which are more consistent with Compton scattering from the active target.

The background comparison spectra for the $T_n \sim 1500$ keV data are shown in figures 6-50 and 6-51. An unusual result arises in BGO1; the spectra for the region determined by kinematics shows no significant peak over background, but when the active target cut is shifted to significantly higher energies, in the 200 to 500 keVee region, there is an extremely large signal over the background in the prompt region. This response is too high to be from deuterons, or even recoiling protons. Based on the results in figure 5-42, it would require a 2 MeV proton to produce a response approaching this range, which is impossible to reach for a neutron energy of 1.5 MeV. For events in the range where we expect capture events based on kinematics, there is no statistically significant signal over background, 2.3 ± 5.7 counts. The peak in the prompt region has an active target response which are more consistent with a γ-ray in the active target. For BGO2, we still see the large background in the 10 to 50 ns range across multiple cuts, but in the prompt region there is a visible signal over the background, 22 ± 8 counts.

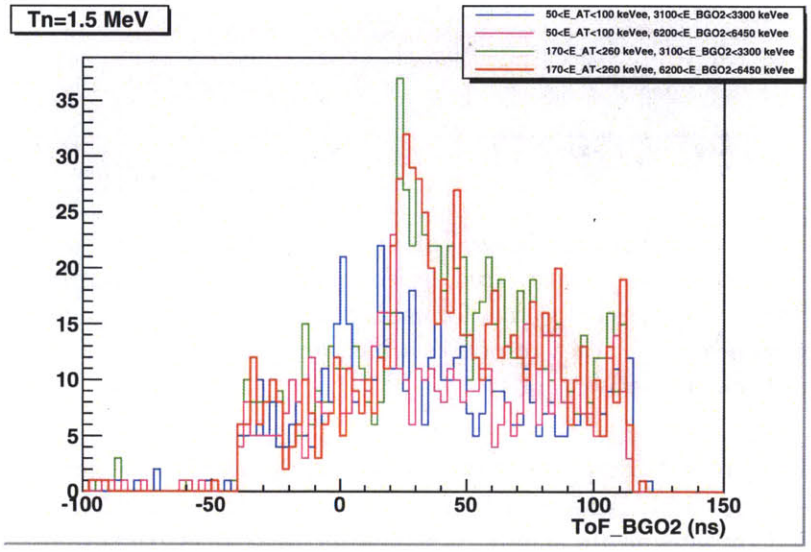

Figure 6-51: Comparison of BGO2 ToF spectra for the capture kinematics (blue) and the background kinematics (red, green, magenta) for $T_n \sim 1.5$ MeV. There is an excess of events for the capture kinematics.

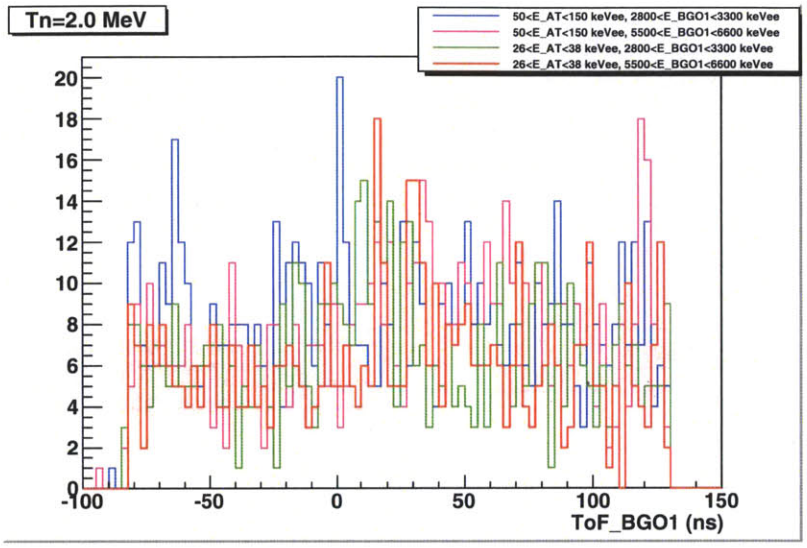

Figure 6-52: Comparison of BGO1 ToF spectra for the capture kinematics (blue) and the background kinematics (red, green, magenta) for $T_n \sim 2.0$ MeV. There is an excess of events in the prompt region for the capture kinematics.

The $T_n \sim 2.0$ MeV background spectra are shown in figures 6-52 and 6-53 for BGO1 and 2, respectively. For BGO1, there is a significant peak above background in the prompt region, yielding a signal of 21.6±7.0 counts over background. BGO2 is less clear at this energy, though the ubiquitous background peak at larger times of flight is still present. There is a resulting signal over background, 9.3±6.3 counts, but it is significantly smaller than the signal in BGO1.

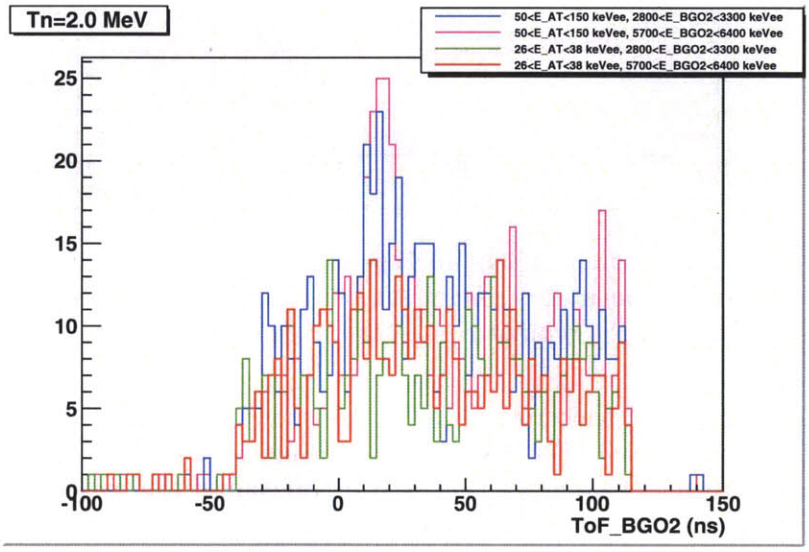

Figure 6-53: Comparison of BGO2 ToF spectra for the capture kinematics (blue) and the background kinematics (red, green, magenta) for $T_n \sim 2.0$ MeV. There is a small excess of events in the prompt region for capture kinematics, but it is significantly smaller than that for BGO1 at this energy.

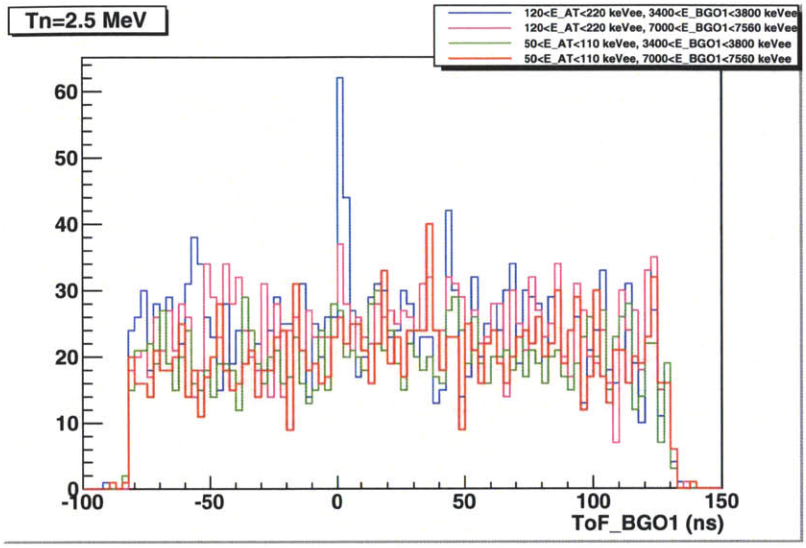

Figure 6-54: Comparison of BGO1 ToF spectra for the capture kinematics (blue) and the background kinematics (red, green, magenta) for $T_n \sim 2.5$ MeV. There is an excess of events in the prompt region for the capture kinematics.

At the highest neutron energy, we expect the highest statistics, due to the higher cross section for the ^{3}H(p,n)^{3}He reaction at this proton energy and the higher current that could be sustained on the tritium cell. The background comparison are shown in figures 6-54 and 6-55 for BGO1 and BGO2. As predicted, BGO1 has a much more significant peak over background in the prompt region, giving a yield of 52 ± 13 over background. BGO2 also shows a significant peak over background in the prompt region, in addition to the large, broad peak at larger flight times that is present in all BGO2 time of flight plots. This peak is smaller than in BGO1, but still shows a signal over background of 22 ± 12 counts.

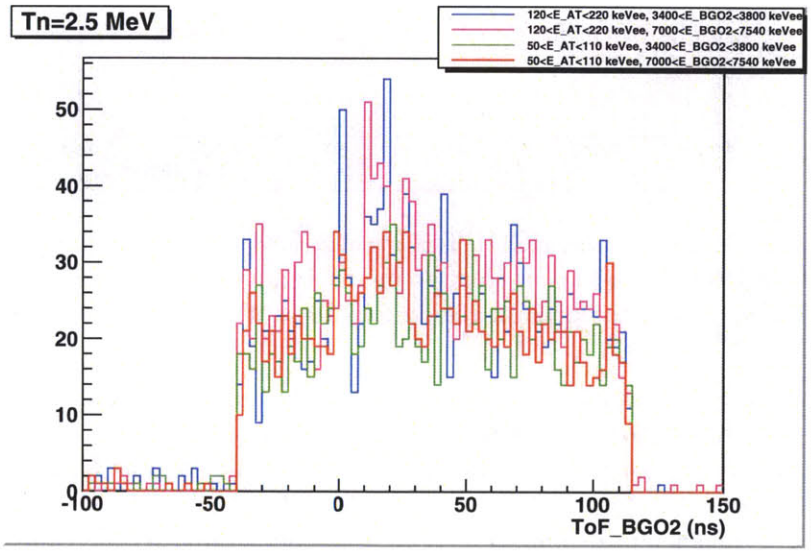

Figure 6-55: Comparison of BGO2 ToF spectra for the capture kinematics (blue) and the background kinematics (red, green, magenta) for $T_n \sim 2.0$ MeV. There is an excess of events in the prompt region for the capture kinematics.

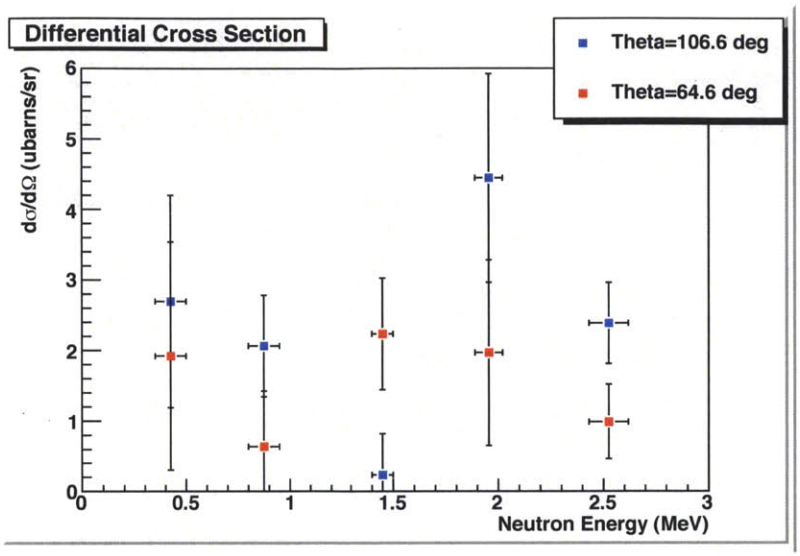

Figure 6-56: Differential cross section for neutron-proton capture at 106.6° and 64.6°.

6.2.6 Results

For each energy and BGO detector, the differential cross section for that angle was calculated by

$$\frac{d\sigma}{d\Omega}(E,\theta) = \frac{N_{det}(E,\theta)}{\Omega_{BGO} \times \eta_{BGO} \times Y_n \times \Omega_{AT} \times \tau_{AT}} \tag{6.3}$$

Where $N_{det}(E,\theta)$ is the yield at that energy and angle, $\Omega_{BGO} = 0.163$ sr is the BGO solid angle, η_{BGO} is the BGO efficiency, Y_n is the neutron beam yield, $\Omega_{AT} = 7.511 \times 10^{-4}$ sr is the active target solid angle, and $\tau_{AT} = 7.782 \times 10^{21}$ p/cm^2 is the active target thickness.

The differential cross sections are shown in figure 6-56. With this limited data set and the small capture cross section, the statistical uncertainty on these points is extremely large, 25% for the 2.3 MeV data point and 58% for the 425 keV data point. With measurements at only two angles, attempting to extract a total cross section by fitting the data by the angular distribution

$$\frac{d\sigma}{d\Omega} = a_0 + a_2 P_2(\cos\theta) \tag{6.4}$$

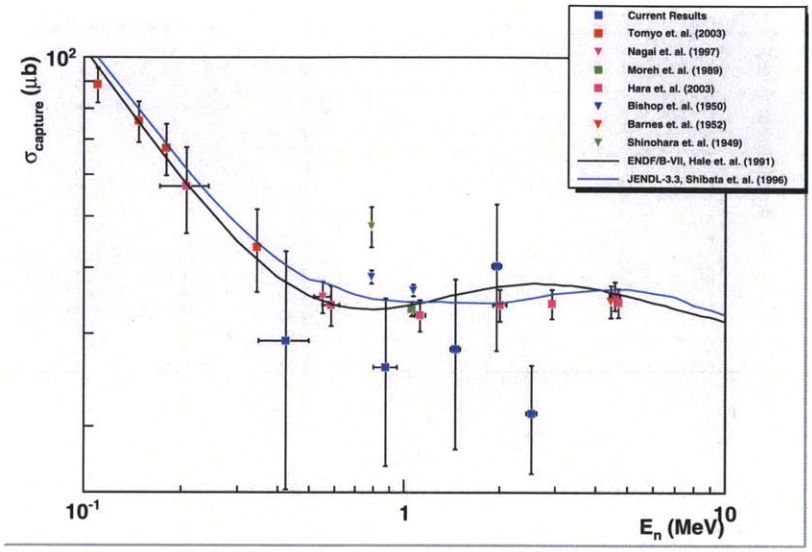

Figure 6-57: Estimate of total cross section obtained by assuming the angular distribution is isotropic. Our results below 2.0 MeV are consistent with existing measurements and theories within the statistical error bars.

yields higher uncertainties and no degrees of freedom.

To make a rough estimate of the total cross section, we assume that the distribution is isotropic and instead take the average of the two angles and multiply by 4π. These total cross sections are shown in figure 6-57 Below 2.0 MeV, our results are consistent with existing measurements within the statistical uncertainty. To obtain a more precise total cross section measurement, additional data at multiple angles will be required.

6.2.7 Signal to Background Ratio

To compare the running conditions of the experiment at LANSCE with the experiment at UKY, we compare the signal to background ratios. Considering events at all energies, the signal to background ratio at UKY was 0.55:1, slightly lower than the 0.66:1 ratio from LANSCE. However, while the signal to background ratio is slightly higher at LANSCE, with the reduced flux necessitated by the presence of the higher energy neutrons at LANSCE, the rate is significantly lower. For a 50 keV bin, the rate at LANSCE was 0.032 ± 0.013 capture events per day, while the rate in the same size bin for a single BGO is 12 ± 4 capture events per day, nearly

three orders of magnitude larger. This is due to the increased neutron flux in the relevant energy range and the increased acceptance and efficiency of the γ-ray detectors at UKY. One BrilLanCe^{TM} detector covers 0.1 sr with 10% efficiency, while two BGO detectors cover 0.32 sr with 70% efficiency. Accordingly, under the current running conditions the UKY will allow a higher precision measurement on a more reasonable time scale.

Chapter 7

Analysis of np Total Cross Section Data

With only a single detector in the absorption configuration, most of the analysis was focused on the reduction and characterization of the backgrounds.

7.1 Determining Cross Sections from Yields

To calculate the cross section from these yields, we consider the transmitted intensity $I(x)$ through a target of thickness x, with proton and carbon densities ρ_p and ρ_c respectively, at a given energy

$$I(x) = I_0 e^{-(\sigma_p \rho_p + \sigma_c \rho_c)x} \tag{7.1}$$

where σ_p and σ_c are the neutron-proton and neutron-carbon total cross sections. Of this transmitted intensity, the neutron detector with efficiency η will detect a yield Y given by

$$Y = I \times \eta \times T \tag{7.2}$$

where T is the dead time corrected measurement time. Substituting equation 7.1 for $I(x)$, we get the yield

$$Y = \eta \times T \times I_0 \times e^{-(\sigma_p \rho_p + \sigma_c \rho_c)x} \tag{7.3}$$

If we take the ratio of the yields with and without the sample in the beam, η divides out, leaving

$$\frac{Y^{\text{in}}}{Y^{\text{out}}} = \frac{(T \times I_0)^{\text{in}}}{(T \times I_0)^{\text{out}}} \times e^{-(\sigma_p \rho_p + \sigma_c \rho_c)x} \tag{7.4}$$

But the beam intensity I_0 for a given energy is proportional to the overall proton beam current, J, so

$$I_0 = \alpha \times J \tag{7.5}$$

where α is an energy dependent parameter, which could be extracted from the $^6\text{Li}(p,n)^7\text{Be}$ cross section and the stopping power of protons in LiF. The proton beam current is measured by a current integrator recorded with a scaler, so Q, the livetime integrated beam current scaler counts, can be written as

$$Q = \beta \times T \times J \tag{7.6}$$

where β is the current integration conversion factor. Using this, we get

$$\frac{Y^{\text{in}}}{Y^{\text{out}}} = \frac{Q^{\text{in}}}{Q^{\text{out}}} \times e^{-(\sigma_p \rho_p + \sigma_c \rho_c)x}. \tag{7.7}$$

The quantities α and β are divided out in this ratio, and the measurement live time T no longer appears.

If we consider a pure carbon target, then $\rho_p = 0$, and we can rearrange the equation to give us the total neutron-carbon cross section

$$\sigma_c = \frac{1}{\tau_c} \ln \frac{(Y/Q)^{\text{out}}}{(Y/Q)^{\text{c}}} \tag{7.8}$$

where $\tau_c \equiv \rho_c x$. For a CH_2 target, we get the result for the proton cross section

$$\sigma_p = \frac{1}{\tau_p} \ln \frac{(Y/Q)^{\text{out}}}{(Y/Q)^{\text{CH}_2}} - \frac{\sigma_c}{2} \tag{7.9}$$

where $\tau_p \equiv \rho_p x$. These results do not require knowledge of the neutron detector efficiency nor the absolute beam flux nor the dead time.

7.1.1 Solid Angle Corrections

The derivations leading to equations 7.8 and 7.9 rely on the assumption that a neutron which is scattered out of the beam will not enter the neutron detector. However, since the neutron detector has finite size, this assumption is not fully valid; the cross sections determined by these equations yield the cross sections integrated over all angles for neutrons which do not enter the detector. For neutrons scattered from carbon, the angular distribution is approximately isotropic in the lab frame. Thus the calculated cross section is given by this approximately constant differential cross section integrated over a solid angle of $\Omega_{scat} = 4\pi - \Omega_{ND}$. This yields a corrected cross section of

$$\sigma_c = \frac{1}{1 - \frac{\Omega_{ND}}{4\pi}} \frac{1}{\tau_c} \ln \frac{(Y/Q)^{\text{out}}}{(Y/Q)^{\text{c}}}. \tag{7.10}$$

For neutrons scattered from protons, the cross section is isotropic in the center of mass frame but not in the lab frame. In this case, the differential cross section is integrated over the solid angle transformed into the center of mass frame. The corrected cross section is then

$$\sigma_p = \frac{1}{1 - \frac{\Omega_{ND,cm}}{4\pi}} \frac{1}{\tau_p} \ln \frac{(Y/Q)^{\text{out}}}{(Y/Q)^{\text{CH}_2}} - \frac{1 - \frac{\Omega_{ND}}{4\pi}}{1 - \frac{\Omega_{ND,cm}}{4\pi}} \frac{\sigma_c}{2} \tag{7.11}$$

7.2 Neutron Energies

We used a thin LiF target, in which 2.25 MeV protons lose approximately 50 keV while passing through, giving us an approximate neutron beam energy spread of 50 keV. With this we were able to measure the backgrounds above and below our target neutron energies. By running with proton energies from 2.00 to 2.55 MeV, we were able to measure cross sections at neutron energies from 150 to 800 keV.

To calibrate the neutron time of flight, we used a sulfur target. With its multiple resonances in our energy range, shown in figure 7-1, we can use the dips in yield and the maximum neutron energy for each proton beam energy to calibrate the absolute time of flight. Neutron energy spectra with a sulfur target for six proton energies are shown in figure 7-2.

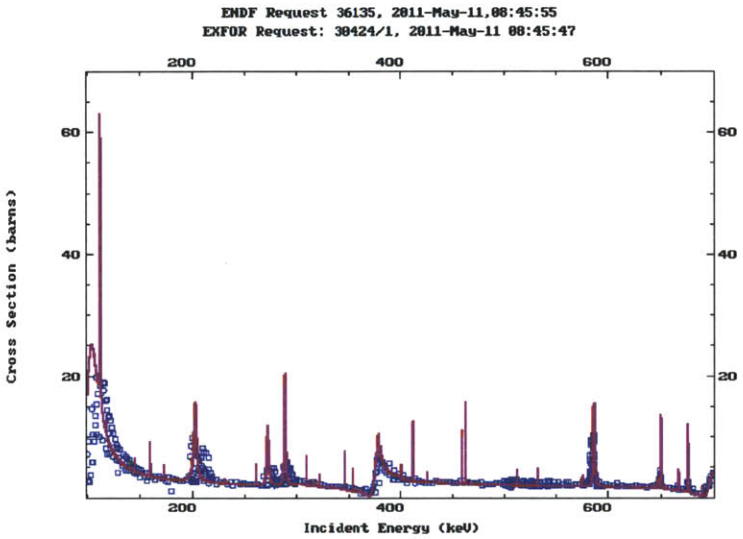

Figure 7-1: Total nS cross section data and theoretical curves. Using the resonances, we can determine a precise absolute neutron energy calibration from time of flight.

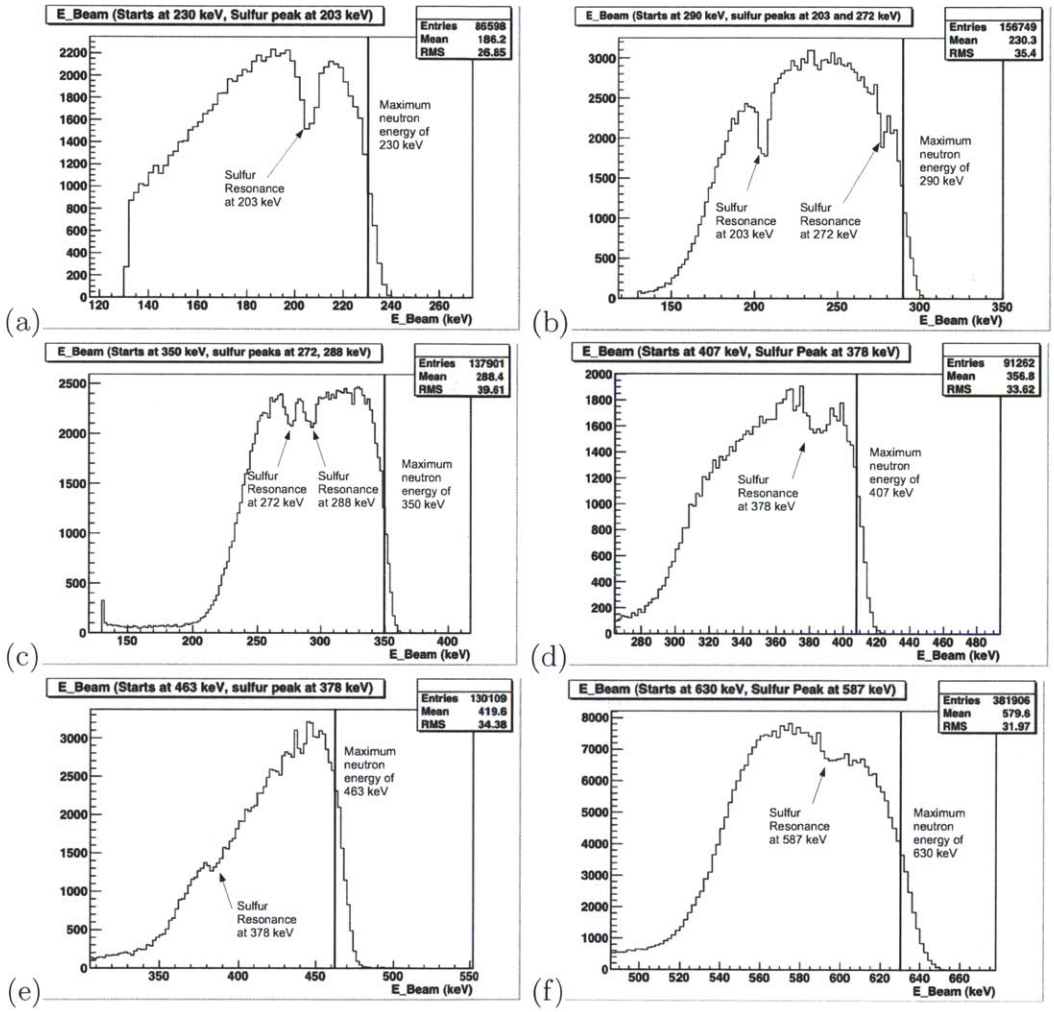

Figure 7-2: Neutron energy spectra with a sulfur target for E_p = (a) 2.00, (b) 2.05, (c) 2.10, (d) 2.15, (e) 2.20, and (f) 2.35 MeV. Sulfur resonances and theoretical neutron energy endpoints are as labeled on each figure.

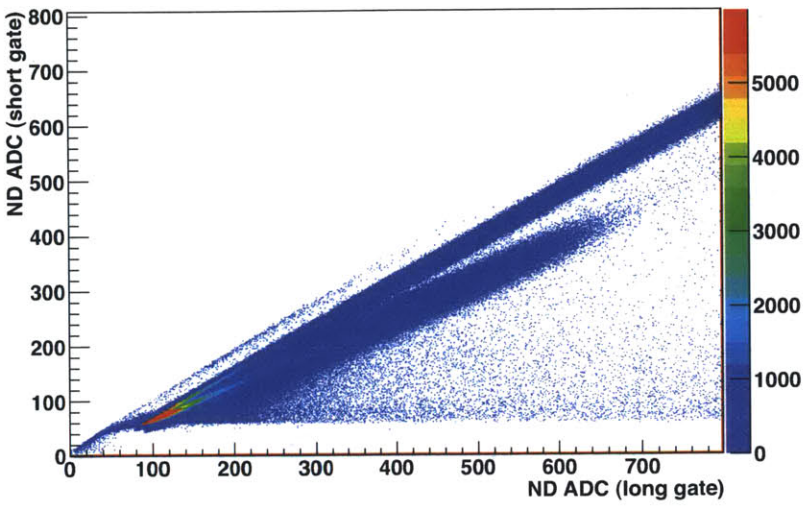

Figure 7-3: Short gate neutron detector ADC versus long gate neutron detector ADC. The upper band is γ-rays, the lower band is neutrons.

7.3 Neutron Detector Response

As with the scintillator response data, we were able to use a long and short ADC gate on the neutron detector to discriminate between neutrons and γ-rays. This plot is shown in figure 7-3. The upper and lower bands in the plot consist of γ-rays and neutrons, respectively. They merge at low pulse heights, where the difference in the long and short portions of the pulse are too small to separate, but if we make a conservative cut, we eliminate all of the higher energy γ-rays.

Cutting on the pulse shape discrimination band from figure 7-3 significantly reduces the background. Figure 7-4 shows the neutron time of flight for the blank target at $E_p = 2.25$ MeV with no conditions (white) and the pulse shape discrimination condition (shaded). When we apply the pulse shape discrimination condition, the background in the region between the γ-flash and the neutron peak is reduced by a factor of three; the neutron spectra are nearly identical.

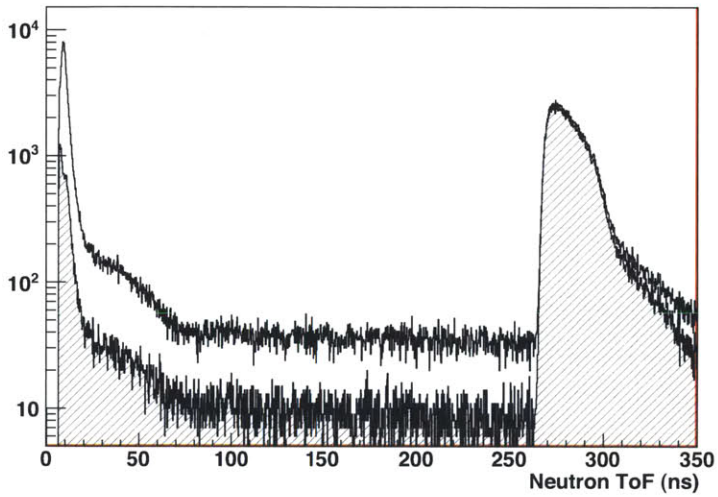

Figure 7-4: Beam TDC stop for the blank target for $E_p = 2.25$ MeV with no conditions (white) and the pulse shape discrimination condition (shaded). The background is reduced by a factor of three, while the neutrons are almost unaffected.

Reference	Year	σ_0 (b)
[61] Melkonian	1949	20.36±0.10
[50] Houk	1971	20.436±0.00023

Reference	Year	a_c (fm)
[62] Koester and Nistler	1971	-3.7400±0.0030
[63] Koester and Nistler	1975	-3.7406±0.000011

Table 7.1: The σ_0 and a_c data used for the fits.

7.4 Results

Our results are shown in figure 7-5. These results include the first order solid angle correction outlined in section 7.1.1 and the systematic uncertainty due to the dead time. The cross sections are calculated in 10 keV bins. Both the np and nC cross sections are consistent with the previous measurements [14–23] and the theoretical tabulations [13, 24].

7.4.1 Experimental Uncertainty

The primary source of systematic uncertainty was due to the uncertainty in the masses and dimensions of the CH_2 and carbon targets are listed in table 3.2. This was a very small, on the order of 0.1 to 0.2%. The systematic and statistical uncertainty is shown for each energy in figure 7-6. The statistical uncertainty is approximately constant in the 0.5 to 1% range, with a few sharp increases to 1.5 and 2.5%. The peaks in statistical uncertainty at 350, 400, 650, 700, and 750 keV are due to the edges of the neutron beam energy distribution giving bins that are only partially filled. The plateau in statistical uncertainty from 450 to 500 is due to fewer data being taken at these energies.

7.4.2 Effective Range Theory

To fit our data by effective range theory, we use several previous measurements of the zero energy elastic cross section σ_0 and the parahydrogen coherent scattering length a_c. The measurements used are shown in table 7.1. Using the equations for effective range theory as described in section 1.2.1, we fit to these measurements and to our total cross section measurements. The parameters from the fit and the previous fit done by Hackenburg [36] are shown in table 7.2. The results of our fit

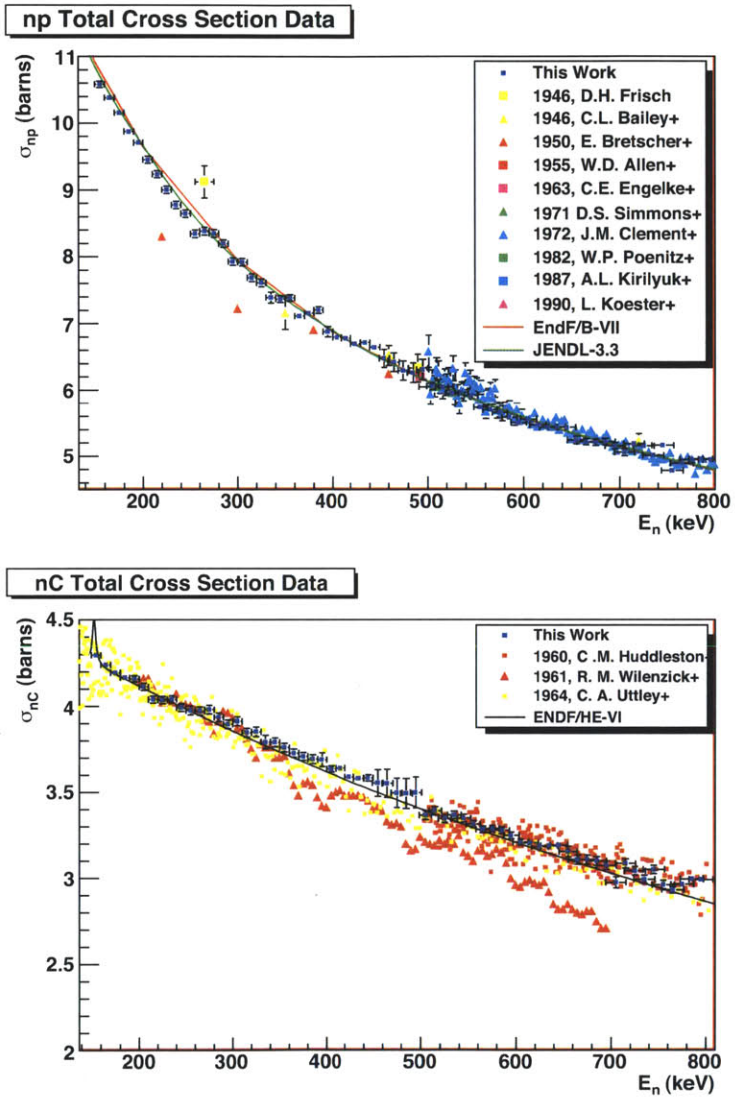

Figure 7-5: Results for np and nC total cross section measurements for neutron energies from 150 to 800 keV, plotted with theoretical tabulations [13, 24, 31] and existing data. [14–23, 32–34] Error bars on the previous carbon data have been suppressed to present a clearer plot.

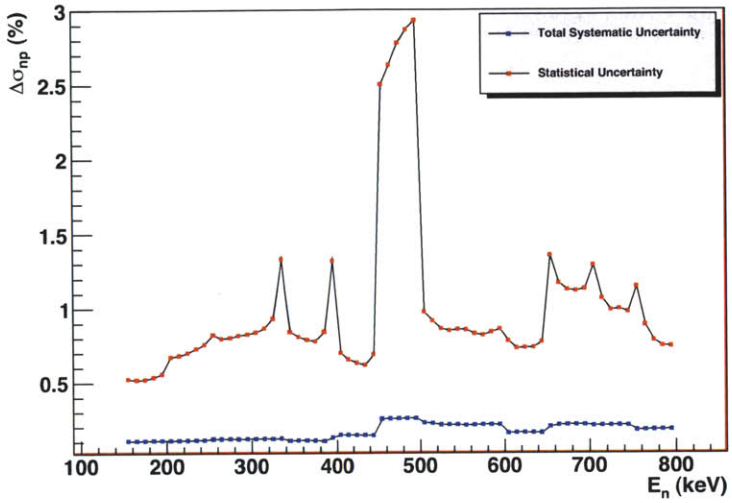

Figure 7-6: Statistical and systematic uncertainty in the measurement of σ_{np} at each energy. The statistical uncertainty is mostly level at 1%. The spikes at 350 and 400 keV are due to energy bins which fall on the edge of the neutron beam distribution receiving fewer counts than the surrounding bins. The plateau in statistical uncertainty between 450 and 500 keV is due to energies where fewer data were taken. The peaks at 650, 700, and 750 keV in statistical uncertainty are due to the narrowing of the neutron beam energy distribution at higher energies.

Parameter	Fit from this work	[36] Fit from Hackenburg
σ_0 (b)	20.43 ± 0.022	20.4278 ± 0.0078
a_c (fm)	-3.7406 ± 0.000011	-3.7406 ± 0.0010
r_{s0} (fm)	2.8 ± 0.12	$2.750 \pm 0.018_{\text{stat}} - 0.059_{\text{syst}}$
a_t (fm)	5.411 ± 0.0041	5.4112 ± 0.0015
a_s (fm)	-23.72 ± 0.012	-23.7148 ± 0.0043
$\rho_t(0, -\epsilon_t)$ (fm)	1.743 ± 0.0052	1.7437 ± 0.0019
χ^2_ν	4.07282	0.749
ν	66	817

Table 7.2: Parameters from the effective range theory fit to our present results and from the fit by Hackenberg [36], and quantities derived from these parameters. $\chi^2_\nu \equiv \chi^2/\nu$, with ν the degrees of freedom.

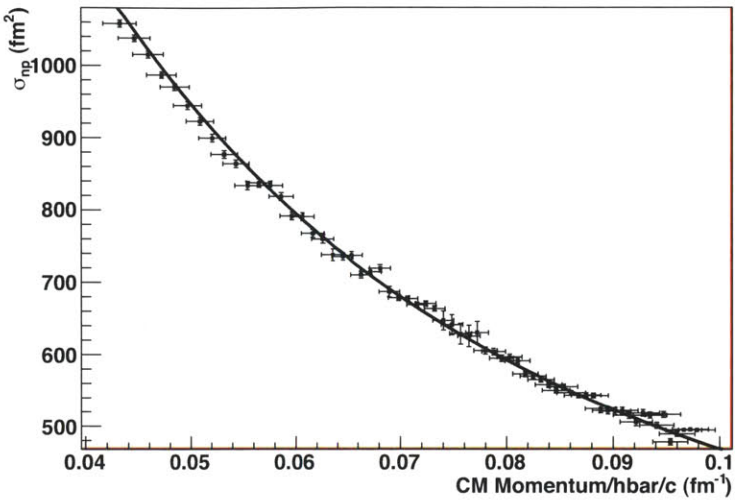

Figure 7-7: NP total scattering cross section with fit from effective range theory.

are in good agreement with the results obtained by Hackenburg. Our fit is shown with the data in figure 7-7.

Chapter 8

Summary and Future Work

8.1 Radiative Capture

We have demonstrated that it is possible to detect recoiling deuterons in plastic scintillator and therefore feasible to use an active target to reduce the backgrounds in an *np* radiative capture measurement at energies relevant to Big Bang nucleosynthesis. We will be able to build on the low statistics results of the feasibility studies in order to obtain precise measurements of the *np* radiative capture cross section below 1 MeV.

Of the two results, currently the UKY result is the only one which has enough events to produce an actual cross section measurement. While the LANSCE results are consistent with currently measured cross sections, with only 24 events spread from 1 to 5 MeV, we cannot directly calculate cross sections. Because of the flux of high-energy neutrons produced at LANSCE, we were forced to run with a very limited flux. The shutter opening was approximately 20% of the full shutter aperture. Without this limited shutter opening or with additional collimation and shielding, the active target was overwhelmed by the pulses from the higher energy neutrons. Currently, the signal to background ratio for each experiment is approximately the same, at 1:2.

With the much higher efficiency of the BGOs, the rate at UKY is significantly higher. Assuming that the backgrounds and signals will scale identically with time, we currently estimate that in order to reduce the statistical uncertainty for the total capture cross section to below 5% for 425 keV, we would need to repeat the experiment using two active targets and four BGO detectors and run continuously for 30 days at 400-450 keV. The additional detectors would also provide more information about the angular distribution of the capture γ-rays and determine

the a_0 and a_2 coefficients in addition to the total cross section. Using a thicker LiF target would allow us to take data for a larger range of energies; however this comes with the risk of increased backgrounds caused by higher accidental coincidences.

With the rate at LANSCE using the BrilLanCe detector and the current neutron flux, it would be a practical impossibility to reach 5% statistical uncertainty in a 50 keV bin between 1 and 5 MeV. However, if the BGOs could be used at LANSCE, we would expect the rate to increase by a factor of ≈ 7. Running under the hypothetical conditions proposed to reach 5% statistical error at UKY, two active targets and four BGOs for one month, running at LANSCE would give approximately 20% statistical error in each 50 keV bin, and would require two years of continuous running to reach 5%. As we are unlikely to receive two years of 3.6 μs beam spacing at LANSCE, we would need to find a way to prevent the active target from being overwhelmed by the high energy neutrons, allowing us to use a much larger shutter opening and flux.

One proposed method for eliminating high energy neutrons is to use a spallation target partially surrounded by a moderator. The low energy flight paths would then collimate neutrons from the moderator and not directly from the target, decreasing the high energy flux. Additionally, the possibility of gating off the first dynode of the photomultiplier tube when the high energy neutrons are present has been investigated. With the current timing structure, driving the capacitive load of the photomultiplier dynode change is problematical.

WNR has recently proposed a new method of operation where multiple proton pulses would be stacked in a proton storage ring and then delivered to the spallation target. This would maintain the average current, but instead of 1.8 or 3.6 microsecond spacing, there would be 10s of microseconds between micropulses. With this beam time structure, the capture experiment could be run on a much longer flight path and still reach the full range of neutron energies of interest. A longer flight path could potentially increase the signal to background ratio, and the longer spaced timing structure could make the proposed gating of the photomultiplier tube an easier task.

8.2 Scintillator Response

We were able to measure the response of BC418 to protons from 100 keV up to 3.6 MeV. The response in very low energy regions below 1 MeV has not been measured for protons. The results from LANSCE and UKY are in fairly good agreement, which is reassuring considering they were performed with the same

active target. However, the second derivatives are in opposite directions where the two measurements overlap, and the inflection points seem to coincide.

This may be caused by a saturation offset. If the results from group 24, to which all the other data are gain matched, were already saturated, then there would be an overall flattening of the LANSCE results. If we were to normalize the LANSCE results to the low energy UKY results, it would indicate that the saturation in the phototube is happening at a much lower proton energy, with saturation beginning as low as 700 keV.

Even with the possible saturation, the two parameter fit to the combined UKY and LANSCE results shows scintillation efficiency and quenching parameters consistent with the electron calibration data and the fit for NE-102 [26, 28]. Studies of the phototube saturation conducted at UKY have shown that saturation begins at approximately 200 keVee at the voltage setting used for this experiment, which is consistent with the unsaturated range seen in the data,.

8.3 Total Cross Section Measurement

Our measurement of the $n-p$ total scattering cross section has filled in a large gap in the total cross section data below neutron energies of 500 keV. The resulting cross sections are in good agreement with the previous measurements and theory, and the effective range theory fit to our data produces parameters consistent with previous fits including data up to 3 MeV.

Additional measurements are planned at the University of Kentucky. Hongwei Yang has been working on a simulation of the experiment in order to design improved collimation and shielding for the neutron beam. We intend to extend the energy range up to approximately 2 MeV and to attempt to extend it down to 100 keV.

The experiments reported on in this thesis have made a start in obtaining improved data for the np total scattering and radiative capture cross sections at low energies. Higher precision measurements for both total scattering and radiative capture are needed for low energy NN potential and Big Bang Nucleosynthesis models, and we plan to take additional data for both processes in the future.

Appendix A

Fitting to Recoil Band Projections

In the following set of figures, Gaussian fits to projections of the recoil proton bands in the scintillator response data are shown. When the peaks show significant asymmetry, the fit was performed for the larger peak. For the UKY data, the projection spacings are based on the maximum uncertainty in the recoil energy. For the LANSCE data, the projections are spaced at 50 keV intervals.

The complete description of the results of these fits is contained in sections 5.1.2 and 5.2.3.

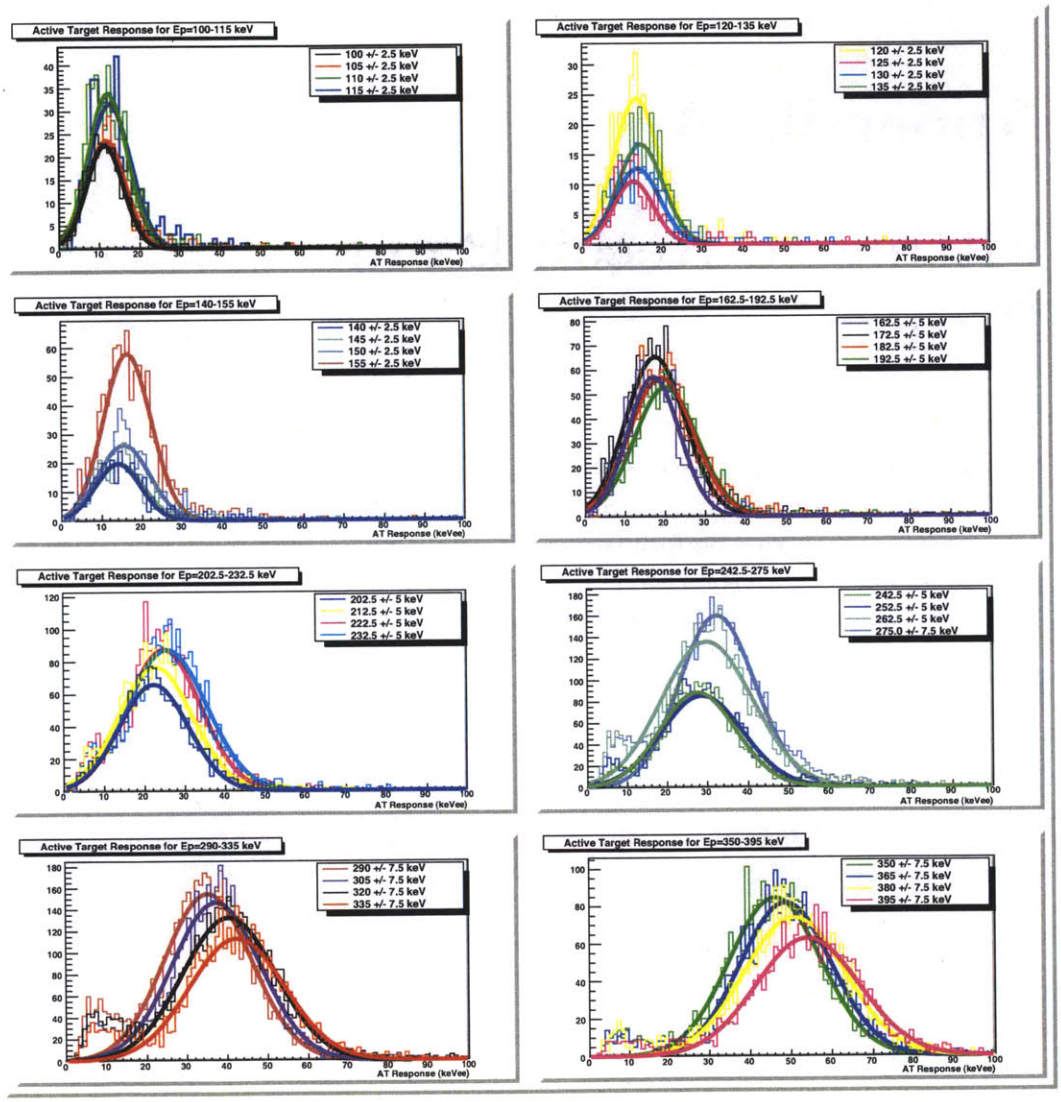

Figure A-1: Fitted slices for the UKY light response measurement for E_p = 100 to 395 keV.

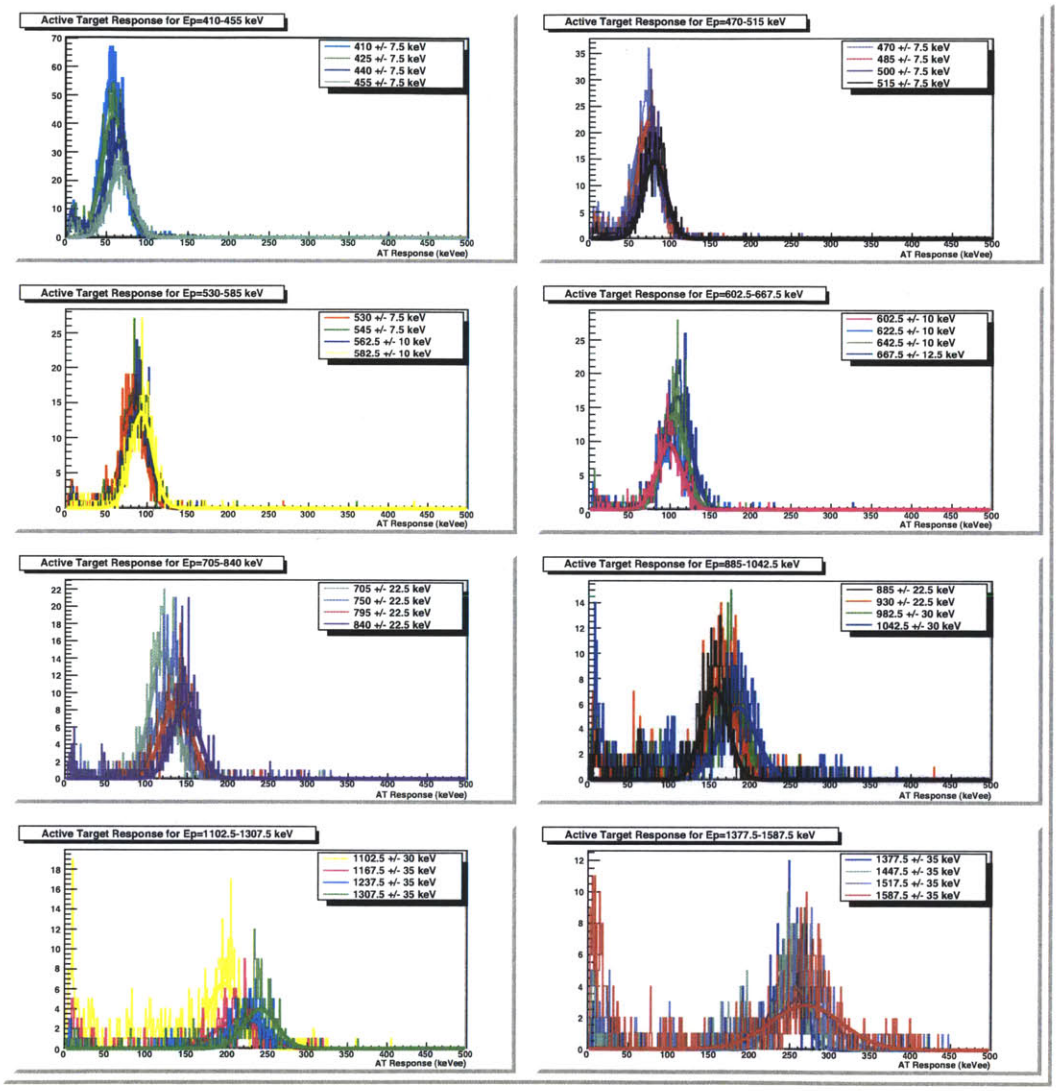

Figure A-2: Fitted slices for the UKY light response measurement for E_p = 410 to 1587.5 keV.

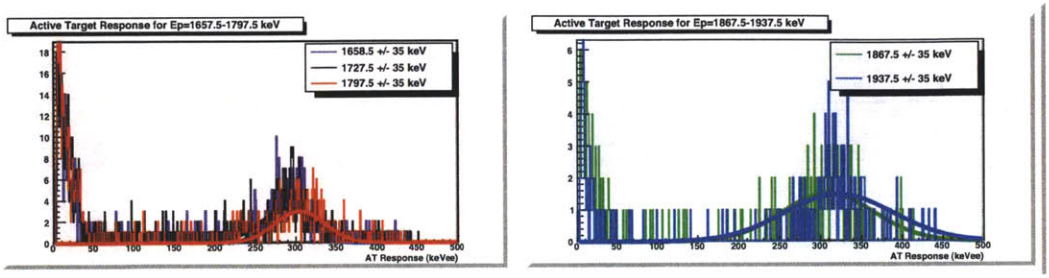

Figure A-3: Fitted slices for the UKY light response measurement for $E_p = 1657.5$ to 1937.5 keV.

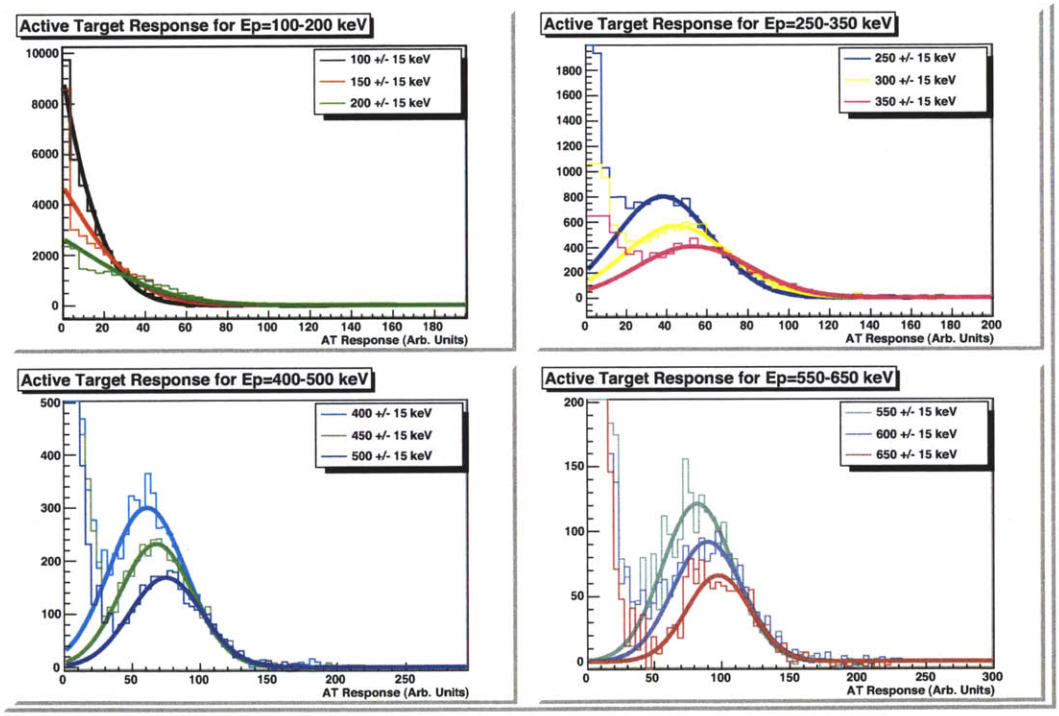

Figure A-4: Fitting the mean active target response for Group 24 in the LANSCE scintillator response measurement for $E_p = 100$ keV to 650 keV. Below 250 keV the recoil peak cannot be distinguished from the low pulse height noise.

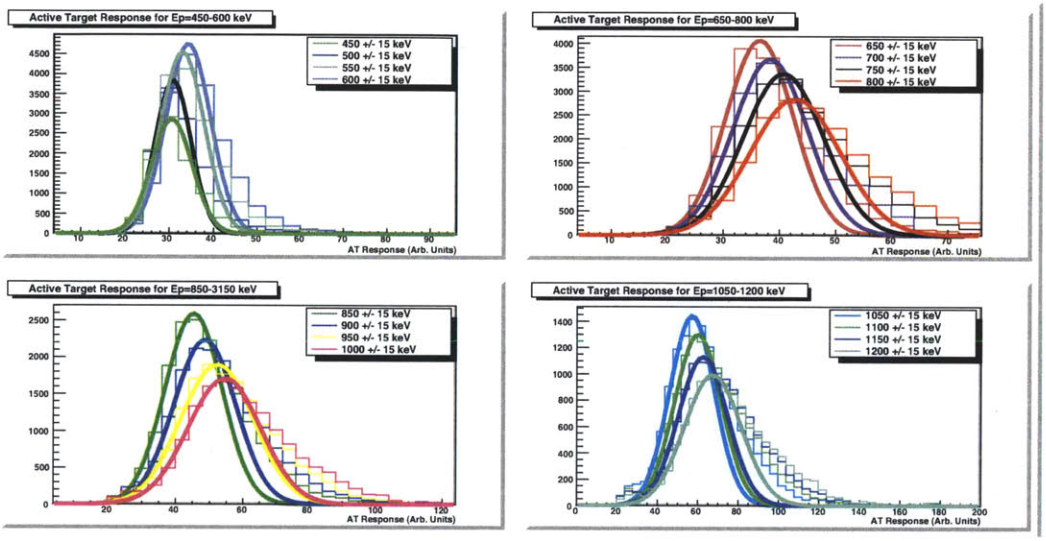

Figure A-5: Fitting the mean active target response for Group 26 in the LANSCE scintillator response measurement for E_p = 450 to 1200 keV. The upper edge of the distribution has a much longer tail than the lower edge.

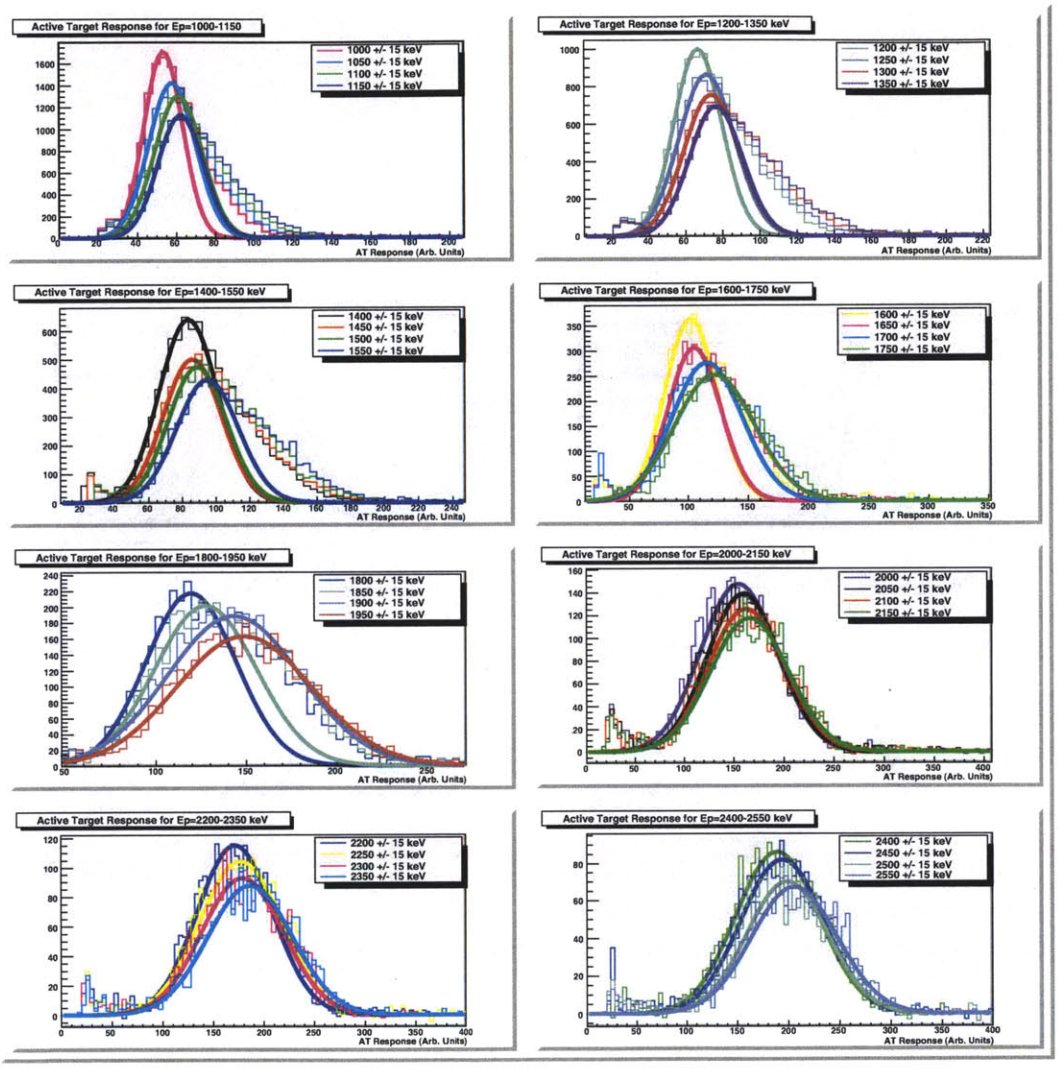

Figure A-6: Fitting the mean active target response for Group 26 in the LANSCE scintillator response measurement for E_p = 1000 to 2550 keV. At approximately 1900 keV, the mean of the distribution shifts dramatically higher, and the peaks no longer show the long tail.

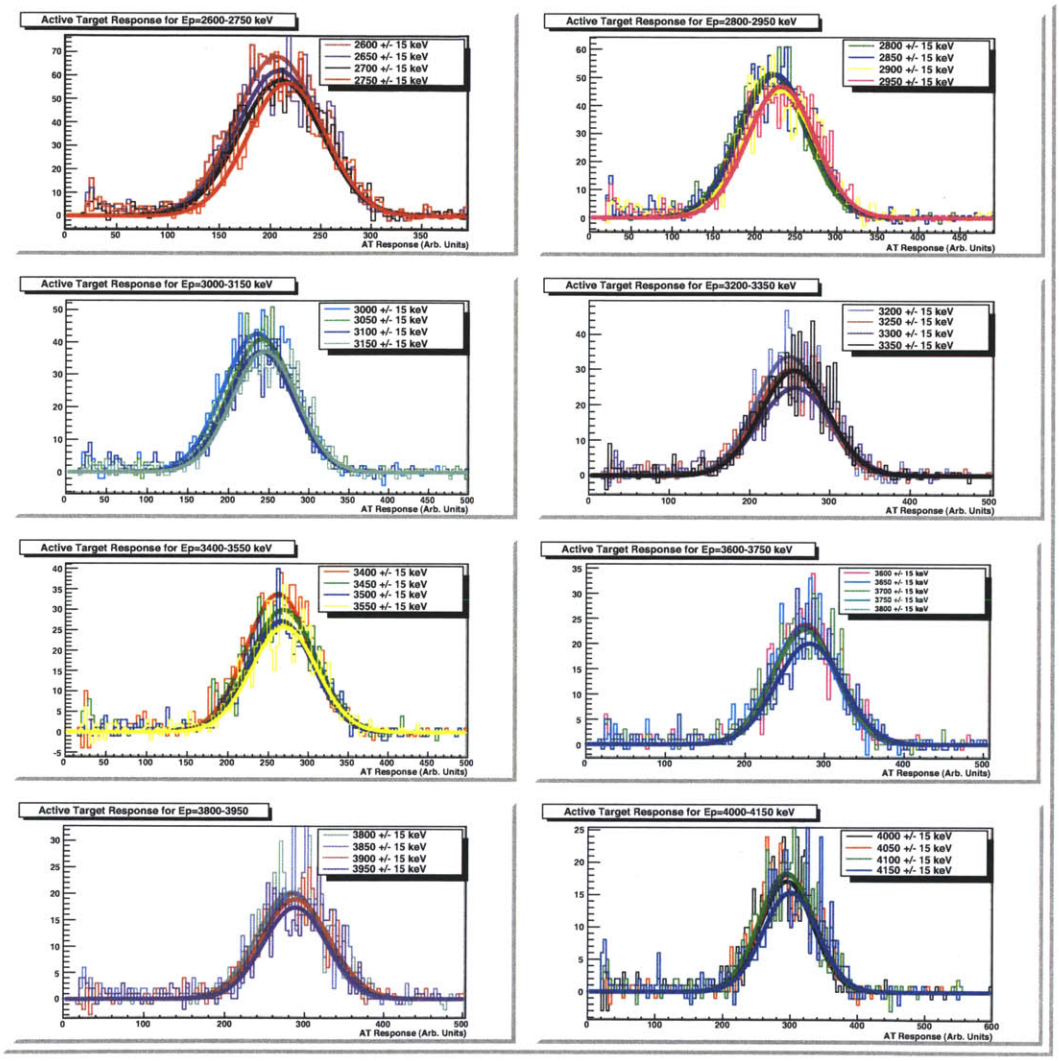

Figure A-7: Fitting the mean active target response for Group 26 in the LANSCE scintillator response measurement for E_p = 2600 to 4150 keV. The means are shifting much less dramatically than at lower energies.

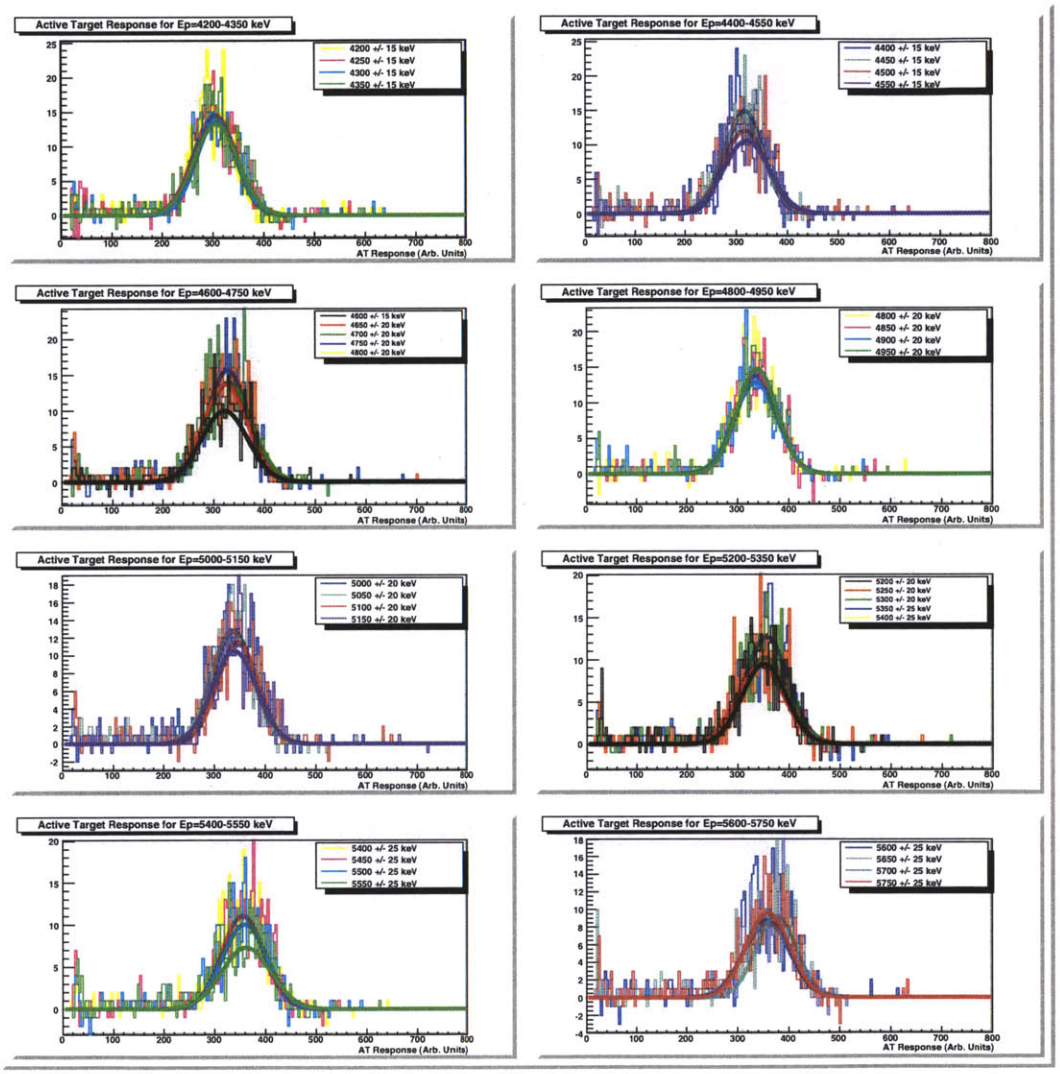

Figure A-8: Fitting the mean active target response for Group 26 in the LANSCE scintillator response measurement for $E_p = 4200$ to 5750 keV. The mean values of the fits are not shifting significantly across all energies in this range.

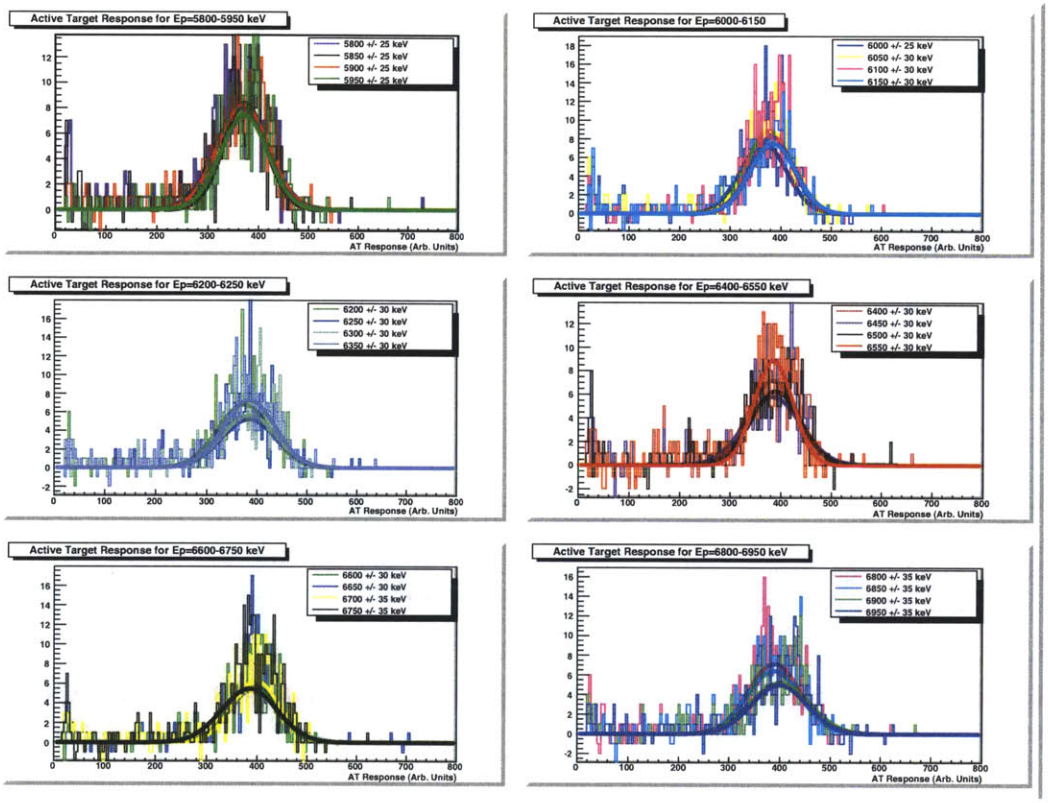

Figure A-9: Fitting the mean active target response for Group 26 in the LANSCE scintillator response measurement for $E_p = 5800$ to 6950 keV. The mean values of the fits are not shifting significantly across all energies in this range.

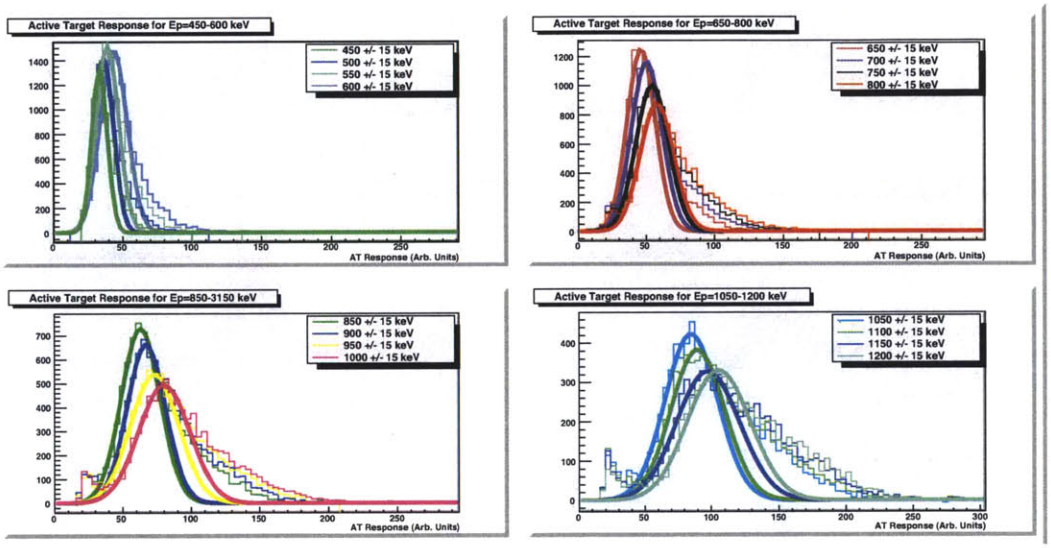

Figure A-10: Fitting the mean active target response for Group 28 in the LANSCE scintillator response measurement for E_p = 450 to 1200 keV. The peaks show significant asymmetry on the upper edge, with a much longer tail than the lower edge.

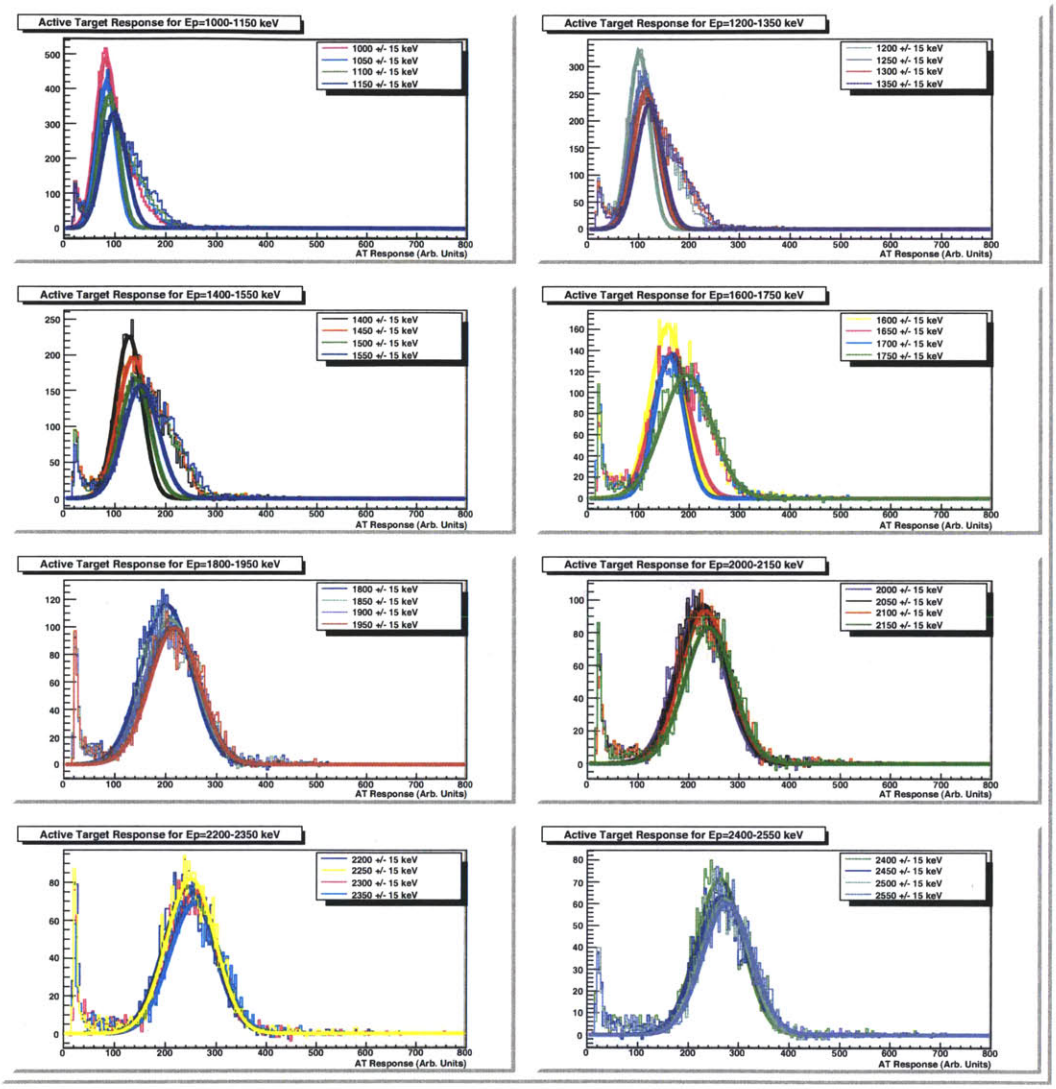

Figure A-11: Fitting the mean active target response for Group 28 in the LANSCE scintillator response measurement for $E_p = 1000$ to 2550 keV. The asymmetry ends at approximately 1750 keV, where the mean shifts to higher pulse height.

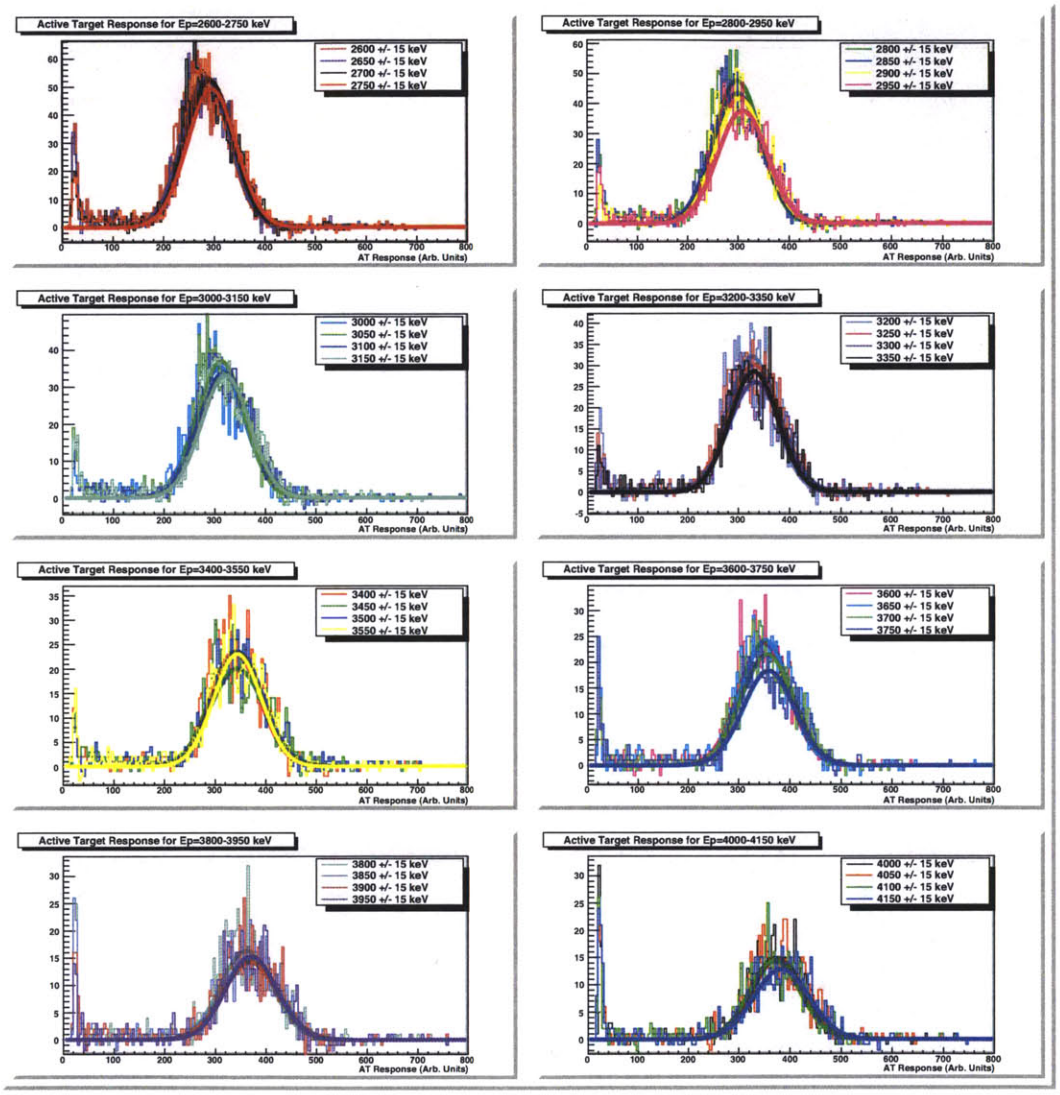

Figure A-12: Fitting the mean active target response for Group 28 in the LANSCE scintillator response measurement for E_p = 2600 to 4150 keV. The change in the mean value of the fitted distribution is much less than at the lower energies.

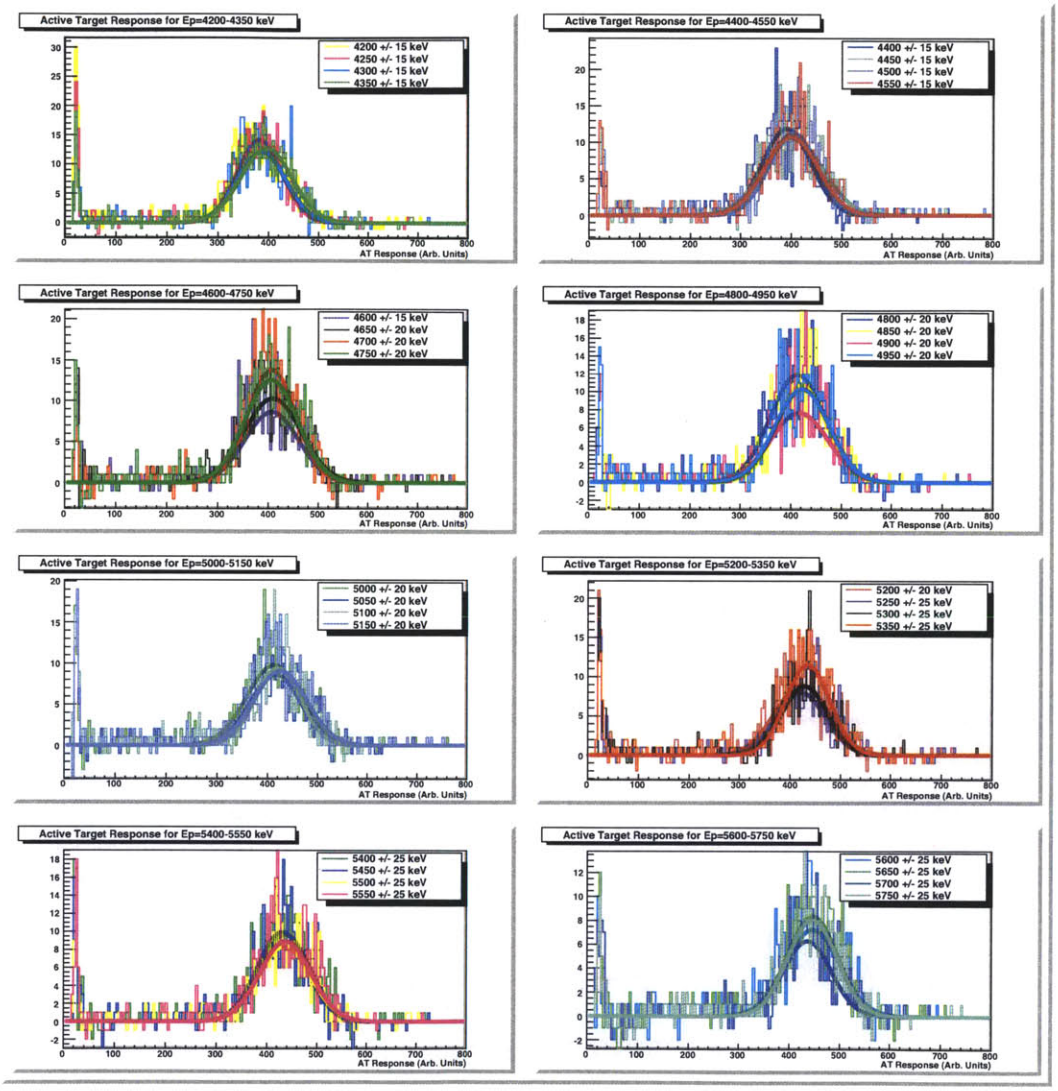

Figure A-13: Fitting the mean active target response for Group 28 in the LANSCE scintillator response measurement for $E_p = 4200$ to 5750 keV. There is almost no change in the mean value in this energy range.

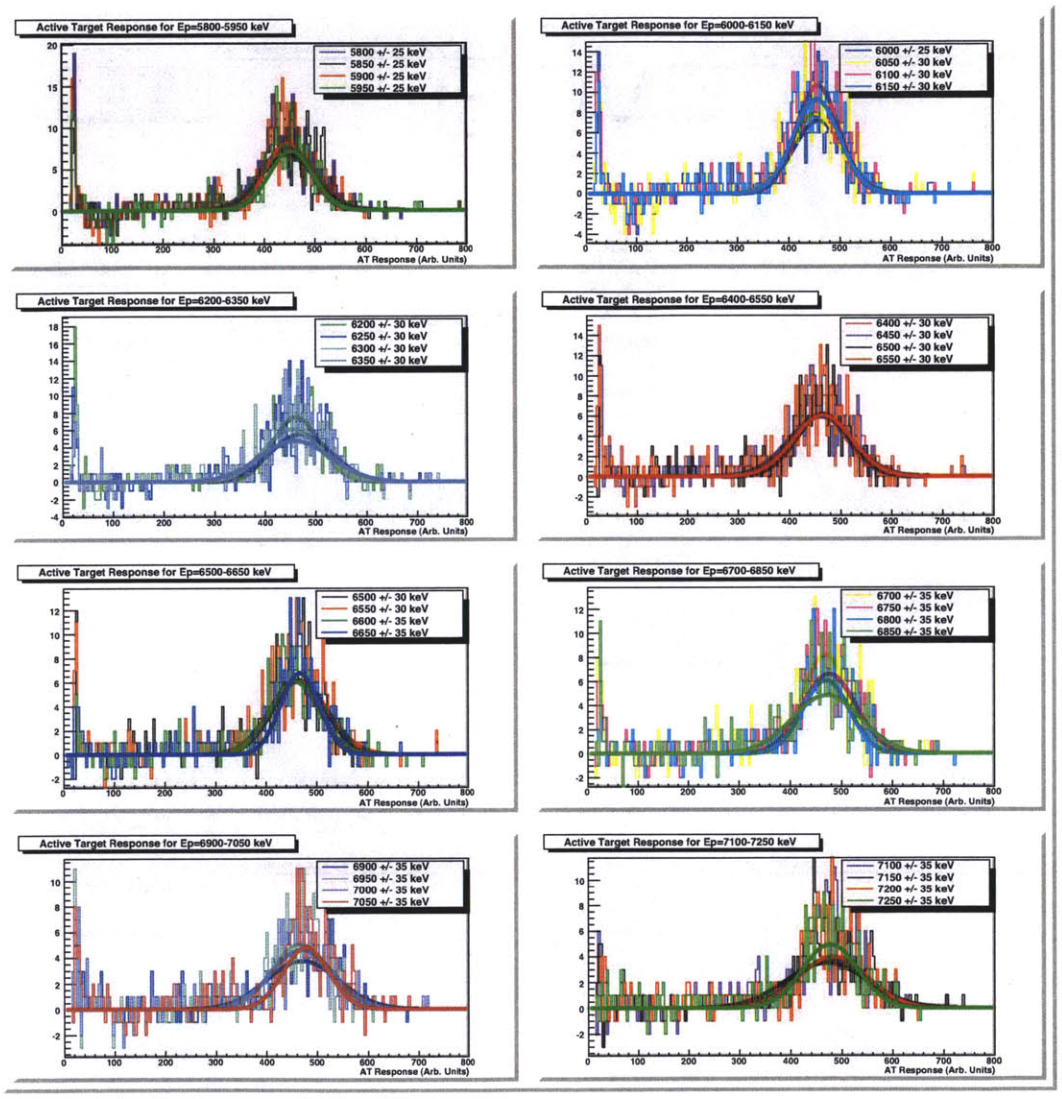

Figure A-14: Fitting the mean active target response for Group 28 in the LANSCE scintillator response measurement for E_p = 5800 to 7250 keV. There are very limited statistics in this range, and the mean of the distribution does not shift as the energy changes.

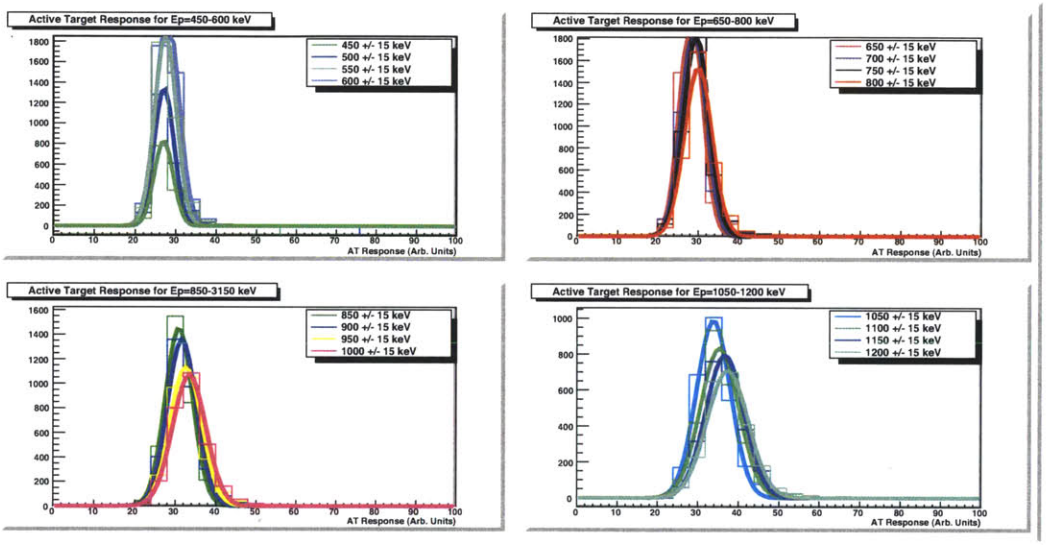

Figure A-15: Fitting the mean active target response for Group 29 in the LANSCE scintillator response measurement for $E_p = 450$ to 1200 keV. These peaks do not show the same asymmetry as the higher gain groups.

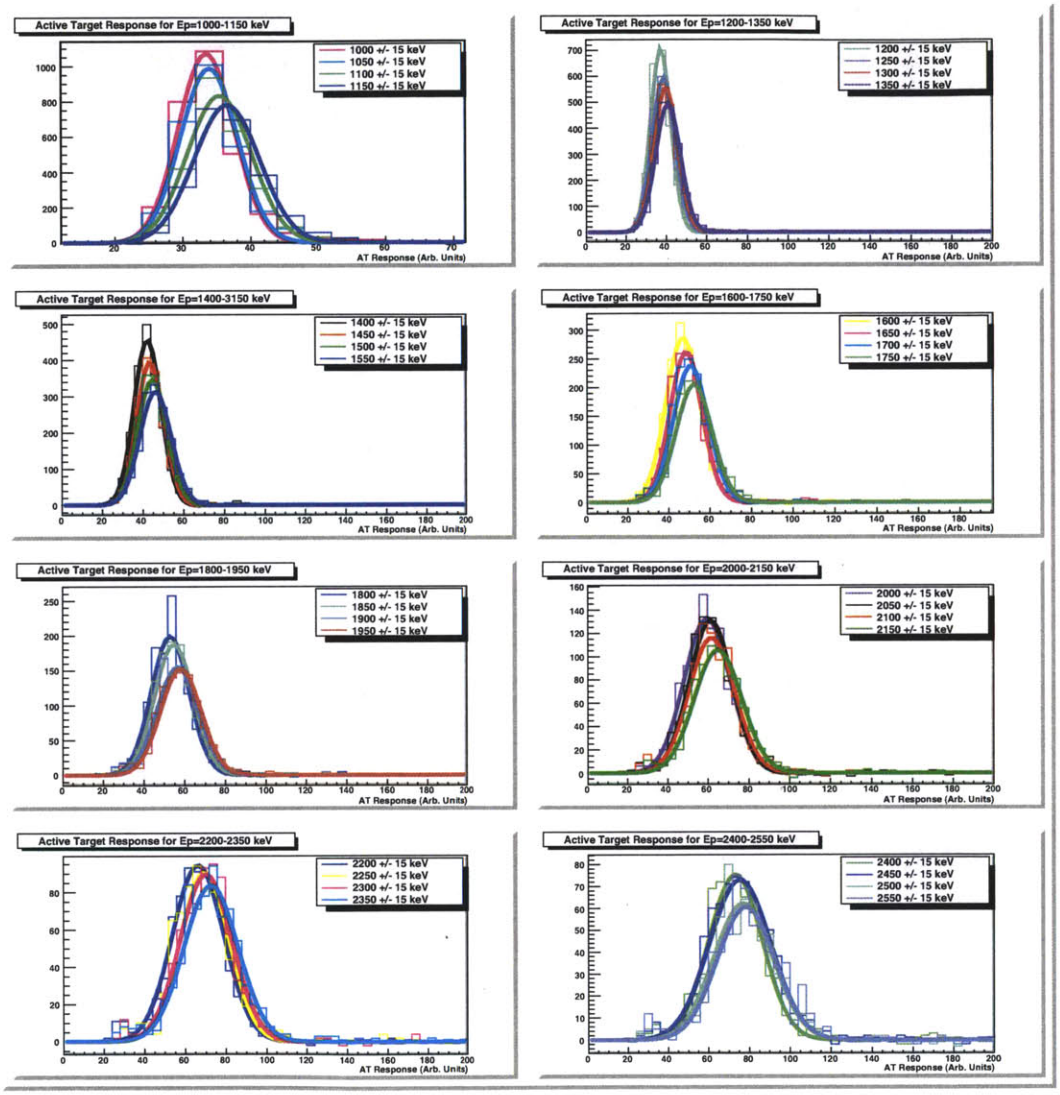

Figure A-16: Fitting the mean active target response for Group 29 in the LANSCE scintillator response measurement for $E_p = 1000$ to 2550 keV.

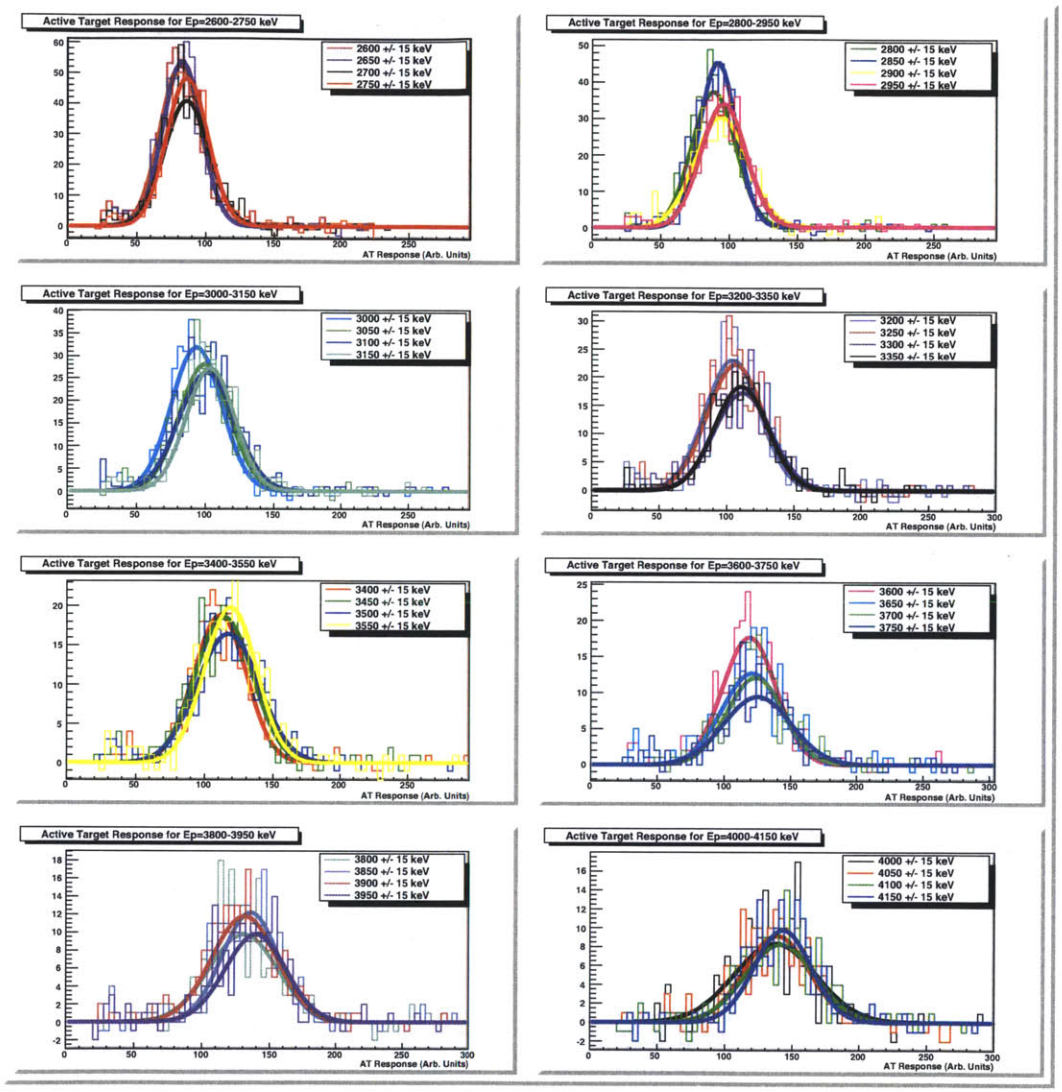

Figure A-17: Fitting the mean active target response for Group 29 in the LANSCE scintillator response measurement for $E_p = 2600$ to 4150 keV.

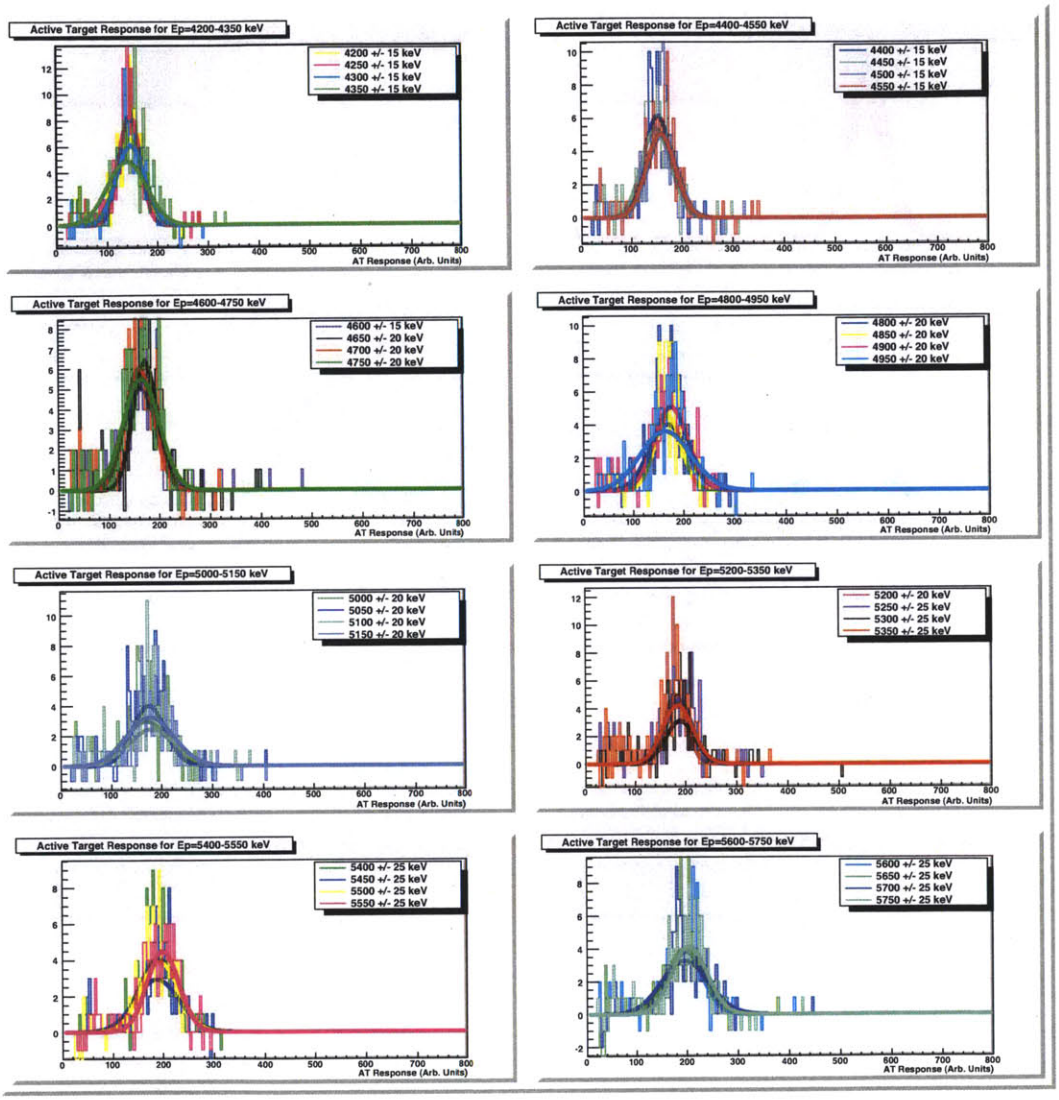

Figure A-18: Fitting the mean active target response for Group 29 in the LANSCE scintillator response measurement for $E_p = 4200$ to 5750 keV.

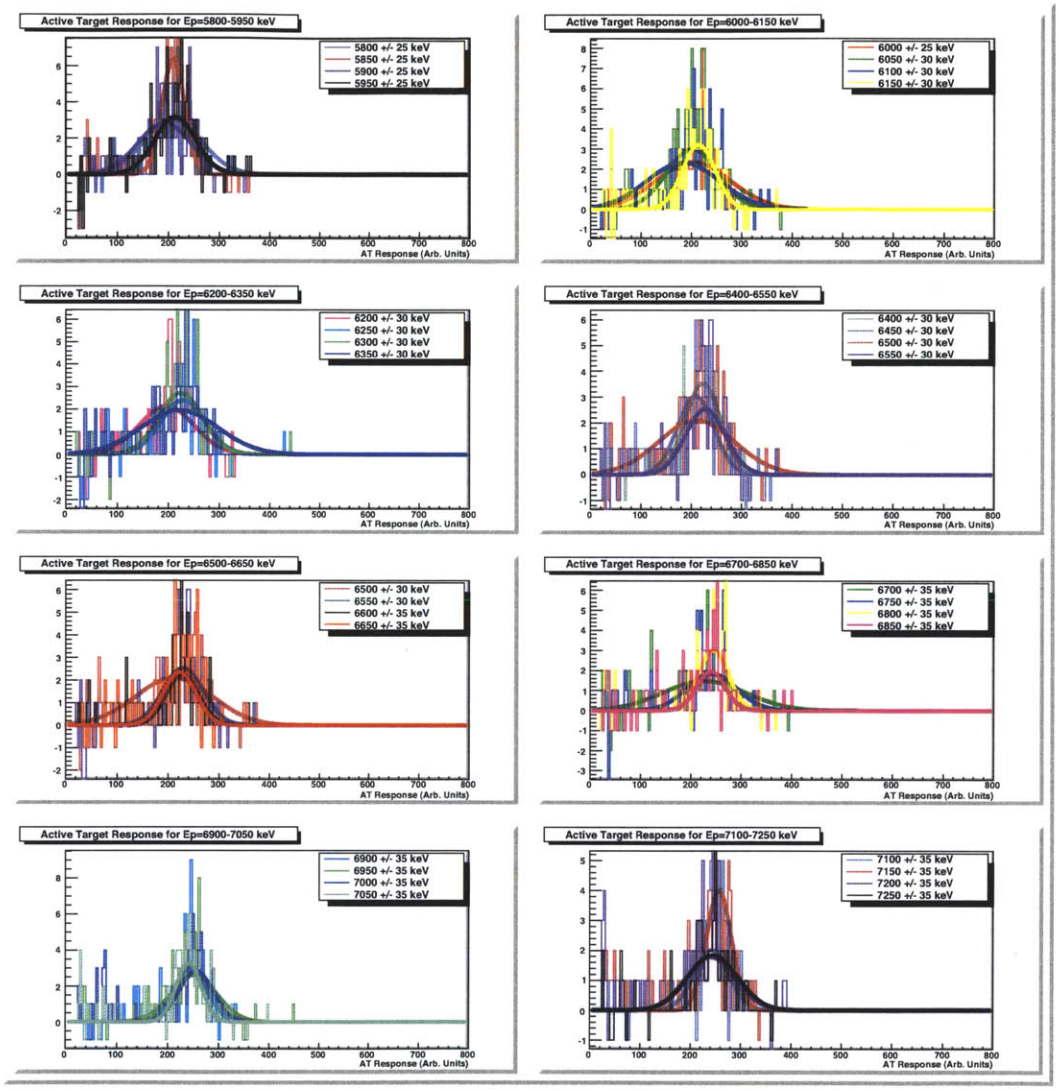

Figure A-19: Fitting the mean active target response for Group 29 in the LANSCE scintillator response measurement for $E_p = 5800$ to 7250 keV.

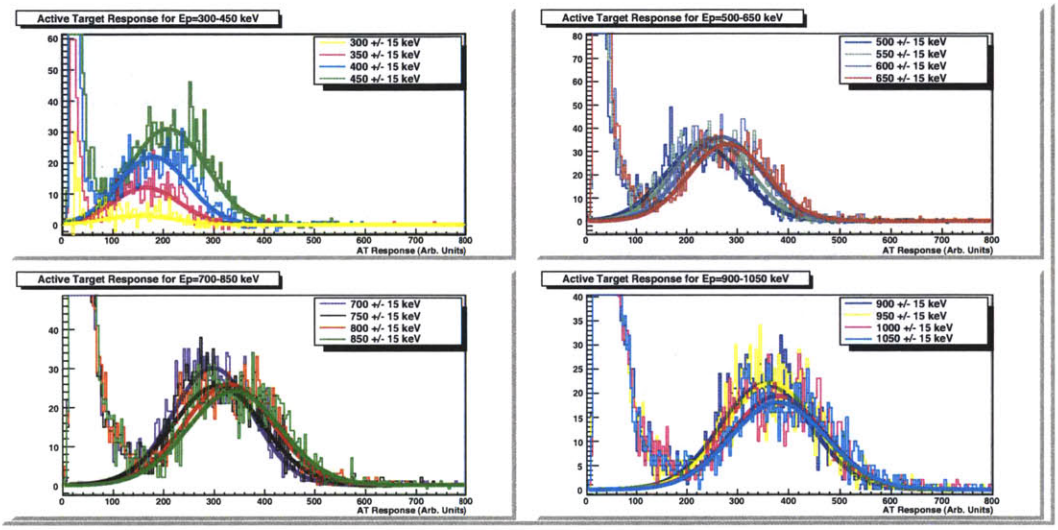

Figure A-20: Fitting the mean active target response for Group 30 in the LANSCE scintillator response measurement for $E_p = 300$ to 1050 keV. With the higher gain, we are able to see to lower energies.

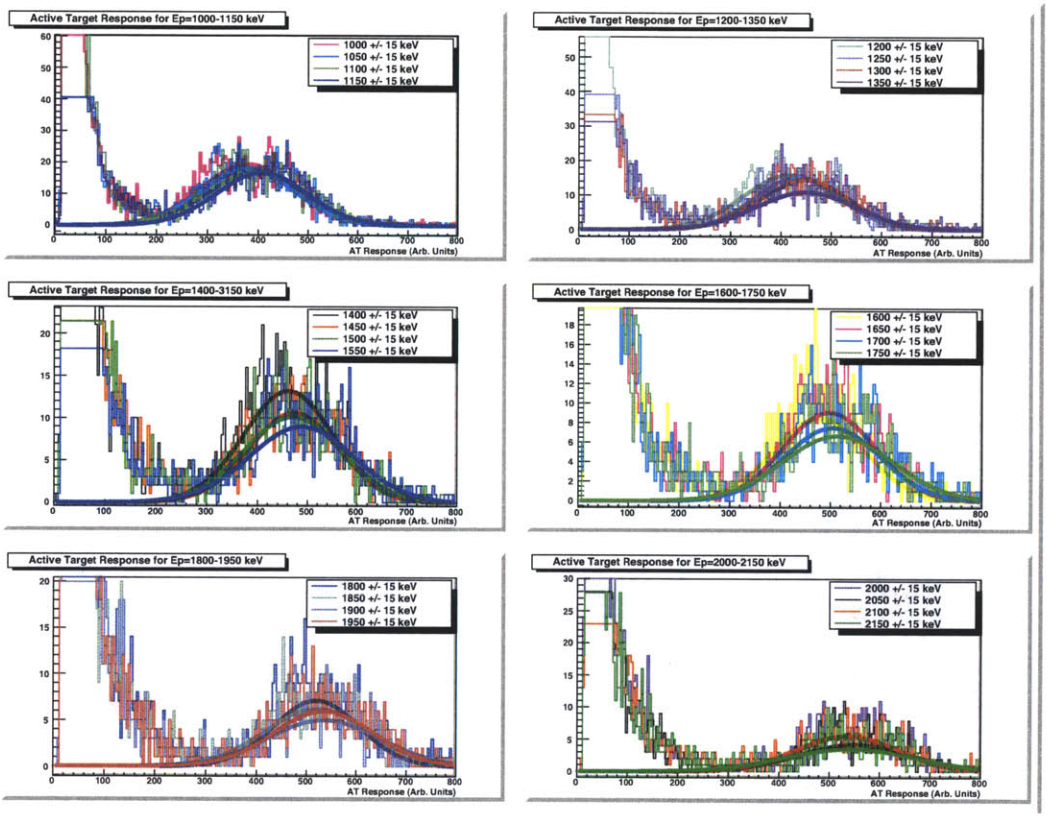

Figure A-21: Fitting the mean active target response for Group 30 in the LANSCE scintillator response measurement for E_p = 1000 to 2150 keV. There is no asymmetry in this group as was seen in the lower gain groups.

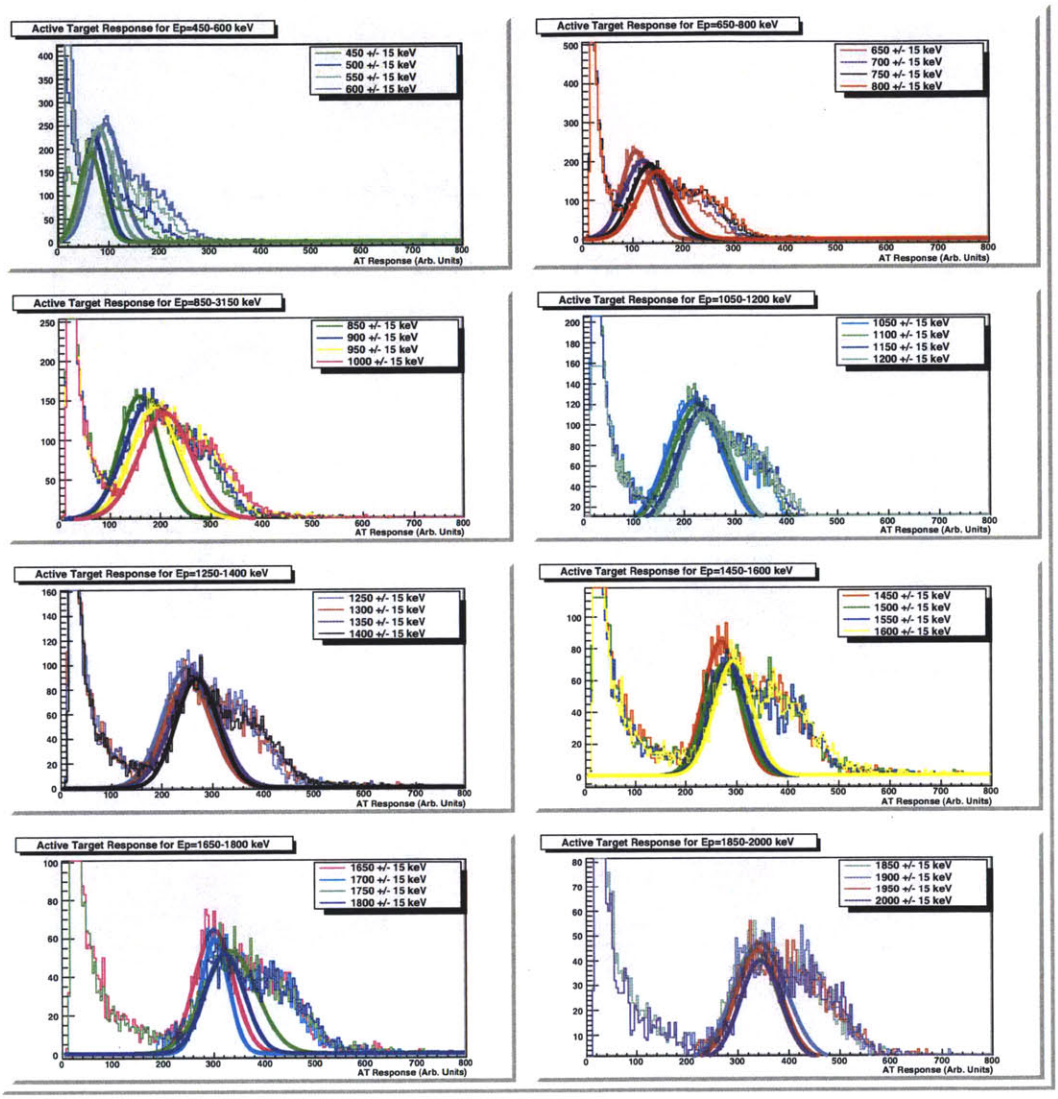

Figure A-22: Fitting the mean active target response for Group 31 in the LANSCE scintillator response measurement for E_p = 450 to 2000 keV. These peaks show significant asymmetry, with a much longer tail on the upper edge which forms a second peak at some energies.

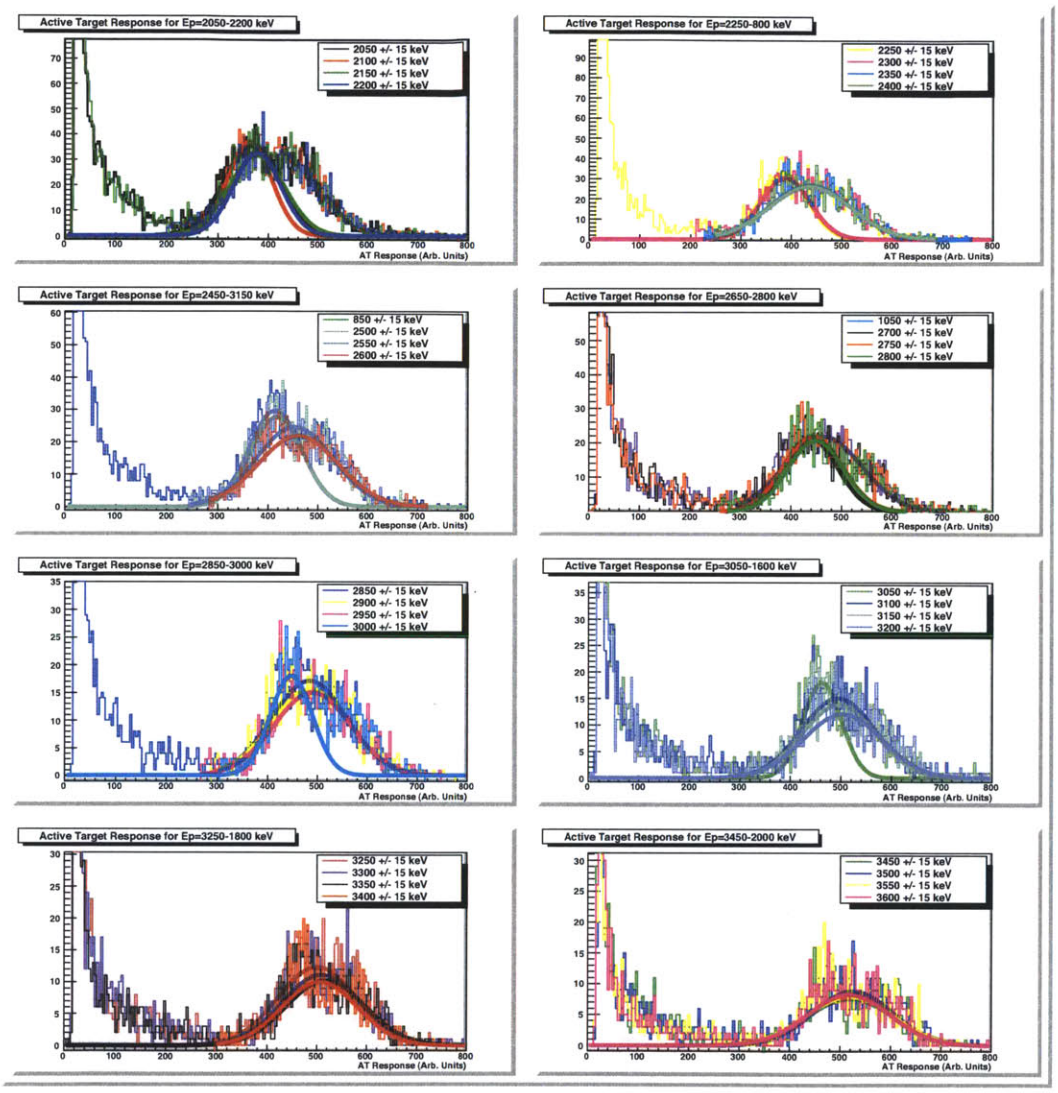

Figure A-23: Fitting the mean active target response for Group 31 in the LANSCE scintillator response measurement for $E_p = 2050$ to 3600 keV. The "second peak" forming in the shoulder becomes more prominent as we move to higher energies, until the distribution begins to fit across a broad, symmetric peak.

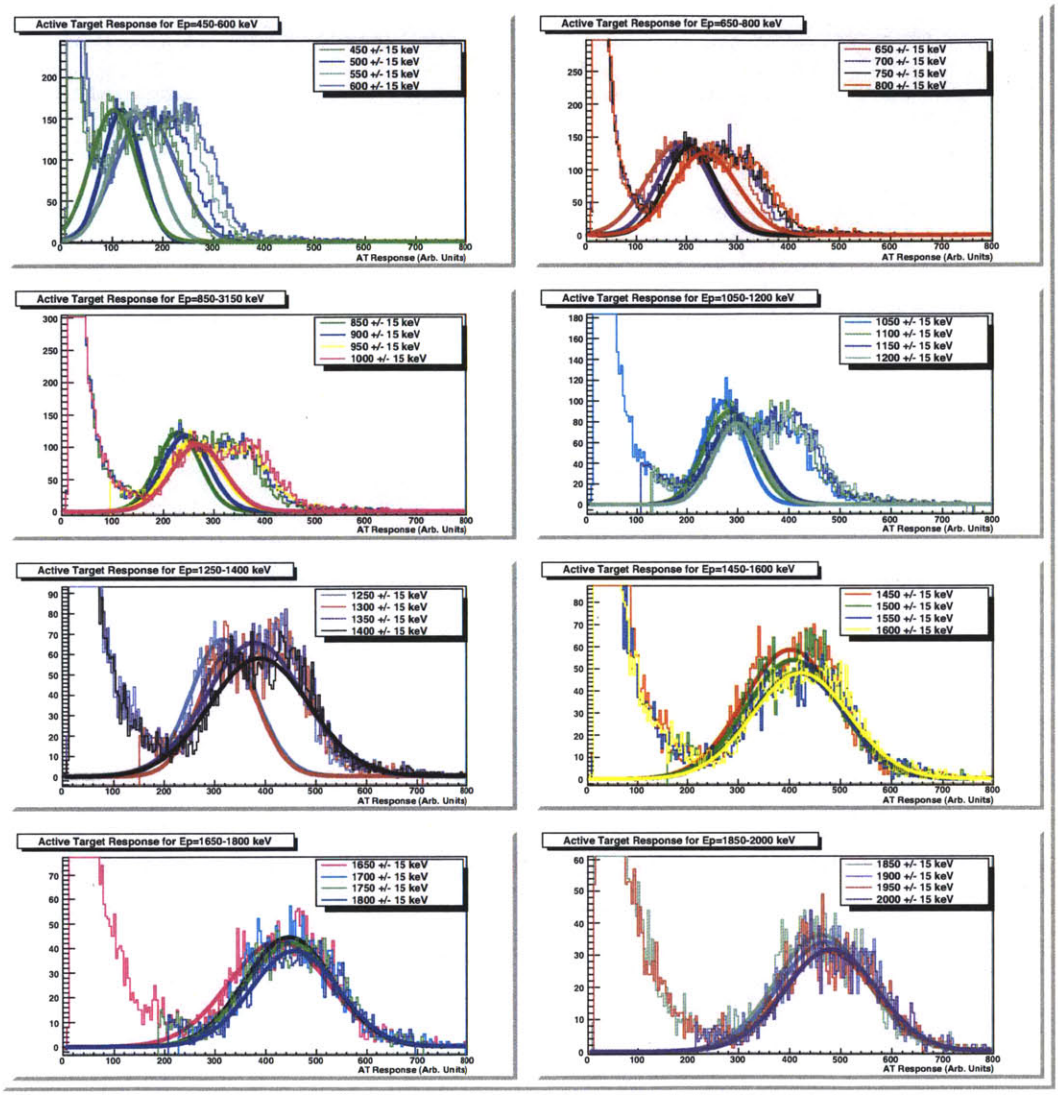

Figure A-24: Fitting the mean active target response for Group 32 in the LANSCE scintillator response measurement for E_p = 450 to 2000 keV. These peaks show a similar large asymmetry as group 31, forming an even more prominent second peak. The distribution begins to fit to both peaks as low as 1300 keV.

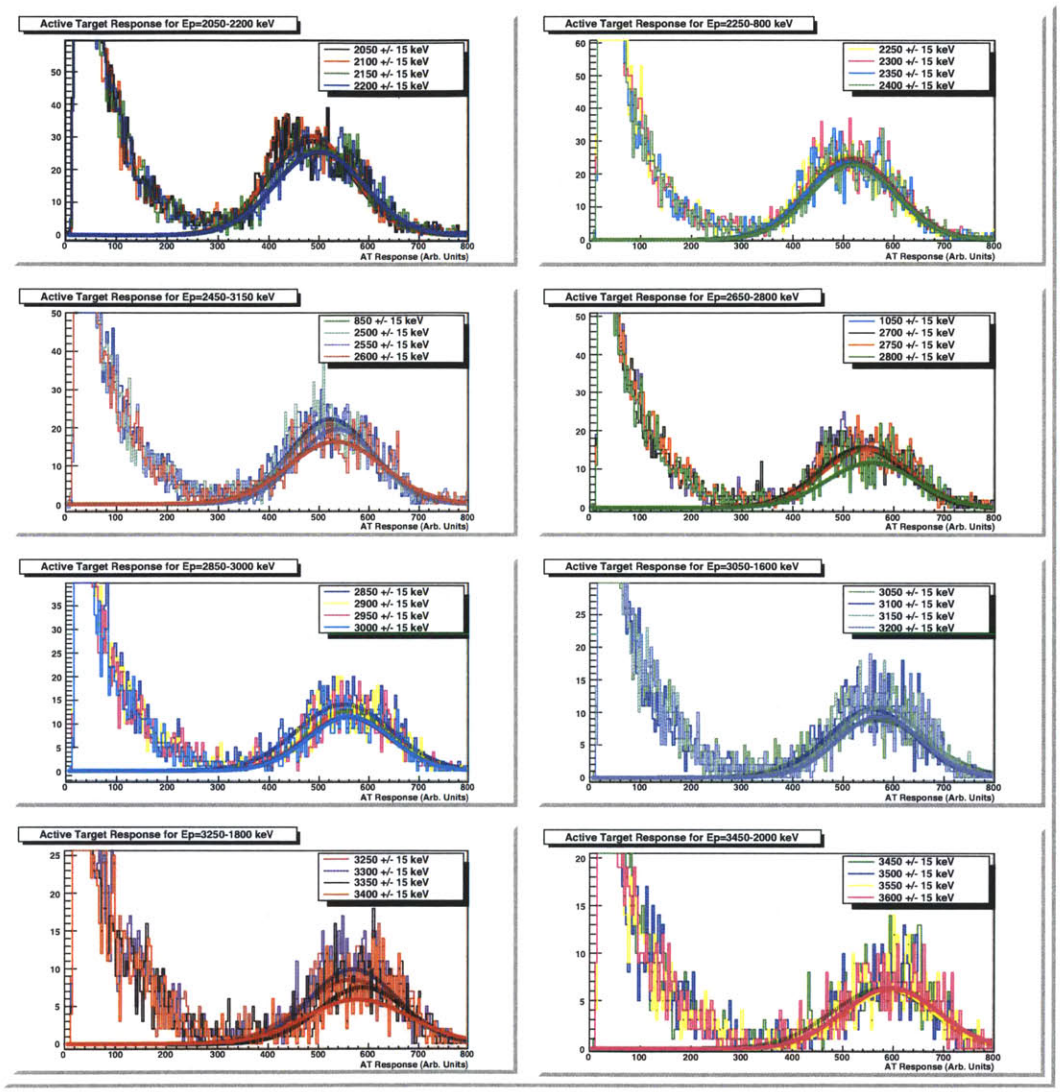

Figure A-25: Fitting the mean active target response for Group 32 in the LANSCE scintillator response measurement for for $E_p = 2050$ to 3600 keV. The asymmetry is no longer visible after the large shift in the mean at 1300 keV, and the mean value of the distributions are no longer changing significantly.

Appendix B

Full Index of Data

These sections summarize chronologically all the data and running conditions.

B.1 LANSCE Data

Data were taken at LANSCE in two running periods, June to July, 2010 and October to November, 2010. The runs were divided into groups based on the running conditions and the order in which the data were taken. A standard run was two hours long.

B.1.1 June to July, 2010

During the summer of 2010, data in groups 1 to 18, comprising runs 1600 to 1966, were performed at LANSCE. This data used the original, lower gain active target. The backgrounds were ultimately too high with this target, and none of this data was used in the results in section 6.1.

B.1.2 October to November 2010

After the development of the high gain active target, described in section 3.1, we returned to LANSCE in October of 2010 to take additional radiative capture and scintillator response data. These data comprised runs 2762 to 3385, divided into groups 19 to 32. Runs 2000 to 2761 were used for testing a new γ-ray rejecting neutron detector developed by UKY which is not discussed in this thesis (see [64] for more details).

Runs 2762 to 2860, groups 19 to 23, were debugging runs used to test the new active target and gain settings. The first data included in this thesis is group 24.

Group 24 Runs 2861 to 2952 comprised group 24, performed from 10/14/2010 to 10/22/2010. These data had active target top and bottom photomultiplier tube voltages of -2300 and -2325 V. The radiative capture results in section 6.1 are drawn entirely from group 24. Additionally, group 24 is the basis for the gain matching for the LANSCE scintillator response results, outlined in section 5.1.3. The liquid scintillator for detecting neutrons was placed at 15° for these data. Calibrations for these runs were conducted in runs 2953 to 2960.

Runs 2965 to 3053 were intended to be runs at a lower gain, with active target top and bottom photomultiplier tube voltages of -2050 and -2075 V, but difficulties with the beam limited their usefulness.

Group 25 Runs 3100 to 3171, performed from 11/5/2010 to 11/11/2010, used the active target as a passive target. We took this data as a single detector experiment, relying on the good energy resolution of the BrilLanCe^{TM} to identify capture events. Under these conditions the noise in the active target from the high energy neutrons which limited our flux was no longer present, and we were able to run with full beam intensity. The backgrounds in the BrilLanCe proved to be too large to enable any capture events to be distinguished. We concluded that the capture measurement required the active target in coincidence.

Group 26 Runs 3173 to 3185 were the first runs for the scintillator response measurement, performed on 11/11/2010. The neutron detector was moved to 45° to reach a larger range of proton recoil energies, and the active target photomultiplier tube voltages were lowered to -1750 V for both the top and bottom. This group is used in the results in section 5.1.

Group 27 Runs 3187 to 3202, performed on 11/12/2010 to 11/15/2010, raised the active target photomultiplier tube voltages to -1800 and -1900 V for the top and bottom, respectively. A gate timing mismatch in the electronics caused most of the scattered neutrons to fall out of the coincidence window. These data were not used in the results in section 5.1.

Group 28 Runs 3204 to 3217, performed on 11/15/2010, had the same conditions as group 27, but with the coincidence gate timing corrected. This group is

used in the results in section 5.1.

Group 29 Runs 3219 and 3220, performed on 11/16/2010, had the lowest active target gains, with top and bottom voltages of -1580 and -1650 V. This group is the only one to cover the entire range of responses in section 5.1 without showing any identifiable signs of saturation.

Group 30 Runs 3221 to 3230, performed on 11/16/2010, moved back up in gain, with top and bottom photomultiplier tube voltages of -2150 and -2300 V. This is the highest gain group used in section 5.1 which does not show significant asymmetry in the response.

Group 31 Runs 3231 to 3250, performed on 11/17/2010 to 11/18/2010, adjusted the top and bottom photomultiplier tube voltages back downwards to -1975 and -2100 V. This group shows significant asymmetry, but was still consistent with the rest of the results and was included in the results of section 5.1.

Group 32 Runs 3251 to 3284, performed on 11/19/2010 to 11/22/2010, moved back to higher gain with top and bottom photomultiplier tube voltages of -2065 and -2200 V. This group also shows significant asymmetry, but was still consistent with the rest of the results and was included in the results of section 5.1.

Group 33 Runs 3285 to 3385, performed on 11/24/2010 to 11/30/2010, moved the neutron detector into the beam in place of the active target, using another liquid scintillator to detect the scattered neutrons in order to measure the response of the liquid scintillator to recoiling protons. These data were intended for an undergraduate thesis, but were never fully analyzed.

B.2 UKY Data

At UKY, data were performed during three running periods: January 2011, April 2011, and June to July 2011.

B.2.1 January 2011

The first set of data used both the scintillator response and absorption configurations. They were performed using a 20 kÅ thick LiF target.

Scintillator Response The scintillator response data were performed in runs 8249 to 8304, from 1/19/2011 to 1/25/2011. The active target voltages were set to -2450 and -2250 V for the top and bottom photomultiplier tubes. With the thicker LiF target, the uncertainty in the neutron energy was much higher. Based on these results, we determined that a much thinner LiF target would be more useful for the scintillator response measurement. These data are not included in the results in section 5.2.

Total Cross Section The total cross section data were comprised of runs 8348 to 8393, from 1/27/2011 to 1/31/2011. These data used proton beam energies ranging from 2.00 to 2.55 MeV. The proton and neutron energy ranges for each set of runs is listed in table B.1. These data yield the total cross section results shown in figure 7-5 on page 223. Runs 8384 and 8385 used different openings for the analyzing magnet slits in order to test for rate dependence.

B.2.2 April 2011

The data taken in April 2011 were intended to be an improvement on the January 2011 results, taken in both the scintillator response and absorption configurations.

Total Cross Section Runs 8448 to 8496 were taken in the absorption configuration from 4/4/2011 to 4/8/2011. Normalization of this data was problematic and produced wildly scattered cross sections. These data were not used in the results in chapter 7.

Scintillator Response Runs 8503 to 8539 were taken in the scintillator response configuration from 4/8/2011 to 4/10/2011. With the high cross section for np elastic scattering, each run was only 1 hour. These data were taken using the 2 kÅ thick LiF target so that the neutron beam had a very narrow spread. The active target top and bottom photomultiplier tube voltages were set at -2500 V. The proton and neutron energies for each run are shown in table B.2. The minimum and maximum scattered neutron energies are determined from the acceptance of the neutron detector. These data were used for the scintillator response measurements shown in section 5.2

Run	Date	E_p (MeV)	$E_{n,\text{min}}$ (keV)	$E_{n,\text{max}}$ (keV)
8348	1/27/2011	2.25	450	500
8350	1/27/2011	2.35	550	600
8351	1/27/2011	2.35	550	600
8352	1/27/2011	2.45	650	700
8353	1/27/2011	2.15	340	400
8354	1/27/2011	2.20	400	450
8355	1/27/2011	2.30	500	550
8356	1/27/2011	2.30	500	550
8357	1/28/2011	2.00	150	200
8358	1/28/2011	2.00	150	200
8359	1/28/2011	2.05	200	250
8360	1/28/2011	2.05	200	250
8362	1/28/2011	2.10	250	350
8363	1/28/2011	2.10	250	350
8364	1/28/2011	2.15	340	400
8365	1/29/2011	2.45	650	700
8366	1/29/2011	2.40	600	650
8367	1/29/2011	2.40	600	650
8368	1/29/2011	2.35	550	600
8369	1/29/2011	2.30	500	550
8370	1/29/2011	2.25	450	500
8371	1/29/2011	2.20	400	450
8372	1/29/2011	2.20	400	450
8374	1/30/2011	2.20	400	450
8375	1/30/2011	2.15	340	400
8376	1/30/2011	2.15	340	400
8377	1/30/2011	2.10	250	350
8378	1/30/2011	2.10	250	350
8379	1/30/2011	2.10	250	350
8380	1/30/2011	2.05	200	250
8381	1/30/2011	2.05	200	250
8382	1/30/2011	2.00	150	200
8383	1/31/2011	2.00	150	200
8390	1/31/2011	2.50	700	750
8391	1/31/2011	2.50	700	750
8392	1/31/2011	2.55	750	800
8393	1/31/2011	2.55	750	800

Table B.1: Neutron and proton energies for each run of the total cross section data.

Run	Date	E_p (MeV)	E_n (keV)	$E_{s,\text{min scat}}$ (keV)	$E_{n,\text{max scat}}$ (keV)
8503	4/8/2011	2.25	520	235	285
8504	4/8/2011	2.40	680	300	375
8505	4/8/2011	2.70	995	450	550
8506	4/8/2011	2.60	890	400	490
8507	4/8/2011	2.50	785	350	430
8508	4/8/2011	2.80	1100	495	605
8509	4/8/2011	2.90	1200	540	660
8512	4/9/2011	4.10	2425	1090	1330
8513	4/9/2011	4.50	2830	1275	1555
8514	4/9/2011	4.90	3230	1455	1775
8515	4/9/2011	2.00	230	100	130
8516	4/9/2011	2.05	290	130	160
8517	4/9/2011	2.10	350	160	190
8520	4/9/2011	2.15	410	185	225
8521	4/9/2011	2.20	460	210	250
8522	4/9/2011	3.50	1815	820	1000
8523	4/9/2011	3.30	1610	725	885
8524	4/9/2011	3.10	1410	635	775
8531	4/10/2011	2.30	570	255	310
8532	4/10/2011	2.35	630	280	350
8533	4/10/2011	2.45	730	330	400
8536	4/10/2011	3.80	2120	955	1165
8537	4/10/2011	3.50	1815	820	1000
8538	4/10/2011	3.30	1610	725	885
8539	4/10/2011	3.60	1920	865	1055

Table B.2: Neutron and proton energies for each run of the scintillator response data.

First Run	Last Run	Start Date	End Date	Target	E_p (MeV)	E_n (MeV)
9044	9055	6/30/2011	7/1/2011	T	2.5	1.5
9056	-	7/1/2011	-	T	2.0	0.9
9057	9069	7/1/2011	7/2/2011	T	3.0	2.0
9070	9092	7/2/2011	7/4/2011	T	2.0	0.9
9096	9108	7/4/2011	7/5/2011	T	2.5	1.5
9109	9132	7/5/2011	7/7/2011	T	3.5	2.5
9133	9149	7/7/2011	7/8/2011	T	1.615	0.45
9150	9176	7/8/2011	7/10/2011	LiF	2.23	0.45

Table B.3: Neutron and proton energies for each set of runs for the radiative capture data.

B.2.3 June to July 2011

During the June to July 2011 running period, the radiative capture data discussed in section 6.2 were collected. The data were taken at 5 energies with the tritium cell target and at one energy with a LiF target. The runs for each proton energy with the resulting proton and neutron energies are shown in table B.3.

Bibliography

[1] S. Burles, K. M. Knollet, and M. S. Turner, "Big-Bang Nucleosynthesis: Linking Inner Space and Outer Space," *arXiv:astro-ph/9903300v1*, 1999.

[2] R. H. Cyburt, B. D. Fields, and K. A. Olive, "An update on the big bang nucleosynthesis prediction for 7 li: the problem worsens," *Journal of Cosmology and Astroparticle Physics*, vol. 2008, no. 11, p. 012, 2008.

[3] K. Nakamura and P. D. Group, "Review of particle physics," *Journal of Physics G: Nuclear and Particle Physics*, vol. 37, no. 7A, p. 075021, 2010.

[4] Y. Nagai, T. S. Suzuki, T. Kikuchi, T. Shima, T. Kii, H. Sato, and M. Igashira, "Measurement of ^{1}H$(n,\gamma)^2$H reaction cross section at a comparable $m1/e1$ strength," *Phys. Rev. C*, vol. 56, pp. 3173–3179, Dec 1997.

[5] A. Tomyo, Y. Nagai, T. Suzuki, T. Kikuchi, T. Shima, T. Kii, and M. Igashira, "Measurement of the p(n,γ)d reaction cross section between En = 100 and 350 keV," *Nuclear Physics A*, vol. 718, no. 0, pp. 401 – 403, 2003.

[6] T. Sato, M. Niwa, and H. Ohtsubo in *Proceedings of the International Symposium on Weak and Electromagnetic Interactions in Nuclei* (H. Ejiri, T. Kishimoto, and T. Sato, eds.), (Singapore), p. 488, World Scientific, 1995.

[7] G. R. Bishop, C. H. Collie, H. Halban, A. Hedgran, K. Siegbahn, S. du Toit, and R. Wilson, "The Cross Section for Photo-Disintegration of the Deuteron at Low Energies," *Phys. Rev.*, vol. 80, pp. 211–222, Oct 1950.

[8] C. A. Barnes, J. H. Carver, G. H. Stafford, and D. H. Wilkinson, "The photodisintegration of the deuteron at intermediate energies. i," *Phys. Rev.*, vol. 86, pp. 359–372, May 1952.

[9] R. Moreh, T. J. Kennett, and W. V. Prestwich, "^{2}H(γ , n) absolute cross section at 2754 kev," *Phys. Rev. C*, vol. 39, pp. 1247–1250, Apr 1989.

[10] K. Y. Hara, H. Utsunomiya, S. Goko, H. Akimune, T. Yamagata, M. Ohta, H. Toyokawa, K. Kudo, A. Uritani, Y. Shibata, Y.-W. Lui, and H. Ohgaki, "Photodisintegration of deuterium and big bang nucleosynthesis," *Phys. Rev. D*, vol. 68, p. 072001, Oct 2003.

[11] K. ichi Shinohara, T. Okada, and S. Morita, "Determination of cross section for the photo-disintegration of deuteron," *Journal of the Physical Society of Japan*, vol. 4, no. 2, pp. 77–82, 1949.

[12] G. Hale, D. Dodder, E. Siciliano, and W. Wilson, "Endf/b-vi, evaluation, material 125, revision 1," 1991.

[13] K. Shibata, "JENDL 3.3 Evaluation, material 125," 2002.

[14] D. H. Frisch, "The Total Cross Sections of Carbon and Hydrogen for Neutrons of Energies from 35 to 490 kev," *Phys. Rev.*, vol. 70, pp. 589–592, Nov 1946.

[15] A. L. Kirilyuk, A. V. Grebnev, P. N. Vorona, and N. L. Gnidak *C87KIEV2*, vol. 289, 1987.

[16] C. E. Engelke, R. E. Benenson, E. Melkonian, and J. M. Lebowitz, "Precision Measurements of the $n - p$ Total Cross Section at 0.4926 and 3.205 MeV," *Phys. Rev.*, vol. 129, pp. 324–337, Jan 1963.

[17] L. Koester, W. Waschkowski, and J. Meier, "Cross sections for neutrons of 1970 ev and contributions to fundamental neutron interactions," *Zeitschrift fr Physik A Hadrons and Nuclei*, vol. 337, pp. 341–348, 1990. 10.1007/BF01289703.

[18] W. D. Allen and A. T. G. Ferguson, "The n-p Cross Section in the Range 60-550 keV," *Proceedings of the Physical Society. Section A*, vol. 68, no. 11, p. 1077, 1955.

[19] C. L. Bailey, W. E. Bennett, T. Bergstralth, R. G. Nuckolls, H. T. Richards, and J. H. Williams, "The neutron-proton and neutron-carbon scattering cross sections for fast neutrons," *Phys. Rev.*, vol. 70, pp. 583–589, Nov 1946.

[20] J. Clement, P. Stoler, C. Goulding, and R. Fairchild, "Hydrogen and deuterium total neutron cross sections in the MeV region," *Nuclear Physics A*, vol. 183, no. 1, pp. 51 - 59, 1972.

[21] W. P. Poenitz and J. F. Whalen, "Measurements of the total neutron cross sections of hydrogen and carbon at 0.5, 1.0 and 2.0 MeV," *Nuclear Physics A*, vol. 383, no. 2, pp. 224 – 232, 1982.

[22] E. Bretscher and E. B. Martin, "Determination of the collision cross section of hydrogen, deuterium, carbon, and oxygen for fast neutrons," *Helvetica Physica Acta*, vol. 23, p. 15, 1950.

[23] D. S. S. et. al., "Precision neutron transmission and energy measurement by time-of-flight," *3rd Conf. Neutron Cross-Sections and Tech.*, vol. 2, p. 543, 1971.

[24] G. M. Hale and A. S. Johnson in *Proc. 17th Int. IUPAP Conf. on Few-Body Problems in Physics, 5-10 June 2003* (W. Gloeckle and W. Tornow, eds.), (Durham NC), pp. S120–S122, Elsevier B.V., 2004.

[25] D. P. Donnelly, J. J. Reidy, and M. L. Wiedenbeck, "High-resolution gamma-ray spectroscopic study of the decay ^{133}Ba $\rightarrow$ ^{133}Cs," *Phys. Rev.*, vol. 173, pp. 1192–1201, Sep 1968.

[26] D. Smith, R. Polk, and T. Miller, "Measurement of the response of several organic scintillators to electrons, protons and deuterons," *Nuclear Instruments and Methods*, vol. 64, no. 2, pp. 157 – 166, 1968.

[27] E. Brannen and G. L. Olde, "The response of organic scintillators to electron energy deposited in them," *Radiation Research*, vol. 16, pp. 1–6, 2012/03/14 1962.

[28] R. Craun and D. Smith, "Analysis of response data for several organic scintillators," *Nuclear Instruments and Methods*, vol. 80, no. 2, pp. 239 – 244, 1970.

[29] S. Saraf, C. Brient, P. Egun, S. Grimes, V. Mishra, and R. Pedroni, "Determination of the light response of BC-404 plastic scintillator for protons and deuterons with energies between 1 and 11 MeV," *Nuclear Instruments and Methods in Physics Research Section A: Accelerators, Spectrometers, Detectors and Associated Equipment*, vol. 268, no. 1, pp. 200 – 203, 1988.

[30] S. Saraf, N. Al-Niemi, C. Brient, S. Grimes, and R. Pedroni, "Determination of the light response of BC-404 plastic scintillator for 3He and 4He with energies between 3 and 13 MeV," *Nuclear Instruments and Methods in Physics*

Research Section A: Accelerators, Spectrometers, Detectors and Associated Equipment, vol. 288, no. 23, pp. 451 – 454, 1990.

[31] S. Pearlstein, "ENDF/HE-VI Evaluation, material 625," 1993.

[32] C. M. Huddleston, R. O. Lane, L. L. Lee, and F. P. Mooring, "Total neutron cross section for c^{12} from 500 kev to 1350 kev," *Phys. Rev.*, vol. 117, pp. 1055–1056, Feb 1960.

[33] R. M. Wilenzick, G. E. Mitchell, K. K. Seth, and H. W. Lewis, "Measurement and interpretation of neutron total cross sections of carbon, calcium, and lead," *Phys. Rev.*, vol. 121, pp. 1150–1158, Feb 1961.

[34] C. A. Uttley, "Data from NNDC, file EXFOR 20909002," 1964.

[35] "BrilLanCe^{TM} Scintillators Performance Summary," January 2009.

[36] R. W. Hackenburg, "Neutron-proton effective range parameters and zero-energy shape dependence," *Phys. Rev. C*, vol. 73, p. 044002, Apr 2006.

[37] D. N. Schramm and M. S. Turner, "Big-bang nucleosynthesis enters the precision era," *Rev. Mod. Phys.*, vol. 70, pp. 303–318, Jan 1998.

[38] S. Burles and D. Tytler, "The Deuterium Abundance toward Q1937-1009," *The Astrophysical Journal*, vol. 499, no. 2, p. 699, 1998.

[39] S. Burles and D. Tytler, "The Deuterium Abundance toward QSO 1009+2956," *The Astrophysical Journal*, vol. 507, no. 2, p. 732, 1998.

[40] S. Burles, K. M. Nollett, J. W. Truran, and M. S. Turner, "Sharpening the predictions of big-bang nucleosynthesis," *Phys. Rev. Lett.*, vol. 82, pp. 4176–4179, May 1999.

[41] R. Sachs, *Nuclear Theory*. Cambridge: Addison-Wesley, 1953.

[42] T. S. Suzuki, Y. Nagai, T. Shima, T. Kikuchi, H. Sato, T. Kii, and M. Igashira, "First measurement of a p(n, gamma)d reaction cross section between 10 and 80 keV," *Astrophysical Journal*, vol. 439, pp. L59–L62, 1995.

[43] R. Hannaske, D. Bemmerer, R. Beyer, E. Birgersson, E. Grosse, A. Hartmann, A. R. Junghans, M. Kempe, T. Kögler, K. Kosev, M. Marta, R. Massarczyk, A. Matic, K.-D. Schilling, G. Schramm, R. Schwngner, M. Sobiella, D. Stach,

A. Wagner, and D. Yakorev, "Towards a precision measurement of the photodissociation of the deuteron at energies relevant to Big Bang nucleosynthesis," in *11th Symposium on Nuclei in the Cosmos*, (Heidelberg, Germany), July 2010.

[44] N. Ryezayeva, H. Arenhövel, O. Burda, A. Byelikov, M. Chernykh, J. Enders, H. W. Grießhammer, Y. Kalmykov, P. von Neumann-Cosel, B. Özel, I. Poltoratska, I. Pysmenetska, C. Rangacharyulu, S. Rathi, A. Richter, G. Schrieder, A. Shevchenko, and O. Yevetska, "Measurement of the reaction ^{2}H(e, e') at 180° close to the deuteron breakup threshold," *Phys. Rev. Lett.*, vol. 100, p. 172501, Apr 2008.

[45] S. R. Beane and M. J. Savage, "Rearranging pionless effective field theory," *Nuclear Physics A*, vol. 694, no. 34, pp. 511 – 524, 2001.

[46] R. Machleidt, F. Sammarruca, and Y. Song, "Nonlocal nature of the nuclear force and its impact on nuclear structure," *Phys. Rev. C*, vol. 53, pp. R1483–R1487, Apr 1996.

[47] S. Nakamura, T. Sato, V. Gudkov, and K. Kubodera, "Neutrino reactions on the deuteron," *Phys. Rev. C*, vol. 63, p. 034617, Feb 2001.

[48] R. Schiavilla, V. G. J. Stoks, W. Glöckle, H. Kamada, A. Nogga, J. Carlson, R. Machleidt, V. R. Pandharipande, R. B. Wiringa, A. Kievsky, S. Rosati, and M. Viviani, "Weak capture of protons by protons," *Phys. Rev. C*, vol. 58, pp. 1263–1277, Aug 1998.

[49] H. A. Bethe, "Theory of the effective range in nuclear scattering," *Phys. Rev.*, vol. 76, pp. 38–50, Jul 1949.

[50] W. Dilg, "Measurement of the neutron-proton total cross section at 132 ev," *Phys. Rev. C*, vol. 11, pp. 103–109, Jan 1975.

[51] H. Liskien and A. Paulsen, "Neutron production cross sections and energies for the reactions ^{7}Li(p,n)^{7}Be and ^{7}Li(p,n)^{7}Be," *Atomic Data and Nuclear Data Tables*, vol. 15, no. 1, pp. 57 – 84, 1975.

[52] H. Liskien and A. Paulsen, "Neutron production cross sections and energies for the reactions T(p,n)^{3}He, D(d,n)^{3}He, and T(d,n)^{4}He," *Atomic Data and Nuclear Data Tables*, vol. 11, no. 7, pp. 569 – 619, 1973.

[53] W. R. Leo, *Techniques for Nuclear and Particle Physics Experiments.* New York: Springer-Verlag, 1994.

[54] S. Wender, S. Balestrini, A. Brown, R. Haight, C. Laymon, T. Lee, P. Lisowski, W. McCorkle, R. Nelson, W. Parker, and N. Hill, "A fission ionization detector for neutron flux measurements at a spallation source," *Nuclear Instruments and Methods in Physics Research Section A: Accelerators, Spectrometers, Detectors and Associated Equipment*, vol. 336, no. 12, pp. 226 – 231, 1993.

[55] S. Ritt, P.-A. Amaudruz, S. Ballestrero, S. Daviel, P. Green, Q. Gu, G. Hackman, G. Hofman, P. Knowles, E. Lee, R. Meier, G. Moloney, D. Morris, J. M. O'Donnell, K. Olchanski, C. Pearson, R. Poutissou, T. Schurman, A. Suter, J. M.Wouters, and P. A. Zolnierczuk, *Midas DOC Version 2.3.0*, 2010.

[56] T. Rinckel, 2007. Private Communication.

[57] J. B. Birks, *The Theory and Practice of Scintillation Counting.* New York: Macmillan, 1964.

[58] C. N. Chou, "The nature of the saturation effect of fluorescent scintillators," *Phys. Rev.*, vol. 87, pp. 904–905, Sep 1952.

[59] S.-G. Crystals, "BC400, BC404, BC408, BC412, BC416 Datasheet," 2008.

[60] S.-G. Crystals, "BC418, BC420, BC422 Datasheet," 2008.

[61] E. Melkonian, "A precise determination of the slow neutron cross section of the free proton," *Phys. Rev.*, vol. 76, pp. 1744–1749, Dec 1949.

[62] L. Koester and W. Nistler, "Neutron-proton and neutron-carbon scattering amplitudes," *Phys. Rev. Lett.*, vol. 27, pp. 956–958, Oct 1971.

[63] L. Koester and W. Nistler, "New determination of the neutron-proton scattering amplitude and precise measurements of the scattering amplitudes on carbon, chlorine, fluorine and bromine," *Zeitschrift fr Physik A Hadrons and Nuclei*, vol. 272, pp. 189–196, 1975. 10.1007/BF01408146.

[64] M. A. Kovash, B. Daub, J. French, V. Henzl, K. Shoniyozov, J. L. Matthews, Z. Miller, and H. Yang, "Detecting sub-MeV neutrons in solid plastic scintillator with gamma-ray discrimination," in *Second International Conference on Advancements in Nuclear Instrumentation, Measurement Methods and their Applications*, (Ghent), June 2011.